

# STUDY OF SOME DOPED SUPERCONDUCTING AND ASSOCIATED OXIDES

by  
SANDEEP SINGH

TH  
Phy/1995/D  
S. 64 S



DEPARTMENT OF PHYSICS

**INDIAN INSTITUTE OF TECHNOLOGY KANPUR**

JULY, 1995

# STUDY OF SOME DOPED SUPERCONDUCTING AND ASSOCIATED OXIDES

*A Thesis Submitted*  
in Partial Fulfilment of the Requirements  
for the Degree of  
DOCTOR OF PHILOSOPHY

by  
SANDEEP SINGH

*to the*  
DEPARTMENT OF PHYSICS  
INDIAN INSTITUTE OF TECHNOLOGY KANPUR

25 AUG 1997  
CENTRAL  
I. I. T., KANPUR  

---

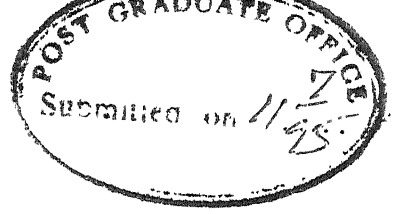
No. A 125033

PHY-1995-D-SIN-STU

100

To my parents





# CERTIFICATE

This is to certify that the work presented in this thesis entitled "STUDY OF SOME DOPED SUPERCONDUCTING AND ASSOCIATED OXIDES" by Sandeep Singh has been done under my supervision and it has not been submitted elsewhere.

D.C. Khan 30.6.95  
Prof. D.C. Khan  
Department of Physics  
Indian Institute of Technology  
Kanpur INDIA

## SYNOPSIS

### STUDY OF SOME DOPED SUPERCONDUCTING AND ASSOCIATED OXIDES

The discovery of superconductivity in LaBaCuO has been followed by intense efforts for search for oxide compounds with higher transition temperature as well as for exploring their physical properties. As a result many new materials have been discovered. The transition temperature has reached as high as 133K in HgBaCaCuO system. The materials exhibit diverse physical properties which are difficult to explain within conventional microscopic theories. The structure determination has revealed that the compounds have layered crystal structure and contain Cu-O planes as common structural elements. The Cu-O planes are separated from each other by layers of other oxides and rare-earths. The layers other than Cu-O planes are called charge reservoir which provide charge carriers or coupling mechanism required for superconductivity. Studies have shown that superconductivity in these materials is predominantly 2-dimensional and occurs in Cu-O plane.

The superconducting properties of oxide materials have been found to be sensitive to chemical composition. In conventional superconductors a large amount of non-magnetic impurities have virtually no effect on superconductivity whereas a small amount of magnetic impurities decrease

transition temperature drastically. The insensitivity of conventional superconductors to non-magnetic impurities is essentially due to zero angular momentum of Cooper pair i.e. s-wave pairing. On the contrary, high temperature superconductors show decrease of transition temperature both for magnetic and non-magnetic impurities. In some compounds non-magnetic impurities have been found to decrease transition temperature faster than magnetic impurities. Many mechanisms for the suppression of superconductivity have been proposed and the subject remains controversial. With increase of impurity concentration superconductivity eventually vanishes and the system becomes insulating. In the insulating state variable range hopping of conduction mechanism is observed and the parameters of hopping mechanism give information about the density of states near Fermi level.

Evidently, an effective tool to probe the parameters essential for superconductivity is the introduction of impurities and study their effect on normal state and superconducting properties. A substantial amount of information to this end may be obtained from the study of polycrystalline samples which are easy to fabricate and handle.

The present thesis is focused on two aspects of superconductivity problem. The first aspect of the problem which forms the major part of the work, discusses the effect of two rare earth impurities (Gd and Sm) on superconducting properties of  $\text{Bi}_2\text{Sr}_2\text{Ca}_1\text{Cu}_2\text{O}_{8+\delta}$  system. The second aspect is the

search for high temperature superconductivity in a series of ferrites.

The first chapter is an introduction to high temperature superconductivity. The salient features of high temperature superconductors such as crystal structure, normal state properties, superconducting properties and magnetic properties have been discussed in this chapter. The behaviour of conventional superconductors have also been presented briefly in each section. In the end we describe some of the theoretical models which have been proposed for the occurrence of high temperature superconductivity.

The second chapter consists of two sections. The first section deals with sample preparation techniques, various experimental set-ups and experimental methodologies. The experiments include electrical resistivity, Hall effect, ac susceptibility and magnetoresistance measurements. The second section is a description of Mössbauer effect and methods of Mössbauer spectroscopy. The experimental details of low temperature Mössbauer spectroscopy have also been discussed.

The third chapter describes the effect of Gd substitution on superconducting properties of  $\text{Bi}_2\text{Sr}_2\text{Ca}_1\text{Cu}_2\text{O}_{8+\delta}$  system. Single phase  $\text{Bi}_2\text{Sr}_{2-x}\text{Gd}_x\text{Ca}_1\text{Cu}_2\text{O}_{8+\delta}$  ( $x=0.0-0.65$ ) samples have been synthesized and are studied through X-ray and transport measurements. The resistivity measurements show that transition temperature increases with  $x$  followed by a decrease till superconductivity is destroyed. The carrier concentration

decreases with increase of Gd concentration in the system. The data interpretation shows that suppression of superconductivity occurs due to hole filling and disorder. In the insulating state 3-D variable range hopping is observed and the data agree well with a model having density of states near Fermi level concave in nature. The magnetoresistance measurement indicates the presence of temperature-dependent activation energy for the flow of flux lines.

The fourth chapter deals with X-ray, ac susceptibility and Mössbauer studies of  $\text{Bi}_2\text{Sr}_{2-x}\text{Gd}_x\text{Ca}_1\text{Cu}_{1.96}\text{Fe}_{0.04}\text{O}_{8+\delta}$  system. X-ray measurement shows all samples consisting of single phase  $\text{Bi}_2\text{Sr}_2\text{Ca}_1\text{Cu}_2\text{O}_{8+\delta}$  system. AC susceptibility measurement which was performed using a pair of pick-up coils and lock-in technique reveals that the dissipative component of ac susceptibility decreases with increase of Gd concentration. Since Fe replaces Cu in the system the relevant information about electronic structure of Cu can be obtained through Mössbauer spectroscopy. The interpretation of room temperature Mössbauer data shows localization of charge carriers induced by Gd doping. Moreover, we have performed temperature dependent Mössbauer measurements also. The temperature dependence of the center shift does not show phonon softening below transition temperature and is well described by the Debye model of the solids. The fact shows that motion of Fe atoms remain harmonic below transition temperature. Debye temperature of the samples have been estimated from the data fitting.

The fifth chapter contains study of  $\text{Bi}_2\text{Sr}_2\text{Ca}_{1-x}\text{Sm}_x\text{Cu}_2\text{O}_{8+\delta}$  and  $\text{Bi}_2\text{Sr}_2\text{Ca}_{1-x}\text{Sm}_x\text{Cu}_{1.95}\text{Co}_{0.05}\text{O}_{8+\delta}$  systems. The transition temperature vs Sm concentration curves determined from susceptibility measurement shows different behaviour in these two systems. The measured susceptibility signal decreases with increasing Sm concentration. Magnetoresistance measurements for samples close to metal insulator transition showed a positive magnetoresistance in  $\text{Bi}_2\text{Sr}_2\text{Ca}_{0.6}\text{Sm}_{0.4}\text{Cu}_{1.95}\text{Co}_{0.05}\text{O}_{8+\delta}$  sample. An unusual maxima in magnetoresistance is observed by annealing the sample in flowing oxygen. The suppression of  $T_c$  is discussed to be due to hole filling and disorder rather than magnetic pair breaking effect. We show that metal insulator transition in rare earth doped  $\text{Bi}_2\text{Sr}_2\text{Ca}_1\text{Cu}_2\text{O}_{8+\delta}$  system is of Anderson type.

The sixth chapter deals with the study of electrical and magnetic properties of  $\text{Zn}_x\text{Ca}_{1-x}\text{Fe}_2\text{O}_4$  system. The interest in this study derives from a report of the existence of superconductivity in  $\text{Zn}_{0.5}\text{Ca}_{0.5}\text{Fe}_2\text{O}_4$  system around a dramatically high temperature of 200K. The study of whole series establishes that the above system is not a high temperature superconductor for entire concentration range of x although the data did show an anomaly for x=0.5 concentration. The conductivity data has been interpreted within the framework of small polaron theory.

In the end we have presented the summary of the conclusions of the thesis.



## ACKNOWLEDGMENTS

It is of great pleasure to me to express my profound gratitude to Prof. D.C. Khan for his able guidance, constant help and encouragement in matters both academic and otherwise, throughout the course of my research work.

I am also grateful to Profs. K. Shahi, S.C. Agarwal, R. Prasad, P. Gupta Bhaiya, O.P. Katyal, K.P. Rajeev, Satyendra Kumar, M.K. Verma and Dr. Prem Chand for fruitful discussions and suggestions.

I express my sincere regards to Mrs. S. Khan for affection and many cups of coffee.

I sincerely thank Dr R.C. Srivastava, Dr. V.K. Shankarnarayanan and Debasis for help in various ways.

I am also thankful to Dr. Ram Bilas, Shri D.K. Kanaujia and Rajendra for technical and other help.

I thank people in Physics Workshop in particular Shri Ram Singh and Shri Ram Mangal Singh for their kind cooperation.

I am thankful to Shri A.K. Srivastava for typing and Shri A.K. Ganguly for prompt and nice tracing of figures.

I am also thankful to Shri N.K. Metia for excellent printouts.

I deeply appreciate the endurance and patience of my parents and brother for entire course of work.

Sandeep Singh





## CONTENTS

	Page No
CERTIFICATE	i
SYNOPSIS	ii
ACKNOWLEDGEMENT	vii
CHAPTER 1 INTRODUCTION	1
1.1 Compounds Discovered	2
1.2 Crystal Structure	4
1.3 Normal State Properties	10
1.3.1 Normal State Resistivity	10
1.3.2 Hall Effect	12
1.3.3 Electronic Structure	14
1.4 Superconducting Properties	16
1.4.1 Coherence Length	16
1.4.2 Penetration Depth	18
1.4.3 Energy Gap	20
1.4.4 Isotope Effect	21
1.4.5 Specific Heat	22
1.4.6 Symmetry of Paired Electrons	24
1.5 Effect of Impurities	25
1.6 Magnetic Properties	28
1.7 Proposed Theoretical Models	29
1.8 Motivation of the Present Work	33
1.9 References	34

CHAPTER 2	EXPERIMENTAL TECHNIQUES AND INSTRUMENTATION	43
	SECTION A:	
2.1	Sample Preparation Assembly	43
2.2	Sample Preparation	44
2.2.1	$\text{Zn}_x\text{Ca}_{1-x}\text{Fe}_2\text{O}_4$ system	44
2.2.2	$\text{Bi}_2\text{Sr}_{2-x}\text{Gd}_x\text{Ca}_1\text{Cu}_2\text{O}_{8+\delta}$ and $\text{Bi}_2\text{Sr}_{2-x}\text{Gd}_x\text{Ca}_1\text{Cu}_{1.96}\text{Fe}_{0.04}\text{O}_{8+\delta}$ systems	44
2.2.3	$\text{Bi}_2\text{Sr}_2\text{Ca}_{1-x}\text{Sm}_x\text{Cu}_2\text{O}_{8+\delta}$ and $\text{Bi}_2\text{Sr}_2\text{Ca}_{1-x}\text{Sm}_x\text{Cu}_{1.95}\text{Co}_{0.05}\text{O}_{8+\delta}$ systems	45
2.3	Electrical Resistivity Measurement	46
2.3.1	Set-up	46
2.3.2	Contact Deposition	47
2.3.3	Methodology	50
2.4	AC Susceptibility Measurement	52
2.5	Hall Effect Measurement	56
2.6	Magnetoresistance Measurement	58
	SECTION B:	
2.7	Mössbauer Spectroscopy	59
2.7.1	Isomer Shift and Second Order Doppler Effect	61
2.7.2	Quadrupole Splitting	62
2.7.3	Magnetic Hyperfine Interaction	63
2.8	Mössbauer Spectroscopy Instrumentation	64
2.9	Low Temperature Mössbauer Measurement	67
2.10	References	71

CHAPTER 3	STUDY OF Gd SUBSTITUTED $\text{Bi}_2\text{Sr}_2\text{Ca}_1\text{Cu}_2\text{O}_{8+\delta}$ SYSTEM	
3.1	Introduction	72
3.2	Previous Studies on Y or Rare Earth Doped 2:2:1:2 System	74
	Results and Discussions:	
3.3	Crystal Structure and Lattice Parameters	77
3.4	Hole Concentration and Transition Temperature	80
3.5	Electrical Resistivity	85
3.6	Discussions	88
	3.6.1 Effect of Disorder	88
	3.6.2 Destruction of Superconductivity	94
	3.6.3 The Insulating State	97
3.7	Magnetoresistance	103
3.8	Conclusions	107
3.9	References	107
CHAPTER 4	MÖSSBAUER STUDY OF $\text{Bi}_2\text{Sr}_{2-x}\text{Gd}_x\text{Ca}_1\text{Cu}_2\text{O}_{8+\delta}$ SYSTEM	
4.1	Introduction	113
	Results and Discussions:	114
4.2	X-ray Analysis	114
4.3	AC Susceptibility	114
4.4	Room Temperature Mössbauer Study	123
	4.4.1 Results	123
	4.4.2 Discussions	129
4.5	Temperature Dependent Mössbauer Study	133
4.6	Conclusions	139

4.7	References	139
CHAPTER 5	STUDY OF Sm AND Co SUBSTITUTED $\text{Bi}_2\text{Sr}_2\text{Ca}_1\text{Cu}_2\text{O}_{8+\delta}$ SYSTEM	
5.1	Introduction	143
	Results and Discussions	
5.2	X-ray Study	144
5.3	Transition Temperature	144
5.4	Resistivity Data	152
5.5	Mössbauer Study	168
5.6	Conclusions	170
5.7	References	171
CHAPTER 6	ELECTRICAL AND MAGNETIC PROPERTIES OF $\text{Zn}_x\text{Ca}_{1-x}\text{Fe}_2\text{O}_4$ SYSTEM	
6.1	Introduction	175
	Results and Discussions:	
6.2	X-ray Study	176
6.3	Mössbauer Hyperfine Parameters	177
6.4	Magnetization Measurement	185
6.5	EPR Study	186
6.6	Resistivity Study	188
	6.6.1 Small Polaron Theories of Resistivity	188
	6.6.2 Resistivity Results and Discussions	193
6.7	Conclusions	198
6.8	References	199
	Summary of Conclusions	202

## CHAPTER 1

### INTRODUCTION

The phenomenon of superconductivity was first discovered by Kammerlingh Onnes in 1911. Till 1986, the highest temperature for transition to the superconducting state was 23.2K (in  $\text{Nb}_3\text{Ge}$ ). Within the framework of BCS theory this was considered to be about the highest possible transition temperature. Because of this relatively low transition temperature the use of these materials for technological applications was restricted.

The discovery of superconductivity above 30K in  $\text{LaBaCuO}$  system by Bednorz and Müller [1] triggered a spurt of research activities on high temperature superconductivity. Following their discovery several classes of oxide materials were explored with progressively increasing transition temperature, the highest transition temperature to date being 133K in  $\text{HgBaCaCuO}$  system. The crystal structure of many of these materials feature  $\text{CuO}$  planes leading to anisotropic superconducting properties. These materials are important on two grounds. Firstly, their future technological applications and secondly the conventional electron-phonon interaction

appears not to be the origin of superconductivity. Although the superconducting state is based on electron pairs, the latter fact has left fundamental physics open to investigation. Most of the familiar phenomena which are manifestations of the superconducting effect such as Josephson tunneling, persistent current and vortex lattice have been established conclusively in these materials. At the same time the presence of anisotropy, granular structure and an unusual range of parameter values such as coherence length points to the existence of unusual features. The existence of vortex structure has revealed that these materials are type II superconductors. On the theoretical front many models have been proposed although mechanism of superconductivity remains far from clear.

A typical phase diagram of a high temperature superconductor consists of normal metallic, superconducting and insulating phases and is shown in Fig. 1.1 for  $\text{Y}_1\text{Ba}_2\text{Cu}_3\text{O}_{7-\delta}$  system. The variation of proper dopant concentration, oxygen in this case, leads to formation of different phases. In the present chapter we discuss some of the salient features corresponding to these phases including few proposed models for the occurrence of superconductivity.

### 1.1 Compounds Discovered:

The superconductivity in oxide was first discovered in  $\text{BaPb}_x\text{Bi}_{1-x}\text{O}_3$  ( $T_c=13\text{K}$ ) system back in 1975 [2]. The discovery of superconductivity in  $\text{La}_{2-x}\text{M}_x\text{CuO}_4$  ( $\text{M}=\text{Sr}, \text{Ba}$  or  $\text{Ca}$ ) [1] stimulated

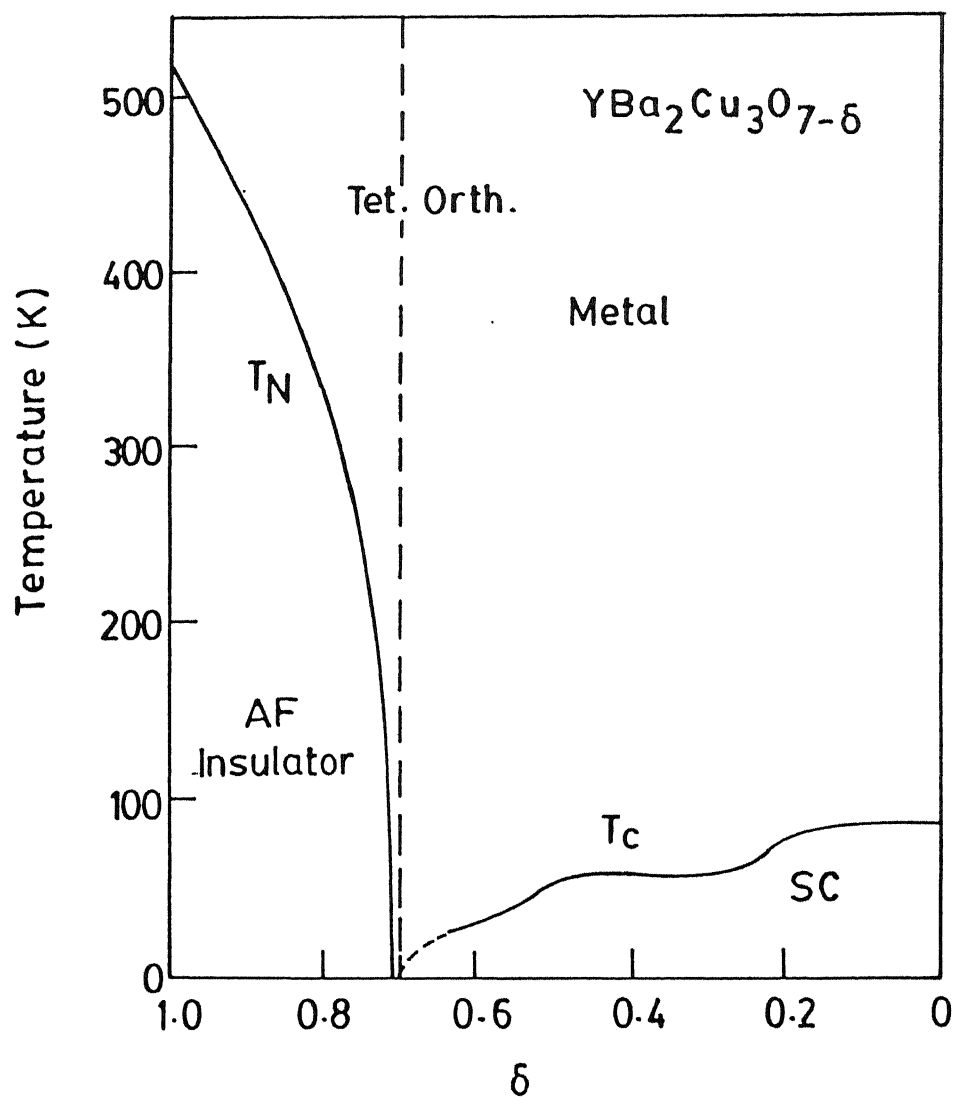


Fig. 1.1 Phase diagram for  $\text{Y}_1\text{Ba}_2\text{Cu}_3\text{O}_{7-\delta}$  as a function of oxygen concentration  $\delta$ . Superconducting (SC), antiferromagnetic (AF) and tetragonal (tet) to orthorhombic (orth) phases are shown.



search for new copper oxide based compounds with higher transition temperature. Subsequently, Wu and coworker discovered superconductivity above 90K in Y-Ba-Cu-O system [3]. The phase was identified as an ordered defect perovskite structure with composition  $Y_1Ba_2Cu_3O_{7-\delta}$  [4]. In 1988, superconductivity above 100K in the Bi-Sr-Ca-Cu-O system was discovered by H. Maeda et.al. [5] and in the Tl-Ca-Ba-Cu-O system by Herman and Sheng [6]. Three superconducting oxides were subsequently identified in the Bi-Ca-Sr-Cu-O system:  $Bi_2Sr_2Cu_1O_{6+\delta}$  ( $T_c=7-22K$ ),  $Bi_2Sr_2Ca_1Cu_2O_{8+\delta}$  ( $T_c=85K$ ) and  $Bi_2Sr_2Ca_2Cu_3O_{10+\delta}$  ( $T_c=110K$ ) [7,8]. Similarly in Tl-Ca-Ba-Cu-O system six perovskite-related oxides have been identified. The highest transition temperature achieved so far was 125K in  $Tl_2Ba_2Cu_2Cu_3O_{10}$  system. With the discovery of superconductivity in  $Hg_1Ba_2Ca_2Cu_3O_{8+\delta}$  compound in 1993, the  $T_c$  has gone upto 133K [9].

## 1.2 Crystal Structure:

The crystal structure of high temperature superconducting materials has been determined by X-ray and neutron diffraction methods. It turns out that common structural element of all cuprates is the presence of one or more  $CuO_2$  planes. Each Cu-atom in the plane is surrounded by four oxygen atoms in a square planar configuration as is shown in Fig. 1.2. In the crystal structure,  $CuO_2$  planes form  $ab$  planes perpendicular to  $c$ -axis. The  $CuO_2$  planes can occur singly or in groups. Within a group, individual  $CuO_2$  planes are separated by metal atoms e.g.

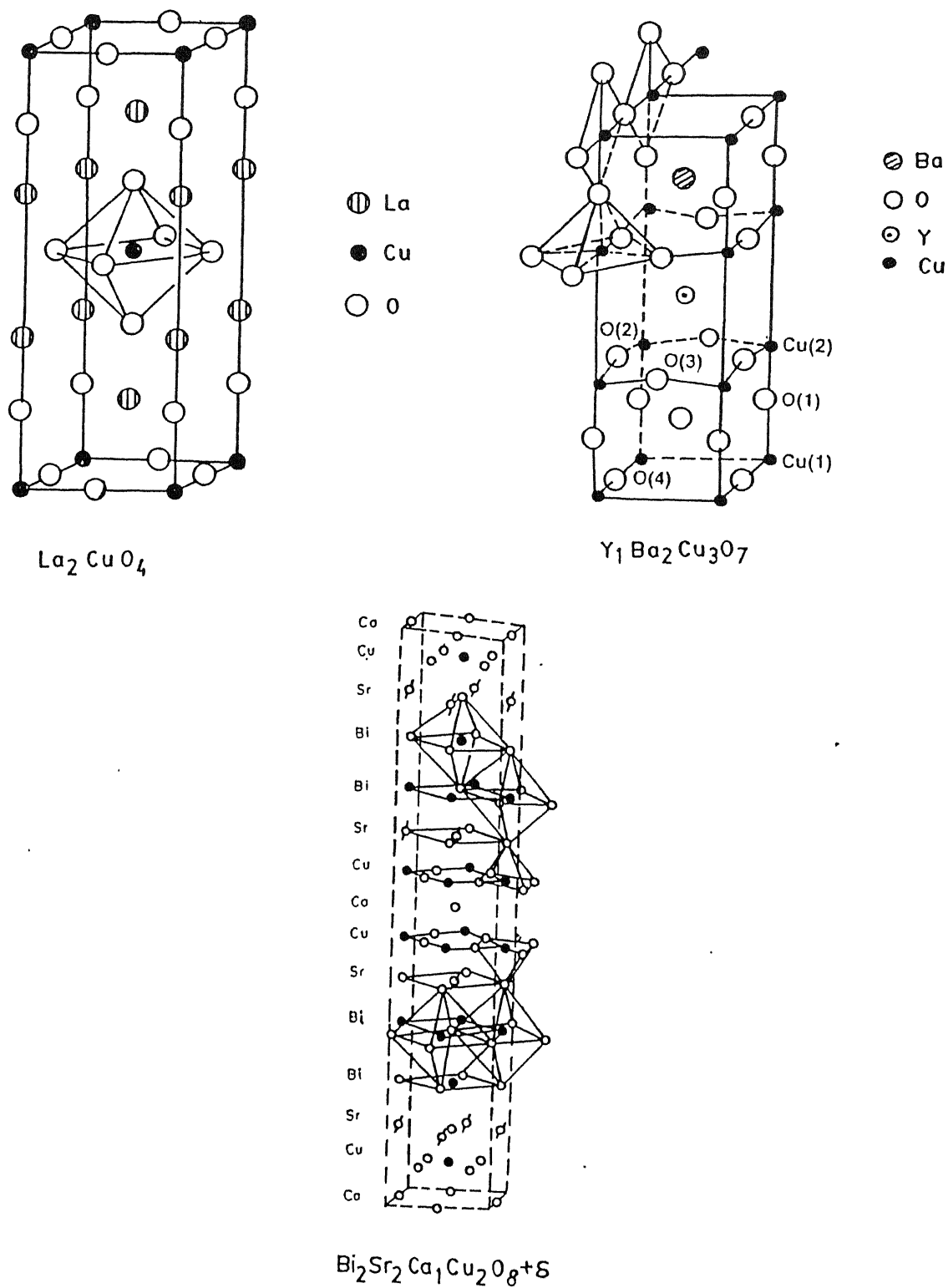


Fig. 1.2 Crystal structure of  $\text{La}_2\text{CuO}_4$ ,  $\text{Y}_1\text{Ba}_2\text{Cu}_3\text{O}_{7-\delta}$  and  $\text{Bi}_2\text{Sr}_2\text{Ca}_1\text{Cu}_2\text{O}_{8+\delta}$  systems.

yttrium or calcium. These groups are intercalated by other layers such as LaO, BiO, CuO etc. In the structure of these oxides, the natural dimension of the  $\text{CuO}_2$  conduction planes and metal oxygen planes making up the intercalated layers are not matched. The  $\text{CuO}_2$  planes control the unit cell dimensions and the intercalated metal-oxygen planes are stretched to match them [10]. The intercalated layers provide carriers or coupling mechanism necessary for superconductivity. In this respect the intercalated layers can be termed as charge reservoir layers or isolation layers, and Cu-O layers as conduction layers. Such models are known as charge transfer model [11]. Any modification in the chemistry of the charge reservoir leads to changes in the number of carriers in conduction layer by a charge transfer process.

Although, the structure of high  $T_c$  oxides has been discussed in several reviews [12,13], here we present important features of the three most studied oxides.

(i)  $\text{La}_{2-x}\text{M}_x\text{CuO}_4$  (2:0:1) System:

In this system superconducting transition temperature of 37, 32 and 17K have been realized for  $M = \text{Sr}, \text{Ba}$  and  $\text{Ca}$  respectively for  $x=0.15$ . For  $x = 0$  the system is an antiferromagnetic insulator. Structural analysis have shown that the unit cell of  $\text{La}_2\text{CuO}_4$  is tetragonal [14]. The Cu-O coordinations form an octahedra with in plane Cu-O distance equal to  $1.889\text{\AA}$  and in perpendicular direction  $2.411\text{\AA}$ . Above and below the Cu-O planes are the planes of LaO. There are two

formula units in the conventional body centered tetragonal unit cell. Primitive cell contains only one formula unit.

A tetragonal to orthorhombic phase transition occurs in  $\text{La}_{2-x}\text{M}_x\text{CuO}_{4-\delta}$  at low temperature and/or at low dopant concentration. The tetragonal to orthorhombic transition temperature changes with doping e.g. from 533K in undoped  $\text{La}_2\text{CuO}_4$  to 12K in  $\text{La}_{1.8}\text{Sr}_{0.2}\text{CuO}_{4-\delta}$ . The transition is caused by tilting of the adjacent  $\text{CuO}_6$  octahedra about the  $[1,1,0]$  direction [15].

(ii)  $\text{Y}_1\text{Ba}_2\text{Cu}_3\text{O}_{7-\delta}$  (1:2:3) System:

The single crystal and powder X-ray diffraction techniques have identified the structure as being related to cubic perovskite with one of the cube axes tripled. The space group of  $\text{Y}_1\text{Ba}_2\text{Cu}_3\text{O}_{7-\delta}$  is Pmmm. In the structure the copper atoms are located at two inequivalent positions. The first Cu(1) has square planar coordination in which nearby  $\text{CuO}_2$  units share one corner and form chains along the b-axis of the unit cell. The second Cu(2) has a pyramidal and almost square planar coordination. The Cu(2) atoms are strongly bonded to the four oxygen atoms O(2) and O(3) of the base of the pyramid and are weakly bonded to the oxygen atom O(1) of the apex. This particular feature establishes in the structure two dimensional layers of copper and oxygen atoms perpendicular to the c-axis. The yttrium atom is eight fold coordinated whereas Ba atoms are ten fold coordinated.

In  $\text{Y}_1\text{Ba}_2\text{Cu}_3\text{O}_{7-\delta}$  system all the O(4) sites are occupied for

$\delta=0$ . When  $0<\delta\leq 1$ , oxygen vacancies in the structure exist and has been shown to be confined to O(4) sites in the chains. Assuming a simple ionic model of the compound, charge compensation in the system can be achieved by oxidation of copper from  $\text{Cu}^{2+}$  to  $\text{Cu}^{3+}$ . Thus for  $\delta=7.0$  average formal valence of the Cu atoms is  $\text{Cu}^{2.33+}$ . As the oxygen content is varied superconducting properties also vary. For  $0<\delta<0.5$  the compound is orthorhombic and superconducting while for  $0.5<\delta<1$  it is tetragonal and non metallic.

(iii)  $\text{Bi}_2\text{Sr}_2\text{Ca}_1\text{Cu}_2\text{O}_{8+\delta}$  (2:2:1:2) System:

The average crystal structure of  $\text{Bi}_2\text{Sr}_2\text{Ca}_1\text{Cu}_2\text{O}_{8+\delta}$  has been determined to be an orthorhombic subcell ( $a=5.410\text{\AA}$ ,  $b=5.439\text{\AA}$  and  $c=30.78\text{\AA}$ ) of space group  $F_{mmm}(D_{2h}^{23})$  using X-ray diffraction technique [16,17]. The subcell which contains four formula units consists of two immediately adjacent  $\text{CuO}_2$  planes separated by a Ca-plane. These  $\text{CuO}_2$  planes have on the other sides a Sr-O plane, two Bi-O planes and another Sr-O plane before the next Cu-O plane is encountered. The stacking sequence is  $-\text{CuO}_2-\text{Ca}-\text{CuO}_2-\text{SrO}-\text{BiO}-\text{BiO}-\text{SrO}-\text{CuO}_2$  - etc.

The Cu-O coordination in the  $\text{CuO}_2$  layer forms a corner sharing pyramid with the inplane Cu-O distance equal to  $1.875\text{\AA}$  and apical oxygen at  $2.05\text{\AA}$ . The Cu-Cu separation between the double layer is  $3.25\text{\AA}$ . The apical oxygen distance is considerably shorter than that for either 1:2:3 ( $2.3\text{\AA}$ ) or 2:0:1 ( $2.4\text{\AA}$ ) systems. The shorter bond distance is due to weakly electropositive character of Bi when compared to the

rare earth or alkaline-earth atoms which share the apical oxygen with Cu. The short Cu-O inplane distance indicates a strong covalent bond very much different from weak apical Cu-O bond. The superconducting and normal state properties are affected by these strong, square planar Cu-O bonding. The infinite  $\text{CuO}_2$  planes are widely separated ( $\sim 12\text{\AA}$ ) by BiO double layers.

X-ray diffraction [17] and transmission electron microscopy studies [7] have shown that the structure is modulated and has incommensurate superlattice modulation along the b-axis with a period of about  $4.8b$ . The modulation consists of Bi-condensed and Bi-dilute regions alternately along the b-axis. Three types of reasons have been proposed to account for the origin for modulation (i). ordering of Sr vacancies [18], (ii). partial substitution of Sr or Ca for Bi [19] and (iii). incorporation of extra oxygen in Bi-O plane [20].

Rietveld analysis of modulated  $\text{Bi}_2\text{Sr}_2\text{Ca}_1\text{Cu}_2\text{O}_{8+\delta}$  structure shows the cause of modulation as due to presence of extra oxygen in Bi-O layers [21]. The extra oxygen increases the Bi-Bi distance, creating condensed and dilute regions of Bi along the b-axis. The apical oxygen of  $\text{CuO}_5$  pyramid follows the movement of Bi and as a result  $\text{CuO}_5$  pyramid is distorted. Thus the role of Bi-O layers in 2:2:1:2 is analogous to that of CuO chains in 1:2:3 system which provide holes in  $\text{CuO}_2$  planes for superconductivity to occur.

### 1.3 Normal State Properties

#### 1.3.1 Normal State Resistivity:

The normal state resistivity (at  $T > T_c$ ) for most of the high temperature superconductors exhibit a linear temperature dependence of the form  $\rho(T) = \rho_0 + \beta T$ . The residual resistivity  $\rho_0$  decreases and eventually vanishes with optimization as the superconducting properties of a material improves. The fact that  $\rho_0$  tends towards zero coupled with the observed linear temperature behaviour of resistivity for  $T > T_c$  suggests that  $\rho(T > T_c)$  is not dominated by impurity scattering [22]. This conclusion is further verified by considering the mean free path say, of  $Y_1Ba_2Cu_3O_7$  at 100K which is estimated to be  $100-200\text{\AA}$ . The mean free path is long compared to the lattice parameter of  $3.8\text{\AA}$  indicating that electrons are weakly scattered and hence these metals are clean.

The linear temperature dependence of resistivity raises question about the possibility of mechanism similar to that observed in a normal metal. In a normal metal total resistivity of the system is expressed by Matthiessen's rule  $\rho = \rho_I + \rho_{\text{defects}}$  where  $\rho_I$  is called intrinsic resistivity and is caused by electron phonon scattering.  $\rho_I$  is strongly temperature dependent. At low temperature electron phonon scattering yields  $\rho_I \propto T^5$  (Bloch-Gruneissen Law) for  $T \ll 0.2\theta_D$  whereas at high temperature it follows  $\rho_I \propto T$  for  $T \geq 0.2\theta_D$ .  $\rho_{\text{defects}}$  which is caused by defects in the crystal such as impurities, grain boundaries etc is normally independent of temperature.

In high temperature superconducting oxides the linear  $\rho_I$ -T behaviour is observed over a wide temperature range. For example in Ni doped  $\text{La}_{2-x}\text{Sr}_x\text{CuO}_4$  ( $x=0.16$ ) system the linear  $\rho_I$  vs T behaviour is observed down to 18K [23]. The behaviour is in contradiction with Bloch-Gruneisen behaviour since the Debye temperature obtained from specific heat data for this compound is 450K. Similarly in  $\text{Bi}_2\text{Sr}_2\text{Cu}_1\text{O}_6$  system linear temperature dependence of resistivity is observed down to 7K [24] which is well below  $0.2\Theta_D$ . This shows that normal state resistivity behaviour of cuprates is unusual and cannot be explained by conventional theories of metals. Studies have shown that Ni doped  $\text{La}_{2-x}\text{Sr}_x\text{CuO}_4$  system satisfies the Matthiessen's rule [23].  $\text{Bi}_2\text{Sr}_2\text{Ca}_{1-x}\text{Y}_x\text{Cu}_2\text{O}_{8+\delta}$  system is also shown to follow Matthiessen's rule [25]. This implies that linear resistivity is caused by some kind of temperature dependent scattering mechanism.

The single crystal transport studies of these materials have reflected their highly anisotropic character [26]. The *ab* plane resistivity ( $\rho_{ab}$ ) behaviour is similar to that observed in sintered polycrystalline samples whereas the out of plane resistivity ( $\rho_c$ ) shows an upward curvature above  $T_c$ . There are reports for metallic behaviour of  $\rho_c$  for  $T > T_c$  [27]. In  $\text{Y}_1\text{Ba}_2\text{Cu}_3\text{O}_7$  system, the ratio of *c*-axis resistivity and *ab* plane resistivity i.e.  $\rho_c/\rho_{ab}$  can vary from ~75 at 275K to ~120 at 100K [26]. On the other hand in  $\text{Bi}_2\text{Sr}_2\text{Ca}_1\text{Cu}_2\text{O}_{8+\delta}$  crystals,  $\rho_c/\rho_{ab}$  can be as high as  $10^5$  which shows that unusually high anisotropy exists in this system [28]. The mean free path in



the  $c$ -direction as determined from absolute value of resistivity turns out to be  $0.03\text{\AA}^2$  for 2:2:1:2 system. This shows that  $c$ -axis conduction is diffusive rather than metallic [29]. It is not clear why  $\rho_c$  should increase with decreasing temperature for  $T > T_c$ . However, Anderson and Zou [30] have suggested that in 1:2:3 system  $\rho_c$  should vary as  $1/T$  since the tunneling amplitude of a physical hole [a holon + a spinon] required for inplane transport, depends on the spinon density which decreases linearly with  $T$ .

### 1.3.2 Hall Effect:

Hall Effect measurements have been performed on high  $T_c$  oxides to identify the type and concentration of charge carriers. The measurements yield Hall coefficient  $R_H$  which is related to carrier density  $n$  as  $R_H = 1/ne$  where  $e$  is the electronic charge. The relationship is obtained assuming a single parabolic band. For a system having complicated band structure, the above simple relationship between  $R_H$  and  $n$  is not valid and it involves complicated integrals over the Fermi surface [31]. In high  $T_c$  superconductors information regarding carrier density has been obtained assuming a single band model.

The Hall effect measurements of cuprate superconductors have shown that  $R_H$  is positive and hence the dominant carriers are holes. An exception is found in  $\text{Nb}_{2-x}\text{Ce}_x\text{CuO}_4$  system in which the sign of  $R_H$  indicates electrons as carriers.

The  $T_c$  of cuprates have been found to be intimately connected to hole concentration in  $\text{CuO}_2$  plane. Maximum

transition temperature corresponds to an optimum hole concentration achieved at by varying appropriate dopant concentration. Within charge transfer model the hole carriers are created in the conduction plane when electrons are transferred to the charge reservoir. For example in  $\text{La}_{2-x}\text{Sr}_x\text{CuO}_4$  system replacement of trivalent  $\text{Ca}^{3+}$  by divalent  $\text{Sr}^{2+}$  introduces one hole for each Sr atom. Maximum transition temperature is obtained for  $x=0.5$  which corresponds to hole concentration of  $\approx 1 \times 10^{21}/\text{cm}^3$  [32]. Thus in cuprates carrier concentration is much smaller than that of metals ( $10^{23}/\text{cm}^3$ ). Similarly  $\text{Y}_1\text{Ba}_2\text{Cu}_3\text{O}_{6.5}$  and  $\text{Bi}_2\text{Sr}_2\text{Ca}_1\text{Cu}_2\text{O}_8$  systems which are insulators can be brought into the metallic and superconducting state by inclusion of oxygen. The oxygen sites of the charge reservoir layer associated with this variation are the chain oxygen atoms in 1:2:3 system whereas in 2:2:1:2 system these are in Bi-O plane.

A measure of redistribution of charge as a result of doping is the change in oxidation state of copper atoms in the conduction plane. The oxidation state of copper and hence the hole content per planar Cu atom can be determined using chemical (redox titration) methods. The maximum transition temperature occurs in all the cuprates when hole content per planar-Cu atom lies between 0.1 to 0.3 [33,34].

The maximum transition temperature can also be achieved by applying pressure to the sample. For example the resistance and  $R_H$  measurements of  $\text{Bi}_2\text{Sr}_2\text{Ca}_1\text{Cu}_2\text{O}_{8+\delta}$  single crystals show the pressure induced maximum  $T_c$  corresponds to hole concentration

passing through the optimum value under pressure [35,36].

Apart from normal state resistivity another puzzling anomaly of the normal metallic state of the cuprates is the temperature dependence of Hall coefficient.  $R_H$  decreases with increasing temperature. Both in  $\text{La}_{2-x}\text{Sr}_x\text{CuO}_4$  [37] and in  $\text{Y}_1\text{Ba}_2\text{Cu}_3\text{O}_{7-\delta}$  [38] systems a strong temperature dependence of  $R_H$  is observed ( $R_H \propto 1/T$ ). On the other hand in  $\text{Bi}_2\text{Sr}_2\text{Ca}_1\text{Cu}_2\text{O}_{8+\delta}$  [39,40] and  $\text{Bi}_2\text{Sr}_2\text{Ca}_3\text{Cu}_3\text{O}_{8+\delta}$  [41] systems  $R_H$  shows a weaker temperature dependence than  $1/T$ .

The temperature dependence of  $R_H$  is suppressed strongly when conditions favouring high  $T_c$  behaviour are removed (either by reducing hole concentration or by creating disorder in the system) and hence is considered to be an intrinsic property of high  $T_c$  cuprates. The latter fact has invalidated multiband Drude models invoked earlier to explain  $1/T$  dependence of  $R_H$  [42]. Whether this unusual property can be described by conventional Fermi liquid theory or by models based on strongly correlated electrons remains a subject of debate [43].

### 1.3.3 Electronic Structure:

In cuprates superconductivity is predominantly confined to  $\text{CuO}_2$  planes. Therefore, the relevant orbitals giving rise to electronic states at the Fermi level are 3d orbitals of Cu and 2p orbitals of oxygen. Band structure calculations have shown that contributions to density of states at Fermi level responsible for conduction come from  $\text{CuO}_2$  plane only [44]. Many spectroscopic measurements have revealed that holes in cuprates

have O(2p) character [45-47]. Moreover, because of large d-d Coulomb repulsion electronic correlation is an important factor. A model which describes O(2p) character of holes is as follows [48]. The five degenerate orbitals of copper d(xy), d(yz), d(zx), d(3z<sup>2</sup>-r<sup>2</sup>) and d(x<sup>2</sup>-y<sup>2</sup>) split due to presence of oxygen ions in the surroundings. For octahedral environment of Cu, as in the case of La<sub>2</sub>CuO<sub>4</sub>, d(x<sup>2</sup>-y<sup>2</sup>) lies highest in energy. In the Cu<sup>2+</sup> state, all d orbitals except the highest d(x<sup>2</sup>-y<sup>2</sup>) are fully occupied. Thus there exists a hole in Cu3d(x<sup>2</sup>-y<sup>2</sup>) orbital. The hole wave function of one Cu site overlaps with the wavefunction of next Cu site through intervening oxygen. Equivalently, one can say a hole hops to an adjacent oxygen ions and then to the next Cu ions. Hence there is an admixture of a Cu d(x<sup>2</sup>-y<sup>2</sup>) hole with surrounding oxygen p $\sigma$  (p<sub>x</sub>-p<sub>y</sub>) hole state.

The energy difference  $\Delta$  between the energy of a p $\sigma$  hole orbital and a d(x<sup>2</sup>-y<sup>2</sup>) hole orbital is called d-p charge transfer energy. If the Cu<sup>2+</sup> ion is doped with a hole, the energy increases due to Coulomb repulsive interaction between holes by U<sub>d</sub> known as correlation energy. The generalization of Mott-Hubbard theory by Zaanen et.al. [49] shows that correlation gap can have either d-d or charge transfer character depending upon the relative magnitudes of parameters U<sub>d</sub> and  $\Delta$ . If U<sub>d</sub> <  $\Delta$  the band gap is proportional to U<sub>d</sub> and the compound is in Mott insulator region with holes on the transition metal site. If U<sub>d</sub> >  $\Delta$ , the gap is proportional to  $\Delta$  and is of charge transfer nature with holes on the ligand bands. In cuprates  $\Delta \approx 2\text{eV}$  and U  $\approx$  8-10 eV therefore  $\Delta < U_d$  [50].

Thus the parents compounds of cuprates are considered as charge transfer insulator since at  $T=0K$  all oxygen orbitals are occupied and it requires energy to create oxygen holes. Doping of holes leads to the metallic state and the doped holes go to oxygen sites (since  $\Delta < U_d$ ). The mobile carriers therefore, are the extra p-holes in the oxygen sites.

Experimentally, optical conductivity data in  $La_2CuO_4$  shows that it is characterized by the  $O(2p)$ - $Cu(3d)$  charge transfer (CT) excitation which is rapidly suppressed upon doping. At higher doping the spectrum is dominated by low-energy excitations with energy below 1.0eV [51]. How exactly the evolution of electronic structure takes place as a function of doping in cuprates is not clear and is described by following models: (i) a rigid band model in which the Fermi level is shifted into the valence or conduction band upon p or n-type doping respectively (ii) a model in which partially filled mid-gap states are formed (iii) a model in which the charge-transfer gap is filled by  $O(2p)$  ( $Cu(3d)$ ) states from the valence (conduction) band upon p(n)-type doping.

## 1.4 Superconducting Properties

### 1.4.1 Coherence Length:

Coherence length is one of the important parameters of the superconducting state. The other parameter is the London penetration depth discussed later. The coherence length ( $\xi_0$ ) essentially sets the length scale of variation of

superconducting order parameter. It can also be regarded as the effective size of a cooper pair. In BCS theory  $\xi_0$  is given as  $\xi_0 \sim 0.2\hbar v_F / kT_C$  (for  $T \ll T_C$ ) where  $v_F$  is the Fermi velocity and  $T_C$  is the transition temperature. Since in conventional superconductors  $T_C$  is small,  $\xi_0$  typically varies from  $\sim 500\text{\AA}$  to  $10^4\text{\AA}$ . If the superconducting material has impurities, the coherence length ( $\xi$ ) is related to the mean free path ( $l$ ) of the normal state by

$$\frac{1}{\xi} = \frac{1}{\xi_0} + \frac{1}{l} \quad (1.1)$$

where  $\xi_0$  is the coherence length of the pure material. For a pure system where  $l$  is large ( $l \gg \xi_0$ ),  $\xi = \xi_0$  and the system is said to be in the clean limit. In presence of strong disorder where electron impurity scattering is appreciable  $l \ll \xi_0$  and  $\xi \approx l$  which is the dirty limit. Close to the transition temperature coherence length is given by Ginzburg-Landau theory and it varies as  $(1 - T/T_C)^{-1/2}$ .

High temperature superconductors have low carrier concentration as compared to metals, and hence have small Fermi velocity. This in combination with high value of  $T_C$  gives a representative average value of  $\xi_0$  as  $10\text{\AA}$ , which is of the order of unit cell dimension. The small value of  $\xi_0$  implies that superconductivity in these materials would be much more sensitive to small scale structural and chemical imperfections than in conventional superconductors where  $\xi_0$  is large. Also the small value of  $\xi_0$  in comparison to normal state mean free

path ( $\sim 100\text{\AA}^{\circ}$ - $200\text{\AA}^{\circ}$ ) classifies high  $T_c$  cuprates in the clean limit and they have high value of  $H_{c2}(100T)$  which is usefull for technological applications. The  $\xi_0$  and  $H_{c2}$  are related as  $H_{c2}(0) \sim \phi_0 / 2\pi\xi_0^2$  where  $H_{c2}(0)$  is the upper critical field measured near  $T=0K$  and  $\phi_0$  is the magnetic flux quantum. Experimental determination of  $H_{c2}(0)$  on single crystals yields the coherence lengths in  $ab$  plane and perpendicular to  $ab$  plane.  $H_{c2}(0)$  is determined by measuring magnetization  $M$  vs  $T$  for different applied fields ( $H$ ). The  $H_{c2}(0)$  measurements have shown in plane ( $\xi_{ab}$ ) and out of plane coherence lengths ( $\xi_c$ ) in  $Y_1Ba_2Cu_3O_{7-\delta}$  system as  $16\text{\AA}^{\circ}$  and  $3\text{\AA}^{\circ}$  respectively [52] whereas in  $Bi_2Sr_2Ca_1Cu_2O_{8+\delta}$  these are  $32\text{\AA}^{\circ}$  and  $0.6\text{\AA}^{\circ}$  respectively [53]. The strong anisotropy of coherence length again reflects the anisotropic character of these materials. Moreover, a very small value of  $\xi_c$  less than the Cu-O layer spacing ( $\sim 15\text{\AA}^{\circ}$ ) suggests a very weak coupling between CuO planes and quasi two-dimensional behaviour.

#### 1.4.2 Penetration Depth:

The response of a superconductor to a magnetic field can be determined in two ways. In the first case the superconductor is cooled in presence of a weak magnetic field below the transition temperature, Meissner effect is observed. Meissner effect is the expulsion of the magnetic flux from the bulk of the sample. It occurs due to generation of persistent supercurrent in the surface region which induces a field that exactly cancels the applied field. In the second case, the

sample is cooled below  $T_c$  in zero external magnetic field and then magnetization is measured with increasing temperature in presence of a field. In this case observed diamagnetic signal is due to screening supercurrents induced on the surface of the sample. The external magnetic field in both cases decays exponentially from the surface into the superconducting bulk i.e.  $B \propto \exp(-r/\lambda)$  with a characteristic length scale  $\lambda$  (the penetration depth) given in two fluid model as

$$\lambda(T) = \frac{\lambda(0)}{[1-(T/T_c)^4]^{1/2}} \quad (1.2)$$

The zero temperature penetration depth  $\lambda(0)$  is given by London formula for type II superconductors

$$\lambda(0) = \left[ \frac{m^*}{4\pi n_s e^2} \right]^{1/2} \quad (1.3)$$

where  $n_s$  is the density of superconducting electrons.

The measurement of magnetic penetration depth in high  $T_c$  superconductors is important in view of the two facts. Firstly  $\lambda$  measures the length over which magnetic fields are attenuated near the surface of a superconductor which is a fundamental property of a superconductor. Secondly its temperature dependence gives information about the nature of pairing state. The experimental techniques which have been used to measure  $\lambda$  include muon-spin rotation ( $\mu$ SR) [54], ac susceptibility [55], magnetic torque [56] and rf-resonance measurements [57]. The value of  $\lambda_{ab}$  in the  $ab$  plane of high  $T_c$  cuprates obtained from



these measurements ranges from  $1500\text{\AA}$  to  $3000\text{\AA}$  whereas c-axis penetration depth is much larger  $\sim 5000\text{\AA}$ . A rather large value of  $\lambda$  in high  $T_c$  cuprates than in conventional superconductor is due to presence of small charge carrier density providing lesser shielding. A consequence of large penetration depth and small coherence length is that their ratio known as Ginzburg-Landau parameter ( $K=\lambda/\xi$ ) is very large ( $K>50$ ). Abrikosov have shown that if  $K>1/\sqrt{2}$ , the materials are type II superconductors [58]. This puts high temperature superconductors in extreme type II limit.

The temperature dependence of magnetic field penetration depth from  $\mu$ SR measurement in  $\text{Y}_1\text{Ba}_2\text{Cu}_3\text{O}_{7-\delta}$  system is shown to follow  $[1-(T/T_c)^4]^{-1/2}$  behaviour of BCS theory and is therefore, consistent with s-wave pairing [59]. In  $\text{Bi}_2\text{Sr}_2\text{Ca}_1\text{Cu}_2\text{O}_{8-\delta}$  system, however, a different behaviour is obtained. In this system temperature dependence of  $\lambda$  is shown to have a large  $T^2$  term at low temperature which is inconsistent with s-wave pairing [57]. This has been attributed to more anisotropic character of 2:2:1:2 than 1:2:1. Another experiment has shown linear temperature dependence of  $\lambda$  which is consistent with d-wave pairing [60]. It is clear that exact nature of pairing symmetry from T dependence of penetration depth alone remains inconclusive.

#### 1.4.3 Energy Gap:

According to BCS theory the quasiparticle spectrum in the superconducting state is characterized by a temperature

dependent energy gap  $\Delta(T)$  which vanishes as  $(1-T/T_c)^{1/2}$  at  $T_c$ . At  $T=0$  energy gap is related to  $T_c$  by  $\frac{2\Delta}{kT_c}=3.52$ . For s-state pairing of BCS, the energy gap is isotropic. However, for higher angular momentum pairing (p-state, or d state) the energy gap will not be isotropic but instead will go to zero on nodal lines or planes in k-space [61]. Such a pairing is known to exist in superfluid  $^3\text{He}$  and heavy fermion systems.

The existence of superconducting energy gap in high temperature superconductors has been verified by various tunneling measurements and photoemission spectroscopy measurements. Tunneling measurements of single crystals give gap to  $T_c$  ratio ( $\frac{2\Delta}{kT_c}$ ) equal to that of BCS for the c-axis gap and a larger gap ratio ( $\sim 6$ ) for ab plane [62]. Photoemission spectroscopy and tunneling measurements of single crystal  $\text{Bi}_2\text{Sr}_2\text{Ca}_1\text{Cu}_2\text{O}_{8+\delta}$  give  $\frac{2\Delta}{kT_c} = 6.8$  and  $6.1$  respectively [63] in ab plane which is much larger than the BCS gap. Temperature dependence of tunneling characteristics have been found to be in agreement with that predicted by BCS theory [64]. Angular resolved photoemission spectroscopy [65] and low temperature scanning tunneling microscopy [66] measurements have shown that the ab plane gap is anisotropic. The gap anisotropy points towards the presence of non-s pairing state in contradiction to the results of temperature dependent tunneling measurements.

#### 1.4.4 Isotope Effect:

The dependence of  $T_c$  on the isotopic mass is generally

regarded as an important measure of electron-phonon interaction. The two quantities are related as  $M^\alpha T_C = \text{constant}$  where  $M$  is the isotopic mass. The original BCS theory predicts (for weak coupling)  $\alpha=0.5$  [67]. The inclusion of Coulomb interaction between the electrons significantly alters the relationship which has been observed in many d-band systems [68].

Isotope effect studies in high temperature superconductors have been carried out by the substitution of  $^{18}\text{O}$  for  $^{16}\text{O}$ . In cuprates of optimum composition isotope exponent  $\alpha$  is small or zero. For example in  $\text{Y}_1\text{Ba}_2\text{Cu}_3\text{O}_{7-\delta}$  system  $\alpha$  is reported to be 0.0-0.10 [69,70] and in  $\text{Bi}_2\text{Sr}_2\text{Ca}_1\text{Cu}_2\text{O}_{8+\delta}$  system it is 0.037 [71]. A significant feature of isotope effect in high  $T_C$  cuprates is the strong dependence on stoichiometry. For example in  $\text{La}_{2-x}\text{Sr}_x\text{CuO}_4$  system  $\alpha=0.40\pm0.05$  for  $x=0.1$  while for  $x\geq0.15$  it is  $0.14\pm0.008$  [72]. Similarly in  $\text{Y}_{1-x}\text{Pr}_x\text{Ba}_2\text{Cu}_3\text{O}_7$ ,  $\alpha$  changes from zero for  $x=0.0$  to  $0.34\pm0.03$  for  $x=0.4$  [73]. The observation of an oxygen-isotope effect in cuprates suggests that electron-phonon coupling does contribute to the pairing.

#### 1.4.5 Specific Heat:

In conventional superconductors, a large fraction of the specific heat at the transition temperature and below is electronic in origin. This is because the electronic specific heat  $C_{el} \sim \gamma T$  falls off more slowly at low temperatures than the lattice contribution  $\sim (T/\theta_D)^3$  to specific heat. Density of states near Fermi level can be obtained from electronic

coefficient  $\gamma$  which for nearly free electron is given by  $\frac{2}{3}\pi^2 k^2 N(E_F)$ . At  $T_C$ , BCS theory predicts a universal jump in the specific heat expressed as  $\frac{\Delta C}{kT_C} = 1.43$  where  $\Delta C = (C_{es} - C_{en})_{T_C}$ .  $C_{es}$  and  $C_{en}$  are electronic contributions to specific heat in superconducting and normal state respectively.

The low temperature specific heat measurements of high temperature superconductors, both ceramic and single crystal  $Y_1Ba_2Cu_3O_{7-\delta}$  [74] and  $La_{2-x}Sr_xCuO_4$  [75] systems have shown the presence of a contribution proportional to temperature i.e.  $\gamma T$ . Typical values of  $\gamma$  obtained for the above systems are  $55 \text{ mJ/mole-K}^2$  and  $24 \text{ mJ/mole-K}^2$  respectively. These values are considerably larger than that obtained for typical metals e.g.  $\gamma = 0.7 \text{ mJ/mole-K}^2$  for Cu. The linear contribution was considered to be due to low lying neutral excitations which could be found in resonating-valence-bond (RVB) based superconducting state [76]. However, theoretical considerations have shown that RVB state can give at best  $T^2$  coefficient in the specific heat [77]. In contrast to an appreciable linear term in 1:2:3 and 2:0:1 systems, single crystal specific heat studies of  $Bi_2Sr_2Ca_1Cu_2O_{8+\delta}$  and  $Tl_2Ba_2Ca_2Cu_3O_{10}$  [78] have shown no measurable linear term in the specific heat at low temperature [ $\gamma \leq 1 \text{ mJ/mole K}^2$ ]. In all high  $T_C$  systems specific heat measurements have shown specific heat anomaly near the transition temperature.

#### 1.4.6 Symmetry of paired electrons:

The flux quantization experiments have shown that superconducting carriers of high temperature superconductors are paired [79]. However, the symmetries of the pairs of oxide materials are controversial problems. The knowledge of the symmetry is important in order to classify the theories which interpret the properties of these materials. The conventional BCS theory has s-wave (zero orbital angular momentum) symmetry of the pairs. Many experiments have suggested similar pairing symmetry in cuprates also. The experiments such as temperature dependence of London penetration depth which follows  $[1-(T/T_c)^4]^{-1/2}$  over a wide temperature range [80], muon spin rotation and magnetization measurements [81], temperature dependence of energy gap [64] and an interference experiments [82] all reflect s-wave pairing. Several recent experiments suggest that the symmetry of the Cooper pair most probably is  $d(x^2-y^2)$ . The conclusion is arrived at by:

(i). strong anisotropy of the energy gap (an order of magnitude larger than that of conventional superconductor) as observed in angular resolved photoemission experiments [65].

(ii). the  $T^3$  temperature dependence of nuclear spin-lattice relaxation rate in NMR experiments (in conventional superconductor  $\exp(-\Delta/kT)$  temperature dependence is expected) [83].

(iii). a phase shift of  $\pi$  in the flux dependence of Josephson current from a conventional superconductor to a high temperature superconductor [84].

(iv). a linear temperature dependence of penetration depth [60].

In view of the fact that a recent experiment [82] has shown s-wave symmetry, the issue remains controversial.

### 1.5 Effect of Impurities:

The effect of impurities and hence disorder in conventional superconductors has been studied in detail. The transition temperature has been found to show a very weak dependence on non-magnetic impurities. Anderson [85] explained the fact by pointing out that Cooper pairs can be formed out of time-reversed exact eigenstates of electrons. The pairing of such time reversed states is not affected by nonmagnetic disorder; therefore,  $T_c$  remains constant. The BCS density of states also remain unaffected by nonmagnetic disorder. This theorem is known as Anderson's theorem of dirty superconductors i.e. nonmagnetic superconducting alloys with mean free path  $l < \xi_0$ . However, the fact that  $T_c$  remains invariant is true only for weak nonmagnetic disorder i.e.  $k_F l > 1$ . On the other hand the presence of even a small concentration of magnetic impurities in conventional superconductors depress  $T_c$  considerably. The explanation to this effect is provided by Abrikosov and Gorkov theory [86] formulated within the framework of BCS theory.

In the above discussion of non-magnetic disorder we considered the case when the disorder was weak. A well known fact about metals is that an increase in the disorder of the crystal lattice tends to restrict the free motion of electrons. If the disorder is strong enough ( $k_F l \approx 1$ ) it will give rise to complete localization of electrons in a bounded region of space [87,88]. The increase of disorder in a superconducting metal leads to the reduction or in the limit complete suppression of superconductivity.

In the Ginzburg-Landau theory the complex order parameter is written as  $\psi = \psi_0 e^{-i\phi}$  where  $\psi_0$  is the amplitude and  $\phi$  the phase of order parameter. Therefore, disorder can destroy superconductivity either by reducing the amplitude of the order parameter or by destroying the phase coherence of superconducting electrons. Both mechanisms frequently operate in a given system. Apart from localization another factor which can decrease  $T_C$  is the enhancement of repulsive Coulomb potential close to a critical disorder [89]. At the critical disorder electron diffusion is very slow. The slow diffusion of electrons reduces their ability to screen out the electric field of any other electron. This gives rise to an enhancement of effective Coulomb repulsion between electron which restricts the formation of a Cooper pair. Hence  $T_C$  is reduced.

The destruction of superconductivity by disorder drives the system from metallic state to the insulating state. In the insulating state conductivity is zero at zero temperature because the states near the Fermi energy are all localized. The

charge transport at finite temperature takes place by the mechanism of variable range hopping (VRH) [90]. In VRH electron can hop to an unoccupied localized state of higher energy by absorption of a phonon.

The suppression of superconductivity in high temperature superconductors due to impurity substitutions has turned out to be equally puzzling as the occurrence of superconductivity. Both magnetic and nonmagnetic impurities suppress  $T_C$  considerably. The  $T_C$  suppression due to nonmagnetic impurities is rather surprising in respect of conventional superconductors where  $T_C$  remains invariant. The insensitivity of conventional superconductors to nonmagnetic impurities is essentially due to the fact that a Cooper pair has zero angular momentum (s-wave pairing). It has been shown that if pair carried angular momentum (p-wave or d-wave)  $T_C$  would be strongly affected by nonmagnetic impurities [91].

The substitutions of magnetic impurities display again a variety of behaviour. The form of  $T_C$  vs magnetic impurity concentration in some systems is satisfied by Abrikosov and Gorkov pair breaking mechanism [92] whereas in others it is not [93]. The metal-insulator transition, in  $Y_1Ba_2Cu_3O_{7-\delta}$  system, for example, which occurs due to reduction in oxygen content is considered to be the result of disorder induced localization of electronic states in the band tails [94]. In the insulating state the Fermi energy lies in the region of localized states in the band tails giving rise to variable range hopping mechanism of charge transport at low temperatures. The



dimensionality of variable range hopping is not universal and turns out to be different for different systems.

### 1.6 Magnetic Properties:

One of the important characteristics revealed by high temperature superconducting oxides is the antiferromagnetic ordering of the insulating state. Muon-spin resonance experiment shows that magnetic moments of these antiferromagnets reside on Cu ion and there are no evidences of magnetic moment on oxygen ions [95]. The Cu-Cu exchange interaction within the  $\text{CuO}_2$  plane is mediated by oxygen ions. The nearest neighbour Cu spins are aligned antiparallel with moment direction in ab plane. Along the c-axis also the spins are aligned antiferromagnetically. The exchange interaction within the  $\text{CuO}_2$  plane ( $J \sim 0.15\text{eV}$ ) as has been shown by inelastic neutron scattering is much larger than the exchange interaction between the planes due to weak interlayer coupling [96]. Above the Neel's temperature ( $T_N$ ) strong spin correlation persists within the  $\text{CuO}_2$  plane. Thus, though these systems display 3d antiferromagnetic ordering below  $T_N$ , the strong exchange interaction in  $\text{CuO}_2$  plane than between the planes results in a 2-d character of the spin-excitations and strong spin correlation in the  $\text{CuO}_2$  plane [97].

Another aspect of the magnetic property of oxide systems is that superconductivity and antiferromagnetism do not coexist in the same spatial regions. In spatially different regions they do coexist. For example in  $\text{R}_1\text{Ba}_2\text{Cu}_3\text{O}_{7-\delta}$  system where R is

a rare-earth, magnetic moments of the rare-earth ions order antiferromagnetically at low temperature ( $< 2\text{K}$ ) [98] along with the superconductivity in  $\text{CuO}_2$  plane. But in  $\text{CuO}_2$  plane superconductivity and antiferromagnetism seems to be mutually exclusive. Despite the fact that long range order is completely suppressed in the superconducting state, Raman scattering experiments have shown that the spin fluctuations do survive in the superconducting state and are energetic [99]. The magnetic correlation length decreases from a typical value of  $\sim 400\text{\AA}$  in antiferromagnetic insulating state ( $x=0$ ) of  $\text{La}_{2-x}\text{Sr}_x\text{CuO}_4$  to  $\sim 10\text{\AA}$  in the metallic state ( $x=0.15$ ). The persistence of spin fluctuation in the superconducting state thus, lends support to the theoretical models based on spin fluctuation [100].

## 1.7 Proposed Theoretical Models

### (i) Bipolaron Theory:

Ranninger et al proposed a variation of phonon-interaction mediated superconductivity in which superconducting charge carriers are bipolarons [101]. The doping in the insulating compounds e.g.  $\text{La}_2\text{CuO}_4$  or  $\text{Y}_1\text{Ba}_2\text{Cu}_3\text{O}_6$  introduces holes in the uppermost occupied band. These holes are "dressed" by a cloud of virtual phonons to form polarons. The polarons attract one another and if the attraction is strong enough they can bound into bipolaron states with very small effective mass. Since bipolaron obey Bose statistics, at low temperature they can Bose-condense .

**(ii) Plasmon Exchange Theory:**

Plasmon exchange theory assumes the electron-electron attraction via exchange of plasmons rather than phonons as in BCS theory. It has been suggested that when conduction electrons belong to more than one band and have different effective masses, an acoustic branch ( $\omega \propto q$ ) is formed in the plasmon spectrum [102]. This implies existence of soft plasmons which are low energy plasmon excitations. These soft plasmons have been found capable of generating net attraction between electrons leading to Bose condensation at high value of  $T_C$  [103]. Gersten explained the linear normal state resistivity as due to emission of soft plasmons [104].

**(iii) Exciton Exchange Mechanism:**

The other proposed electronic excitation responsible for electron pairing is exciton. The exciton constitutes a displacement of electric charge like the phonon and the plasmon. The difference between the exciton exchange and plasmon exchange is that whereas a plasmon is a collective excitation of many electrons or holes in the conduction band around  $E_F$ , an exciton is an excitation of a single electron-hole pair both away from  $E_F$ . Oftenly, exciton involves transfer of charge and is called charge transfer excitation. Such an excitonic model for high  $T_C$  oxides in which the pairing excitons are charge transfer excitations between copper and oxygen atoms in  $\text{CuO}_2$  plane has been proposed by Verma et.al. [105]. The bands are formed by hybridization of  $\text{Cu}d(x^2-y^2)$  and

O(px or py) orbitals. An excitation results when an electron is transferred from  $O^{2-}$  to  $Cu^{2+}$  due to relatively small pd charge transfer energy that exists in these systems. They show that exchange of these excitons or in other words electronic polarization fluctuations mediate the inter electronic attraction for Cooper pairing. The deficiency of the model is that it overscreens the Coulomb repulsion.

**(iv) Interlayer Coupling Model:**

The crystal structure of high temperature superconductors reveals a layered structure with two-dimensional character of conduction electrons. The density of states of such two dimensional electrons is large near the band centre which increases electron phonon coupling constant in favour of high  $T_c$ . The model [106] supposes that electrons propagate freely in each layer and the overlap integral between different layers is negligible. A Cooper pair is formed when an electron on a layer interacts with another electron on the neighboring layer through the exchange of three dimensional phonons. The large Coulomb interaction that exists as a result of reduced dimensionality is shown to be largely suppressed once the electrons on different layers are coupled into Cooper pair. High  $T_c$  is achieved due to reduced Coulomb potential.

**(v) Spin-fluctuation Theory:**

The metallic and superconducting phase of high temperature superconductors is close to the insulating antiferromagnetic

phase. The experimental results reveal that strong spin correlation with short correlation length  $\sim 10-15\text{\AA}$  persist in the superconducting state even though long range spin order is destroyed by doping. Since there is a strong antiferromagnetic coupling between copper spins (coupling energy  $J$  is of the order of  $10^3\text{K}$ ), as carriers move spins are disturbed leading to emission of spin waves. This leads to the pairing of carriers via exchange of antiferromagnetic spin fluctuation [107].

(vi) Resonating Valence Bond (RVB) Theory:

In RVB picture, a single valence bond is defined as a singlet state constructed from any pair of spin which need not be nearest neighbors. The RVB ground state then corresponds to a coherent superposition of all possible configurations of valence bonds [108]. The essence of RVB theory is that strong electron-electron correlation e.g. in  $\text{La}_2\text{CuO}_4$  results in the separation of charge degrees of freedom from spin degrees of freedom [109]. Thus, the elementary excitations relative to an RVB ground state are of two principal types. The first excitation is an unpaired spin which acts as an uncharged, spin  $1/2$  fermion known as a spin soliton or spinon. The second excitation is the hole produced by removing such a spin which acts as a charge  $e$ , spin zero boson called holon. A physical pole is a combination of a holon and a spinon. The RVB concept has been found relevant to the metallic phase of the cuprates and some of the normal state properties especially tunneling and anisotropic resistivity have been explained using this

theory [110].

### 1.8 Motivation of the present work:

The discovery of superconductivity in LaBaCuO has been followed by intense efforts for search for oxide compounds with higher transition temperature as well as exploring their physical properties. The present work features activities in both of these categories.

As we have seen superconducting properties of high  $T_c$  superconductors are sensitive to chemical impurities. In conventional superconductors the transition temperature remains unaffected by non-magnetic impurities whereas a small amount of magnetic impurities affect  $T_c$  considerably. The response of superconductivity to magnetic and non magnetic impurities is related to the symmetry of the Cooper pair. The high  $T_c$  superconductors, on the contrary, show decrease of transition temperature both for magnetic and non magnetic impurities. With increase of impurity concentration superconductivity eventually vanishes and the system becomes insulating. Many mechanisms for suppression of superconductivity have been proposed and the subject remains controversial. Thus it is evident that an effective tool to probe the parameters essential for superconductivity is the introduction of impurities and study their effect on normal state and superconducting properties. Also, it is of interest to study the properties of the system in the insulating state as the superconductivity appears close to metal insulator transition. These issues motivated us to

take a close look at the problem of magnetic impurities in superconducting oxides.

The present work focusses at two aspects of the superconductivity problem. The first aspect deals with effect of rare earth impurities on superconducting properties of  $\text{Bi}_2\text{Sr}_2\text{Ca}_1\text{Cu}_2\text{O}_{8+\delta}$  system. This forms the major part of the work. The second aspect is the search for superconductivity in  $\text{Zn}_x\text{Ca}_{1-x}\text{Fe}_2\text{O}_4$  system which promised an exceptionally high  $T_c$  of  $200^\circ\text{K}$ .

### 1.9 References:

1. J.G. Bednorz and K.A. Muller, Z. Phys. B 64, 189 (1986).
2. A.W. Sleight, J.L. Gillson and P.E. Bierstedt, Solid State Commn. 17, 27 (1975).
3. M.K. Wu, J.R. Ashburn, C.J. Torng, P.H. Hor, R.L. Meng, L. Gao, Z.J. Huang, Y.Q. Wang and C.W. Chu, Phys. Rev. Lett. 58, 908 (1987).
4. R.M. Hazen, L.W. Finger, R.J. Angel, C.T. Prewitt, W.L. Ross, H.K. Mao, C.S. Hadidiacos, P.H. Hor, R.L. Meng and C.W. Chu, Phys.Rev. B 35, 7238 (1987).
5. H. Maeda, Y. Tanaka, M. Fukutomi and A. Asano, Jpn. J. Appl. Phys. 27, L209 (1988).
6. Z.Z. Sheng and A.M. Hermann, Nature 332, 55 and 138 (1988).
7. R.M. Hazen, C.T. Prewitt, R.J. Angel, N.L. Ross, L.W. Finger C.F. Hadidiacos, D.R. Veblen, P.J. Heaney, P.H. Hor, R.L. Meng, Y.Y. Sun, Y.Q. Wang, Y.T. Xue, Z.J. Huang, L.

- Gao, J. Bechtold and C.W. Chu, *Phys. Rev. Lett.* **60**, 1174 (1988).
8. Y. Bando, T. Kijima, T. Kitami, J. Tanaka, F. Izumi and M. Yokoyama, *Jpn. J. Appl. Phys.* **27**, L358 (1988).
  9. A. Schilling, M. Cantoni, J.D. Guo and H.R. Ott; *Nature* **363**, 56 (1993).
  10. J.D. Jorgensen, M.A. Beno, D.G. Hinks, L. Soderholm, K.J. Volin, R.L. Hitterman, J.D. Grace, I.K. Schuller, C.V. Segre K. Zhung and M.S. Klecfisch, *Phys. Rev. B* **36**, 3608 (1987).
  11. J.D. Brown, *J. Solid State Chem* **82**, 122 (1989).
  12. Klaus Yyon and Michel Francois, *Z. Phys. B* **76**, 413 (1989).
  13. J.W. Lynn (ed.), *High Temperature Superconductivity*, (Springer Verlag, 1990).
  14. C. Michel and B. Raveau, *Rev. Chim. Miner.* **21**, 407 (1984).
  15. R.M. Fleming, B. Batlogg, R.J. Cava and E.A. Rietman, *Phys. Rev. B* **35**, 7191 (1987).
  16. S.A. Sunshine, T. Siegrist, L.F. Schneemeyer, D.W. Murphy, R.J. Cava, B. Batlogg, R.B. van Dover, R.M. Fleming, S.H. Glarum, S. Nakahara, R. Farrow, J.J. Krajewski, S.M. Zahurak, J.V. Waszczak, J.H. Marshall, P. Marsh, L.W. Rupp, Jr., and W.F. Peck, *Phys. Rev. B* **38**, 893 (1988).
  17. M.A. Subramaniam, C.C. Torardi, J.C. Calabrese, J. Gopalakrishnan, K.J. Morrissey, T.R. Askew, R.B. Flippen, U Chowdhry, and A.W. Sleight, *Science* **239**, 1015 (1988).
  18. A.K. Cheetham, A.M. Chippindale, and S.J. Hibble, *Nature* **21**, 333 (1988).



- 
19. T.M. Shaw, S.A. Shivashankar, S.J. La Placa, J.J. Cuomo, T.R. McGuire, R.A. Roy, K.H. Kelleher and D.S. Yee, Phys. Rev. B 37, 9856 (1988).
  20. E.A. Hewat, M. Dupuy, P. Bordet, J.J. Capponi, C Chaillout, J.L. Hodeau, M. Marezio, Nature 333, 53 (1988).
  21. A. Yamamoto, M. Onoda, E.T. Muromachi, F. Izumi, T. Ishigaki and H. Asano, Phys. Rev. B 42, 4228 (1990).
  22. M. Gurvitch and A.T. Fiory, Phys. Rev. Lett. 59, 1337 (1988).
  23. J.M. Tarascon, L.H. Greene, B.G Bagley, W.R. McKinnon, P. Barboux and G.W. Hull, Novel Superconductivity, 705 (1987).
  24. S. Martin, A.T. Fiory, A.M. Fleming, L.F. Schneemeyer and J.V. Waszczak, Phys. Rev. B 41, 846 (1990).
  25. D. Mandrus, L. Forro, C. Kendziora and L. Mihaly, Phys. Rev. B 45, 12640 (1992).
  26. S.W. Tozer, A.W. Kleinasser, T. Penney, D. Kaiser, F. Holtzberg, Phys. Rev. Lett. 59, 1768 (1987).
  27. T.A. Friedmann, M.W. Robin, J. Giapinlzbis, J.P. Rice and D.M. Gingserg, Phys. Rev. B 42, 6217 (1990).
  28. S. Martin, A.T. Fiory, R.M. Fleming, L.F. Schneemeyer and J.V. Waszczak, Phys. Rev. Lett. 60, 2194 (1988).
  29. C. Kendziora, M. C. Martin, J. Hartge, L. Mihaly and L. Forro, Phys. Rev. B 48, 3531 (1993).
  30. P.W. Anderson and Z. Zou, Phys. Rev. Lett. 60, 132 (1988).
  31. J.M. Ziman, Principle of the Theory of Slids, (Cambridge University Press, 1965).

- 
32. H. Takagi, T. Ido, S. Ishibashi, M. Uota, S. Schida and Y. Tokura, Phys. Rev. B 40, 2254 (1990).
  33. T. Penney, M.W. Shafer and B.L. Olson, Physica C 162, 63 (1989).
  34. Y. Koike, Y. Iwabuchi, S. Hosoya, N. Kobayashi and T. Fukase, Physica C 159, 105 (1989).
  35. L. Forro and J.R. Cooper, Phys. Rev. B 41, 9551 (1990).
  36. T. Huang, M. Itoh, J. Yu, Y. Inaguma, T. Nakamura, Phys. Rev. B 48, 7712 (1993).
  37. J. Clayhold, N.P. Ong, Z.Z. Wang, J.M. Tarascon and P. Barbona, Phys. Rev. B 39, 777 (1989).
  38. J. Clayhold, N.P. Ong, Z.Z. Wang, J.M. Tarascon and P. Barboux, Phys. Rev. B 39, 7324 (1989).
  39. L. Forro, D. Mandrus, C. Kendziora, L. Mihaly and R. Reeder, Phys. Rev. B 42, 8704 (1990).
  40. A.P. Mackenzie, S.D. Hughes, J.R. Cooper, A. Carlinghton, C. Chan and B.M. Wanklyn, Phys. Rev. B 45, 527 (1992).
  41. J. Clayhold, N.P. Ong, P.H. Hor and C.W. Chu, Phys. Rev B 38, 7016 (1988).
  42. A. Davidson, P. Santhanam, A. Palevski and M.J. Brady, Phys. Rev. B 38, 2828 (1988).
  43. W.E. Pickett, H. Krakauer, R.E. Cohen and D.J. Singh, Science 25, 46 (1992).
  44. J. Yu, A.J. Freeman and J.H. Xu, Phys. Rev. Lett. 58, 1035 (1987).
  45. P. Kuiper, G. Kruizinga, J. Ghijsen, M. Grioni, P.J.W. Weijn, F.M.F. de Groot, G.A. Sawatzky, H. Verweij, L.F.

- Feiner and H. Peterson, Phys. Rev. B 38, 6483 (1988).
46. P. Kriper, M. Grioni, G.A. Sawatzky, D.B. Mitzi, A. Kapitulnik, A. Santaniello, P. De Padova and P. Thiry, Physica C 157, 260 (1989).
47. W. Drube, F.J. Himpsel, G.V. Chandrashekhara and M.W. Shafer, Phys. Rev. B 39, 7328 (1989).
48. J. Zaanen, O. Jepsen, O. Gunnarsson, A.T. Paxton and O.K. Anderson, Physica C 153-155, 1636 (1988).
49. J. Zaanen, G.A. Sawatzky and J.W. Allen, Phys. Rev. Lett. 55, 428 (1985).
50. P. Fulde, Physica C 153-155, 1769 (1988).
51. Y. Tokura, S. Koshihara, T. Arima, H. Takagi, S. Ishibashi, T. Ido and S. Uchida, Phys. Rev. B 41, 11657 (1990).
52. U. Welp, M. Grimsditch, H. You, W.K. Kwok, M.M. Fang, G.W. Crabtree and J.Z. Lin, Physica C 161, 1 (1989).
53. M.J. Naughton, R.C. Yu, P.K. Davies, J.E. Fisher, R.V. Chamberlin, Z.Z. Wang, T.W. Jing, N.P. Ong and P.M. Chaikin, Phys. Rev. B 38, 9280 (1988).
54. D.R. Harshman, L.F. Schneemeyer, J.V. Waszczak, G. Aeppli, R.J. Cava, B. Batlogg, L.W. Rupp, E.J. Ansaldo and D. L.L. Williams, Phys. Rev. B 39, 851 (1989).
55. J.R. Cooper, T.C. Chu, L.W. Zhou, B. Dunn and G. Gruner, Phys. Rev. B 37, 638 (1988).
56. J.C. Martinez, S.H. Brongersma, A. Koshelev, B. Ivlev, P.H. Kes, R.P. Griessen, D.G. de Groot, Z. Tarnavski and A.A. Menovsky, Phys. Rev. Lett. 69, 2276 (1992).

- 
57. A. Maeda, T. Shibauchi, N. Kondo, K. Uchinokura and M. Kobayashi, *Phys. Rev. B* **46**, 14234 (1992).
  58. A.A. Abrikosov, *Soviet Phys. JETP* **5**, 1174 (1957).
  59. S.M. Anlage, B.W. Langley, G. Deutscher, J. Halbritter, M.R. Beasley, *Phys. Rev. B* **44**, 9764 (1991).
  60. W.N. Hardy, D.A. Brown, D.C. Morgan, R. Liang, K. Zhang *Phys. Rev. Lett.* **70**, 3999 (1993).
  61. T.M. Rice, *Z. Physics B* **67**, 141 (1987).
  62. M. Boekholt, M. Hoffmann and G. Guntherodt, *Physica C* **175**, 127 (1991).
  63. C.G. Olson, R. Liu, D.W. Lynch, R.S. List, A.J. Arko, B.W. Veal, Y.C. Chang, P.Z. Jiang, A.P. Paulikas, *Phys. Rev. B* **42**, 381 (1990),
  64. S.I. Vedenev, A.G.M. Jansen, P. Samuely, V.A. Stepanov, A.A. Tsvetkov and P. Wyder, *Phys. Rev. B* **49**, 9823 (1994).
  65. Z.X. Shen, D.S. Dessau, B.O. Wells, D.M. King, W.E. Spicer, A.J. Arko, D. Marshall, L.W. Lambardo, A. Kapitulnik, P. Dickinson, S. Doniach, J. DiCarlo, A.G. Loeser, C.H. Park, *Phys. Rev. Lett.* **70**, 1553 (1993).
  66. J. Kane, Q. Chen, K.W. Ng and H.J. Tao, *Phys. Rev. Lett.* **72**, 128 (1994).
  67. J. Bardeen, L.N. Cooper and J.R. Schrieffer, *Phys. Rev.* **108**, 1175 (1957).
  68. G. Gladstone, M.A. Jensen and J.R. Schrieffer in *Superconductivity* edited by R.D. Parks (Marcell Dekker, Inc N.Y. 1969) p. 665.

- 
69. H.C. Zur Loye, K.J. Leary, S.W. Keller, W.K. Haur, T.A. Faltens, J.N. Mechaels and A.M. Stacy, *Science* 238, 1558 (1987).
70. B. Batlogg, G. Kourouklis, R.J. Cava, A. Jayaraman, A.E. White, K.T. Short, L.W. Rupp and E.A. Rietman, *Phys. Rev. Lett.* 59, 912 (1987).
71. H. Katayama, T. Hirooka, A. Oyamada, Y. Okabe, T. Takahashi, T. Sasaki, A. Ochiai, T. Suzuki, A.J. Mascarenhas, J.I. Pankove, T.F. Cixaek, S.K. Deb, R.B. Goldfarb and Y. Li, *Physica C* 156, 481 (1988).
72. M.K. Crawford, M.N. Kunchur, W.E. Farneth, E.M. McCarron and S.J. Poon, *Phys Rev B* 41, 282 (1990).
73. J.P. Frank, J. Jurag, M.A.K. Mohamed, S. Gyga and G.I. Sproule, *Phys. Rev. B* 44, 5318 (1991).
74. M.E. Reeves, T.A. Friedman and D.M. Ginsberg, *Phys. Rev. B* 35, 7207 (1987).
75. G. Nieva, E.N. Martinez, F de la Cruz, D.A. Esparza and C.A. D'Ovidio, *Phys. Rev. B* 36, 8780 (1987).
76. P.W. Anderson, *Physica C* 153-155, 1038 (1988).
77. H. Fukuyama, Y. Hasegawa and Y. Suzumura, *Physica C* 153-155, 1630 (1988).
78. J.S. Urbach, D.B. Mitzi, A. Kapitulnik, J.Y.T. Wei and D.E. Moris, *Phys. Rev. B* 39, 12391 (1989).
79. C.E. Gough, M.S. Colciough, E.M. Forgan, R.G. Jordon, M. Keene, C.M. Muirhead, A.I.M. Care, N. Thomas, J.S. Abell and S. Sutton, *Nature* 326, 855 (1987).

- 
80. L. Krusin-Elbaum, R.L. Greene, F. Holtzberg, A.P. Malozemoff and Y. Yeshurun, *Phys. Rev. Lett.* **62**, 217 (1989).
  81. D.R. Harshman, G. Aepli, E.J. Ansaldo, B. Batlogg, J.H. Brewer, J.F. Carolan, R.J. Cava, M. Celio, A.C.D. Chaklader, W.N. Hardy, S.R. Kreitzman, G.M. Luke, D.R. Noakes and M. Senba, *Phys. Rev. B* **36**, 2386 (1987).
  82. P. Chaudhari and S.Y. Lin, *Phys. Rev. Lett.* **72**, 1084 (1994).
  83. J.A. Martindale, S.E. Barrett, K.E. O'Hara, C.P. Slichter, W.C. Lee and D.M. Ginsberg, *Phys. Rev. B* **44**, 7764 (1991).
  84. Y. Tanaka, *Phys. Rev. Lett.* **72**, 3871 (1994).
  85. P.W. Anderson, *J. Phys. Chem. Solids* **11**, 26 (1959).
  86. A.A. Abrikosov and L.P. Gor'kov, *Sov. Phys. JETP* **12**, 1243 (1961).
  87. N.F. Mott and E.A. Davis, *Electron Processes in Non Crystalline Materials* (Clarendon, Oxford, 1979).
  88. P.A. Lee and T.V. Ramakrishnan, *Rev. Mod. Phys.* **52**, 287 (1985).
  89. P.W. Anderson, K.A. Muttalib and T.V. Ramakrishnan, *Phys. Rev. B* **28**, 117 (1983).
  90. N.F. Mott, *J. Non- Crystalline Solids* **1**, 1 (1968).
  91. M. Sigrist and K. Ueda, *Rev. Mod. Phys.* **63**, 239 (1991).
  92. J.L. Peng, P. Klavins, R.N. Shelton, H.B. Rodousky, P.A. Hahn and L. Bernardez, *Phys. Rev. B* **40**, 4517 (1989).
  93. F.W. Lytle, G van der Laan, R.B. Greegor, E.M. Larson, C.E. Violet and J. Wong, *Phys. Rev. B* **41**, 8955 (1990).
  94. A.J. Heeger and G. Yu, *Phys. Rev. B* **48**, 6492 (1993).

- 
95. D. Vaknin, S.K. Sinha, D.E. Moncton, D.C. Johnston, J.M. Newsam, C.R. Safinya and H.E. King, Jr., Phys. Rev. Lett. 58, 2802 (1987).
  96. P. Bourges, P.M. Gehring, B. Hennion, A.H. Moudden, J.M. Tranquada, G. Shirane, S. Shamoto and M. Sato, Phys. Rev. B 43, 8690, (1991).
  97. G. Shirane, Physica C 185-189, 80 (1991).
  98. A.I. Goldman, B.X. Yang, J. Tranquada, J.E. Crow and C.S. Jee, Phys. Rev. B 36, 7234 (1987).
  99. K.B. Lyons and P.A. Fleury, J. Appl. Phys. 64, 6075 (1988).
  100. V.J. Emery, Phys. Rev. Lett. 58, 2794 (1988).
  101. J. Ranninger, R. Micnas and S. Robaszkiewicz, Annals de Physique 13, 455 (1988).
  102. H. Frohlich, J. Phys C 1, 544 (1968).
  103. J. Ruvalds Phys. Rev. B 35, 8869 (1987).
  104. J.I. Gersten, Phys. Rev B 37, 3366 (1988).
  105. C.M. Verma, S. S. Rink and E. Abrahams, Solid State Commun. 63, 201 (1987).
  106. M. Inoue, T. Takemori, K. Ohtaka, R. Yoshizaki and T. Sakudo, Solid State Commun. 63, 201 (1987)
  107. J.R. Shrieffer, G.X. Wen and S.C. Zhang, Phys. Rev. Lett. 60, 1330 (1988).
  108. P.W. Anderson, Mat. Res. Bull. 8, 153 (1973).
  109. P.W. Anderson, Science 235, 1196 (1987).
  110. P.W. Anderson and Z. Zou, Phys. Rev. Lett. 60, 132 (1988).

## CHAPTER 2

### Experimental Techniques and Instrumentation

#### Section A

##### 2.1 Sample Preparation Assembly:

All samples were prepared in our laboratory. The required powders were weighed in a chemical balance having a sensitivity of 0.01mg. The powders were ground in an agate mortar and pestle and were fired in a furnace of tolerance 1200°C. The temperature in the furnace was measured using a calibrated Pt-13%Rh thermocouple placed near the alumina crucible containing the sample powder. A programmable Indotherm temperature controller (MPC-500) with proportional integral and derivative temperature control and built in room temperature compensation was used to control the temperature of the furnace. The temperature controller was connected to a power controller which regulated power supply to the furnace. A temperature stability of  $\pm 1^{\circ}\text{C}$  was realized for properly determined PID parameters for the furnace. The pellets of the sintered powders were made in a high carbon high chromium steel die by applying an axial pressure of 6 tons/cm<sup>2</sup> with a



hydraulic press. The pellets were handled carefully thereafter to avoid mechanical stress.

## 2.2 Sample Preparation:

### 2.2.1 $\text{Zn}_x\text{Ca}_{1-x}\text{Fe}_2\text{O}_4$ System:

For the preparation of  $\text{Zn}_x\text{Ca}_{1-x}\text{Fe}_2\text{O}_4$  ( $x=0.0-1.0$ ) samples, high purity  $\text{ZnO}$ ,  $\text{CaCO}_3$  and  $\text{Fe}_2\text{O}_3$  powders were weighed in required amounts and were ground thoroughly in mortar and pestle. The mixed powders were fired in an alumina crucible in air at  $900^\circ\text{C}$  for 24 hrs. The reacted powder was then reground, pressed into pellets and refired at  $1000^\circ\text{C}$  for 24 hrs. After each firing the sample was furnace cooled to room temperature. The samples were characterized by powder X-ray diffraction using  $\text{CrK}\alpha$  radiation.

### 2.2.2 $\text{Bi}_2\text{Sr}_{2-x}\text{Gd}_x\text{Ca}_1\text{Cu}_2\text{O}_{8+\delta}$ and $\text{Bi}_2\text{Sr}_{2-x}\text{Gd}_x\text{Ca}_1\text{Cu}_{1.96}\text{Fe}_{0.04}\text{O}_{8+\delta}$ systems:

All the above systems were prepared by conventional solid state reaction method. High purity (99.99%) powders of  $\text{Bi}_2\text{O}_3$ ,  $\text{SrCO}_3$ ,  $\text{CaCO}_3$ ,  $\text{CuO}$  (Aldrich) and  $\text{Gd}_2\text{O}_3$  (Indian Rare Earth Ltd) were weighed in the required stoichiometric amounts.  $\text{Fe}_2\text{O}_3$  powder enriched with Fe-57 (95.2%) and obtained from NEN Medical Products was used for iron doped samples. The weighed powders were intimately dry ground for two hours using mortar and pestle. The product was kept in the furnace in an alumina crucible and was calcined at  $700^\circ\text{C}$  for 2 hrs and then at  $800^\circ\text{C}$

for 12 hrs. The heating rate of the furnace was 5°C/min. The black powder thus obtained was reground carefully for nearly an hour. The samples without iron were pressed into several pellets at this stage at 6 tons/cm<sup>2</sup>. The pellets were sintered for 40 hrs followed by furnace cooling. The sintering temperature was increased from 860°C for x=0.0 to 880°C for x=0.65 in order to obtain single phase samples. The iron doped samples were powder sintered at the sintering temperatures of 870-890°C for 12 hrs followed by furnace cooling. The powder was ground again for an hour and resintered at temperature chosen within the above range for 12 hrs. This process was repeated two more times followed by furnace cooling of the samples. All the final products were characterized by CuK $\alpha$  radiation.

### 2.2.3 $\text{Bi}_2\text{Sr}_2\text{Ca}_{1-x}\text{Sm}_x\text{Cu}_2\text{O}_{8+\delta}$ and $\text{Bi}_2\text{Sr}_2\text{Ca}_{1-x}\text{Sm}_x\text{Cu}_{1.95}\text{Co}_{0.05}\text{O}_{8+\delta}$ systems:

Ceramic samples of  $\text{Bi}_2\text{Sr}_2\text{Ca}_{1-x}\text{Sm}_x\text{Cu}_2\text{O}_{8+\delta}$  and  $\text{Bi}_2\text{Sr}_2\text{Ca}_{1-x}\text{Sm}_x\text{Cu}_{1.95}\text{Co}_{0.05}\text{O}_{8+\delta}$  were also prepared by solid state reaction method. The powders of  $\text{Bi}_2\text{O}_3$ ,  $\text{SrCO}_3$ ,  $\text{CaCO}_3$ ,  $\text{CuO}$  (Aldrich 99.99%) and  $\text{Sm}_2\text{O}_3$  (Indian Rare Earth 99.99%) were used for synthesis of samples. For Co doped samples, cobalt powder of 99.9% purity obtained from Alpha Products was weighed in the required amount and was dissolved in Conc  $\text{HNO}_3$ . The solution was slowly dried on a heater till a tan color product was obtained. In this way excess nitric acid was evaporated. Appropriate precautions were taken to avoid the decomposition

of the nitrate. In order to transfer the nitrate which stuck to the bottom of the beaker, distilled water was slowly poured in the beaker with continuous stirring. The solution was then transferred to the mortar with two more washings of the beaker. This was then lamp dried and rest of the oxides were added to it. The powders of both type of samples were mixed thoroughly for two hours and were calcined at  $700^{\circ}\text{C}$  for 2 hrs and at  $800^{\circ}\text{C}$  for 12 hrs. The heating rate of the furnace was kept at  $5^{\circ}\text{C}/\text{min}$ . The calcined powder was reground for one hour and was sintered for 12 hrs at  $860^{\circ}\text{C}$ - $890^{\circ}\text{C}$  depending upon the value of  $x$ . The sintered powder was reground and refired with the repetition of the process three more times. The powders were pelletized at this stage followed by sintering at appropriate temperatures. After each sintering the samples were furnace cooled to about  $500^{\circ}\text{C}$  and then were taken out from the furnace. We found an increase in transition temperature when the samples were taken out at  $500^{\circ}\text{C}$  than when they were furnace cooled.

## 2.3 Electrical Resistivity Measurement

### 2.3.1 Set-up:

D.C. resistivity was measured in a closed cycle Helium refrigeration system. The refrigerator consists of a compressor and a displacer. The compressor supplies Helium gas at high pressure ( $\sim 300$  psig) to displacer where the gas expands cooling down the cold head. The region where the gas expands is enclosed by a jacket which is evacuated to make expansion of

the gas adiabatic. The sample was placed in the sample well below the cold tip of the refrigerator. Helium at a pressure of 4 psig was introduced in the sample well as an exchange gas to allow the cooling of the sample down to 14K. A constant current source (Keithley Model 224) with an accuracy of 0.05% was used to supply current to the sample. The rated stability of the current source was 100 ppm. The voltage drop across the sample was measured with a high input impedance ( >10G-ohms ) sensitive digital voltmeter (Keithley Model 182) having a resolution of 1nV in the lowest range of 3mV. The rated accuracy in 3mV range was 60ppm of reading and stability was 16ppm. A micro processor based temperature controller (Scientific Instruments) in PID mode was used to monitor and control the temperature of the sample. The temperature was measured using a silicon diode sensor with a resolution of 0.01K. The cryostat and measurement circuit is shown in Fig. 2.1 and Fig 2.2 respectively.

### 2.3.2 Contact Deposition:

For the measurement of resistivity a sintered pellet of the sample was first polished to a uniform thickness. Thick spots of silver paint (approximately a millimeter in size) were deposited in desired geometry on the pellet surface. The pellet with silver spots was kept under an IR lamp for nearly 15 minutes and then was fired in the furnace at 450°-550°C for half an hour. The furnace was cooled at rate of 1°C/min to 250°C and then switched off. Thin insulated copper wires were

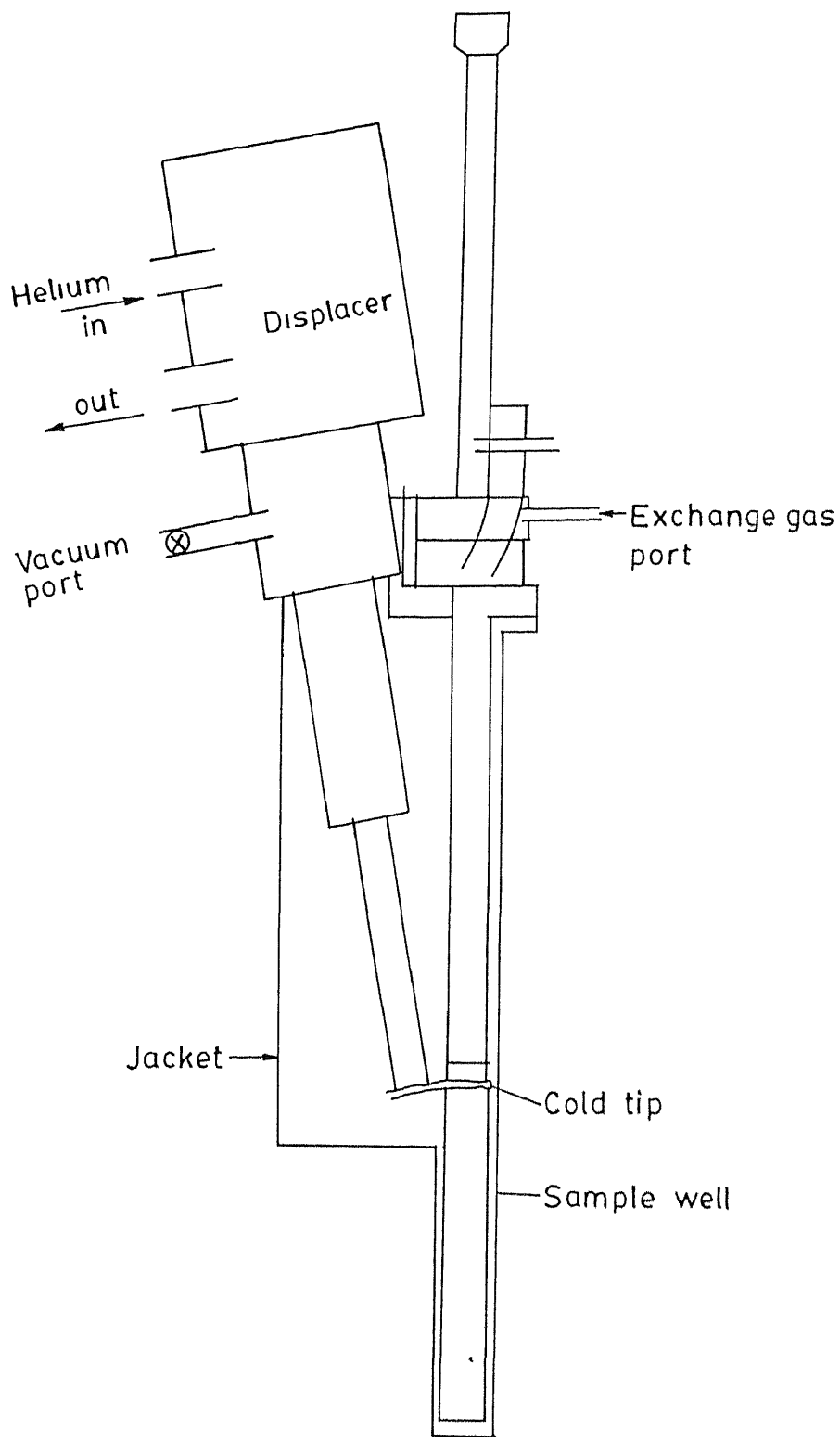


Fig. 2.1 Schematic diagram of closed cycle Helium refrigerator.

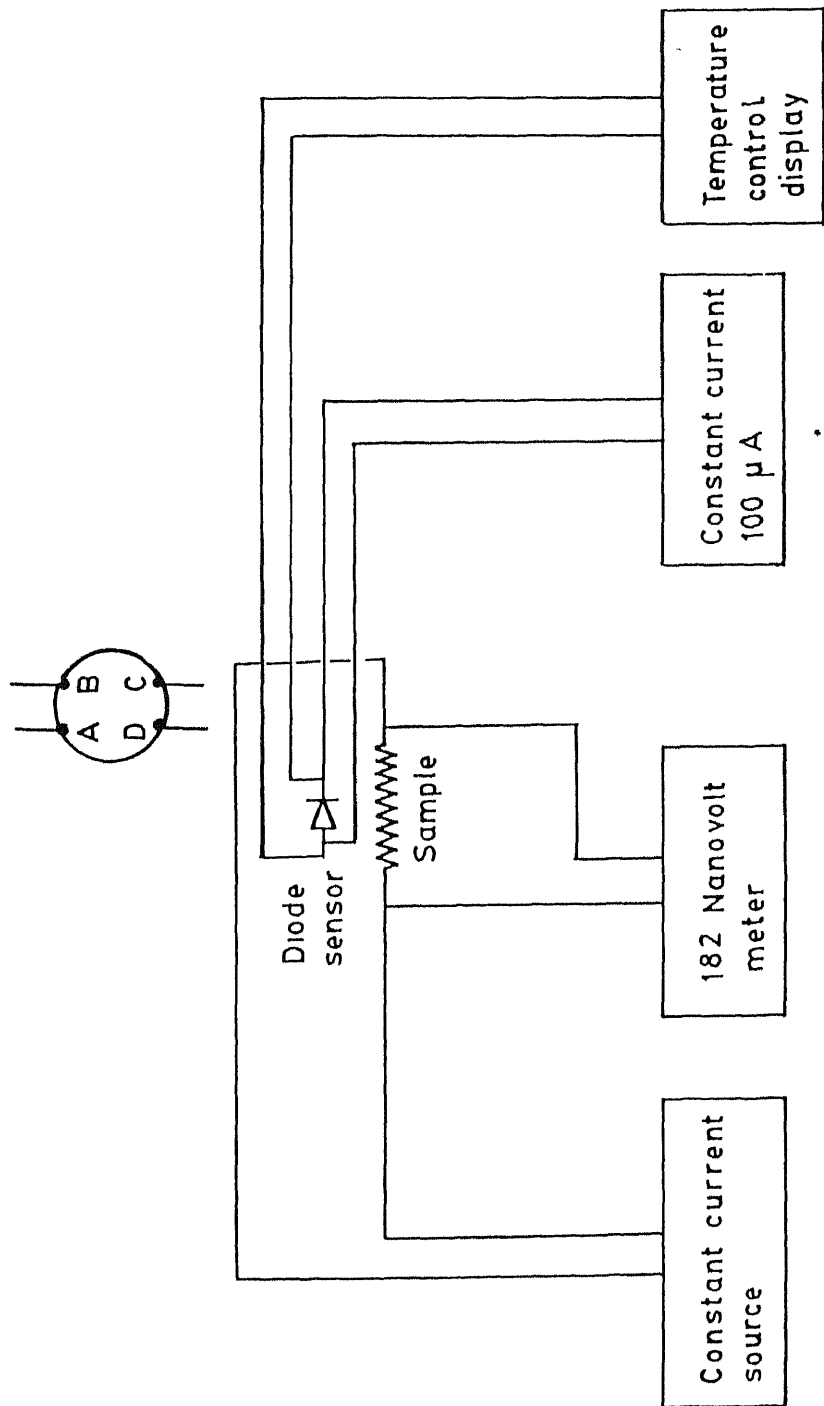


Fig. 2.2 Van der Pauw configuration and circuit diagram for resistivity measurement.

soldered on these silver pads with a pencil tip soldering iron and Indium solder. Better soldering performance was achieved by: (a) dipping copper wire ends in ortho-phosphoric acid before soldering and (b) keeping the temperature of the soldering iron close to the melting point of Indium. To meet the latter requirement the voltage applied to the soldering iron was kept near 150-170 volts using a variac. The resistance thus measured between any two contacts was found to be less than 10 ohms. No fluctuation in the measured voltage was observed in the resistivity measurement and resistivity could be measured accurately near the transition temperature.

### 2.3.3 Methodology:

The electrical resistivity of the samples was measured using four probe technique. A constant current of 0.5mA-1mA from the constant current source is passed through the sample. The voltage across a sample section is measured with a high impedance nanovoltmeter. The measurement is repeated with the reverse direction of current. If the thermo-emfs ( $\epsilon$ ) are assumed to be independent of current direction then

$$V_1 = RI + \epsilon \qquad V_2 = -RI + \epsilon$$

$$R = (V_1 - V_2)/2 \qquad (2.1)$$

where  $V_1$  and  $V_2$  are voltages across the samples in the forward and the reverse directions of current ( $I$ ) respectively and  $R$  is

the sample resistance.

In order to calculate resistivity of bulk high  $T_c$  superconductors any of the following two techniques could be employed. The first technique assumes a rectangular bar shaped samples. The resistivity is obtained by using  $\rho = R(A/l)$  where  $\rho$  is the resistivity,  $A$  is the cross sectional area and  $R$  is the resistance between two voltage probes separated by a distance  $l$ . In the second technique known as Van der Pauw technique [1], the contacts are deposited on the circumference of disk-shaped sample as shown in Fig. 2.2. For the determination of resistivity, a quantity  $R_{AB,CD}$  is calculated by passing a current  $I$  through the leads  $A$  and  $B$  and the voltage ( $V_{CD}$ ) across leads  $C$  and  $D$  is measured. Then  $R_{AB,CD} = V_{CD}/I$ . In a similar manner  $R_{BC,DA}$  is also determined. The resistivity of the specimen is obtained by solving

$$\exp\left(-\frac{\pi R_{AB,CD}}{\rho d}\right) + \exp\left(-\frac{\pi R_{BC,DA}}{x\rho d}\right) = 1 \quad (2.2)$$

where  $\rho$  is the resistivity,  $d$  is the thickness of the sample and  $x = R_{AB,CD}/R_{BC,DA}$ . We used Van der Pauw technique to determine the resistivity of Gd doped samples whereas for Sm and Co doped samples rectangular bar shape samples were used.

The resistivity measurements of  $Zn_xCa_{1-x}Fe_2O_4$  samples were performed using two probe method. An I.C. regulated power supply (Aplab, type LVE 30/2) was used to provide a constant voltage (50V) to the sample. A Keithley solid state electrometer (model 602) with a maximum current sensitivity of



$5 \times 10^{-15}$  amp was connected in series to determine current through the sample. Since the measured current was small, shielded cables were used for all electrical connections. For measurements below room temperature (14K-300K), the sample was inserted in the metallic samples well of the closed cycle Helium refrigerator, the details of which have already been described. For high temperature measurements (300K-500K) the sample was placed inside an oven with metallic walls around it. Thus the sample was properly shielded in both the cases by metallic enclosures which were grounded. The sample temperature was measured using a Si diode sensor and a temperature controller for measurements below room temperature. A copper-constantan thermocouple was used to determine temperature for high temperature measurements. The voltage across the thermocouple was measured using a Mecro multimeter. For resistivity determination samples were cut into rectangular bars and contacts made using silver paste. The main source of error in the determination of resistivity was the uncertainty in measurement of current I.

#### 2.4 A.C. Susceptibility Measurement:

The susceptibility measurements were carried out in a closed cycle Helium refrigerator using a primary coil and a pair of secondary coils. The measurement involves the application of an alternating magnetic field to the sample by means of an AC current through the primary. The system of two oppositely wound secondary coils connected in series detect

the variation in flux created when the sample is placed in one of the secondary coils. The resultant signal from the secondary is measured by a phase sensitive detector which produces output proportional to the susceptibility of the sample [2,3]. The set-up and measurement process is shown schematically in Fig. 2.3. The primary coil is wound on an epoxy cloth tube of length 40cm and the secondary coils on a plastic tube of length 45cm. The specifications of the primary and a secondary coil are given in the following table:

	number of turns	length (cm)	I. D. (cm)	O. D. (cm)	resistance (ohm)
Primary	1067	11.5	1.25	1.60	17
Secondary	1078	2.0	0.50	1.23	56

The turns in the two coils of the secondary are in opposite directions and are connected in series. The pair of secondary coils is inserted in the tube of primary coil and is held to it by a pair of screws. A copper-constantan thermocouple is placed just below the bottom coil of the secondary to monitor sample temperature. The exact location of the secondary inside the primary is determined by observing minimum signal across it when moved in the inhomogeneous field

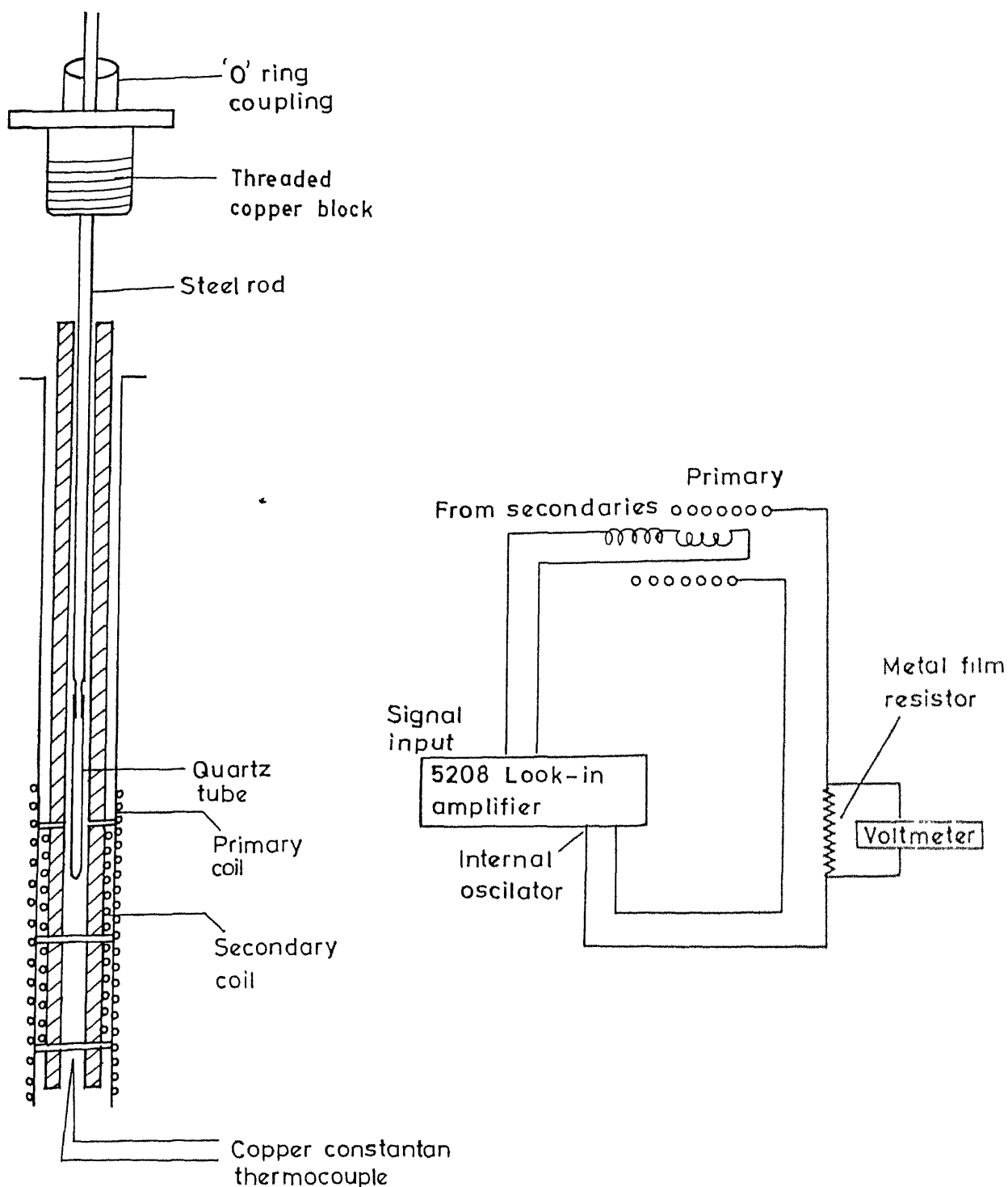


Fig. 2.3 Schematic representation of susceptibility set-up and measurement process.

of the primary. The field is generated by applying small AC current to the primary. The offset voltage thus obtained was  $\sim 1\mu\text{V}$ . The assembly consisting of primary and secondary coils is then positioned in the sample area of the cryostat below the cryotip. The sample is placed in a quartz tube which is held from the top by a stainless steel rod. The sample could be moved between the centres of the two secondaries by moving the rod through an O-ring coupling.

AC current to the primary was supplied by the internal oscillator of a two phase lock-in amplifier (PAR 5208). A metal film resistor of 15 ohm (1% tolerance) was put in series to measure current through the primary. The voltage across the resistor was measured using a multimeter with a sensitivity of  $10\mu\text{V}$ . The thermocouple voltage was measured using a Keithley 182 voltmeter. The reference temperature of the thermocouple was at room temperature and thermocouple ends were imbedded in a beaker full of cotton. The temperature of the cold tip and hence the temperature of the sample area was controlled by a microprocessor based temperature controller (Scientific Instruments). The voltage across the secondary was measured to a maximum accuracy of 1% using above mentioned lock-in amplifier, operated in the internal mode. The time constant and roll-off of the filter was 300ms and 12dB/octave respectively. To eliminate any ground loop current, the signal from the secondary was fed to the lock-in amplifier in its differential input. All connections were made using shielded cables.

AC susceptibility which is a complex quantity is defined

using the Fourier transforms of time dependent magnetization  $M(t)$ .

$$\chi = \chi' + i\chi''$$

$$\chi = \frac{1}{2\pi Vh} \int_0^{2\pi} M(t) e^{i\omega t} d(\omega t) \quad (2.3)$$

where  $V$  is the sample volume,  $h$  is AC field amplitude and  $\omega$  is AC field frequency. The imaginary component  $\chi''$  measures the dissipation in the sample.

In order to determine real and imaginary components of the susceptibility, the phase difference  $\theta$  between the sample and the reference to the lock-in amplifier was determined when the superconducting sample was in low loss state i.e.  $\chi''=0$ .  $\theta$  was determined to an accuracy of  $0.5^\circ$ . Under this condition, the out of phase component was proportional to  $\chi''$  and the in phase component was proportional to  $\chi'$ . The offset voltage which varied with temperature was eliminated by moving the sample between two secondary coils.

## 2.5 Hall Effect Measurement:

Hall effect measurements at room temperature were performed by positioning the sample in the sample well of the cryostat. A bar shaped sample was cut carefully from the sintered pellet of the sample using a diamond wheel saw. The length of the bar was kept more than twice the width to minimize the shorting effect of the Hall field due to current electrodes [4]. The thickness of the sample was reduced to 0.5

mm or less by polishing it on an emery paper. The current for the measurement was chosen from the linear portion of the I-V curve of the sample. The Hall contacts were deposited on a line mark made in the middle portion of the sample using the diamond wheel while the sample was loaded on the diamond wheel saw set-up. The contacts were made using silver paste according to the description given in resistivity section.

A constant current source and a nanovoltmeter the details of which are mentioned in section 2.2 were used for the flow of current and voltage measurement respectively. The magnetic field was applied using a Nd-B-Fe based permanent magnet having a strength of 3.5 kG. The magnetic field was directed approximately along the normal to the sample surface and perpendicular to the current flow. A model 650 (South Bay Technology Inc) low speed diamond wheel saw equipped with a facility of angular rotation was used to cut the samples.

The method of the measurement involved the determination of the Hall voltage ( $V_H$ ) which is a function of magnetic field (B) and current (I) for a given specimen. In practice thermal and misalignment voltages are superimposed on the Hall voltage i.e.

$$V = V_H + V_{MIS} + V_{TH} \quad (2.4)$$

where V is the measured voltage,  $V_H$  is the Hall voltage (a function of B and I),  $V_{MIS}$  is the misalignment voltage (a function of I only) and  $V_{TH}$  is the thermal voltage assumed to be independent of B and I. The elimination of thermal voltage

requires the determination of  $V$  with the reversed direction of current. The misalignment voltage is eliminated by reversing the directions of current followed by averaging the four observations. This gives

$$V_H = \frac{1}{4} \left[ \{V(B, I) - V(B, -I)\} - \{V(-B, I) - V(-B, -I)\} \right] \quad (2.5)$$

The Hall coefficient  $R_H$  is related to  $V_H$  as  $R_H = (V_H d / IB)$  where  $d$  is the thickness of the sample. The carrier concentration was calculated assuming a single band model which gives  $R_H = 1/ne$  where  $n$  is the electronic charge. The sign of the  $R_H$  was determined keeping in mind the Lorentz force equation  $\vec{F} = e \vec{v} \times \vec{B}$ . For each sample 25-30 readings were taken for both the directions of magnetic field. As the measurement time was long care was taken to stabilize the ambient temperature any variation of which could change the misalignment voltage leading to errors in the determination of Hall voltage. The primary source of error in the measurement of  $V_H$  was the heating effects at contacts resulting in the variation of misalignment voltage.

## 2.6 Magnetoresistance Measurement:

The magnetoresistance measurements were performed in the same set-up as that of resistivity. The magnetic field was applied using an electromagnet which could provide magnetic field upto 2kG. The applied magnetic field was perpendicular to both current direction and surface of the sample. The

temperature was measured using a silicon diode sensor which is sensitive to magnetic fields. Temperature correction data for each required value of magnetic field were obtained by measuring temperature with and without applied external magnetic fields. The corrections to the sample temperature in presence of magnetic field were performed using correction data and interpolation technique.

### Section B

#### 2.7 Mossbauer Spectroscopy:

The nuclear transition of an isolated atom of mass  $M$  from its excited state to the ground state is accompanied by emission of a  $\gamma$ -ray photon. During the process the atom recoils with an energy  $E_R = E_0 / 2Mc^2$  (2meV for  $^{57}\text{Fe}$ ) where  $E_0$  is the energy difference between excited state and the ground state. The momentum and energy conservation requires  $\gamma$ -ray energies to be smaller by an amount  $E_R$ . In the absorption process, the required  $\gamma$ -ray energy to make up a transition from the ground state to the excited state is  $E_0 + E_R$ . The large separation between the absorption and the emission lines on the energy scale ( $10^6$  times larger than the natural line width of  $4.5 \times 10^{-9}$  eV) does not lead to overlap between the lines and hence nuclear resonance absorption is not possible. However, the thermal motion of the atoms Doppler broadens the emission and absorption lines (width~10meV) and a low probability for



resonance is thus possible due to overlap of lines in a small regions. If the nucleus is embedded in a solid its effective mass is very large and the recoil energy is small. If the recoil energy is larger than the characteristic vibration (phonon) energy, the nucleus recoils by transferring energy to the lattice vibrational spectrum. However, there is a certain probability  $f$  that no lattice excitation takes place (zero phonon process) during  $\gamma$ -ray emission or absorption process. The recoil free fraction  $f$  which denotes the fraction of nuclear transition without recoil is expressed as [5-6]

$$f = \exp(-k^2 \langle x^2 \rangle) \quad (2.6)$$

where  $\langle x^2 \rangle$  is mean square vibrational amplitude in the direction of  $\gamma$ -ray.  $f$  is called the Debye-Waller factor (or Lamb-Mossbauer factor). For  $^{57}\text{Fe}$  Mossbauer spectroscopy  $^{57}\text{Co}$  radioactive isotope (half life=270 days) is used which decays into  $^{57}\text{Fe}$  nuclear excited state by electron capture. Three  $\gamma$ -rays are of energies 14.4, 123 and 137 keV are emitted on decay to the stable ground state. The commonly used radiation is 14.4keV due to its large  $f$ -value.

In a solid the embedded Mossbauer nuclei experience electric and magnetic fields which are created by the shell electrons of the nuclei and charges in the neighbourhood. The perturbation of nuclear energy levels due to interaction of nuclear moments with electric and magnetic fields generates various nuclear hyperfine interactions. The important hyperfine

interactions include the shifting of the nuclear energy levels and splitting of degenerate energy levels into sublevels. The detailed discussion is given further.

### 2.7.1 Isomer Shift and Second Order Doppler Effect:

The Coulomb interaction between the nuclear charge which spreads over the finite volume and electron charge density at the nuclear site shift the energy levels of Mossbauer nuclei. The shift will be different for excited ( $I=3/2$ ) and ground ( $I=1/2$ ) states as the nuclear radius is different in each state of excitation. The difference of electrostatic shift between the source and the absorber depends on the electron densities at the nucleus and is expressed as

$$\delta = -\frac{2}{5}\pi Ze^2 \left\{ |\Psi(0)|_A^2 - |\Psi(0)|_S^2 \right\} (R_e^2 - R_g^2) \quad (2.7)$$

where  $Ze$  is the total nuclear charge,  $|\Psi(0)|_A^2$  and  $|\Psi(0)|_S^2$  are electron densities at the absorber and the source nuclei and,  $R_e$  and  $R_g$  are nuclear radii in the excited state and the ground state respectively.  $\delta$  is called the isomer shift. The Doppler velocity  $v_d$  needed to restore resonance between the source and absorber in a Mossbauer experiment is therefore  $v_d = (c/E_\gamma)\delta$  where  $E_\gamma$  is  $\gamma$ -ray energy. Since only electrons with zero angular momentum (s-electron) have non-zero probabilities at the the nucleus, Isomer shift is a measure of difference of s-electron densities between the source and the absorber. The s-electron densities can be altered by directly varying

s-electron population in the valence shell or indirectly by shielding of s-electron by electrons of non-zero angular momentum (p, d or f states). For  $^{57}\text{Fe}$  since  $R_e < R_g$  an increase (decrease) of Isomer shift corresponds to decrease (increase) of s-electron density at the nucleus.

The second order Doppler shift ( $\delta_{\text{SOD}}$ ) also shift the  $\gamma$ -ray energy. It is a relativistic effect and arises due to harmonic motion of Mossbauer atom.  $\delta_{\text{SOD}}$  is proportional to mean square velocity of the nucleus and is given as  $\delta_{\text{SOD}} = -E_\gamma (\langle v^2 \rangle / 2c^2)$ . The experimentally observed shift determined by the distance of resonance line from zero Doppler velocity is the sum of isomer shift and  $\delta_{\text{SOD}}$ .

### 2.7.2 Quadrupole Splitting:

A nucleus carries a nuclear electric quadrupole moment due to deviation of nuclear charge from spherical symmetry. The electric quadrupole moment (Q) of the nucleus interacts with the electric field gradient at the nucleus. The components of the electric field gradient in the principal axes system are chosen such that  $|V_{zz}| > |V_{yy}| \geq |V_{xx}|$ . The eigenvalues  $E_Q$  of the Hamiltonian describing the interaction can be written as

$$E_Q = \frac{eQV_{zz}}{4I(2I-1)} \left[ 3m_I^2 - I(I+1) \right] (1-\eta^2/3)^{1/2} \quad (2.8)$$

where  $I$  is the nuclear spin,  $m_I$  is the nuclear spin quantum number and  $\eta = (V_{xx} - V_{yy}) / V_{zz}$  is the asymmetry parameter. The electric quadrupole interaction causes a splitting of  $2I+1$  fold

degenerate energy level of the nucleus with  $I > 1/2$  into substates  $|I, \pm m_I\rangle$ . For  $^{57}\text{Fe}$  with  $I=3/2$  in the excited state and  $I=1/2$  in ground state, the  $I=3/2$  splits into two doubly degenerate substates  $|\frac{3}{2}, \pm\frac{3}{2}\rangle$  and  $|\frac{3}{2}, \pm\frac{1}{2}\rangle$ . The position of these two lines are  $E_Q(\pm 3/2) = (eQV_{zz}/4)(1+\eta^2/3)$  and  $E_Q(\pm 1/2) = (-eQV_{zz}/4)(1+\eta^2/3)$ . The energy difference ( $\Delta E_Q$ ) between the two substates are  $(eQV_{zz}/2)(1+\eta^2/3)$  and is called quadrupole splitting. If the recoil free fraction is anisotropic (caused by anisotropic amplitudes of the atomic vibration) then for a polycrystalline absorber, the doublets will be asymmetric. The phenomenon is called Goldanskii Karyagin effect. Other effect which can cause asymmetry spectrum is the texture effect i.e. preferred orientation of crystallites in the absorber introduced during the absorber preparation.

### 2.7.3 Magnetic Hyperfine Interaction:

The non-zero magnetic dipole moment of the nucleus may interact with a magnetic field  $\underline{H}$  at the nucleus. The eigenvalues of the Hamiltonian describing the interaction is given as

$$E_M(m_I) = -g_N \mu_N H m_I \quad (2.9)$$

where  $g_N$  is Landè splitting factor and  $\mu_N$  is the Bohr magneton. A state with spin quantum number  $I$  splits into  $2I+1$  nondegenerate substates  $|I, m_I\rangle$ . The possible sources which contribute to the effective magnetic field at the nucleus are

- (a). the Fermi contact term which is due to net spin up or spin down s-electron density at the nucleus.
- (b). a contribution from the orbital motion of valence electron.
- (c). a contribution from the Dipolar interaction of the nucleus with the neighbouring spins.

The sum of the above three terms is usually referred to as the internal magnetic field (H). The dominant contribution to the internal magnetic field comes from the Fermi contact term. The imbalance of s-electron spin density at Mossbauer nuclei may originate from intrinsic pairing of s-electron or indirectly via polarization effect of filled s-orbitals by unpaired electrons in d-orbitals. The time scale of observation of internal magnetic field is  $10^{-8}$  s as the electronic spin which generate H are subject to change of direction. In paramagnetic compounds fast spin relaxation results in zero time averaged value of H so that no splitting is observed. The presence of cooperative phenomenon such as ferromagnetism or antiferromagnetism decreases spin relaxation rate and magnetic hyperfine splitting occurs. The effect of above interactions on nuclear energy levels is shown in Fig. 2.4.

## 2.8 Mossbauer Spectroscopy Instrumentation:

The Mossbauer experiments were carried out using a Co-57 source deposited on a Rh matrix and a spectrometer obtained from Wissel, West Germany. The measurements were done in transmission geometry and in constant acceleration mode. The

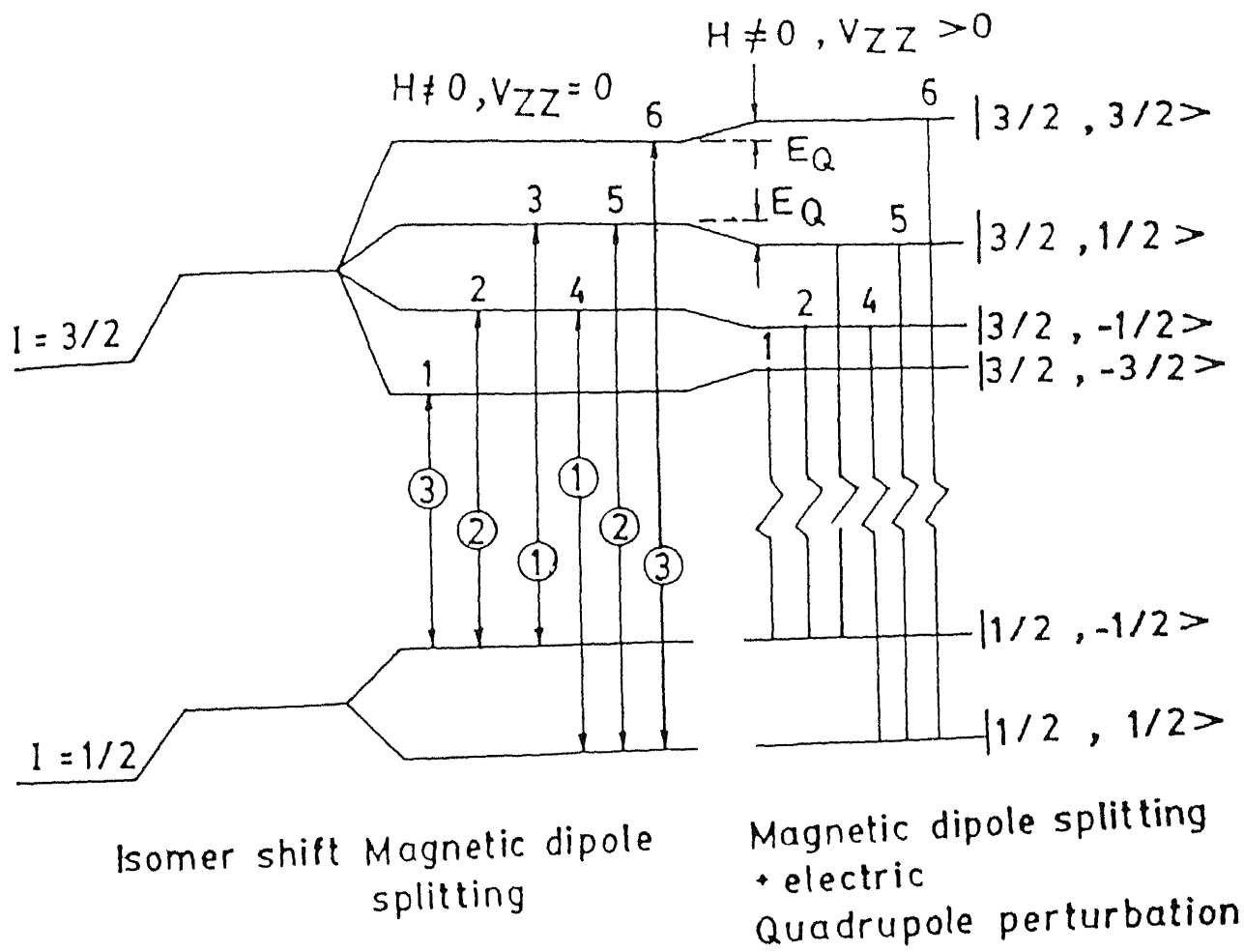


Fig. 2.4 Effect of various interactions on the nuclear energy levels of the absorber.

spectrometer consists of a digital function generator (Model DFG-1200), a Mossbauer drive unit (model MR-360) and a velocity transducer (model MA-260). The velocity transducer was driven by the drive unit coupled to the function generator for receiving waveforms. A triangular waveform of frequency 23Hz and amplitude 12Vpp obtained from the function generator was fed to the drive unit to provide parabolic displacement to the transducing element. The function generator also provided start and channel advance pulses to the multichannel analyzer. The start pulses were generated at the time of positive maximum of the waveform.

An argon filled proportional counter (obtained from Technical Physics Division BARC Bombay) with an aluminized mylar window was used for detection of gamma( $\gamma$ )-rays. The counter was operated at 1500 volt using a Hewlett Packard high voltage power supply (model Harrison 6522A). A preamplifier (model 401) and an amplifier (model 512), both from Mech-Tronics Nuclear, were connected to the proportional counter. The output of the amplifier was fed to the multichannel analyzer.

The ND-62 multichannel analyzer (MCA) having maximum 2048 channels was used in PHA mode for selecting 14.4 keV gamma-rays and was operated in multichannel scaling mode for data acquisition. The synchronization of the drive motion with the channel sweep of MCA was achieved by advancing the address register of the memory one by one using channel advance pulses from the function generator. Each sweep was triggered by a

start pulse obtained from the spectrometer. Data acquired in each subsequent sweep was added to the data stored in the previous sweep. Data from MCA were transferred to a computer for analysis. The experiment is shown schematically in Fig. 2.5.

The spectra obtained from MCA were folded to eliminate geometrical effect caused by relative motion between the source and the absorber [7]. The relative motion changes source-detector distance periodically and consequently the count rate will be a function of velocity. Several folding points were obtained by taking sum of the squares of the difference between the left half and the right half in a region near a proposed folding point. The optimum folding point was the value with the minimum sum.

All The spectra were recorded in 512 channels of MCA. The calibrations were done using a metallic iron foil (NEN Products) of thickness  $6.4\mu\text{m}$ . The line widths for innermost lines of six finger pattern of the natural iron foil was  $0.25\text{mm/s}$ .

## 2.9 Low Temperature Mossbauer Measurement:

Mossbauer measurements as a function of temperature were performed in an exchange gas variable temperature system obtained from Janis. The system was installed as an integral part of a closed cycle Helium refrigerator. It consists of a copper-tube with mylar windows mounted on the cold head. The tube is surrounded by a double wall steel shroud in order to



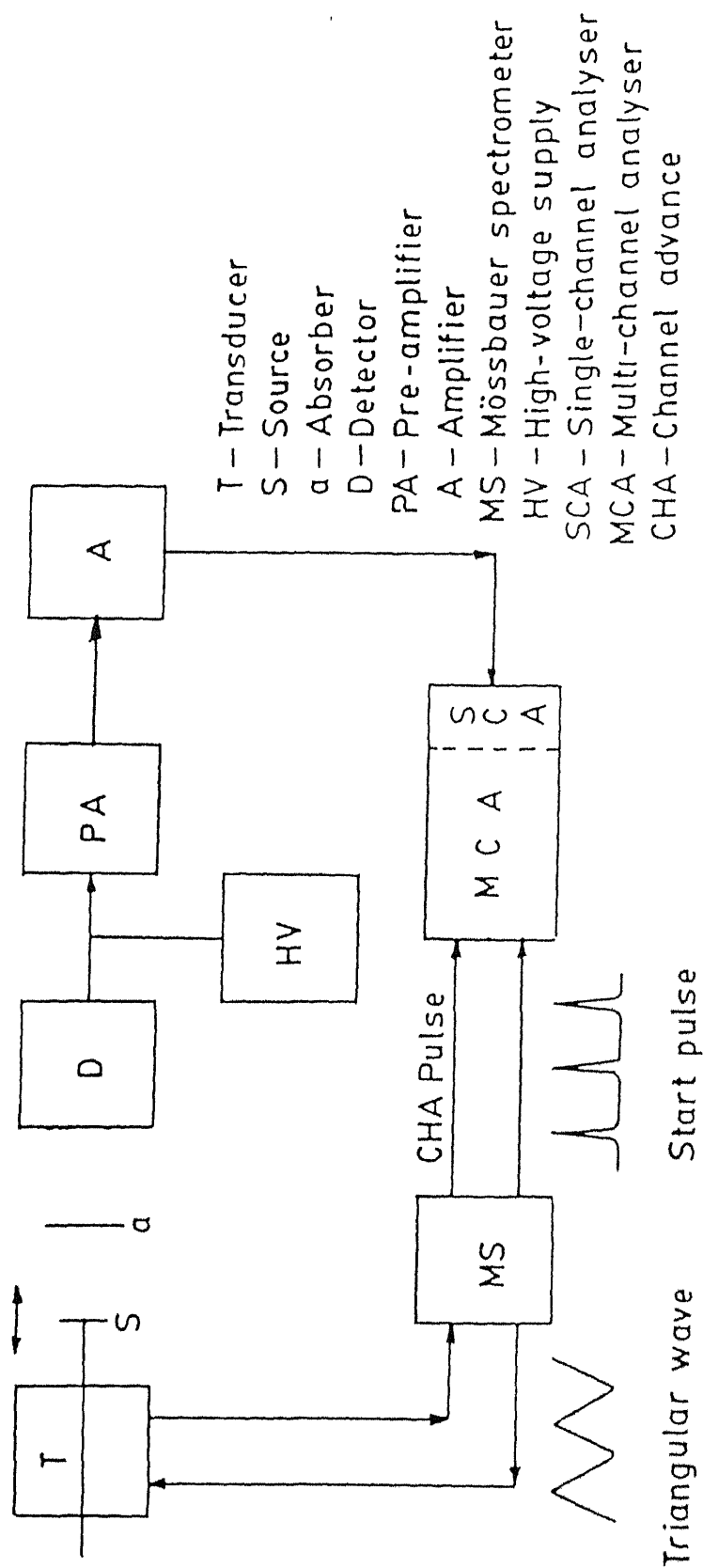
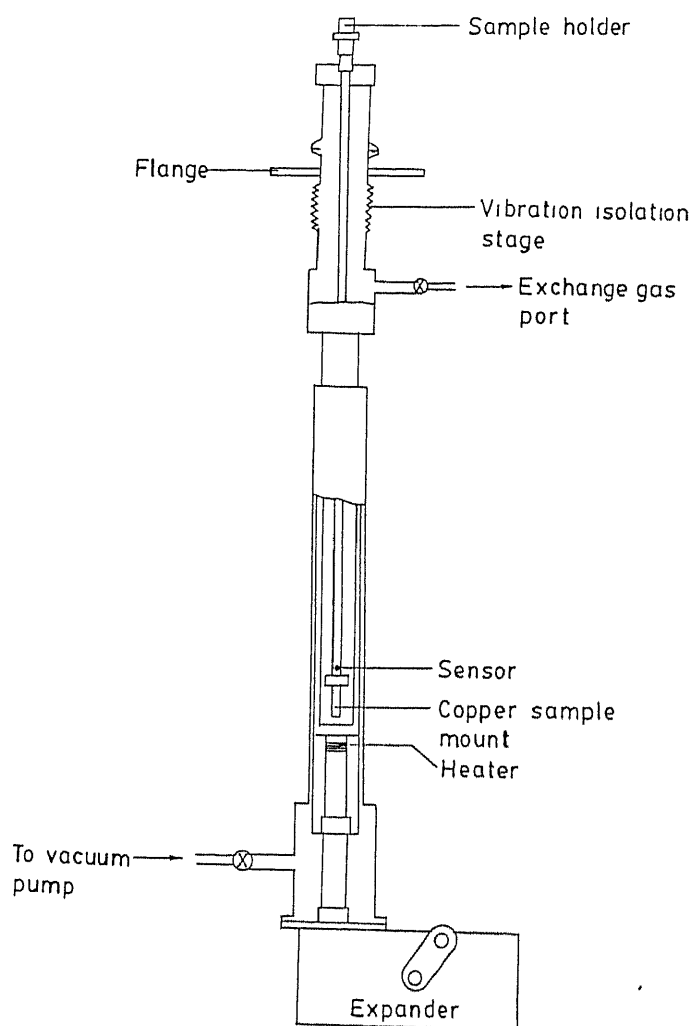


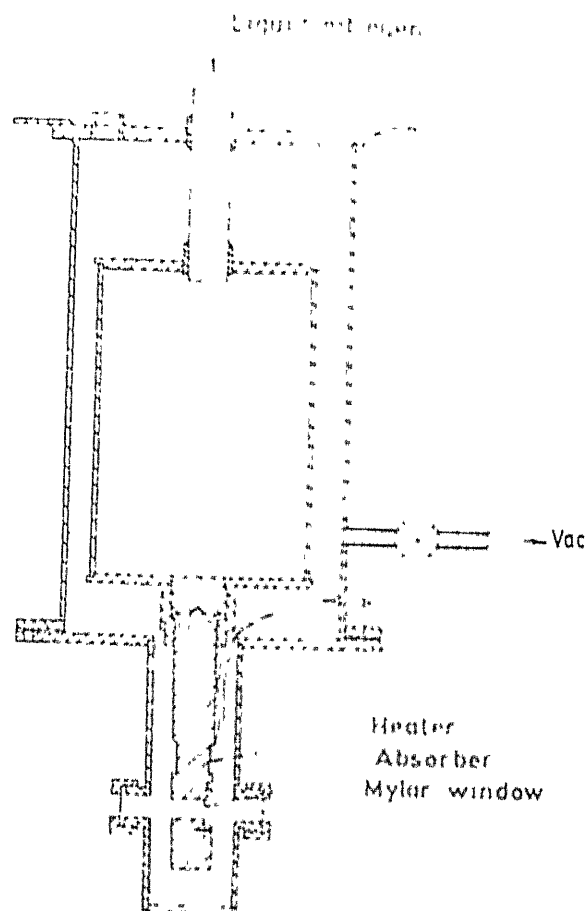
Fig. 2.5 Schematic diagram of instruments involved in Mössbauer spectroscopy.

isolate cold head and sample area from the surroundings. The sample is positioned inside the copper tube and the sample holder is separated from the shroud by metallic bellows which absorb vibrations generated during refrigerator's operation. The whole assembly was fixed on a concrete bench. The portion above the vibration isolation stage was fixed to a thick aluminium plate which in turn was rigidly bolted to two supporting concrete columns. The refrigerator is shown in Fig. 2.6(a). The transducer and the detector were separated from the concrete bench by thick foam to eliminate transmission of vibrations present in the bench. An oil diffusion pump (IBP type 0-500) was used to evacuate the shroud. The temperature of the sample was determined using a Si-diode sensor (Lake Shore Cryotronics model DT-470) placed on the copper mount above the sample. A 25 $\Omega$  heater was fixed above the sample mount to vary the sample temperature. A temperature controller (Lake Shore Cryotronics model DRC-91C) equipped with three term temperature control: proportional integral and derivative was used for accurate temperature control. Temperature stability of 0.01K was realized for properly evacuated vacuum shroud. For the measurement purpose the sample was wrapped in a thin aluminium foil and was properly anchored to the copper sample mount of the sample holder.

The Mossbauer measurements of  $\text{Zn}_x\text{Ca}_{1-x}\text{Fe}_2\text{O}_4$  at 77K were carried out in a home-built liquid nitrogen cryostat. The cryostat which is shown in Fig. 2.6(b) consists of two concentric cylindrical brass vessels connected by a thin walled



(a)



(b)

fig. 2.6 (a) Variable temperature closed cycle refrigerator and  
b) liquid nitrogen cryostat for Mossbauer measurements.

stainless steel tube. The tube is used for pouring liquid nitrogen in the inner vessel. The absorber is mounted on a copper cold finger attached to the bottom of the inner vessel. The cold finger is enveloped by a brass tube equipped with mylar windows. The thermal insulation between the two vessel is provided by evacuating the space in between them. The flange of the tube is connected to outer vessel using an O ring coupling. The temperature of the sample is measured using a copper-constantan thermocouple. The leads of the thermocouple are taken out through glass to metal seals fixed at the outer vessel. All parts of the dewar are nickel electroplated to provide radiation shield.

#### 2.10 References:

1. L.J. van der Pauw, Philips Research Reports 13, 1 (1958).
2. L. Hartshorn, J. Sci. Instrum. 2, 145 (1925).
3. C.M. Brodbeck, R.R. Bukrey and J.T. Hoeksema, Rev. Sci. Instrum. 49, 1279 (1978).
4. The Hall effect and related phenomena by E.H. Putley, Butterworths (1960).
5. G.K. Wertheim, Mossbauer Effect: Principle and Applications (Academic Press, New York, 1964).
6. N.N. Greenwood and T.C. Gibb, Mossbauer Spectroscopy (Chapman and Hall, London, 1971).
7. J.J. Spijkerman, F.C. Ruegg and J.R. de Voe in Mossbauer Effect and Methodology (Plenum Press, New York, 1965).

## CHAPTER 3

### Study of Gd Substituted $\text{Bi}_2\text{Sr}_2\text{Ca}_1\text{Cu}_2\text{O}_{8+\delta}$ System

#### 3.1 Introduction:

As we noted in Chapter (1) doping of holes by appropriate elements is an essential mechanism to bring about superconductivity in an otherwise insulating parent compound of high temperature superconductor. Since the mechanism of superconductivity is unclear, doping the cuprate superconductors by different cation elements and the response of various physical properties to the dopants constitute an effective means to study these compounds. The substitution generally alters the superconducting properties, oxygen ordering, carrier concentration and magnetic properties. Also, the response of physical properties is different for different dopants as well as the compounds. For example, the introduction of non-magnetic Zn for Cu in  $\text{Y}_1\text{Ba}_2\text{Cu}_3\text{O}_{7-\delta}$  system suppresses  $T_c$  faster than the magnetic Fe, Co or Ni [1,2]. In other systems however no such dramatic behaviour due to Zn substitution is found [3,4]. Again, the  $T_c$  of  $\text{Y}_1\text{Ba}_2\text{Cu}_3\text{O}_{7-\delta}$  remains unchanged by doping of rare-earth elements, except Pr at Y site [5]. The introduction of Pr destroys superconductivity and the system

becomes insulating. We have seen in section 1.5 that the substitutions of magnetic and nonmagnetic impurities in conventional superconductors have entirely different effects on superconductivity. Whereas magnetic impurities suppress  $T_c$  considerably, non-magnetic impurities have virtually no effect on transition temperature. This is correlated to s-state pairing mechanism which exist in conventional superconductors. The above two examples on  $Y_1Ba_2Cu_3O_{7-\delta}$  system illustrate that cuprates have unusual responses to the impurities. Thus it is of fundamental interest to study in high temperature superconductors what causes superconductivity to disappear and also their properties in the insulating state. Due to proximity of superconducting and insulating phases in cuprates such studies gain more importance. The study of insulating state gives information about the density of states and magnetic properties of these materials.

The proposed mechanisms for the suppression of superconductivity are many and there is no consensus on this issue. The destruction of superconductivity in  $La_{1.85}Sr_{0.15}CuO_4$  system due to magnetic and non-magnetic impurities at Cu-site occurs because of pair-breaking effect caused by generation of local magnetic moments in  $CuO_2$  planes [4]. On the other hand the suppression of superconductivity in  $Y_{1-x}Pr_xBa_2Cu_3O_{7-\delta}$  system is suggested to be due to strong hybridization between Pr 4f states and conduction band leading to depairing of cooper pairs [6,7]. The pair breaking caused by non-magnetic disorder has been interpreted as the cause of suppression of

superconductivity in  $Y_1Ba_2Cu_{3-x}Zn_xO_{7-\delta}$  as well as in  $Bi_2Sr_2Ca_{1-x}Y_xCu_2O_{8+\delta}$  systems [8]. Thus it is evident that there is no single generally accepted mechanism at present. Even for a single system  $Bi_2Sr_2Ca_{1-x}Gd_xCu_2O_{8+\delta}$  two different mechanisms for the destruction of superconductivity have been proposed. Ref.[9] proposes increased Coulomb interaction between electrons as the basic reason for the suppression of superconductivity whereas ref.[10] proposes disruption of  $Cu3d-O2p$  hybridization as the dominant mechanism. Therefore we carried out a detailed study on Gd doped  $Bi_2Sr_2Ca_1Cu_2O_{8+\delta}$  (2:2:1:2) system to get more insight into the issue.

In  $Bi_2Sr_2Ca_1Cu_2O_{8+\delta}$ , the crystallographic site of Sr is identical to that of La in  $La_2CuO_4$  (2:0:1) [11]. Hence by analogy with the substitution of La by Sr in 2:0:1 system, Sr can be replaced by rare earth elements in 2:2:1:2 system. In the present chapter we study the consequences of Gd doping in this system by experiments on lattice parameter, Hall effect, temperature dependence of electrical resistivity and magnetoresistance measurements. Hall effect and magnetoresistance measurements are done for the first time for this system. In the next section we present a brief overview of rare-earth substituted 2:2:1:2 system.

### 3.2 Previous studies on Y or rare-earth doped 2:2:1:2 system:

In  $Bi_2Sr_2Ca_1Cu_2O_{8+\delta}$  system, the transition from superconducting to insulating state due to substitution of Ca by rare-earth elements (Y, Eu, Nd) was first reported by Noburu

Fukushima et.al. [12]. A detailed study of electrical and magnetic properties of  $\text{Bi}_2\text{Sr}_2\text{Ca}_{1-x}\text{M}_x\text{Cu}_2\text{O}_{8+\delta}$  (M= Y or rare earth) system was carried out following their discovery. Yoshizaki et.al. [13] in Y doped samples found that the resistivity behaviour of  $x=0.5$  samples from 5K to 300K could be well described by the three dimensional (3-D) variable range hopping mechanism (VRH) which indicated that the system was essentially insulating. The presence of antiferromagnetic ordering above room temperature in insulating  $\text{Bi}_2\text{Sr}_2\text{Y}_1\text{Cu}_2\text{O}_{8+\delta}$  system was observed by Nishida et.al. [14] using positive muon spin rotation ( $\mu^+\text{SR}$ ) technique. Similar antiferromagnetic ordering was reported earlier in insulating  $\text{La}_2\text{CuO}_4$  [15] and  $\text{Y}_1\text{Ba}_2\text{Cu}_3\text{O}_6$  [16] systems also. Tamegai et.al. [17] studied the consequence of Y doping in  $\text{Bi}_2\text{Sr}_2\text{Ca}_1\text{Cu}_2\text{O}_{8+\delta}$  system using structural, transport and magnetic measurements. The lattice parameters changed with Y doping and metal to insulator transition was considered to be driven by reduction of the charge carrier concentration estimated by Hall effect measurement. Their electron diffraction pattern showed a decrease in period of modulation from 4.74b in  $\text{Bi}_2\text{Sr}_2\text{Ca}_1\text{Cu}_2\text{O}_{8+\delta}$  to 4.0b in  $\text{Bi}_2\text{Sr}_2\text{Y}_1\text{Cu}_2\text{O}_{8+\delta}$ . The studies related to structural and physical properties for most of the rare-earth doped  $\text{Bi}_4\text{Sr}_4\text{Ca}_{2-x}\text{RE}_x\text{Cu}_4\text{O}_y$  (RE = La, Pr, Nd, Sm, Eu, Gd, Dy, Y, Tb, Ho, Er, Tm, Yb and Lu) were done by Tarascon et.al. [11]. They found a complete solid solution existing upto  $x=2.0$ . With more than one RE ( $x>1$ ) substitution,  $T_c$  was depressed and compound became insulating beyond  $x=1.5$ . They correlated depression in



$T_c$  from 85K ( $x=0.0$ ) to less than 4.2K ( $x=1.5$ ) to decrease in formal valence of copper irrespective of whether the rare-earth element was magnetic or non-magnetic (Lu). Temperature dependence of magnetization measurements using SQUID magnetometer showed the effective magnetic moment ( $\mu_{eff}$ ) of magnetic rare-earth doped samples, close to that expected for free trivalent rare-earth ions. However, no magnetic ordering over the range of temperature 1.7-400K was observed in all the substituted compounds. Clayhold et.al. [18] reasoned the depletion of holes in  $\text{CuO}_2$  plane by Tm doping as responsible for driving the  $\text{Bi}_2\text{Sr}_2\text{Ca}_{1-x}\text{Tm}_x\text{Cu}_2\text{O}_{8+\delta}$  system in the insulating state. A linear decrease of Hall carrier density  $n_H$  with Tm concentration was observed which led them to conclude  $\text{Bi}_2\text{Sr}_2\text{Ca}_{1-x}\text{Tm}_x\text{Cu}_2\text{O}_{8+\delta}$  to be a strongly correlated Mott-Hubbard system. Mandal et.al. [19] found the metal-insulator transition at  $x=0.55$  in  $\text{Bi}_2\text{Sr}_2\text{Ca}_{1-x}\text{Y}_x\text{Cu}_2\text{O}_{8+\delta}$  system as originating from the change of carrier concentration. In the insulating region their analysis showed transport to be governed by variable range hopping mechanism at low temperature and phonon assisted hopping of polarons at high temperature. They also observed a linear decrease of charge carrier concentration with  $x$ . Jayaram et.al. [9] argued the enhancement in Coulomb interaction due to disorder between the electrons as the basic reason for the suppression of superconductivity in  $\text{Bi}_2\text{Sr}_2\text{Ca}_{1-x}\text{Gd}_x\text{Cu}_2\text{O}_{8+\delta}$  system. For the same system, Gao et.al. [10] reasoned breaking of  $\text{Cu}3d\text{-O}2p$  hybridization caused by hole filling as the main factor for suppression of superconductivity. The disorder was

thought to be induced due to depletion of the carriers with doping. A dimensionality crossover from two to three dimensional variable range hopping was observed as the system moved from superconductor to insulator boundary. Similar analyses were executed by V.P.S. Awana et.al. in  $\text{Bi}_2\text{Sr}_2\text{Ca}_{1-x}\text{M}_x\text{Cu}_2\text{O}_{8+\delta}$  (M = Eu, Dy, Tm, Pr and Ce) systems [20,21].

### Results and Discussions:

The method of preparations of  $\text{Bi}_2\text{Sr}_{2-x}\text{Gd}_x\text{Ca}_1\text{Cu}_2\text{O}_{8+\delta}$  ( $x=0.0-0.65$ ) systems and experimental techniques have already been described in chapter 2. The various experimental results and the discussions follow further.

### 3.3 Crystal structure and Lattice parameters:

X-ray measurement showed all samples  $\text{Bi}_2\text{Sr}_{2-x}\text{Gd}_x\text{Ca}_1\text{Cu}_2\text{O}_{8+\delta}$  ( $x=0.0-0.65$ ) consisting of single phase  $\text{Bi}_2\text{Sr}_2\text{Ca}_1\text{Cu}_2\text{O}_{8+\delta}$  system with no noticeable impurity phase present. The lines were indexed with the previously reported values of 2:2:1:2 system [22]. Since 2:2:1:2 has very small orthorhombicity [23,24], the lattice parameters were calculated considering a pseudo tetragonal cell and using first seven prominent peaks.

The variations in lattice constant  $a$  and  $c$  with Gd concentration ( $x$ ) as well as  $c/a$  ratio is shown in Fig. 3.1. The straight line is the linear best fit to the data points. The lattice constant  $a$  shows a small increase while  $c$ -axis

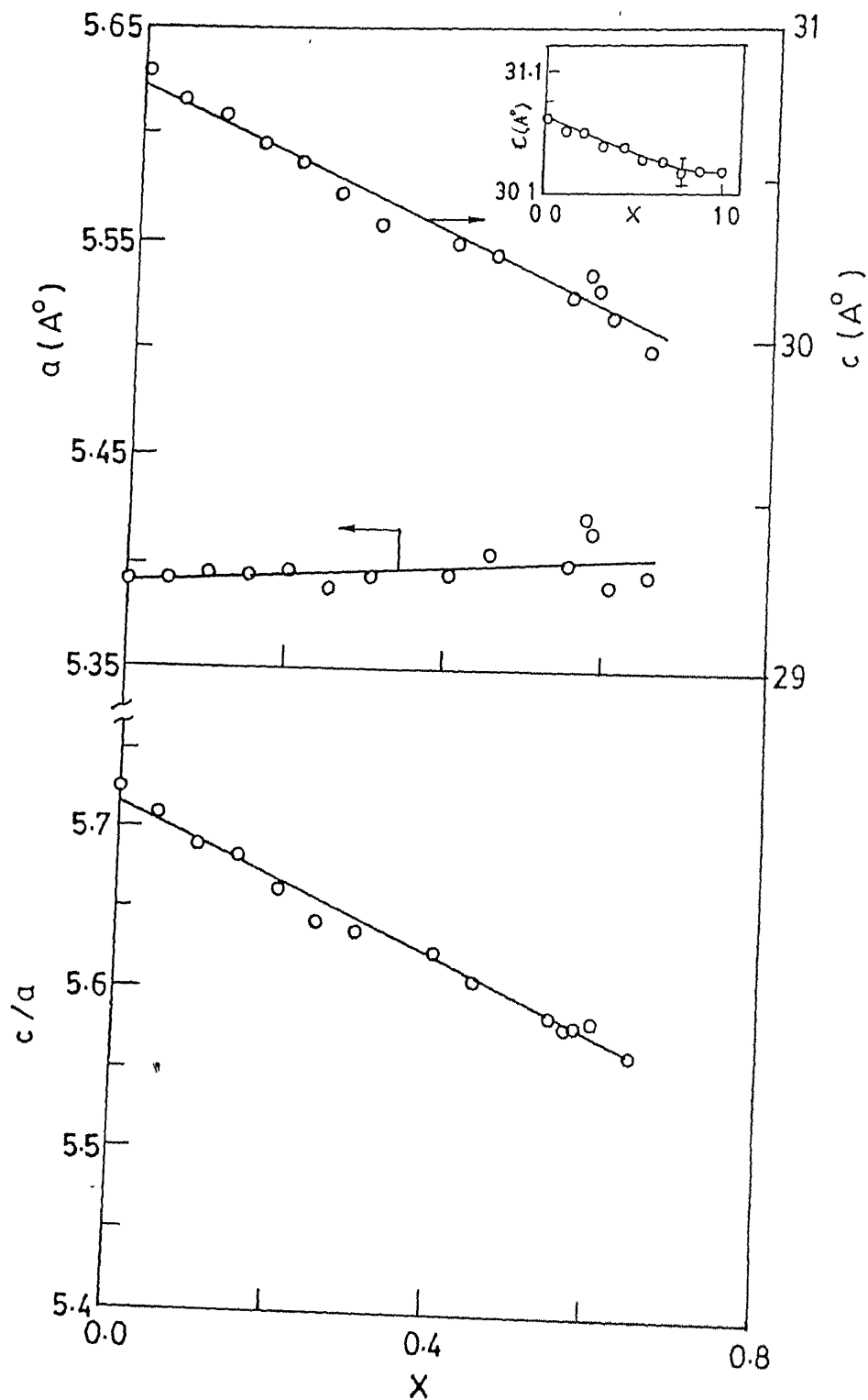


Fig. 3.1 Variation of lattice parameters  $a$  and  $c$ , and ratio  $c/a$  with Gd concentration  $x$  in  $\text{Bi}_2\text{Sr}_{2-x}\text{Gd}_x\text{Ca}_1\text{Cu}_2\text{O}_{8+\delta}$  system.

decreases appreciably from  $30.85\text{\AA}$  for  $x=0.0$  to  $29.99\text{\AA}$  for  $x=0.65$ . Similar trends were observed in  $\text{Bi}_2\text{Sr}_2\text{Ca}_{1-x}\text{RE}_x\text{Cu}_2\text{O}_{8+\delta}$  ( $\text{RE}=\text{Y}, \text{Pr}, \text{Gd}$ ) system also [10,16,25] while a decrease in lattice parameter  $a$  was reported in Ce and Pr doped 2:2:1:2 system [21]. The obtained lattice constants  $a$  and  $c$  for pure 2:2:1:2 system from our data are  $5.39\text{\AA}$  and  $30.85\text{\AA}$  respectively. This is in agreement with the previously reported values for the same system [23].

The systematic variation of lattice constants with  $x$  indicates that Gd has been incorporated into the crystal structure. The incorporation of Gd at Sr site can be established from the following argument also. The ionic radii of  $\text{Sr}^{2+}$ ,  $\text{Ca}^{2+}$  and  $\text{Gd}^{3+}$  are  $1.10\text{\AA}$ ,  $0.99\text{\AA}$  and  $0.93\text{\AA}$  respectively. The substitution of Gd at Ca site yield  $\frac{dc}{dx}=-0.78$  as reported in ref. [10] and is reproduced in the inset of Fig. 3.1. The substitution of Gd at Sr site in the present case gives  $\frac{dc}{dx}=-1.17$  as obtained from Fig. 3.1. The rather large slope in the latter case is evidently due to larger ionic radii difference of  $\text{Gd}^{3+}$  and  $\text{Sr}^{2+}$  ions. This shows that  $\text{Gd}^{3+}$  has replaced  $\text{Sr}^{2+}$  ions and hence causing larger contraction in  $c$ -axis. In  $\text{Bi}_2\text{Sr}_2\text{Ca}_1\text{Cu}_2\text{O}_{8+\delta}$  a decrease in  $c$ -axis is observed upon oxygenation [26]. Therefore, the decrease in  $c$ -axis could be a consequence of increase in the oxygen content due to higher valence cation substitution. However, the dependence of slope ( $dc/dx$ ) on ionic radii difference indicates that  $c$ -axis decrease is predominantly due to replacement of a bigger  $\text{Sr}^{2+}$  ion by a smaller  $\text{Gd}^{3+}$  ion. Since  $ab$  parameters in high  $T_c$

superconductors is governed by Cu-O bond lengths, the increase in lattice constant  $a$  with doping is caused by the decrease in formal valence of copper which weakens Cu-O bond.

### 3.4 Hole concentration and transition temperature:

The band structure calculations of 2:2:1:2 system show that the states which cross Fermi level ( $E_F$ ) are the 3d-2p states from the  $\text{CuO}_2$  planes and the 6p-2p states of the Bi-O layers [27]. The scanning tunneling spectroscopy in combination with photoemission spectroscopies reveals that the Bi-O layers in 2:2:1:2 are non-metallic and the holes are confined in  $\text{CuO}_2$  plane [28,29]. This implies that charge carrier concentration determined from Hall coefficient ( $R_H$ ) may be taken as being equal to the hole concentration determined by estimating the formal oxidation state of Cu using Iodometric titration technique [16]. To give an example when they are different we consider  $\text{Y}_1\text{Ba}_2\text{Cu}_3\text{O}_{6+\delta}$  system. In this system the states which cross  $E_F$  are the 3d-2p states from the  $\text{CuO}_2$  plane and  $\text{CuO}_\delta$  chains [30]. The holes are distributed over  $\text{CuO}_2$  planes and  $\text{CuO}_\delta$  chains. It has been suggested that the holes on the chains are immobile [31]. Therefore, for this system the carrier concentration determined from Hall effect measurement does not represent the hole concentration determined by chemical methods.

In Fig. 3.2 we have shown the variation of hole concentration ( $n_H$ ) with Gd concentration ( $x$ ).  $n_H$  was obtained from Hall effect measurements at room temperature. We notice

that  $n_H$  decreases exponentially with  $x$ . The variation of transition temperature  $T_C$  (defined as the temperature when resistivity becomes zero) with  $x$  is shown in Fig. 3.3.  $T_C$  first increases to a maximum value of 78K at  $x=0.10$  and then decreases to zero at  $x=0.55$ . The parabolic dependence of  $T_C$  on  $x$  has been observed in  $\text{La}_{2-x}\text{Sr}_x\text{CuO}_4$  [32] and  $\text{Bi}_2\text{Sr}_2\text{Ca}_{1-x}\text{Y}_x\text{Cu}_2\text{O}_{8+\delta}$  [33,34] systems also and appears to be a typical characteristic of high temperature superconductors.

A common way to examine the consequence of doping on transition temperature is to determine the hole content per Cu ion. We calculate the hole content ( $p$ ) per Cu ion by considering unit cell volume obtained from X-ray measurements and using the fact that average crystal structure of 2:2:1:2 has four formula units in the pseudotetragonal cell [23]. Thus  $p=n_H V/8$  where  $n_H$  is the hole concentration and  $V$  is the volume of the unit cell. The hole content  $p$  vs  $x$  is also shown in Fig. 3.2. It is evident that the maximum  $T_C$  at  $x=0.10$  is obtained for an optimum hole concentration of  $p = 0.38$  holes/Cu ion and superconductivity is suppressed for higher and lower number of holes/Cu ion. The superconductivity vanishes for 0.05 holes/Cu ion. Similar results of optimum hole concentration were obtained by J. Clayhold et.al. [18] on Tm doped  $\text{Bi}_2(\text{Sr,Ca})_3\text{Cu}_2\text{O}_{8+\delta}$  system and Mandal et.al. [19] on  $\text{Bi}_2\text{Sr}_2\text{Ca}_{1-x}\text{Y}_x\text{Ca}_1\text{Cu}_2\text{O}_{8+\delta}$  system. The maximum transition temperature for these systems were obtained for 0.40 and 0.35 holes/Cu-ion respectively which are in close agreement with our results. Groen et.al. [35] studied the dependence of transition

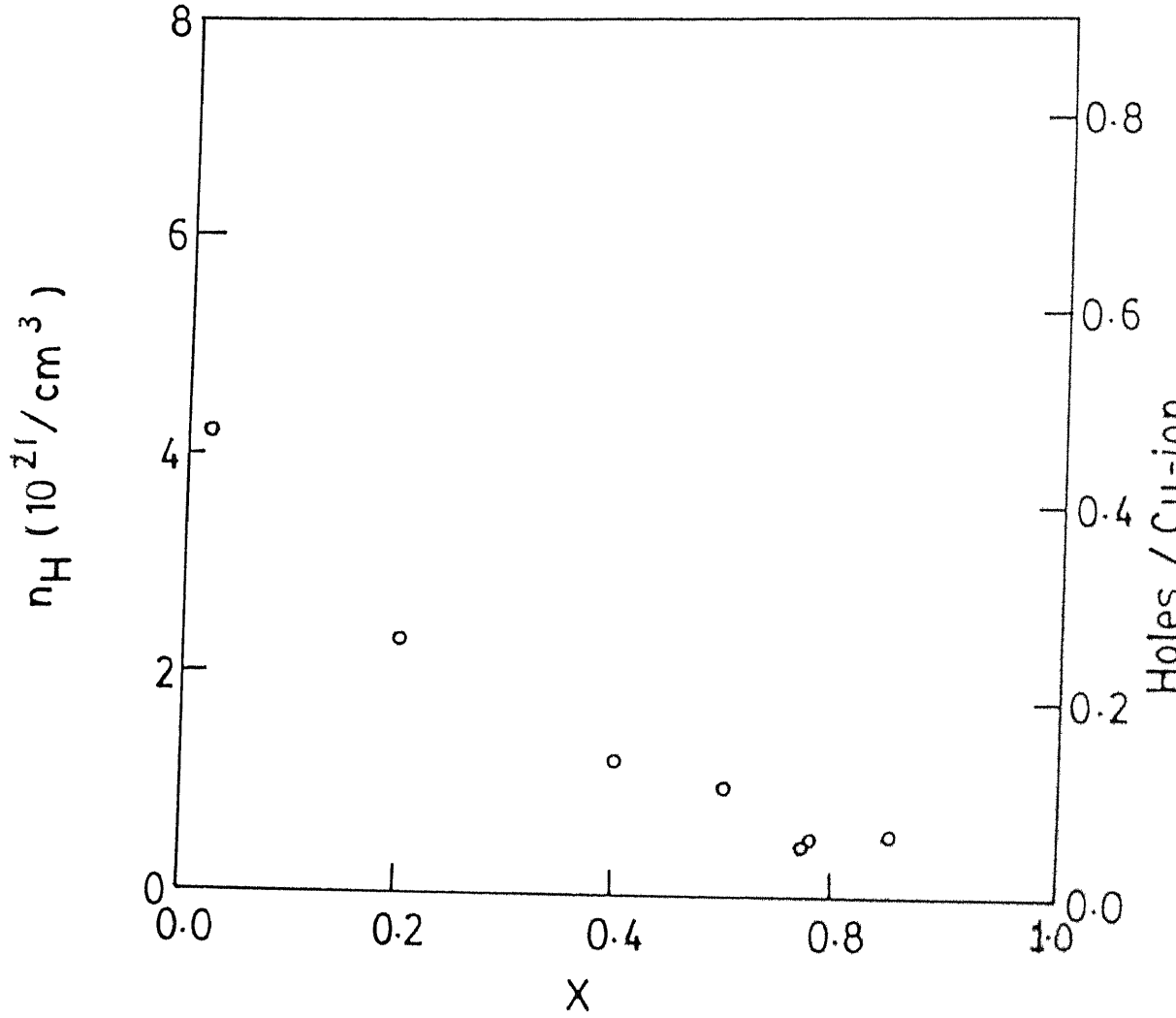


Fig. 3.2 Variation of hole concentration ( $n_H$ ) with Gd concentration  $x$  in  $\text{Bi}_2\text{Sr}_{2-x}\text{Gd}_x\text{Ca}_1\text{Cu}_2\text{O}_{8+\delta}$  system.

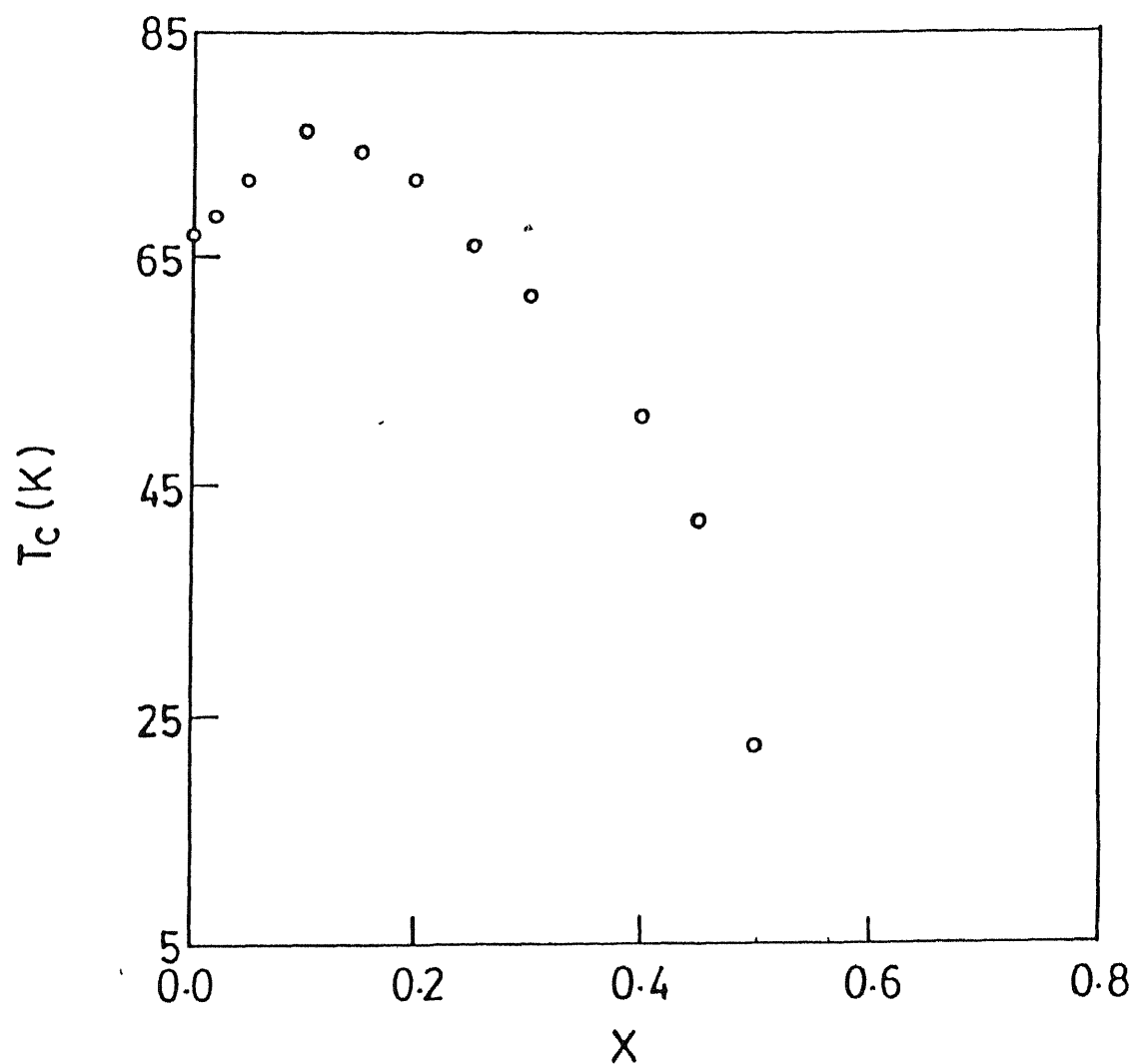


Fig. 3.3 Variation of transition temperature ( $T_c$ ) with Gd concentration  $x$  in  $\text{Bi}_2\text{Sr}_{2-x}\text{Gd}_x\text{Ca}_1\text{Cu}_2\text{O}_{8+\delta}$  system.



temperature on oxygen content in 2:2:1:2 by annealing the sample in different partial pressures of oxygen. The maximum  $T_C$  was obtained for partial pressure less than the atmosphere pressure. Since our samples were fired in air which is well above the optimum partial pressure,  $x=0.0$  sample has too much oxygen ( $\delta$ ) i.e. excess holes which results in depressed  $T_C$ . The addition of trivalent  $Gd^{3+}$  for divalent  $Sr^{2+}$  fills the excess holes which causes holes content being closer to the optimum value hence  $T_C$  increases. Further hole filling depresses  $T_C$  again.

A rather surprising feature of  $n_H$  vs  $x$  curve is the non-linear dependence of hole concentration on Gd concentration. The Hall coefficient ( $R_H$ ) for a strongly correlated Hubbard system has been calculated by Fukuyama and Hasegawa [36]. They show that for low doping concentration  $R_H \propto z^{-1}$  where  $z$  is the doping concentration. Assuming a single band model where  $R_H = 1/(n_H e)$  we obtain  $n_H \propto z$ . The linear dependence of  $n_H$  on  $z$  has been observed in  $La_{2-z}Sr_zCuO_4$  for Sr concentration  $z < 0.15$  [37]. In 2:2:1:2 when trivalent Tm is substituted for divalent Ca, a linear decrease in  $n_H$  is observed with increasing Tm content. This suggested that the system was approaching Mott-Hubbard insulating regime [18]. An exponential decrease of  $n_H$  in our case suggests the presence of an exponential term in  $n_H(x)$ . The origin of this term can be understood within the charge transfer model in which the charges are transferred from the charge reservoir layers to the  $CuO_2$  plane [38]. If the hole content in the  $CuO_2$  plane is

assumed to depend on the transfer integral 't' between  $\text{CuO}_2$  plane and Sr-O plane, the relatively large decrease in c-axis caused by Gd doping would increase the transfer integral 't' considerably. Such an increase of the transfer integral thereby increases the electron transfer between the two layers exponentially [39]. A dominant role of this mechanism results in the exponential decrease of  $n_H$ . The decrease of  $n_H$  with doping in the present system seems to be analogous to that observed in Co substituted  $\text{Y}_1\text{Ba}_2\text{Cu}_3\text{O}_{7-\delta}$  system [39].

### 3.5 Electrical Resistivity:

The variation of electrical resistivity with temperature is shown in Fig. 3.4(a,b,c) for the  $\text{Bi}_2\text{Sr}_2\text{Ca}_{1-x}\text{Gd}_x\text{Ca}_1\text{Cu}_2\text{O}_{8+\delta}$  system. The resistivity behaviour of the samples can be divided into three categories:

(i) Samples with  $x=0.0-0.45$  show metallic behaviour at high temperature followed by superconducting transition as the temperature is lowered. The linear portion of the resistivity data in the normal state may be fitted to  $\rho(T)=\rho_0+\beta T$ . Residual resistivity  $\rho_0$  and slope  $\beta$  show an exponential increase with  $x$  as shown in Fig. 3.5.  $\rho_0$  increases by two orders of magnitude whereas slope increases four times only.

(ii) As  $x$  is increased beyond 0.50 an upturn in resistivity is observed as the temperature is lowered which is a characteristic of electron localization and is discussed later

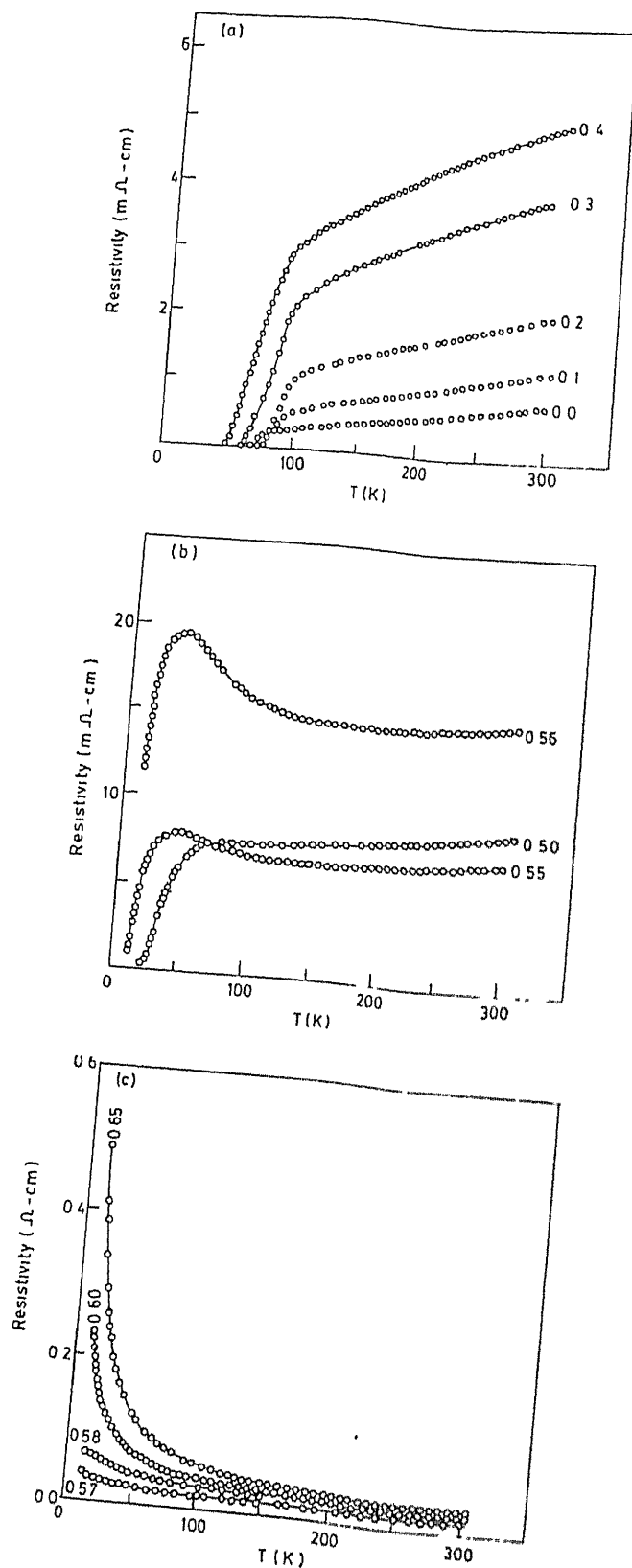
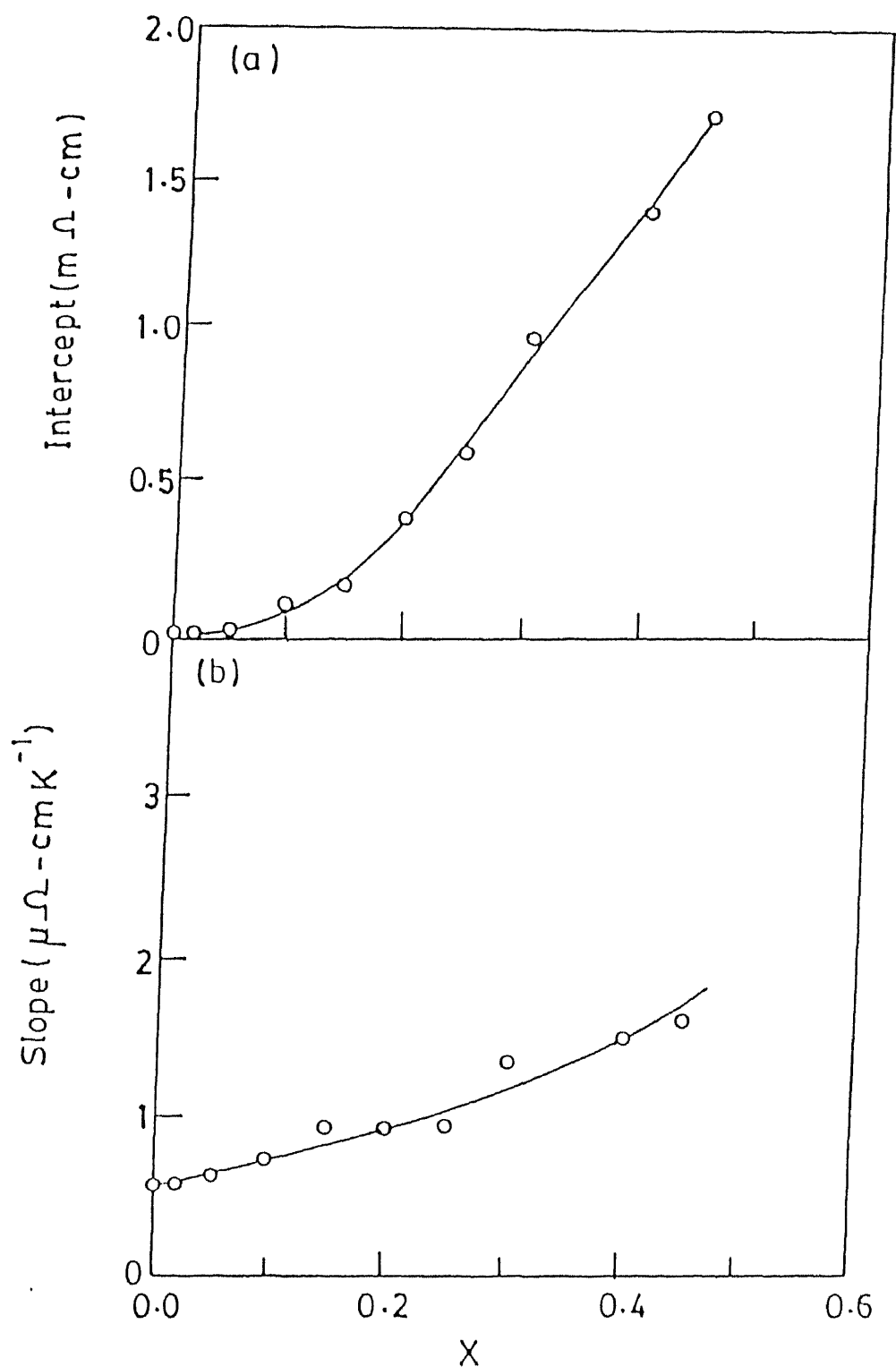


Fig. 3.4 Temperature dependence of electrical resistivity for various Gd concentration  $x$  in  $\text{Bi}_2\text{Sr}_{2-x}\text{Gd}_x\text{Ca}_1\text{Cu}_2\text{O}_{8+\delta}$  system.



**Fig. 3.5** Dependence of (a) residual resistivity ( $\rho_0$ ) and (b) slope ( $\beta$ ) on Gd concentration  $x$  in  $\text{Bi}_2\text{Sr}_{2-x}\text{Gd}_x\text{Ca}_1\text{Cu}_2\text{O}_{8+\delta}$  system.

in this section.  $x=0.50$  shows a shallow minimum in resistivity at around 95K. This minimum becomes more prominent in  $x=0.55$ , 0.56 and 0.57. The temperature ( $T_{\min}$ ) at which minimum in resistivity occurs increases as  $x$  changes from 0.50 to 0.57. Above  $T_{\min}$ , these samples show metallic behaviour ( $\rho \propto T$ ) while below  $T_{\min}$ ,  $x=0.50-0.56$  samples show semiconducting behaviour followed by transition to the superconducting state. The resistivity of  $x=0.58$  sample is weakly temperature dependent above 200K. At lower temperatures both  $x=0.57$  and 0.58 samples show an increase in resistivity to the lowest temperature of 14K measured by us.

(iii) At  $x=0.60$  superconductivity disappears and transition to the insulating state occurs. Both  $x=0.60$  and  $x=0.65$  show a strong increase in resistivity at low temperatures. The crossover from the metallic state to the insulating state with increasing Gd concentration is accompanied by a sudden jump in normal state resistivity as shown in Fig. 3.6.

### 3.6 Discussions:

#### 3.6.1 Effect of Disorder:

In conventional 2-D superconductor, normal state resistivity is regarded as a measure of disorder and superconductivity occurs only below a critical disorder [40,41]. In Fig. 3.6 we plot normal state resistivity ( $\rho_n$ ) measured at room temperature against Gd concentration ( $x$ ) in

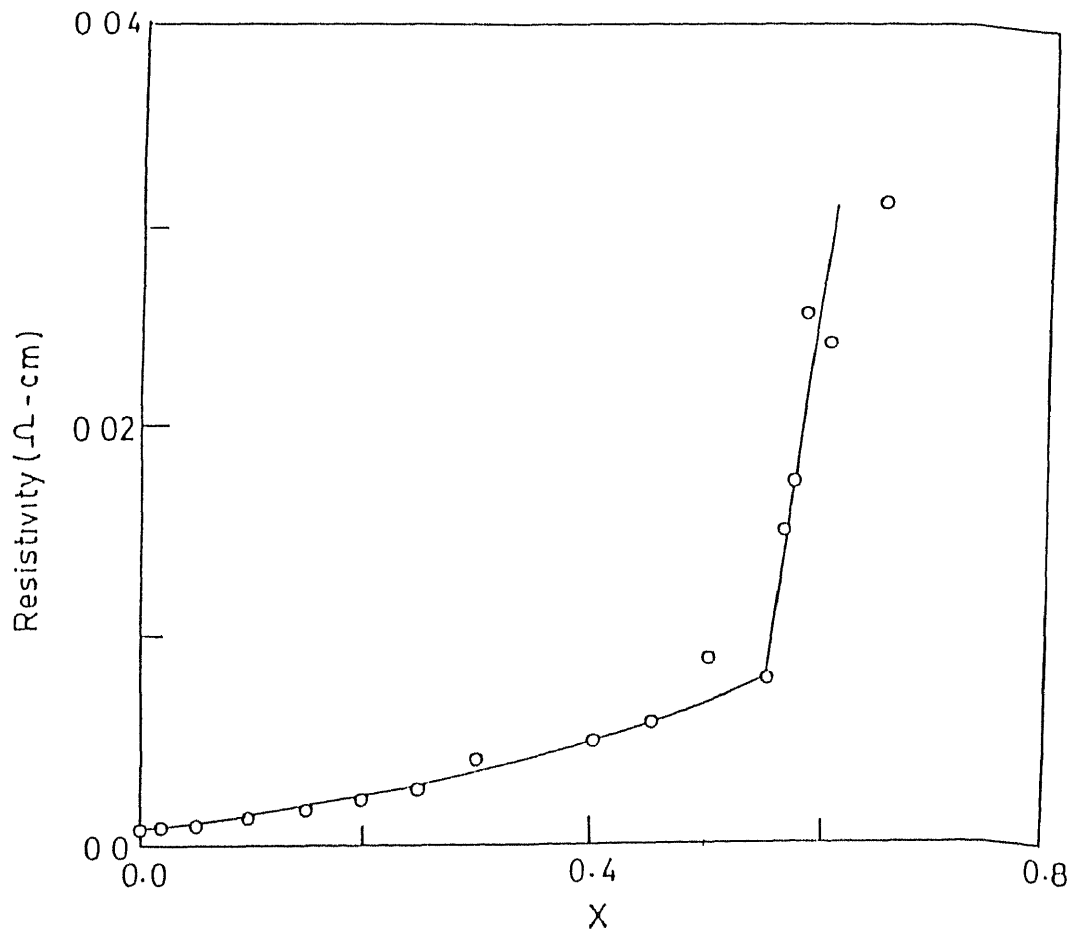


Fig. 3.6 Plot of room temperature resistivity  $\rho(300K)$  as a function of Gd concentration  $x$  in  $\text{Bi}_2\text{Sr}_{2-x}\text{Gd}_x\text{Ca}_1\text{Cu}_2\text{O}_{8+\delta}$  system.

our samples. The 2D nature of high  $T_C$  superconductors and analogy with the conventional superconductors suggest the increase of  $\rho_n$  with  $x$  as a result of increasing disorder in the system. The disorder is caused by random distribution of Gd at Sr site which presumably generates random potentials in  $\text{CuO}_2$  plane. A decrease in hole concentration also contributes to the increase in the normal state resistivity.

Qualitatively, the above behaviour can be understood within Drude's model in which resistivity is expressed as

$$\rho(T) = \frac{m^*}{ne^2} \left[ \frac{1}{\tau_0} + \frac{1}{\tau(T)} \right] \quad (3.1)$$

where  $m^*$  is the effective mass of the electrons and  $n$  is the charge carrier density.  $\tau_0$  is the temperature independent relaxation time and arises due to elastic scattering of electrons by impurities.  $\tau(T)$  is the inelastic temperature dependent relaxation time caused by electron phonon (say) scattering. The electron phonon coupling strength  $\lambda$  is related to inelastic scattering rate  $\tau^{-1}(T)$  as  $\hbar\tau^{-1}(T) = 2\pi\lambda kT$  [42] where  $k$  is Boltzmann constant. Thus comparing Eqn. 3.1 with  $\rho(T) = \rho_0 + \beta T$  and using plasma frequency  $\omega_p = \left( \frac{4\pi ne^2}{m^*} \right)^{1/2}$

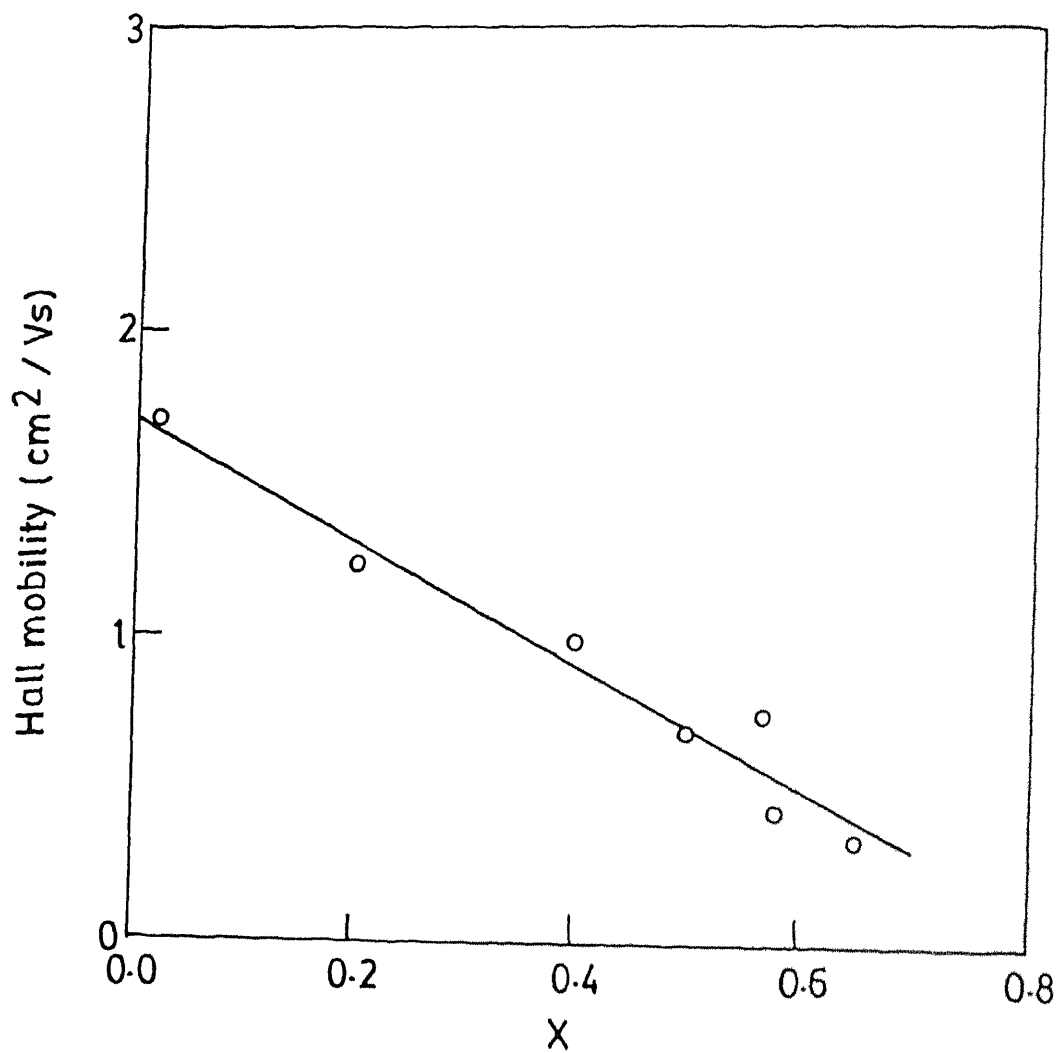
$$\text{residual resistivity } \rho_0 = \frac{4\pi}{\omega_p^2 \tau_0}$$

$$\text{slope } \beta = \frac{2\pi k \lambda m^*}{ne^2 \hbar} \quad (3.2)$$

It is evident that the decrease of  $n$  and  $\tau_0$  caused by the substitution increases  $\rho_0$ . As we have seen in Fig. 3.5, the residual resistivity  $\rho_0$  increases by orders of magnitude as Gd concentration increases. To have an idea of how mean free path ( $l_0$ ) at  $T=0K$  changes with Gd doping we use Fermi velocity  $v_F = (\hbar/m^*) (3\pi^2 n)^{1/3}$  for free electron model where  $n$  is the carrier density. Mean free path can be estimated using  $l_0 = v_F \tau_0$  and experimental values of  $\rho_0$  and  $n$ .

In our samples  $\rho_0$  increases from  $3.72 \times 10^{-5}$  ohm-cm for  $x=0.02$  to  $2.79 \times 10^{-3}$  ohm-cm for  $x=0.40$  sample while  $n$  decreases from  $4.24 \times 10^{21}/\text{cm}^3$  for  $x=0.02$  to  $1.26 \times 10^{21}/\text{cm}^3$  for  $x=0.40$ . The values give  $l_0 = 130 \text{ \AA}$  for  $x=0.02$  while for  $x=0.40$  it is  $4 \text{ \AA}$ . Comparing  $l_0$  with coherence length of pure 2:2:1:2 system  $\xi_0(0K) = 32 \text{ \AA}$  [43] shows that with increasing Gd concentration the system goes from clean limit to dirty limit ( $l_0 < \xi_0$ ). The single crystal conductivity of 2:2:1:2 system shows that  $ab$  plane conductivity is five orders of magnitude larger than the  $c$ -axis conductivity [44]. The fact indicates predominantly 2D character of observed conductivity (i.e.  $\text{CuO}_2$  plane conductivity) in polycrystalline sample. The above analysis of mean free path therefore, suggests that although Gd doping is beyond  $\text{CuO}_2$  plane it generates disorder in  $\text{CuO}_2$  plane giving rise to increasing residual resistivity at 0K. The conclusion is further supported by decrease of Hall mobility ( $\mu_H = R_H \sigma$ ) with  $x$  at  $T=300K$  as shown in Fig. 3.7. With increasing Gd concentration the defects generated in  $\text{CuO}_2$  plane also increases leading to decrease of  $\mu_H$ . Moreover,  $\mu_H$  shows a





ig. 3.7 Variation of Hall mobility with Gd concentration  $x$  in  $i_2Sr_{2-x}Gd_xCa_1Cu_2O_{8+\delta}$  system.

linear decrease with  $x$  rather than an exponential as in the case of  $n_H$  vs  $x$  curve. This shows that reduction of holes and generation of disorder in  $\text{CuO}_2$  plane are uncorrelated processes.

With the increase of Gd concentration a minimum in  $\rho$ -T curve appears in  $x=0.50$  just before the onset of superconducting transition. Such a minimum in resistivity is a manifestation of incipient electron (hole) localization [45]. The localization effect becomes progressively evident with further increment of Gd concentration and results in semiconducting behaviour at low temperature for  $x \geq 0.57$ . The Ioffe Regel limit [46] for strongly disordered system  $k_F l \leq 1$  is also satisfied for  $x=0.57$ .  $k_F l$  was estimated using free electron model and is expressed as  $k_F l = [\hbar(3\pi^2)^{2/3}] / (e^2 \rho_0 n^{1/3})$ . Residual resistivity  $\rho_0$  was obtained by fitting a straight line in higher temperature region (200K-300K) in which a metallic behaviour is obtained for this system. The sudden jump in normal state resistivity at the same concentration also follows the localization effect.

$x=0.55$  and  $x=0.56$  samples show metallic behaviour at high temperature and semiconducting behaviour as the temperature is lowered followed by transition to superconducting state. In 2D weakly disordered electronic system the conductivity is shown to vary in accordance with

$$\sigma = \sigma_0 + \frac{e^2}{2\pi^2 \hbar} \ln[ T/T_0 ] \quad (3.3)$$

where  $\sigma_0$  is the Boltzmann transport conductivity [47]. We interpret the upturn in resistivity with temperature in the above samples as due to 2-D weak localization effect. This leads to logarithmic correction in conductivity as shown in Fig. 3.8 for  $x=0.56$  producing an apparent metal-insulator transition.

### 3.6.2 Destruction of superconductivity:

A well established fact about high  $T_c$  cuprates is that superconducting electrons are paired in the singlet state. Within the framework of BCS theory Abrikosov and Gorkov (AG) have shown that magnetic impurities in a superconductor break the time-reversal symmetry of the pair leading to strong suppression of  $T_c$  [48]. AG mechanism essentially involves an exchange interaction between spin of an electron and that of an impurity atom. The spin of the impurity atom also inhibits the appearance of superconductivity. Evidently, the rate of  $T_c$  suppression would depend on the magnetic moment of the impurity atom and would be larger for the impurity atom having higher magnetic moment (see chapter 5). In order to check the validity of the AG mechanism for suppression of superconductivity in our system, we find that the substitution of Nd ( $\mu_{eff} \approx 3.5 \mu_B$ ) for Sr in 2:2:1:2 in ref.[49] leads to disappearance of superconductivity at nearly the same concentration as for our case of Gd ( $\mu_{eff} = 7.94 \mu_B$ ) substitution. This shows that the suppression of superconductivity in our system involves mechanisms other than the magnetic pair breaking.

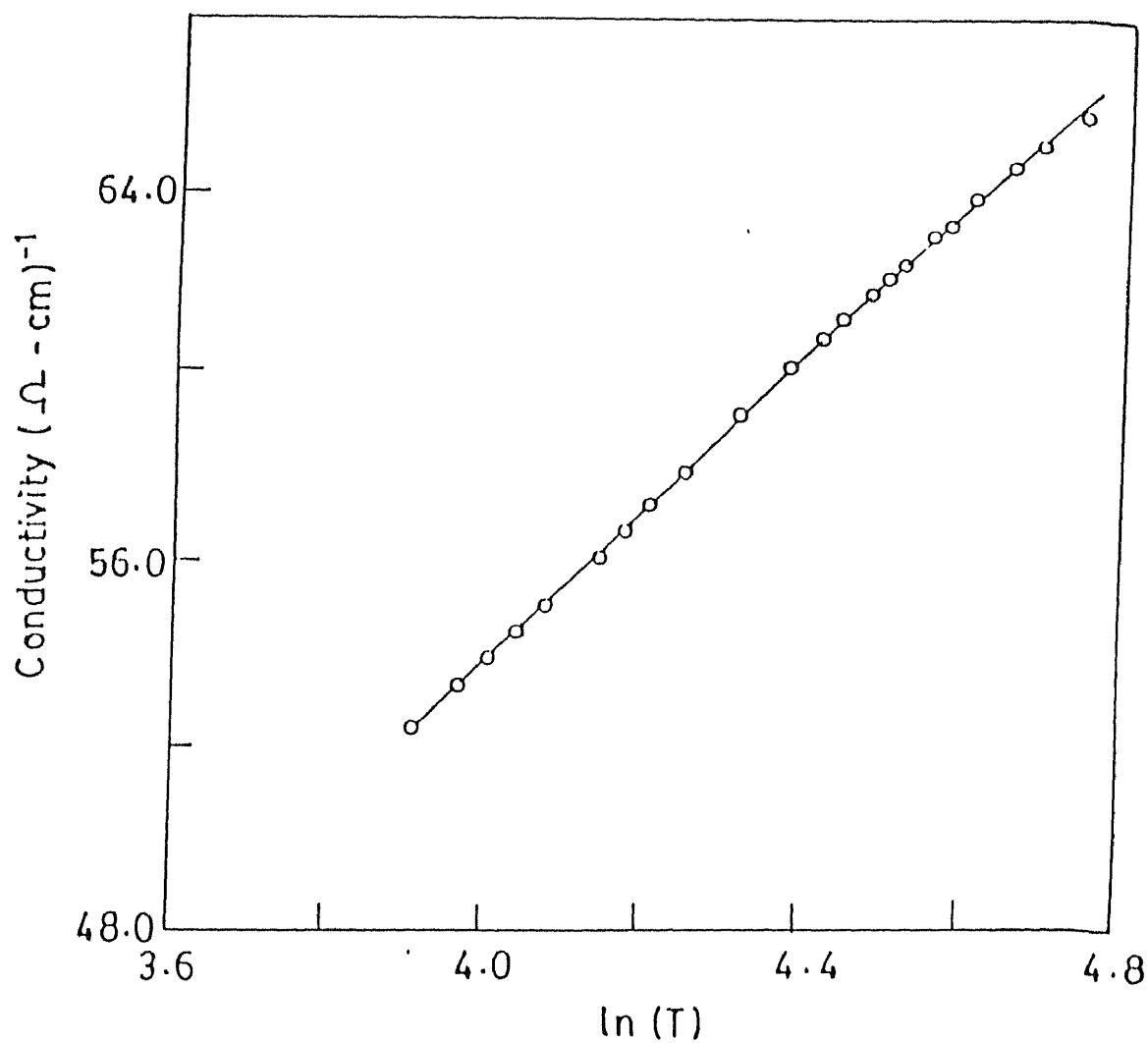


Fig. 3.8 Plot of conductivity vs  $\ln(T)$  for sample  $x=0.56$  in the temperature region 50K to 115K showing logarithmic correction to conductivity.

The polycrystalline  $\text{Bi}_2\text{Sr}_2\text{Ca}_1\text{Cu}_2\text{O}_{8+\delta}$  can be modelled as consisting of grains of ideal crystalline superconductors which are weakly coupled to each other. The grains consist of stack of superconducting bilayers connected by Josephson couplings. This leads to observation of superconductivity perpendicular to  $\text{CuO}_2$  plane [50]. As we have seen earlier conductivity is predominantly  $\text{CuO}_2$  plane conductivity therefore, the dominant mechanism responsible for the destruction of superconductivity and suppression of  $T_c$  are those which affect charge carriers in  $\text{CuO}_2$  plane. As per the result of our Hall measurement, one of the mechanism is hole filling. The other mechanism is disorder which causes localization of charge carriers. For lower Gd concentration major role in suppression of  $T_c$  is played by reduction in hole concentration. As the Gd concentration increases localization effect becomes evident and superconductivity is destroyed completely due to disorder when all the charge carriers become localized. In the latter regime variable range hopping of conduction mechanism is observed at low temperature which we discuss in the next section. Thus our data show hole filling and disorder induced localization as the basic reasons for the suppression of superconductivity and concomitant metal-insulator transition.

We must mention that the mechanism responsible for destruction of superconductivity in our system is different from that in  $\text{Bi}_2\text{Sr}_2\text{Ca}_{1-x}\text{Gd}_x\text{Cu}_2\text{O}_{8+\delta}$  system [9] where metal insulator transition was seen to occur due to enhanced Coulomb interaction between electrons. It is true that in a disordered

electronic system localization effect and Coulomb interaction terms often compete [47]. The presence of a dominant Coulomb interaction between electrons leads to opening up of an energy gap at the Fermi level [51,52]. Efros and Shklovskii have shown that the gap results in variable-range hopping conductivity with exponent  $1/2$  in two as well as three dimension [53] in the insulating state. We observed an exponent  $1/4$  of VRH in our samples (see next section) which shows that localization is the dominant term. Moreover, recently suppression of superconductivity originating from increased Coulomb interaction due to disorder has been questioned [54,55].

### 3.6.3 The Insulating State:

The study of charge transport in the insulating state is important because it provides information about electronic density of states at Fermi level and electronic correlations. In the insulating state, electron states at the Fermi level are all localized and conductivity vanishes at 0K. The mechanism involves hopping of an electron (hole) from an occupied to unoccupied state of higher energy by the absorption of a phonon. At sufficiently low temperature the electron is most likely to hop to a nearby localized state. It is also favourable for an electron to hop to a state close in energy to the state of the electron. The states which are close in energy are likely to be distributed far apart in space due to disorder. Thus the electron hops occur over a wide range of distances. The conductivity in this case is given by [56]

$$\sigma = \sigma_o \exp \left[ - (T_o/T)^{\frac{1}{n+1}} \right] \quad (3.4)$$

where  $n$  determines the dimensionality of the hopping mechanism involved. The localization length  $\alpha^{-1}$  which determines the spatial extent of localized wave function  $[\psi(r) \sim \exp(-\alpha r)]$  can be deduced from [57,58]

$$T_o = \frac{27\alpha^2}{4\pi k N(E_F)} \quad \text{for 2D} \quad (3.5)$$

$$= \frac{16\alpha^3}{k N(E_F)} \quad \text{for 3D} \quad (3.6)$$

where  $k$  is Boltzmann constant and  $N(E_F)$  is the density of states at the Fermi level. The optimum hopping distance for 3D case is given by

$$R = \left[ \frac{3}{2\pi\alpha N(E_F) kT} \right]^{\frac{1}{4}} \quad (3.7)$$

The condition of variable range hopping is  $R > \alpha^{-1}$  [57]. The pre-exponential factor  $\sigma_o$  has been worked out by many workers. Brodsky and Gambino [59] assume a constant density of states  $N(E) = N(E_F)$  near the Fermi level and obtain

$$\sigma_o = (2\pi)^{-1/2} \left( \frac{3e^2\nu}{2} \right) \left( \frac{N(E_F)}{\alpha kT} \right) \quad (3.8)$$

where  $\nu$  is the phonon frequency. On the other hand, Ortuno and

Pollak [60] assumed a concave density of localized states near the Fermi level derived from  $N(E) = N(E_F) \exp(E/E_0)$  where  $E$  is the energy measured from the Fermi energy and  $E_0$  is the decay rate. They obtained following expression for  $\sigma_0$ .

$$\sigma_0 = 1.7e^2 \nu N(E_F)^{0.58} (\alpha)^{-0.74} (kT)^{-0.42} \quad (3.9)$$

The theory of the above results did not take into account the Coulomb interaction between hopping sites. The presence of electron-electron interaction causes the density of states to vanish at the Fermi energy (Coulomb gap). In such a case Efros and Shklovskii theory [53] predicts a power law dependence in the density of states as  $N(E) \propto |E - E_F|^\gamma$  and the conductivity follows following behaviour with temperature for all dimensions

$$\sigma = \sigma_0 \exp \left[ - \frac{T_0}{T} \right]^{\frac{1}{2}} \quad (3.10)$$

For the analysis of the samples in the insulating state we consider  $x=0.60$  and  $0.65$  samples which lie well on the insulating side. In practice, due to strong temperature dependence of the exponential factor in Eqn. 3.4, temperature dependence of  $\sigma_0$  is not taken into account and a graph is plotted between  $\ln \sigma$  vs  $T^{-\beta}$ . We tried fitting with  $\beta=1/2$ ,  $1/3$  and  $1/4$ . A kink was observed at around 32K in all the plots. The least square fitting below 32K gives best fit for  $\beta=1/4$ .

Fig 3.9 shows  $\ln \sigma$  vs  $(T)^{-1/4}$  curves for samples  $x=0.60$  and  $0.65$ . A linear fit is observed in two different regions which



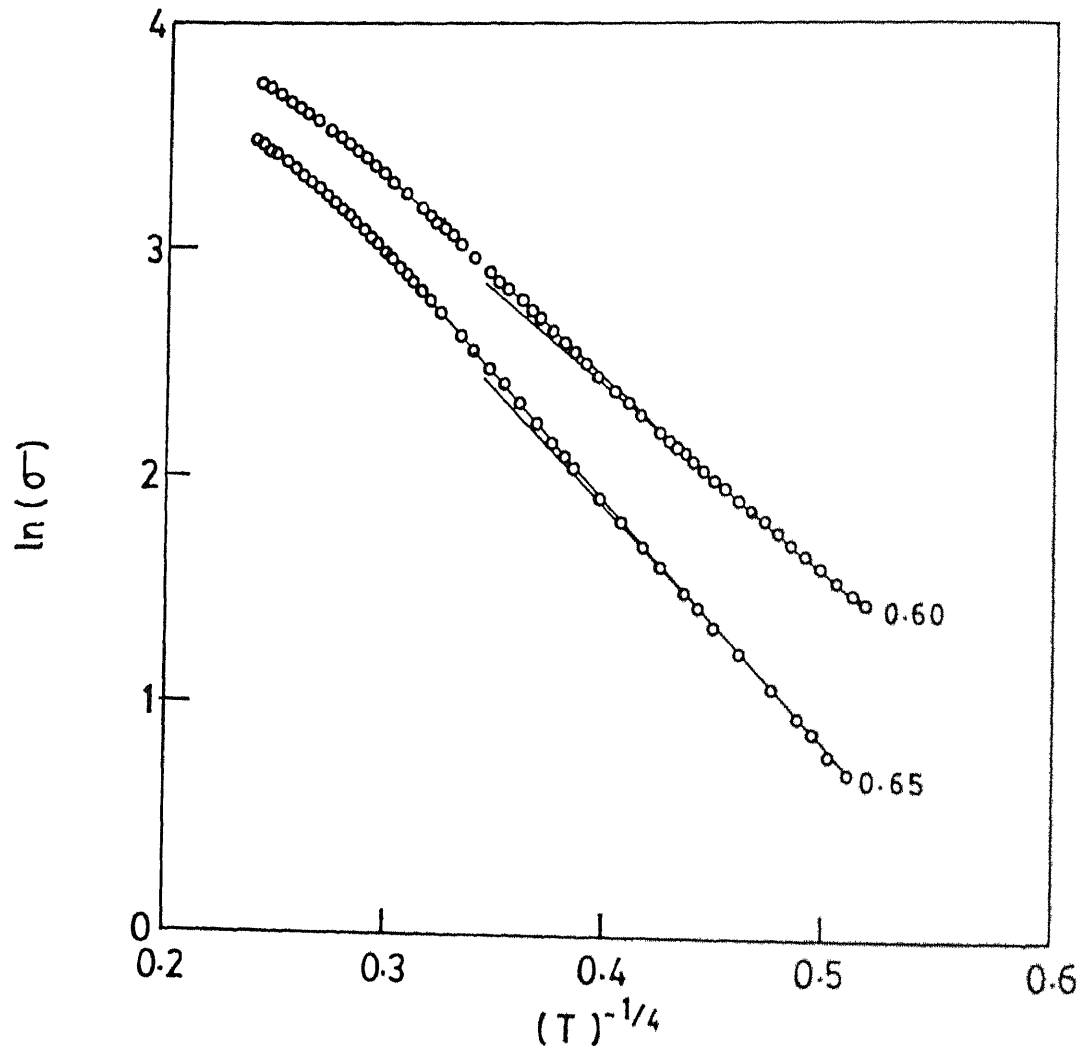


fig. 3.9 Plot of  $\ln(\sigma)$  vs  $(T)^{-1/4}$  for samples  $x=0.60$  and  $0.65$ . The solid lines are linear fits in two separate temperature regions:  $14\text{K} \leq T < 32\text{K}$  and  $32\text{K} < T \leq 110\text{K}$ .

are separated by a knee at around 32K. We used region below 32K where VRH is considered to be more appropriate to calculate VRH parameters. The values of  $T_0$  for samples  $x=0.60$  and  $0.65$  are  $5.0 \times 10^3 \text{K}$  and  $1.3 \times 10^4 \text{K}$  respectively. Specific heat measurements on 2:2:1:2 determined density of states at Fermi level to be  $2.0\text{--}3.4 \times 10^{22} \text{ states/eV/cm}^3$  [61,62]. Using Eqn. 3.6, the slope of the plot and above values of  $N(E_F)$ , localization length ( $\alpha^{-1}$ ) falls in the range  $11\text{--}13 \text{\AA}$  for  $x=0.60$  and  $7\text{--}9 \text{\AA}$  for  $x=0.65$ . Lesser value of  $\alpha^{-1}$  in  $x=0.65$  shows that the localization of charge carriers is stronger in  $x=0.65$  than in  $x=0.60$ . This is in agreement with the fact that disorder is larger in  $x=0.65$ . The optimum hopping distance which is estimated using Eqn. 3.7 at 20K is  $18 \text{\AA}$  for  $x=0.60$  and  $17 \text{\AA}$  for  $x=0.65$ . Evidently, both these samples satisfy the condition of VRH i.e.  $R > \alpha^{-1}$ .

We next calculate  $N(E_F)$  from our resistivity data using Eqns. 3.6, 3.8 and Eqns. 3.6, 3.9. The former eqns assume constant density of states near  $E_F$  whereas latter concave density of states. In the analysis the temperature dependence of  $\sigma_0$  is taken into account. Thus the values of  $\sigma_0$  and  $T_0$  as obtained from  $\ln(\sigma T^{0.42})$  vs  $(T)^{-1/4}$  plots are  $5.05 \times 10^3 (\text{ohm-cm})^{-1}$  and  $1.74 \times 10^4 \text{K}$  for  $x=0.60$  while for  $x=0.65$  these are  $8.96 \times 10^3 (\text{ohm-cm})^{-1}$  and  $4.05 \times 10^4 \text{K}$  respectively. By using these values of  $\sigma_0$  and  $T_0$  and Eqns. 3.6 and 3.9 we obtain

$$N(E_F) = \frac{8.45 \times 10^{60}}{\nu^3} \text{ states/eV cm}^3 \quad \text{for } x=0.60$$

$$= \frac{8.75 \times 10^{61}}{\nu^3} \text{ states/eV cm}^3 \quad \text{for } x=0.65$$

Taking  $\nu \sim 10^{13}$  Hz and considering uncertainty in  $\nu$ ,  $N(E_F)$  thus obtained for both the samples are in close agreement with that obtained for 2.2.1.2 by specific heat measurements. On the other hand the values of  $\sigma_0$  and  $T_0$  obtained from  $\ln(\sigma\nu/T)$  vs  $(T)^{-1/4}$  curves are  $8.78 \times 10^3 \text{ (ohm-cm)}^{-1}$  and  $2.18 \times 10^4 \text{ K}$  for  $x=0.60$  whereas for  $x=0.65$  these are  $1.54 \times 10^4 \text{ (ohm-cm)}^{-1}$  and  $4.91 \times 10^4 \text{ K}$  respectively.  $N(E_F)$  derived from these values are found to be two orders of magnitude larger than the experimental value of  $N(E_F)$ . These results suggest Ortuno and Pollak gives best fit to our data and therefore, density of states near Fermi energy is concave in nature. The concavity of density of state near Fermi energy gives rise to the observation of upward trend of  $\ln(\sigma T^{0.42})$  vs  $(T)^{-1/4}$  curve below the knee. Similar upward trend of  $\sigma$  at low temperature was obtained in  $\text{Bi}_2\text{Sr}_2\text{Ca}_{1-x}\text{RE}_x\text{Cu}_2\text{O}_{8+\delta}$  [RE = Gd, Nd] systems also [9,61] and was attributed to the presence of either localized superconducting grains or to the crossover from VRH to multiphonon assisted hopping mechanism. In case the upward trend occurs due to localized superconducting grains, the application of an external magnetic field would show a positive magnetoresistance. We did not observe any positive

magnetoresistance by application of an external magnetic field of 3.5kG in our samples. The interpretation of multiphonon assisted hopping is based on the simplified assumption of constant density of states at  $E_F$ . However our analysis shows that the behaviour can be explained by considering energy dependent density of states near the Fermi level.

### 3.7 Magnetoresistance:

$x=0.10$  which lies on the maximum in  $T_C$  vs  $x$  curve, Fig. 3.3, was chosen for the study of broadening of resistive transition. Fig. 3.10 displays variation of resistivity of  $x=0.10$  sample with temperature in presence of external magnetic fields of 0, 0.128, 0.560 and 1.1 kOe. As we notice the broadening occurs below the mean field transition temperature  $T_{CO}=85.8K$  of the present system.  $T_{CO}$  was obtained by applying Aslamasov-Larkin theory of fluctuation conductivity in 2-D systems above  $T_{CO}$  [64,65]. Since conductivity in 2:2:1:2 is mostly 2-D due to large anisotropy ratio of c-axis and a-b plane conductivity above theory could be applied.

The resistivity below  $T_{CO}$  can be described by the thermally activated motion of flux lines with the temperature dependent activation energy. The estimate of the activation energy  $U_o$  which must be overcome to allow flux motion, can be written as [66]

$$U_o = \frac{H_C \xi^2 \phi_o}{B} \quad (3.11)$$

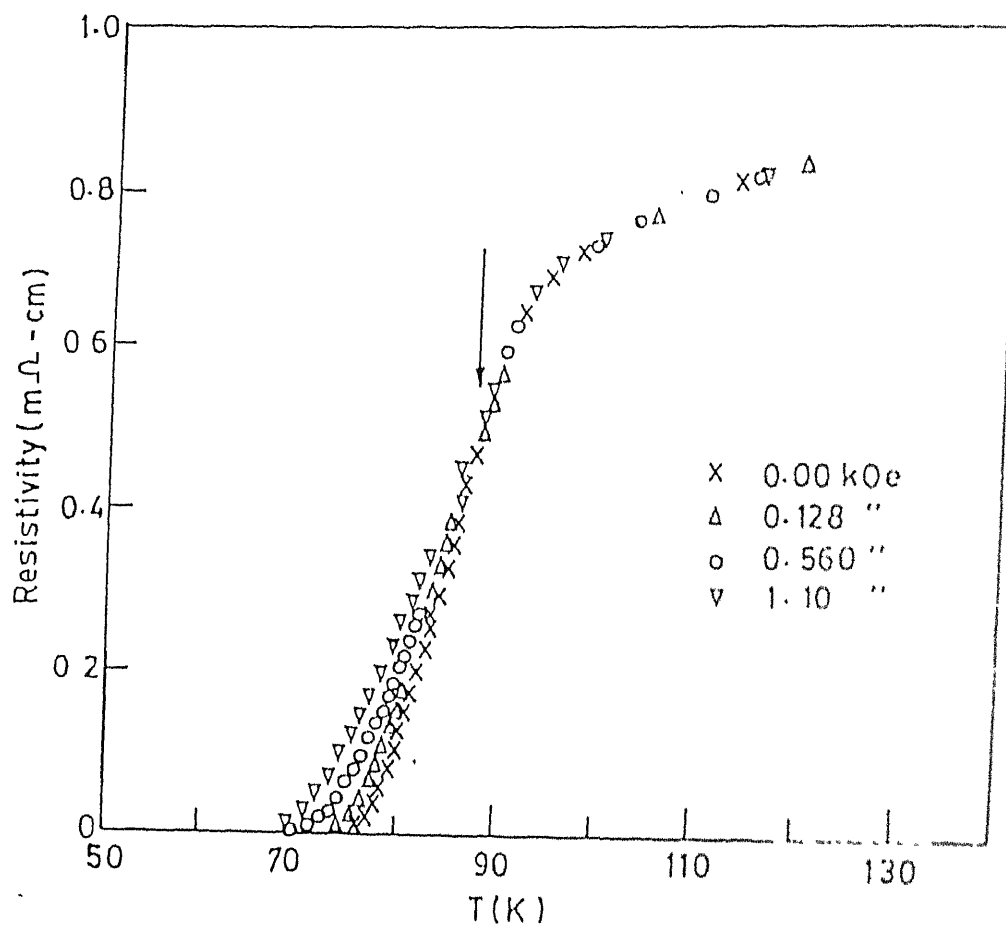


Fig. 3.10 Temperature dependence of resistivity for  $x=0.10$  in the presence of low external magnetic fields.

where  $\xi$  is the coherence length,  $H_c$  is the thermodynamic critical field,  $B$  is the flux density in the sample and  $\phi_0 = \frac{hc}{2e}$  is superconducting flux quantum. An explicit expression for the temperature dependence of  $U_0$  is obtained by using results of Ginzburg-Landau theory

$$\xi(T) = \xi(0) \left[ \frac{T_{co} - T}{T_{co}} \right]^{-1/2} \quad (3.12)$$

where  $T_{co}$  is the mean field transition temperature. The thermodynamic critical field  $H_c(T)$  can be expressed in terms of upper critical field  $H_{c2}$  as  $H_c(T) = H_{c2} / \sqrt{2} \chi$  where  $\chi$  is Ginzburg-Landau parameter and is temperature independent. Moreover,  $H_{c2}(T) = \frac{\phi_0}{2\pi\xi^2(T)}$ . All these expressions combine to give

$$U_0(T) = U_0(0) \left[ \frac{T_{co} - T}{T_{co}} \right]^{3/2} \quad (3.13)$$

where  $U_0(0) = \frac{\phi_0^3}{8\pi^2 \chi \xi^3(0) B}$ . Thermally activated resistivity can now be written as  $\rho(T) = \rho(0) \exp\left[-\frac{U_0(T)}{kT}\right]$  with  $U_0(T)$  as given above.

Fig. 3.11 shows the fitting represented by solid curve by using Eqn. 3.13.  $U_0(0)$  decreases with increasing magnetic field. The dissipation in the present system involves temperature dependent activation energies due to temperature dependence of coherence length.

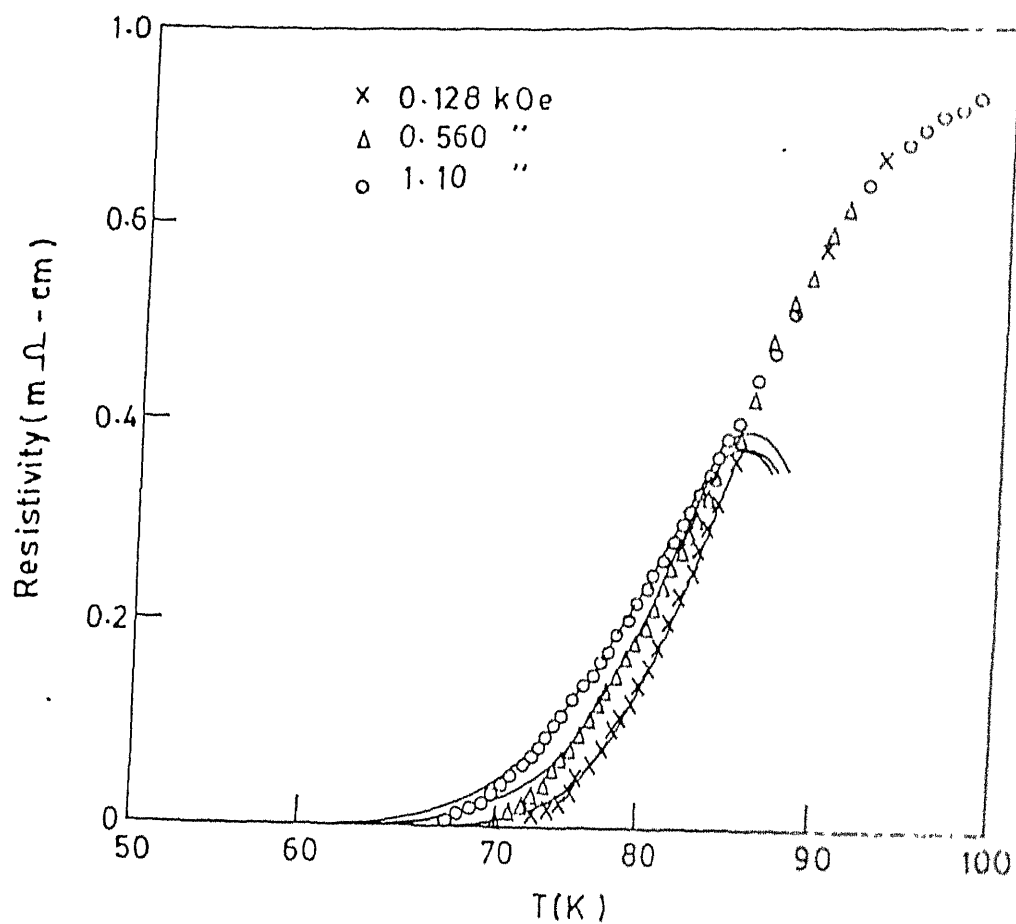


Fig. 3.11 Temperature dependence of resistivity for  $x = 0.10$  in the presence of low external magnetic fields. The solid lines are fitted curves by using Eqn. 3.13.

### 3.8 Conclusions:

We studied the  $\text{Bi}_2\text{Sr}_{2-x}\text{Gd}_x\text{Ca}_1\text{Cu}_2\text{O}_{8+\delta}$  system, through X-ray, electrical resistivity and Hall effect measurements. With increasing Gd concentration (x) the lattice parameter c decreases while a increases. Resistivity measurements show that the transition temperature first increases with x and then decreases till superconductivity is destroyed. Hall effect measurement reveals decrease of carrier concentration with increasing x. The suppression of superconductivity due to Gd substitution occurs due to combined effect of hole filling and disorder induced localization of charge carriers. The samples which are in the insulating state satisfy the condition of 3-D variable range hopping of conductivity at low temperatures. The resistivity data for these samples are in best agreement with a model having density of states near  $E_F$  concave in nature. The magnetoresistance measurement of a low Gd sample indicates the presence of temperature-dependent activation energy for the flow of flux lines.

### 3.9 References:

1. G. Xiao, M.Z. Cieplak, A. Garvin, F.H. Streitz, A. Bakhshai and C.L. Chien, Phys. Rev. Lett. 60, 1446 (1988).
2. J.M. Tarascon, P. Barboux, P.F. Miceli, L.H. Greene, G.W. Hull, M. Eibschutz and S.A. Sunshine, Phys. Rev. B 37, 7458 (1988).
3. A. Maeda, T. Yabe, S. Takebayashi, M. Hase and K. Uchinokura, Phys. Rev. B 41, 4112 (1990).



4. Gang Xiao, Marta Z. Cieplak, J.Q. Xiao and C.L. Chien, *Phys. Rev. B* 42, 8752 (1990).
5. L. Soderholm, K. Zhang, D.G. Hinks, M.A. Beno, J.D. Jorgensen; C.V. Segree and Ivan K. Schuller, *Nature* 328, 604 (1987).
6. C.S. Jee, A. Kebede, D. Nichols, J.E. Crow, T. Mihalism, G.H. Myer, I. Perez and R.E. Salomon, *J. Magn Mater* 76, 617 (1990).
7. G.Y. Guo and W.M. Temmerman, *Phys. Rev. B* 41, 6372 (1990).
8. N.F. Mott, *Physica C* 196, 369 (1992).
9. B. Jayaram, P.C. Lanchester and M.T. Weller, *Phys. Rev. B* 43, 5444 (1991).
10. Y. Gao, P. Pernambuco-Wise, J.E. Crow, J.O' Reilly, N.Spencer, H. Chen and R.E. Salomon, *Phys. Rev. B* 45, 7436 (1992).
11. J.M. Tarascon, P. Barboux, G.W. Hull, P. Ramesh, L.H. Greene, M Giroud, M.S. Hegde and W.R. McKinnon, *Phys. Rev. B* 39, 4316 (1989).
12. N. Fukushima, H. Niu and K Ando, *Jpn. J. Appl. Phys.* 27, L790 and L1432 (1988).
13. R. Yoshizaki, Y. Saito, Y. Abe and H. Ikeda, *Physica C* 152, 408 (1988).
14. N. Nishida, S. Okuma, M. Miyatake, T. Tamegai, Y. Iye, R. Yoshizaki, K. Nishiyama, K. Nagamine, R. Kadono and J.H. Brewer, *Physica C* 168, 23 (1990).
15. Y.J. Uemura, C.E. Stronach, D.C. Johnston, M.S. Alvarez and D.P. Goshorn, *Phys. Rev. Lett.* 59, 1045 (1987).

16. P. Burlet, C. Vettier, M.J.G.M. Jurgens, J.Y. Henry, J. Rossat - Mignod, H. Noel, M. Potel, P. Gougeon, and J.C. Levet, *Physica C* 153-155, 1115 (1988).
17. T. Tamegai, K. Koga, K. Suzuki, M. Ichihara, F. Sakai and Y. Iye, *Jpn. J. Appl. Phys.* 28, L112 (1989).
18. J. Clayhold, S.J. Hagen, N.P. Ong, J.M. Tarascon and P. Barboux, *Phys. Rev. B* 39, 7320 (1989).
19. P. Mandal, A. Poddar, B. Ghosh and P. Choudhury, *Phys. Rev. B* 43, 13102 (1991).
20. V.P.S. Awana, S.K. Agarwal, R. Ray, S. Gupta, and A.V. Narlikar, *Physica C* 191, 43 (1992).
21. V.P.S. Awana, S.K. Agarwal, A.V. Narlikar and M.P. Das, *Phys. Rev. B* 48, 1211 (1993).
22. N.H. Wang, C.M. Wang, H.C.I. Kao, D.C. Ling, H.C. Ku, and K.H. Lii, *Jpn. J. Appl. Phys.* 28, 1505 (1989).
23. A. Yamamoto, M. Onoda, E. Takayama-Muromachi, F. Izumi, T. Ishigaki and H. Asano, *Phys. Rev. B* 42, 4228 (1990).
24. J.J. Lin, E.L. Benitez, S.J. Poon, M.A. Subramanian J. Gopalakrishnan and A.W. Sleight, *Phys. Rev. B* 38, 5095 (1988).
25. T. Onozuka, Y. Iwabuchi, T. Fukase, H. Sato and T.E. Mitchell, *Phys. Rev.* 43, 13066 (1991).
26. R.G. Buckley, J.L. Tallon, I.W.M. Brown, M.R. Presland, N.E. Flower, P.W. Gilberd, M. Bowden and N.B. Milestone, *Physica C* 156, 629 (1988).
27. M.S. Hybersten and L.F. Mattheiss; *Phys. Rev. Lett.* 60, 1661 (1988).

- 
28. M. Tanaka, T. Takahashi, H. Katayama-Yoshida, S. Yamazaki, M. Fujinami, Y. Okabe, W. Mizutani, M. Ono and K. Kajimura, *Nature* **339**, 691 (1989).
  29. W. Drube, F.J. Himpsel, G.V. Chandrashekhar and M.W. Safer, *Phys. Rev. B* **39**, 7328 (1989).
  30. L.F. Mattheiss and D.R. Hamman, *Solid State Commun.* **63**, 395 (1987).
  31. Y. Tokura, J.B. Torrance, T.C. Huang and A.I. Nazzal, *Phys. Rev. B* **38**, 7156 (1988).
  32. J.B. Torrance, Y. Tokura, A.I. Nazzal, A. Benzing, T.C. Huang and S.S.P. Pakin, *Phys. Rev. Lett.* **61**, 1127 (1988).
  33. A. Maeda, H. Hase, I. Tsukada, K. Noda, S. Takebayashi and K. Uchinokura, *Phys. Rev. B* **41**, 6418 (1990).
  34. H. Yasuoka, M. Kakihana and H. Mazaki; *Physica C* **185-189**, 803 (1991).
  35. W.A. Groen, D.M. de Leeuw and L.F. Feiner, *Physica C* **165**, 55 (1990).
  36. H. Fukuyama and Y. Hasegawa, *Physica B* **148**, 204 (1987).
  37. N.P. Ong, Z.Z. Wang, J. Clayhold, J.M. Tarascon, L.H. Greene and W.R. McKinnon, *Phys. Rev. B* **35**, 8807 (1987).
  38. R.J. Cava, A.W. Hewat, E.A. Hewat, B. Batlogg, M. Marezio, K.M. Rabe, J.J. Krajewski, W.F. Peck Jr and L.W. Rupp Jr., *Physica C* **165**, 419 (1990).
  39. J. Clayhold, S.J. Hazen, Z.Z. Wang, N.P. Ong, J.M. Tarascon and P. Bardoux, *Phys. Rev. B* **39**, 777 (1989).
  40. A.W. White, R.C. Dynes and J.P. Garno, *Phys. Rev. B* **33**, 3549 (1989).

41. D.B. Haviland, Y. Liu and M.A. Goldman, Phys. Rev. Lett. 62, 2180 (1989).
42. P.B. Allen, T.B. Beaulac, F.S. Khan, W.H. Butler, F.J. Pinski and J.C. Swihart, Phys. Rev. B 34, 4331 (1986).
43. M.J. Naughton, R.C. Yu, P.K. Davies, J.E. Fisher, R.V. Chamberlin, Z.Z. Wang, T.W. Jing, N.P. Ong and P.M. Chaikin, Phys. Rev. B 38, 9280 (1988).
44. S. Martin, A.T. Fiory, R.M. Flemming, L.F. Schneemeyer and J.V. Waszczak, Phys. Rev. Lett. 60, 2194 (1988).
45. Y. Imery, Phys. Rev. Lett. 44, 469 (1980).
46. A.F. Ioffe and A.R. Regel, Prog. Semicond. 4, 237 (1960).
47. P.A. Lee and T.V. Ramakrishnan, Rev. Mod. Phys. 57, 287 (1985).
48. A.A. Abrikosov and L.A. Gor'kov, Sov. Phys. JETP 12, 1243 (1961).
49. K. Koyama, N. Tahata and S. Noguchi, Jpn. J. Appl. Phys. 31, 1313 (1992).
50. K. Kleiner, F. Steinmeyer, G. Kunkel and P. Miller, Phys. Rev. Lett. 68, 2394 (1992).
51. S. Maekawa and H. Fukuyama, J. Phys. Soc. Jpn. 51, 1380 (1981).
52. S. Maekawa, H. Ebisawa and H. Fukuyama, J. Phys. Soc. Jpn. 53, 2681 (1984).
53. A.L. Efros and B.I. Shklovskii, J. Phys. C 8, L49 (1975).
54. N. Missert and M.R. Beasley, Phys. Rev. Lett. 63, 672 (1989).
55. G. Bergmann, Physica B 169, 231 (1991).

- 
56. N.F. Mott and E.A. Davis, *Electronic Processes in Non Crystalline Materials* (Clarendon, Oxford 1979).
  57. W. Bremig, G.H. Dohler and H. Heyszenau, *Philos. Mag.* 27, 1093 (1973).
  58. V. Ambegaokar, B.I. Halperin and J.S. Langer, *Phys. Rev. B* 4, 2612 (1971).
  59. M.H. Brodsky and R.J. Gambino, *J. Non Cryst. Solids* 8-10, 739 (1972).
  60. M. Ortuno and M. Pollak, *Phil. Mag. B* 47, L93 (1983).
  61. J.S. Urbach, D.B. Mitzi, A. Kapitulnik, J.Y.T. Wei and D.E. Moris, *Phys. Rev. B* 39, 12391 (1989).
  62. A. Chakraborty, A.J. Epstein, D.L. Cox, E.M. McCann and W.E. Farneth, *Phys. Rev. B* 39, 12267 (1989).
  63. B. Jayaram, P.C. Lanchester, M.T. Weller, *Physica C* 160, 17 (1989).
  64. L.G. Aslamasov and A.I. Larkin, *Sov. Phys. Solid State* 10, 875 (1968).
  65. A.T. Fiory, A.F. Hebard and W.I. Glaberson, *Phys. Rev. B* 28, 5075 (1983).
  66. M. Tinkham, *Phys. Rev. Lett.* 61, 1958 (1988).

## CHAPTER 4

### Mossbauer Study of $\text{Bi}_2\text{Sr}_{2-x}\text{Gd}_x\text{Ca}_1\text{Cu}_2\text{O}_{8+\delta}$ System

#### 4.1 Introduction:

In the previous chapter the interpretation of experimental results showed that the substitution of Gd for Sr in  $\text{Bi}_2\text{Sr}_2\text{Ca}_1\text{Cu}_2\text{O}_{8+\delta}$  generated disorder in  $\text{CuO}_2$  plane. The disorder has deleterious effects on superconductivity and drives the system in the insulating state. It is well established that Fe (ionic radius =  $0.55\text{\AA}$ ) can be partially substituted for Cu (ionic radius =  $0.62\text{\AA}$ ) in high temperature superconductors. Therefore, in order to investigate electronic properties as well as local structural variations around Cu atoms as a function of doping in charge reservoir Mossbauer spectroscopy serves as an important tool. In the present chapter we study  $\text{Bi}_2\text{Sr}_{2-x}\text{Gd}_x\text{Ca}_1\text{Cu}_{1.96}\text{Fe}_{0.04}\text{O}_{8+\delta}$  system through X-ray, ac susceptibility and Co-57 Mossbauer spectroscopy.

## Results and Discussions

### 4.2 X-Ray Analysis:

The samples  $\text{Bi}_2\text{Sr}_{2-x}\text{Gd}_x\text{Ca}_1\text{Cu}_{1.96}\text{Fe}_{0.04}\text{O}_{8+\delta}$  ( $x=0.0, 0.2, 0.4$  and  $0.6$ ) were prepared by ceramic method according to the detailed description given in chapter 2. The X-ray diffraction (XRD) patterns of the samples, recorded using  $\text{CuK}\alpha$  radiation, are shown in Fig. 4.1. It is evident that samples consist of single phase 2:2:1:2 system with no observable trace of impurity phases. The lattice parameters are calculated for a tetragonal structure due to absence of splitting of  $(2,0,0)$  and  $(0,2,0)$  peaks which would indicate the presence of orthorhombic symmetry. The variation of lattice constants with  $x$  is shown in Fig. 4.2. The lattice constant  $a$  increases slightly whereas  $c$  axis shows an appreciable decrease. The slope of lattice constant  $c$  vs  $x$  curve  $dc/dx = -1.0$  is in reasonable agreement to that observed for  $\text{Bi}_2\text{Sr}_{2-x}\text{Gd}_x\text{Ca}_1\text{Cu}_2\text{O}_{8+\delta}$  system of previous chapter. This confirms that structurally, the effect of substitution of Gd for Sr in the present system follows the same trend as that observed by its substitution in pure 2:2:1:2 system. The systematic variation of lattice constants show that both Fe and Gd have been incorporated in the crystal structure.

### 4.3 AC Susceptibility:

The results of the complex ac susceptibility  $\chi = \chi' + i\chi''$  for the samples  $x=0.0$  and  $0.2$  are shown in Fig. 4.3(a). Here  $\chi'$  is the in phase (inductive) component and  $\chi''$  is the out-of-phase

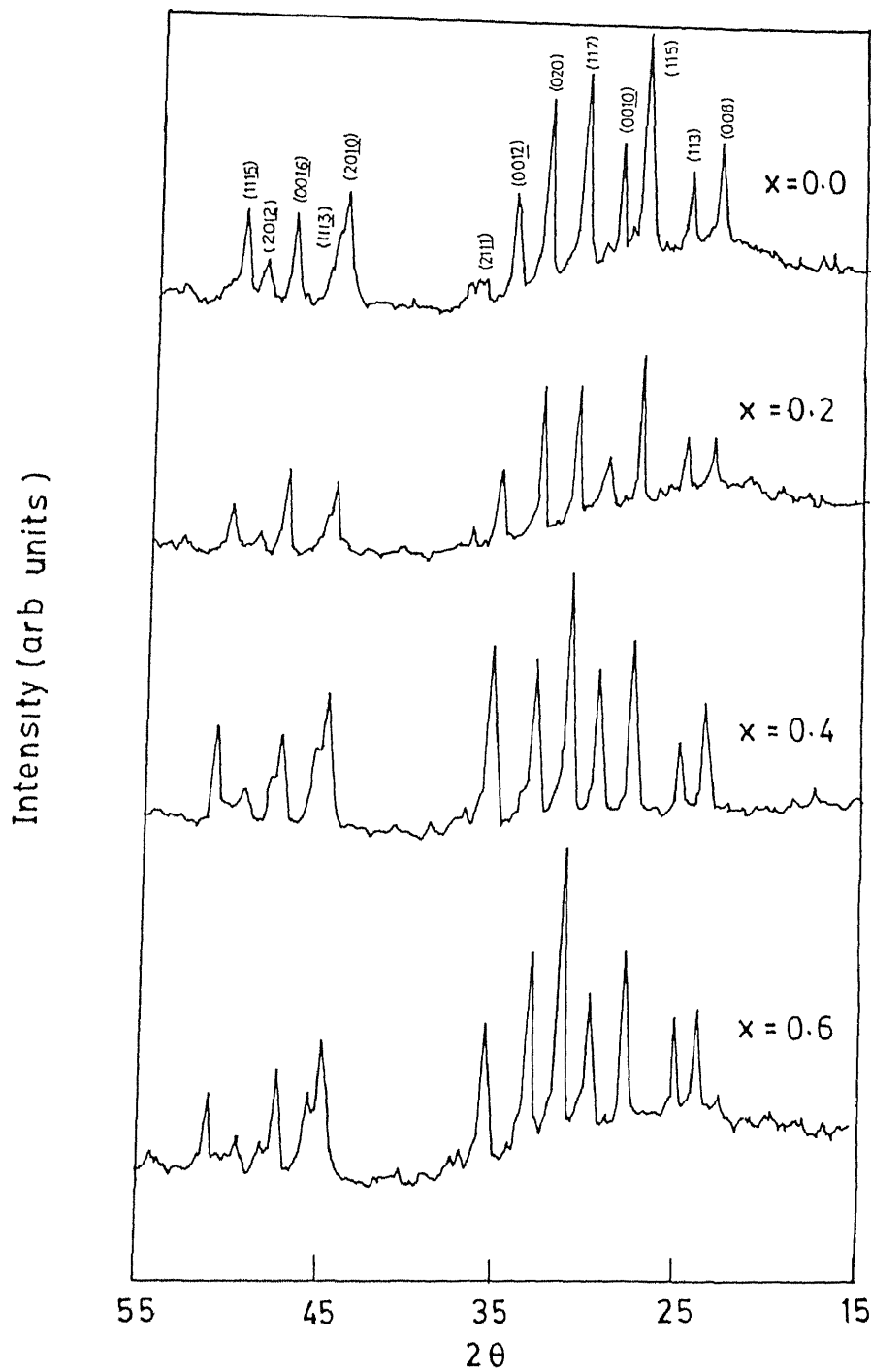


Fig. 4.1 X-ray diffraction patterns of  $\text{Bi}_2\text{Sr}_{2-x}\text{Gd}_x\text{Ca}_1\text{Cu}_{1.96}\text{Fe}_{0.04}\text{O}_{8+\delta}$  samples



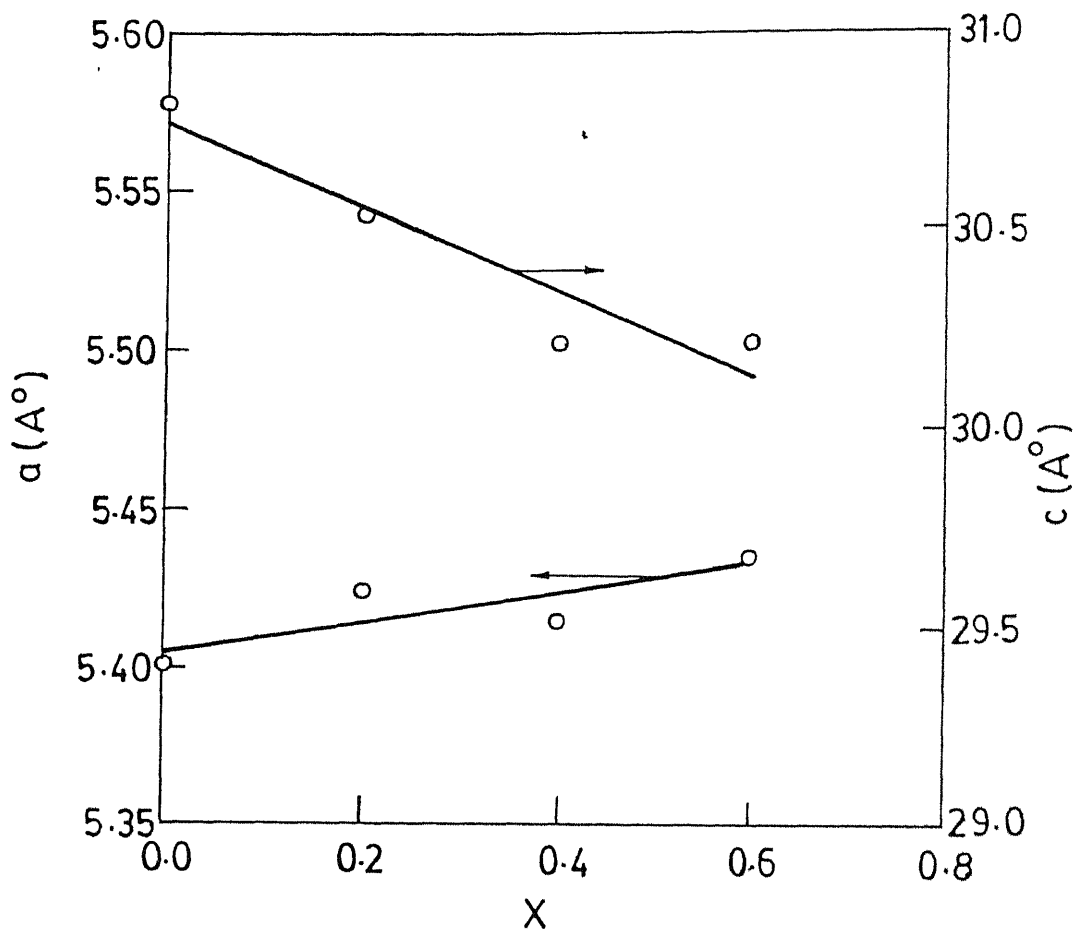
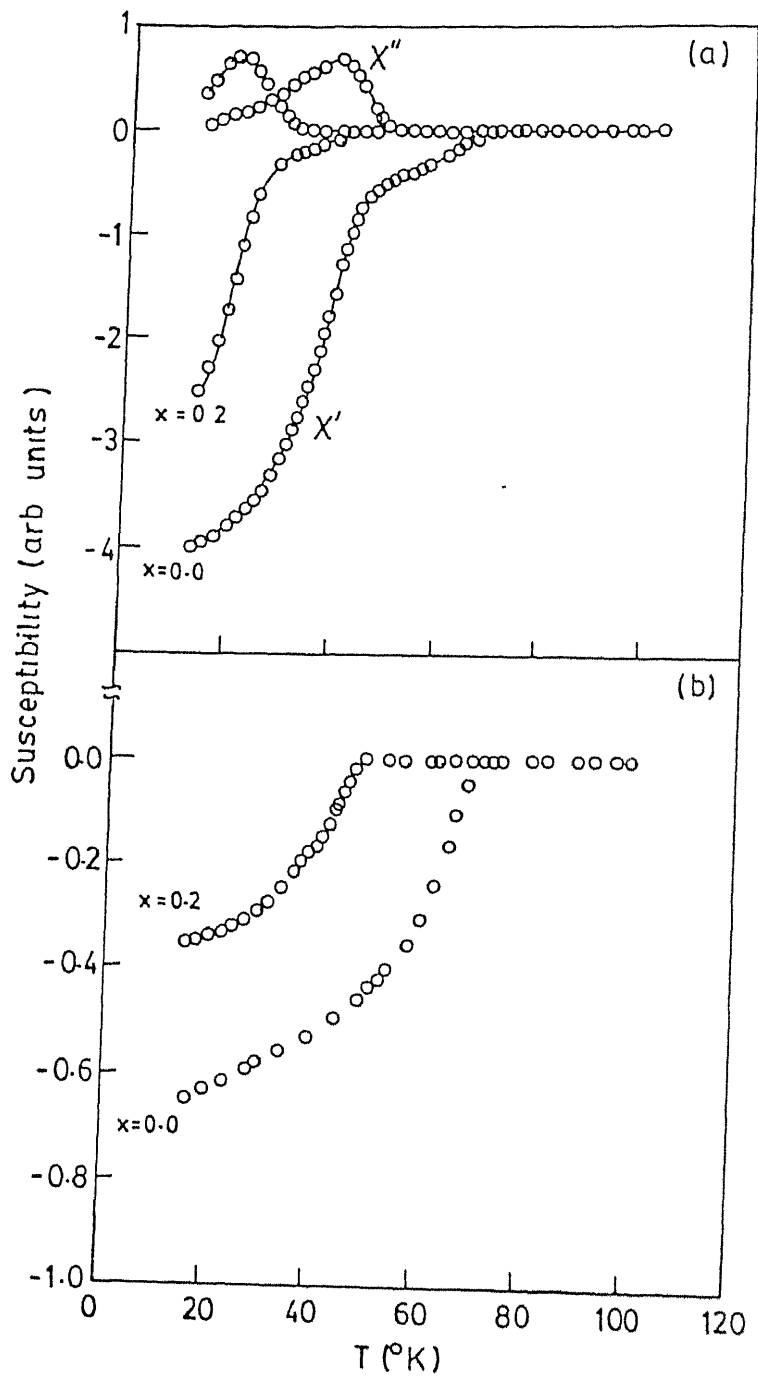


Fig. 4.2 Variation of lattice constants  $a$  and  $c$  with Gd concentration  $x$  in  $\text{Bi}_2\text{Sr}_{2-x}\text{Gd}_x\text{Ca}_1\text{Cu}_{1.96}\text{Fe}_{0.04}\text{O}_{8+\delta}$  system.

(resistive) component. The measurements were carried out at 73.3 Hz and at a field of 0.20 Oe. For the measurement purpose the sintered pellets were cut into rectangular bars and were placed in the coils with the largest dimension along the axis of the coils. The transition temperature (defined as the temperature where  $\chi'$  signal becomes negative) for  $x=0.0$  and  $x=0.2$  samples are 70K and 46K respectively.  $\chi'$  signal measured per gram in  $x=0.2$  sample is smaller than the same in  $x=0.0$  sample indicating that Gd substitution leads to reduction in superconducting volume fraction.  $x=0.2$  sample showed a small paramagnetic behaviour in the normal state due to presence of Gd ions.

We notice in Fig. 4.3(a) that  $\chi'$  shows a two step transition in the superconducting state as the temperature is lowered. This might indicate the presence of impurity phases remained unnoticed by XRD technique. To verify this, measurements were repeated with the samples in powder form. A well defined transition in the superconducting state was observed for both the samples as shown in Fig. 4.3(b). The absence of two step transition in powder samples shows that its presence is related to the property of the sample in the pellet form. This can be explained by invoking granular model of high  $T_c$  superconductor in which a superconductor is considered as an array of weakly Josephson coupled, strongly superconducting anisotropic grains [1]. In such a case upper transition corresponds to onset of superconductivity within the grains while the lower one when the superconductivity is established



**Fig. 4.3** Temperature dependence of ac susceptibility for  $x=0.0$  and  $x=0.2$  samples in  $\text{Bi}_2\text{Sr}_{2-x}\text{Gd}_x\text{Cu}_1\text{Cu}_{1.96}\text{Fe}_{0.04}\text{O}_{8+\delta}$  system.

globally. Powdering the samples removes the weak link coupling of the grains and hence only one transition is observed.

It is known that the imaginary component  $\chi''$  is related to the energy absorption in magnetic field which in turn is related to flux pinning. The Gd substitution reduces the temperature ( $T_{\max}$ ) at which maxima in  $\chi''$  vs  $T$  occurs. The  $T_{\max}$  in  $\chi''$  vs  $T$  in critical state model corresponds to the point when ac magnetic field ( $H_{ac}$ ) penetrates to the center of the sample [2]. At temperature below  $T_{\max}$  and for  $H_{ac} < H_{cl}$  (lower critical field) screening currents generated by ac field are confined to the sample surface. As the temperature is raised,  $H_{cl}$  decreases and  $H_{ac}$  starts penetrating the sample reaching the center at  $T_{\max}$ . In this regime screening currents flow through the intergranular junctions. With further increase of temperature,  $\chi'$  vs  $T$  profile shows that superconducting volume fraction decreases. This leads to lesser magnetic energy absorption in the system. The decrease of the peak in  $\chi''$  suggests that the substitution of Gd decreases critical current density.

The susceptibility curves of  $x=0.4$  and  $x=0.6$  samples are shown in Fig. 4.4. The absence of superconducting transition shows that the systems are in the insulating state. The phase diagram of  $\text{Bi}_2\text{Sr}_2\text{Ca}_1\text{Cu}_2\text{O}_{8+\delta}$  reveals that in the insulating state Cu spins in the  $\text{CuO}_2$  plane are antiferromagnetically coupled [3]. Therefore, the increase of  $\chi$  with decrease of  $T$  could be due to local magnetic moment of Cu ions ( $\mu_{\text{eff}} = 1.9\mu_B$ ) and/or due to magnetic moments of  $\text{Gd}^{3+}$  ( $\mu_{\text{eff}} = 7.9\mu_B$ ). That the

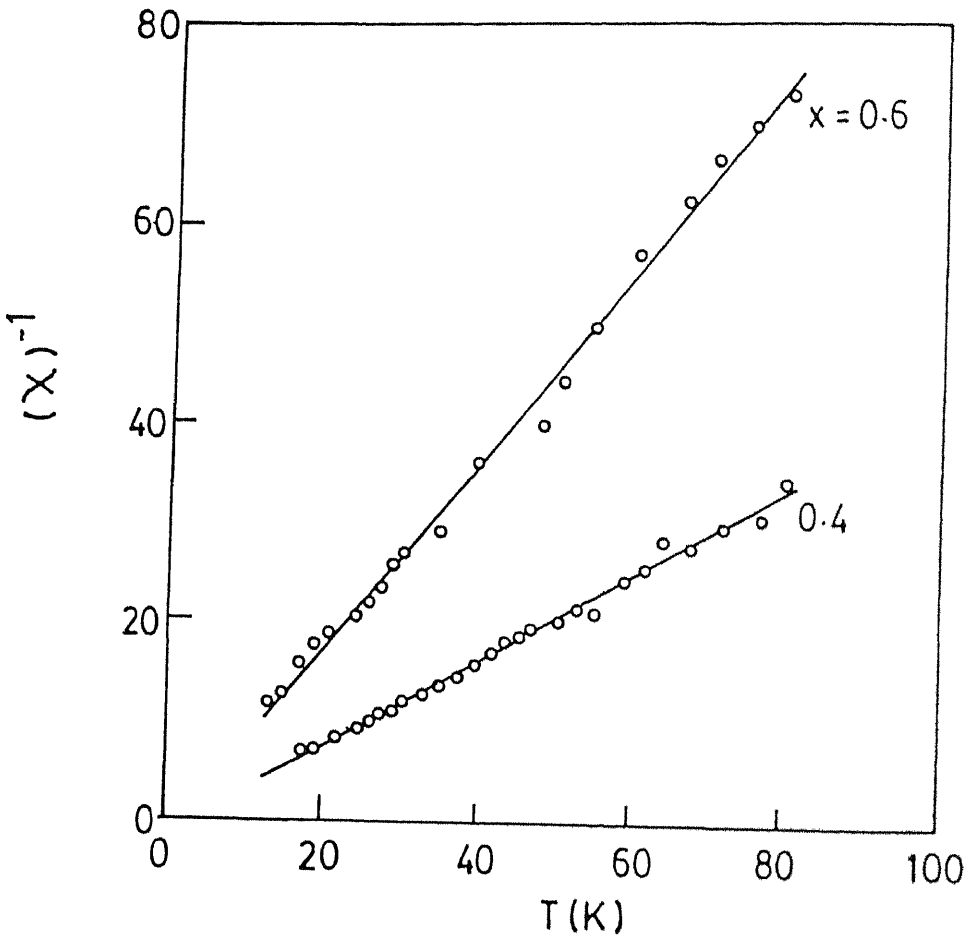


Fig. 4.4 Inverse of susceptibility signal vs  $T$  for  $x=0.40$  and  $x=0.60$  samples in  $\text{Bi}_2\text{Sr}_{2-x}\text{Gd}_x\text{Ca}_1\text{Cu}_{1.96}\text{Fe}_{0.04}\text{O}_{8+\delta}$  system.

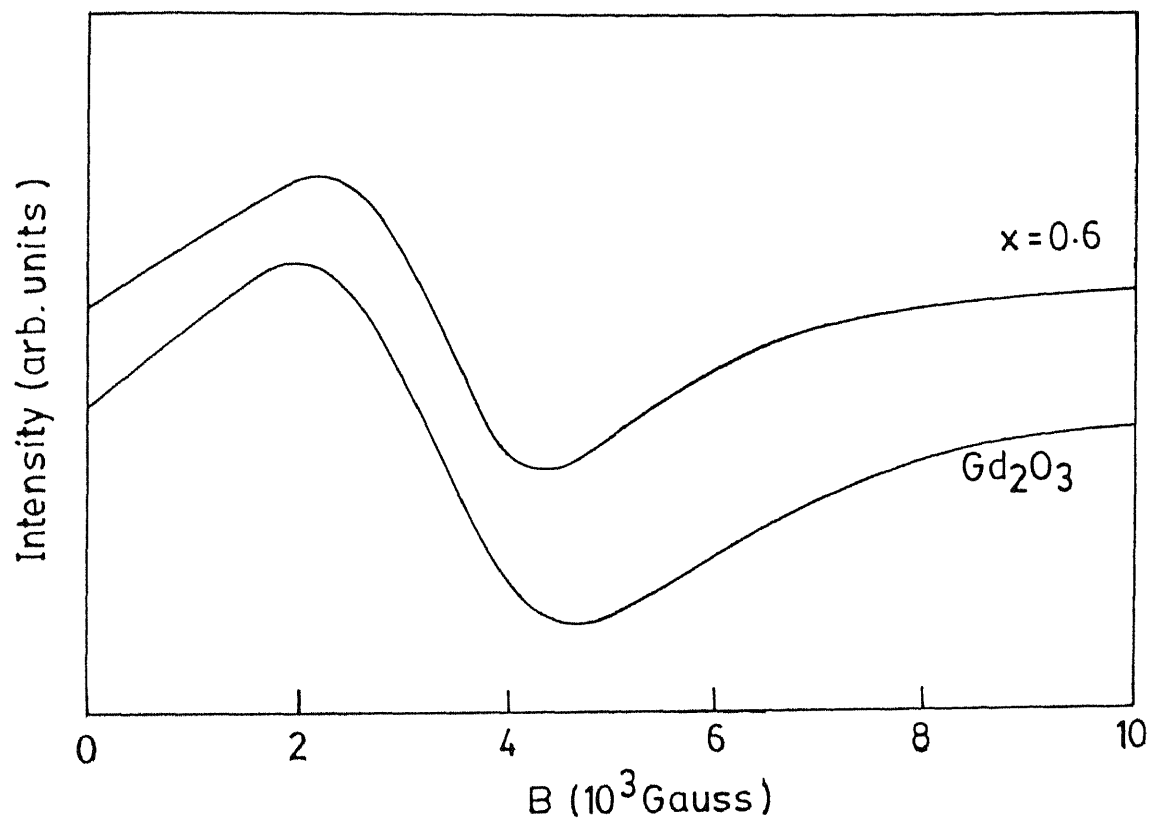


Fig. 4.5 EPR spectra of  $\text{Gd}_2\text{O}_3$  powder and  $x=0.6$  in  $\text{Bi}_2\text{Sr}_{2-x}\text{Gd}_x\text{Ca}_1\text{Cu}_{1.96}\text{Fe}_{0.04}\text{O}_{8+\delta}$  system.

Gd retains its ionic character in the samples is confirmed by comparison of room temperature EPR spectra of  $x=0.6$  and  $\text{Gd}_2\text{O}_3$  as shown in Fig. 4.5.  $g_{\text{eff}}$  obtained for the two samples are  $2.06 \pm 0.01$  and  $2.04 \pm 0.01$  respectively. It must be noted that EPR signal obtained in  $x=0.6$  sample is not due to possible presence of  $\text{Gd}_2\text{O}_3$  as an impurity phase. For the same mass of  $x=0.6$  and  $\text{Gd}_2\text{O}_3$ , the measured intensity ratio from EPR spectrum is  $\frac{I(x=0.6)}{I(\text{Gd}_2\text{O}_3)} \approx 0.2$ . If the EPR signal in  $x=0.6$  sample is due to  $\text{Gd}_2\text{O}_3$  impurity phase, it is unlikely that 20% mass proportion of  $\text{Gd}_2\text{O}_3$  remains undetected by XRD. Therefore, the EPR signal obtained in our samples, except  $x=0.0$  which was EPR silent, is due to presence of  $\text{Gd}^{3+}$  ion in the crystal structure. This implies that  $\chi$  vs  $T$  behaviour for the insulating samples are due to large magnetic moment of Gd ions. The susceptibility for these samples can be described by Curie- Weiss law

$$\chi = \frac{C}{T-\theta} \quad (4.1)$$

where  $C$  is the Curie constant and  $\theta$  is the Curie temperature. The solid curve in Fig. 4.4 is the fitted curve using Curie-Weiss law.  $\theta$  values obtained for  $x=0.40$  and  $x=0.60$  samples are 2.5K and 1.3K respectively. This suggests the presence of weak ferromagnetic coupling of Gd ions at low temperature.

#### 4.4 Room Temperature Mossbauer Study:

##### 4.4.1 Results:

The Mossbauer spectra of the samples were recorded using absorber thickness of  $25\text{-}30\text{mg}/\text{cm}^2$ . The absorbers thus contained  $0.06\text{-}0.07\text{mg}/\text{cm}^2$  of Fe-57 and were therefore thin absorber.

The room temperature Mossbauer spectra of the samples are shown in Fig. 4.6. All the spectra were least square fitted with three pairs of doublets with three different quadrupole splittings. The doublets are marked as A, B and C in the figure. The three pair fitting is in accordance with previously reported fitting procedure of Fe doped  $\text{Bi}_2\text{Sr}_2\text{Ca}_1\text{Cu}_2\text{O}_{8+\delta}$  system [4-7]. The parameters obtained from fitting of  $x=0.0$  sample were taken as initial parameters for curve fitting of other samples.

The data of quadrupole splitting ( $\Delta E_Q$ ), isomer shift (I.S.), line widths (L.W.) measured as full width at half maximum and relative areas of the doublets are presented in Table 4.1. Our results of I.S., L.W. and relative areas for the samples with no Gd doping ( $x=0.0$ ) are in close agreement with those reported in ref [7]. Although the  $\Delta E_Q$  for doublets B and C are found to be same as in above references, the doublet A however shows a quadrupole splitting of  $1.91 \pm 0.02$  mm/s in our samples as compared to the reported value of 1.81mm/s. We attribute the difference to the different method of preparation of the samples. Since Mossbauer parameters depend on the method of preparation of the



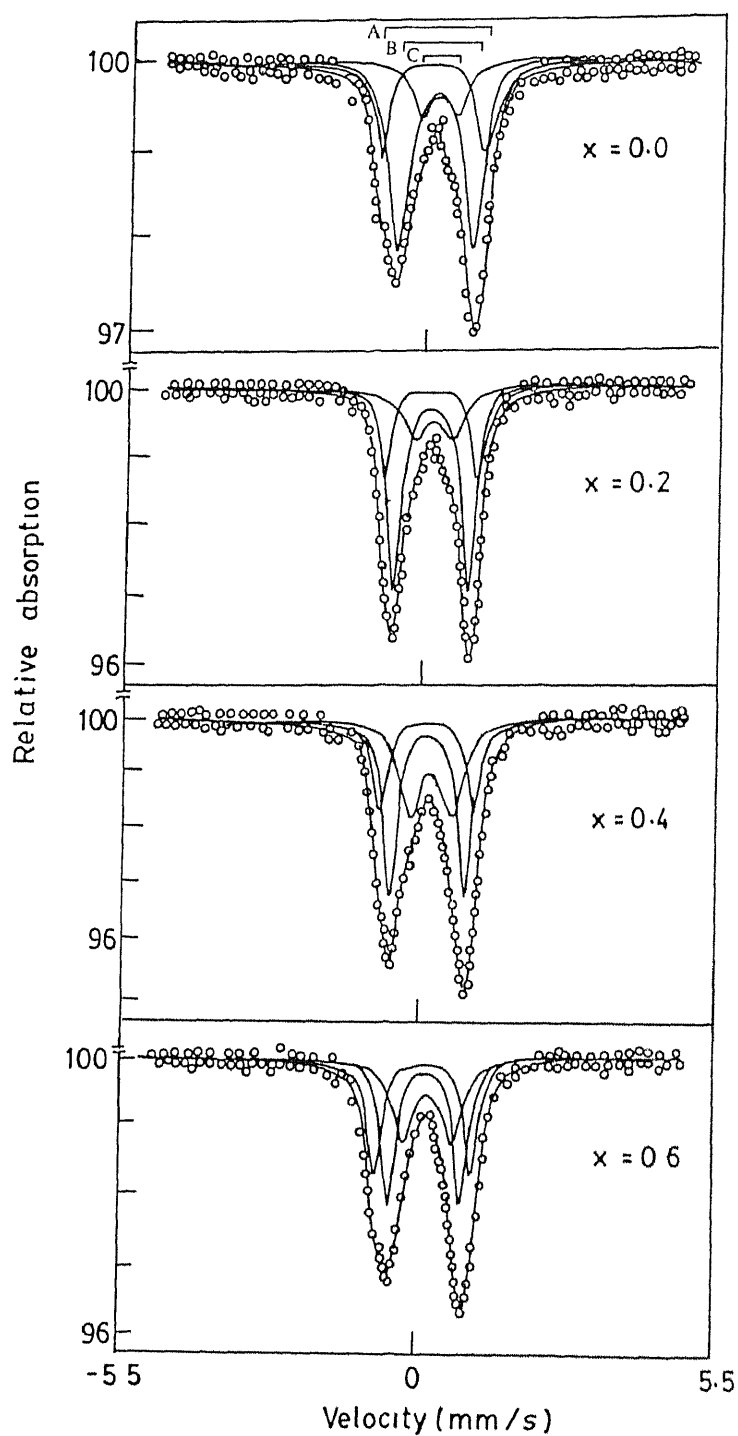


**Fig. 4.6** Room temperature Mossbauer spectra for various  $x$  in  $\text{Bi}_2\text{Sr}_{2-x}\text{Gd}_x\text{Ca}_1\text{Cu}_{1.96}\text{Fe}_{0.04}\text{O}_{8+\delta}$  system.

our samples in identical ways except the sintering temperature which was increased with  $x$ .

In Fig. 4.7 we have shown the variation of isomer shift with Gd concentration ( $x$ ). The isomer shift is measured w.r.t. metallic iron. We have neglected the second order Doppler shift which is very small at room temperature. The isomer shift of the doublets lie in the range 0.16-0.33 mm/s. This shows that iron ion is in high spin  $\text{Fe}^{3+}$  state. We notice that I.S. increases as Gd is introduced in  $\text{Bi}_2\text{Sr}_2\text{Ca}_1\text{Cu}_{1.96}\text{Fe}_{0.04}\text{O}_{8+\delta}$  system. The isomer shift of the doublets B and C increases from 0.25 and 0.28 mm/s respectively for  $x=0.0$  to 0.28 and 0.31 mm/s respectively for  $x=0.2$ . On the other hand, the I.S. of doublet A shows a rather large increase from 0.16 mm/s for  $x=0.0$  to 0.25 mm/s for  $x=0.2$ . For higher Gd concentration I.S. remains nearly constant. Since I.S. arises due to interaction of s-electron density at Fe nucleus with the nuclear charge its increase indicates that s-electron density at Fe nucleus decreases.

The variation of quadrupole splitting ( $\Delta E_Q$ ) with  $x$  is plotted in Fig. 4.8. The  $\Delta E_Q$  for doublet A decreases from 1.91 mm/s for  $x=0.0$  to 1.73 mm/s at  $x=0.2$ . With further increase of  $x$  the  $\Delta E_Q$  for this doublet shows an increasing tendency. The quadrupole splitting of doublet B remains practically invariant with Gd concentration. The  $\Delta E_Q$  for doublet C shows an increase from 0.66 mm/s for  $x=0.0$  to 0.89 mm/s for  $x=0.60$ .

The relative areas corresponding to the relative occupancies of the three different Fe(Cu) sites is shown in

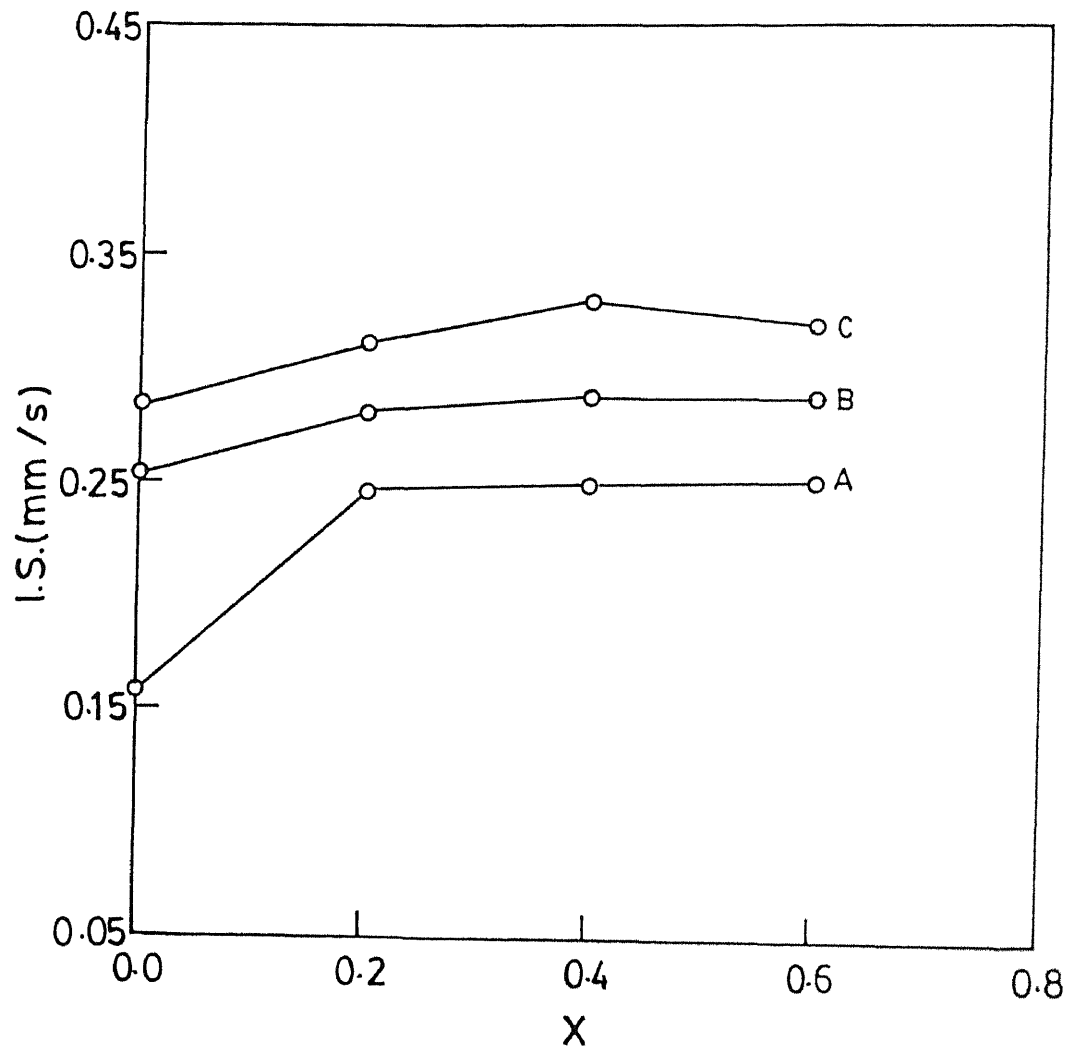


Fig. 4.7 Variation of isomer shift with Gd concentration in  $\text{Sr}_{2-x}\text{Gd}_x\text{Ca}_1\text{Cu}_{1.96}\text{Fe}_{0.04}\text{O}_{8+\delta}$  system.

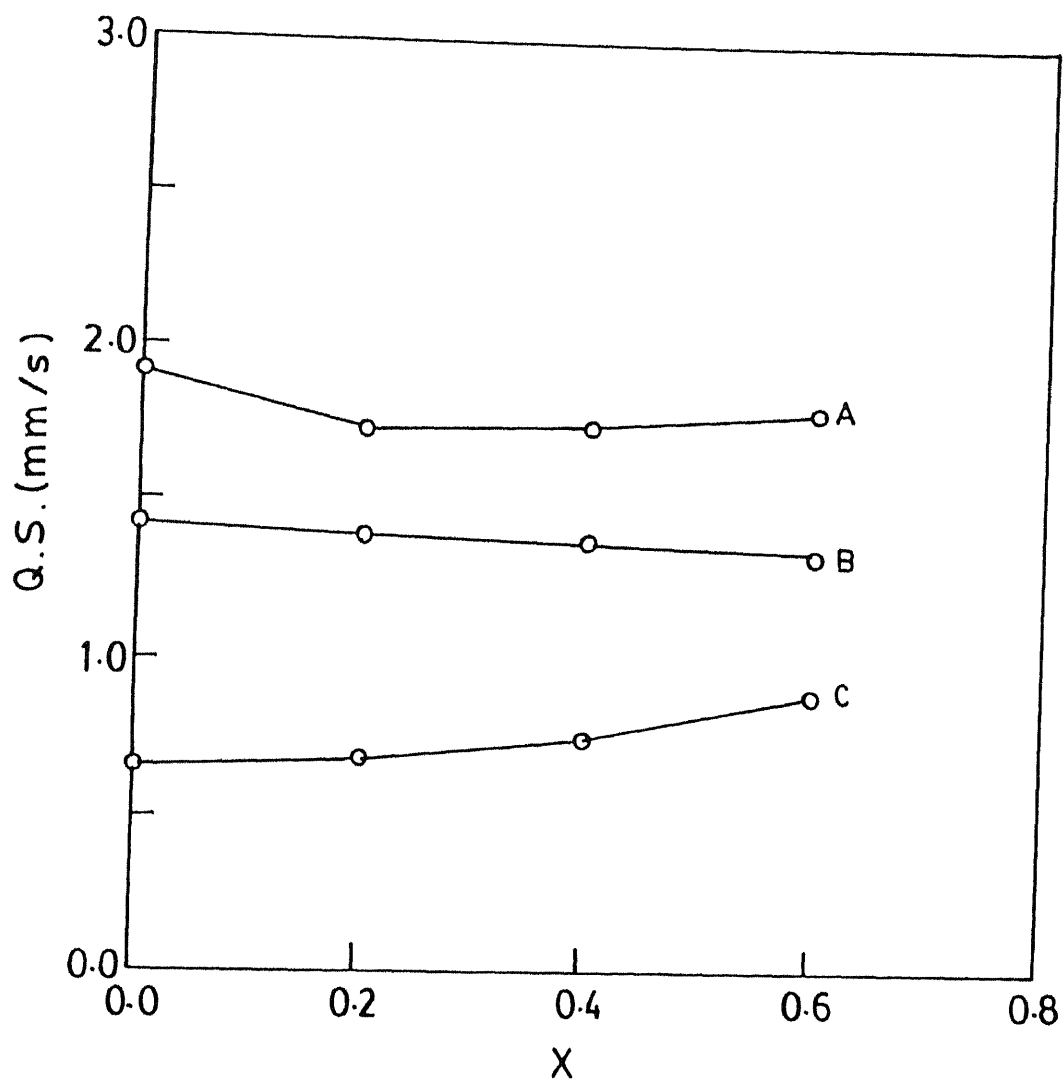


Fig. 4.8 Variation of quadrupole splitting with Gd concentration in  $\text{Bi}_2\text{Sr}_{2-x}\text{Gd}_x\text{Ca}_1\text{Cu}_{1.96}\text{Fe}_{0.04}\text{O}_{8+\delta}$  system.

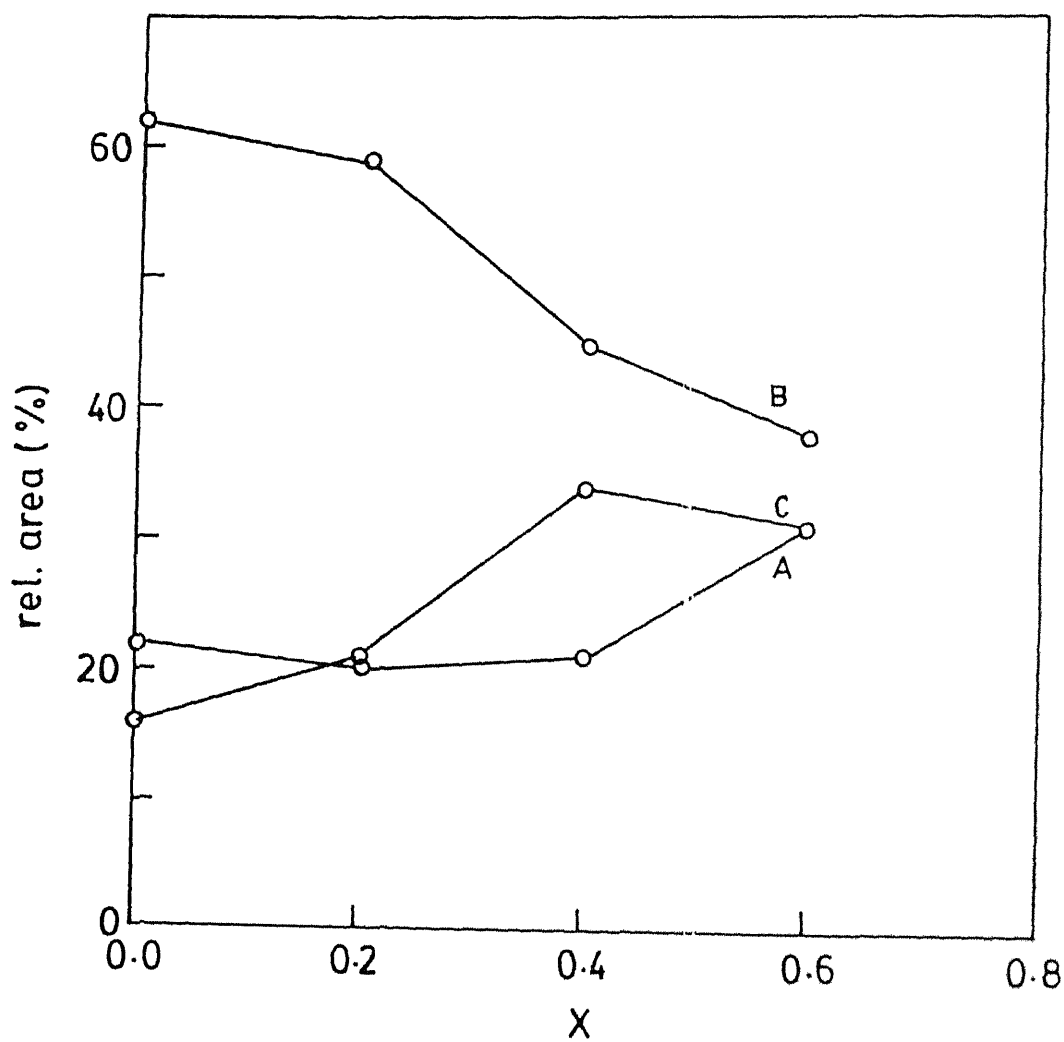


Fig. 4.9 Variation of relative area with Gd concentration in  $\text{Bi}_2\text{Sr}_{2-x}\text{Gd}_x\text{Ca}_1\text{Cu}_{1.96}\text{Fe}_{0.04}\text{O}_{8+\delta}$  system.

Fig. 4.9. With increasing Gd concentration, relative area of doublet B which is the most populous site decreases while that of doublet C increases. The doublet A shows an increase in relative area only at higher Gd concentration ( $x > 0.4$ ).

The observed line width for all the doublets in  $x=0.0$  is much larger than the natural line width. This shows the presence of distribution of electric field gradients at these sites. With the introduction of Gd in the system, the line width of doublets A and B decreases while the line width of doublet C increases. For Gd concentration beyond  $x=0.2$  the line width of doublet A shows an increase whereas that of doublets B and C remains constant.

#### 4.4.2 Discussions:

Since iron replaces Cu in the samples, the presence of three pairs of doublets with different  $\Delta E_Q$  indicate the presence of three distinct Cu sites in all the systems. The quadrupole splitting is usually given by [8]

$$\Delta E_Q = \frac{1}{2} eQ V_{zz} (1 + \eta^2/3) \quad (4.2)$$

where  $V_{zz}$  is the largest component of electric field gradient (EFG) tensor,  $Q$  is the nuclear quadrupole moment and  $\eta = (V_{xx} - V_{yy})/V_{zz}$  is the asymmetry parameter. The sources which contribute to EFG are the lattice contribution  $(V_{zz})_{lat}$  and valence electron contribution  $(V_{zz})_{val}$ . Thus,

increase in relative area of doublet C with  $x$  implies an increase in relative phase content of 2:2:0:1 phase in the samples. A large ratio of 2:2:0:1 phase content ~30% at  $x=0.6$  as is evidenced from the relative area of doublet (C) can not remain undetected by X-ray diffraction. The single phase XRD patterns of  $x=0.6$  and other samples show that Cu site corresponding to doublet (C) is not related to an impurity phase.

As noted earlier in Fig. 4.8 the quadrupole splitting of doublet B remains nearly constant with increasing Gd concentration. A consequence of rare-earth substitution in 2:2:1:2 system has been found to decrease the formal valence of copper which weakens CuO bonds [12]. The weakening of the bond causes an increase in lattice parameter  $a$  which has been observed in XRD pattern of the present system. It appears that an increase in Cu-O bond length in  $ab$  plane is compensated for by a decrease in  $c$ -axis Cu-O bond length as a result of which  $\Delta E_Q$  of doublet B remains unchanged. On the other hand the quadrupole splitting of doublet (C) increases gradually for small  $x$  and shows an appreciable increase at higher values of  $x$ . The quadrupole splitting of doublet (A) also shows an increase at higher values of  $x$ . This suggests that Gd substitution has resulted in the increased local distortion of Fe(Cu) site attributed to doublet A and C. As the correlation time ( $\tau_c$ ) defined as  $\tau_c = \hbar / \Delta E_Q$  [13] ( $\sim 10^{-12}$  s) is much smaller than the observation time ( $10^{-7}$  s for  $^{57}\text{Fe}$ ) no fluctuating EFG will be observed. Thus the increased  $\Delta E_Q$  is the result of

static local distortion of Fe(Cu) sites.

The increase in  $\Delta E_Q$  could be due to displacement of apical oxygen located in SrO plane or due to rearrangement of atoms in  $\text{CuO}_2$  plane or both. The electronic band structure of 2:2:1:2 shows that oxygen atoms in SrO plane are coupled strongly ( $\sigma$  bonds) to Cu atoms in  $\text{CuO}_2$  plane as well as Bi atoms in Bi-O plane. It is therefore more likely that Gd substitution has resulted in rearrangement of atoms in  $\text{CuO}_2$  plane leading to increased local distortion. The site intensity ratio of these sites determined by relative area of the doublets also increases with Gd concentration at the expense of Fe(Cu) sites attributed to doublet (B). The presence of growing local distortion in the system can have an adverse effect on superconductivity by localizing electron on distorted Cu-O bond [14]. More interesting is the doublet (C) which shows rather large increase of  $\Delta E_Q$ . The nearest neighbour Fe sites related to doublet (C) become more inhomogeneous as is evident from increase of line width. Moreover, Nowik et.al. [3] found doublet (C) converting into magnetic sextuplet in the insulating region of 2:2:1:2 system. It appears that this site plays a crucial role in suppression of superconductivity.

The increase of isomer shift as observed in Fig. 4.7 indicates that Gd substitution has affected the electronic structure of iron ion in  $\text{CuO}_2$  plane. Pressure dependent measurements on oxide compounds reveal that in general an increase in pressure and corresponding decrease in volume leads to a decrease in isomer shift [15]. Therefore, it is evident



that the change in isomer shift in the present system is not related to the decrease in unit cell volume. From the band structure calculation of 2:2:1:2 we find that 3d orbitals of Cu hybridize with oxygen 2p states [16]. The bands which intersect Fermi level ( $E_F$ ) are the antibonding Cu  $d(x^2-y^2)$  - O  $p(xy)$  states. The high spin  $Fe^{3+}$  state of iron ion, therefore, suggests that the highest occupied states at  $E_F$  are the half filled  $d(x^2-y^2)$  states of  $Fe^{3+}$  which are strongly hybridized with the neighbouring O( $p\sigma$ ) states. In such a case, the increase in isomer shift is presumably as a result of localization of electrons at  $dp\sigma$  bonds at  $E_F$  which increases shielding effects. The localization is induced by disorder in the system caused by Gd substitution. A similar increase of isomer shift due to changes in d level population has been observed during metal insulator transition in  $V_2O_3$  compound [17]. The trends of isomer shift corroborates the conclusion arrived at in the discussion of quadrupole splitting.

#### 4.5 Temperature Dependent Mossbauer Study:

Temperature dependent Mossbauer measurements were carried out for  $x=0.0$ , 0.2 and 0.6 samples. All the spectra were fitted with three symmetric quadrupole doublets. No qualitative change in spectra was observed for  $x=0.0$  and 0.2 samples below the transition temperature. In Fig. 4.10 we have shown the Mossbauer spectra of  $x=0.2$  sample for temperatures above and below the transition temperature. The quadrupole splitting remains same at these temperatures.  $x=0.6$  sample which is in

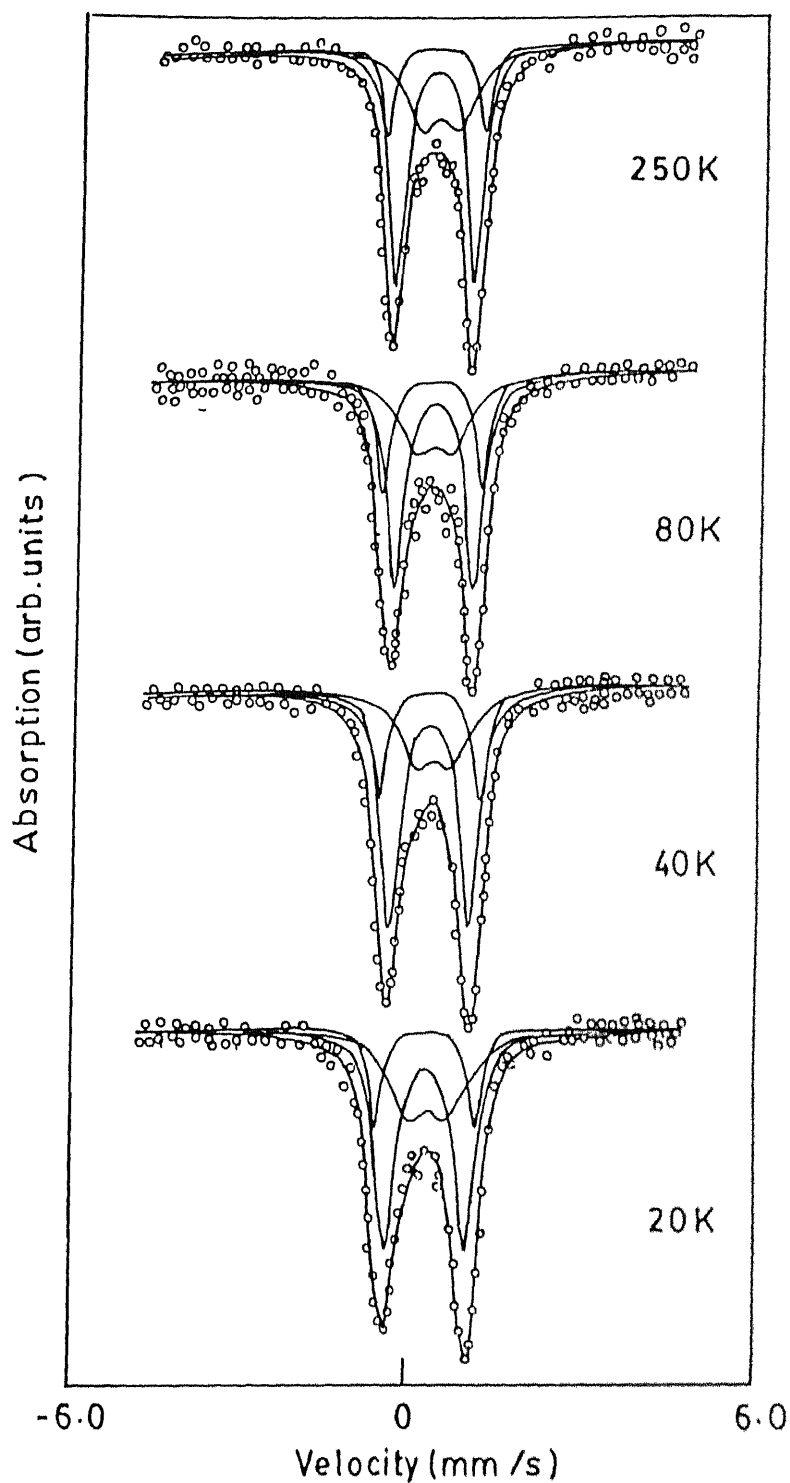


Fig. 4.10 Mossbauer spectra of  $x=0.2$  sample in  $\text{Bi}_2\text{Sr}_{2-x}\text{Gd}_x\text{Cu}_{1.96}\text{Fe}_{0.04}\text{O}_{8+\delta}$  at various temperatures.

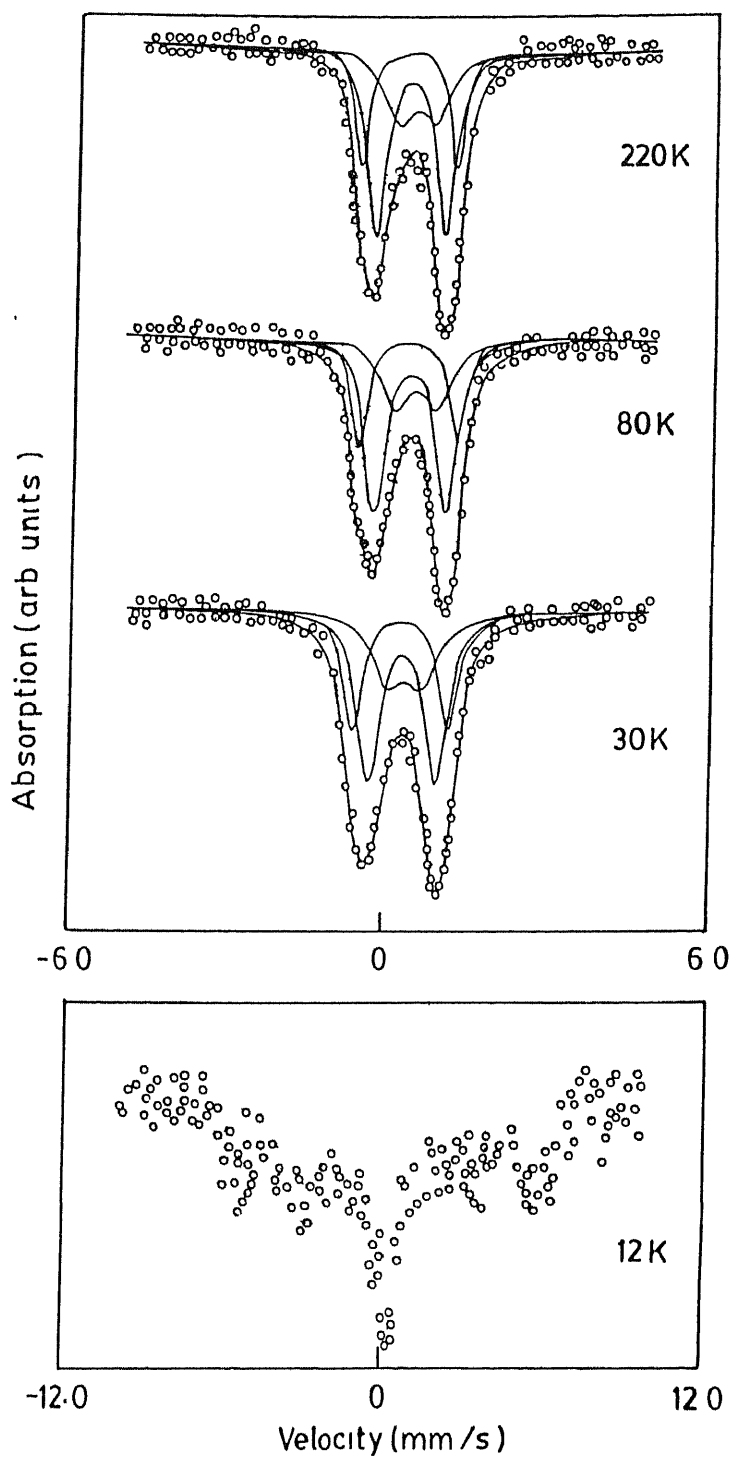


Fig. 4.11 Mössbauer spectra of  $x=0.6$  sample in  $\text{Bi}_2\text{Sr}_{2-x}\text{Gd}_x\text{Ca}_1\text{Cu}_{1.96}\text{Fe}_{0.04}\text{O}_{8+\delta}$  at various temperatures.

the insulating state shows signature of magnetic splitting at 12K. This shows that at 12K Cu spins in the  $\text{CuO}_2$  plane are magnetically ordered. Similar ordering has been observed in insulating Y doped 2:2:1:2 system. The spectra of  $x=0.6$  sample at various temperature is shown in Fig. 4.11.

The variation of center shifts with temperature corresponding to doublet (B) for  $x=0.0$ , 0.2 and 0.6 samples are shown in Figs. 4.12(a, b and c) respectively. Due to large uncertainties involved in center shift of doublets A and C their temperature dependence is not shown. The experimentally observed shift ( $\delta$ ) is the sum of two terms,

$$\delta = \delta_{\text{iso}} + \delta_{\text{SOD}} \quad (4.4)$$

where  $\delta_{\text{iso}}$  is the term describing interaction of s-electron densities at Fe-57 nucleus and  $\delta_{\text{SOD}}$  is the second order Doppler shift or thermal shift. The second order Doppler shift is related to lattice dynamics and is given as

$$\delta_{\text{SOD}}(T) = - \frac{\langle v^2 \rangle}{2c} \quad (4.5)$$

where  $\langle v^2 \rangle$  is the mean square velocity of the Mössbauer atom and  $c$  is the velocity of light. For a Debye solid, vibrational motion  $\langle v^2 \rangle$  is given as [18]

$$\langle v^2 \rangle = \frac{9k\theta_D}{8M} + \frac{9kT}{M} \left( \frac{T}{\theta_D} \right)^3 \int_0^{\theta_D/T} \frac{x^3}{e^x - 1} dx \quad (4.6)$$

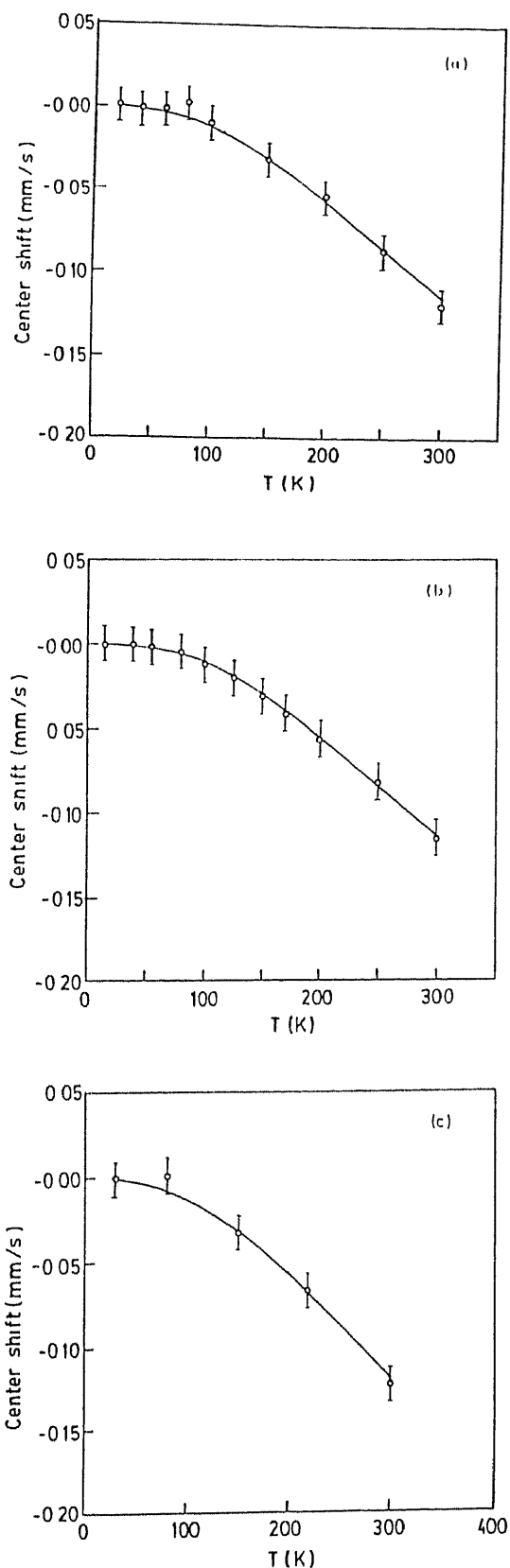


Fig. 4.12 Temperature dependence of center shift for (a)  $x=0.0$ , (b)  $x=0.2$  and (c)  $x=0.6$  in  $\text{Bi}_2\text{Sr}_{2-x}\text{Gd}_x\text{Cu}_{1.96}\text{Fe}_{0.04}\text{O}_{8+\delta}$ . The solid curve is the fit using Eqn. 4.7.

where  $M$  is the mass of the resonating atom and  $\theta_D$  is the Debye temperature. Thus it is clear that the temperature dependence of center shift gives information about the vibrational spectrum of the solid. The experimental data were fitted to

$$\delta(T_1) - \delta(T_2) = \frac{9k}{Mc} \left[ T_2 \left( \frac{T_2}{\theta_D} \right)^3 \int_0^{\theta_D/T_2} \frac{x^3}{e^x - 1} dx - T_1 \left( \frac{T_1}{\theta_D} \right)^3 \int_0^{\theta_D/T_1} \frac{x^3}{e^x - 1} dx \right] \quad (4.7)$$

Here isomer shift  $\delta_{iso}$  was assumed independent of temperature.  $T_2$  was taken as the lowest measured temperature and  $\theta_D$  was obtained by minimum standard deviation method.

In Figs. 4.12(a, b and c) the solid curves show results of fitting using above expression. It is clear that Debye model well describes our data. The Mossbauer data reveal no electronic structural anomaly or phonon softening below the transition temperature in  $x=0.0$  and  $0.2$  samples. The softening corresponds to the case of lattice vibration when average vibrational velocity decreases. The results of inelastic neutron scattering experiment of  $\text{Bi}_2\text{Sr}_2\text{Ca}_1\text{Cu}_2\text{O}_{8+\delta}$  have also shown that the phonon density of states remain unchanged below the transition temperature [19]. Since the expression for  $\langle v^2 \rangle$  (Eqn. 4.6) is true for a harmonic crystal, the fitting shows that motion of Fe atoms remain harmonic below  $T_C$ . The absence of vibrational instabilities shows that the occurrence of superconductivity is not related to it. The fitting yields the

value of  $\theta_D$  for  $x=0.0$ ,  $0.2$  and  $0.6$  samples as  $452\pm 20K$ ,  $463\pm 18K$  and  $453\pm 30K$  respectively. The observed values of  $\theta_D$  for  $^{57}Fe$  is significantly lower than in  $Y_1Ba_2Cu_3O_{7-\delta}$  ( $\theta_D\sim 650K$ ) [20] but higher than in  $Bi(Pb)_2Sr_2Ca_2Cu_3O_{10}$  system ( $\theta_D\sim 350K$ ) [21].

#### 4.6 Conclusions:

We prepared single phase  $Bi_2Sr_{2-x}Gd_xCa_1Cu_{1.96}Fe_{0.04}O_{8+\delta}$  ( $x=0.0$ ,  $0.2$ ,  $0.4$  and  $0.6$ ) samples and studied through X-ray, ac susceptibility and Mossbauer measurements. XRD patterns indicate inclusion of both Gd and Fe ions in the system. AC susceptibility measurement shows that peak of the dissipative component of ac susceptibility decreases with Gd substitution. Room temperature Mossbauer spectra reveal presence of three different Cu environment in the samples. The variation of room temperature isomer shift with Gd concentration shows localization of electrons near  $E_F$  during metal insulator transition. Temperature dependence of center shifts for  $x=0.0$  and  $0.2$  samples show that motion of Fe ions remain harmonic and no phonon softening is observed below transition temperature.

#### 4.7 References:

1. J.R. Clem, Physica C 153-155, 50 (1988).
2. K.H. Muller, Physica C 159, 717 (1989).
3. I. Nowik, I. Felner and E.R. Bauminger, Phys. Rev. B 45, 4912 (1992).
4. O. Bremert, C. Michaelsem and H.U. Krebs, J. Appl. Phys. 65, 1018 (1989).

- 
5. H. Tang, Z.Q. Qiu, Y.W. Du and J.C. Walker, J. Appl. Phys. 67, 4512 (1990).
  6. S.T. Lin, W.S. Chung, C.Y. Chou and C.M. Lin, J. Phys. C 2, 8673 (1990).
  7. I. Tittonen, J. Hietaniemi, J. Linden, T. Katila, T. Karlemo, M. Karppinen, L. Niinistö and K. Ullakko, Phys. Rev. B 42, 4212 (1990).
  8. N.N. Greenwood and T.C. Gibb, Mössbauer Spectroscopy (Chapman and Hall Ltd, 1971).
  9. S.A. Sunshine, T. Siegrist, L.F. Schneemeyer, D.W. Murphy, R.J. Cava, B. Batlogg, R.B. van Dover, R.M. Fleming, S.H. Glarum, S. Nakahara, R. Farrow, J.J. Krajewski, S.M. Zahurak, J.V. Waszczak, J.H. Marshall, P. Marsh, L.W. Rupp, Jr., and W.F. Peck, Phys. Rev. B 38, 893 (1988).
  10. C.M. Lin and S.T. Lin, J. Phys. C 3, 9713 (1991).
  11. M. Micklitz, W. Zimmermann, V. Moshchalkov and L. Leonjuk, Solid State Commun 75, 995 (1990).
  12. Y. Shichi, Y. Inoue, F. Munakata and M.Yamanaka, Phys. Rev. B 42, 939 (1990).
  13. M. Tanaka, T. Tokoro and Y. Aiyama, J. Phys. Soc. Jpn. 21, 262 (1966).
  14. F. Bridges, G. Li, J.B. Boyce and T. Claeson, Phys. Rev. B 48, 1266 (1993).
  15. G.K. Shenoy and F.E. Wagner (eds), Mössbauer Isomer Shifts (North-Holland, 1978)
  16. Mark S. Hybertsen and L.F. Mattheiss, Phys. Rev. Lett. 60, 1661 (1988).



- 
17. G.K. Wertheim, J.P. Remeika, H.J. Guggenheim and D.N.E. Buchanan, Phys. Rev. Lett. 25, 94 (1970).
  18. R.M. Housley and F. Hess, Phys. Rev. 146, 517 (1966).
  19. B. Renker, F. Gompf, D. Ewert, P. Adelman, H. Schmidt, E. Gering and H. Mutka, Z. Phys. B 77, 65 (1989).
  20. C.W. Kimball, J.L. Matykiewicz, H. Lee, J. Giapintzakis, A.E. Dwight, B.D. Dunlap, J.D. Jorgensen, B.W. Veal and F.Y. Fradin, Physica C 156, 547 (1988).
  21. Th. Sinnemann, R. Job and M. Rosenberg, Phys. Rev. B 45, 4941 (1992).

TABLE 4.1

		I.S. (mm/s)	Q.S. (mm/s)	L.W. (mm/s)	Rel Area (%)
x=0.0	A	0.16(1)	1.91(2)	0.33(1)	22
	B	0.25(1)	1.42(1)	0.47(2)	62
	C	0.28(2)	0.66(1)	0.44(3)	16
x=0.2	A	0.25(1)	1.73(1)	0.26(1)	20
	B	0.28(1)	1.39(1)	0.34(1)	59
	C	0.31(1)	0.68(2)	0.52(3)	21
x=0.4	A	0.25(1)	1.74(1)	0.31(2)	21
	B	0.29(1)	1.37(1)	0.33(1)	45
	C	0.33(1)	0.75(1)	0.50(2)	34
x=0.6	A	0.25(1)	1.79(1)	0.33(1)	31
	B	0.29(1)	1.34(2)	0.32(1)	38
	C	0.32(1)	0.89(2)	0.50(3)	31

## CHAPTER 5

### Study of Sm and Co Substituted $\text{Bi}_2\text{Sr}_2\text{Ca}_1\text{Cu}_2\text{O}_{8+\delta}$ System

#### 5.1 Introduction:

A well known fact about  $\text{RECo}_5$  (RE=rare earth) compound is that there exists a strong exchange interaction between rare-earth and cobalt ions [1]. Of particular interest is the  $\text{SmCo}_5$  compound where such an exchange interaction is found to be maximum thereby leading to high value of saturation magnetization [2]. The average distance between rare-earth and Co ions in these compounds is  $3.0\text{\AA}$  [3]. This distance is comparable to the distance between Ca and Cu ions which lie in different planes of  $\text{Bi}_2\text{Sr}_2\text{Ca}_1\text{Cu}_2\text{O}_{8+\delta}$  system. In the present chapter we make a comparative study of  $\text{Bi}_2\text{Sr}_2\text{Ca}_{1-x}\text{Sm}_x\text{Cu}_2\text{O}_{8+\delta}$  and  $\text{Bi}_2\text{Sr}_2\text{Ca}_{1-x}\text{Sm}_x\text{Cu}_{1.95}\text{Co}_{0.05}\text{O}_{8+\delta}$  systems where the presence of an interplanar exchange correlation in the latter system is expected to lead to a strong suppression of superconductivity.

## Results and Discussions

### 5.2 X-ray study:

The X-ray diffraction patterns of some of the samples are shown in Fig. 5.1 and Fig. 5.2 . All the samples show a single phase behaviour consisting of  $\text{Bi}_2\text{Sr}_2\text{Ca}_1\text{Cu}_2\text{O}_{8-\delta}$  (2:2:1:2) phase. The variation of lattice parameters obtained assuming a pseudo-tetragonal cell is shown in Fig. 5.3. As observed in the case of Gd substituted systems of the previous chapters the present samples also exhibit an increase in a lattice parameter and a decrease in c lattice parameter. The slope  $\frac{dc}{dx} = -0.60$  when compared to  $\frac{dc}{dx} = -1.17$  of Gd doped samples is in agreement with the smaller ionic radii difference of  $\text{Sm}^{3+}$  (ionic radius =  $0.964\text{\AA}$ ) and  $\text{Ca}^{2+}$  (ionic radius =  $0.99\text{\AA}$ ) ions. The decrease in c lattice parameter in Gd and Sm doped samples however, is not proportional to the ionic radii difference of the ions. This is due to the fact that a large contraction would be opposed by the repulsive forces between the cationic layers.

### 5.3 Transition Temperature:

Fig. 5.4 (a and b) show the results of ac susceptibility measurements of  $\text{Bi}_2\text{Sr}_2\text{Ca}_{1-x}\text{Sm}_x\text{Cu}_2\text{O}_{8-\delta}$  (Sm samples) and  $\text{Bi}_2\text{Sr}_2\text{Ca}_{1-x}\text{Sm}_x\text{Cu}_{1.95}\text{Co}_{0.05}\text{O}_{8+\delta}$  (SmCo samples) respectively. The measurements were done on powdered samples. We notice that the superconducting transition remains sharp for lower Sm concentration but significantly broadened at higher dopant concentration indicating inhomogeneous distribution of Sm ions.

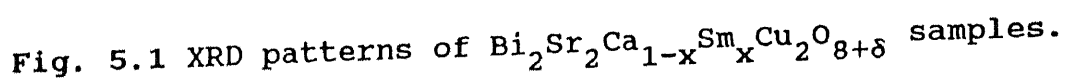


Fig. 5.1 XRD patterns of  $\text{Bi}_2\text{Sr}_2\text{Ca}_{1-x}\text{Sm}_x\text{Cu}_2\text{O}_{8+\delta}$  samples.

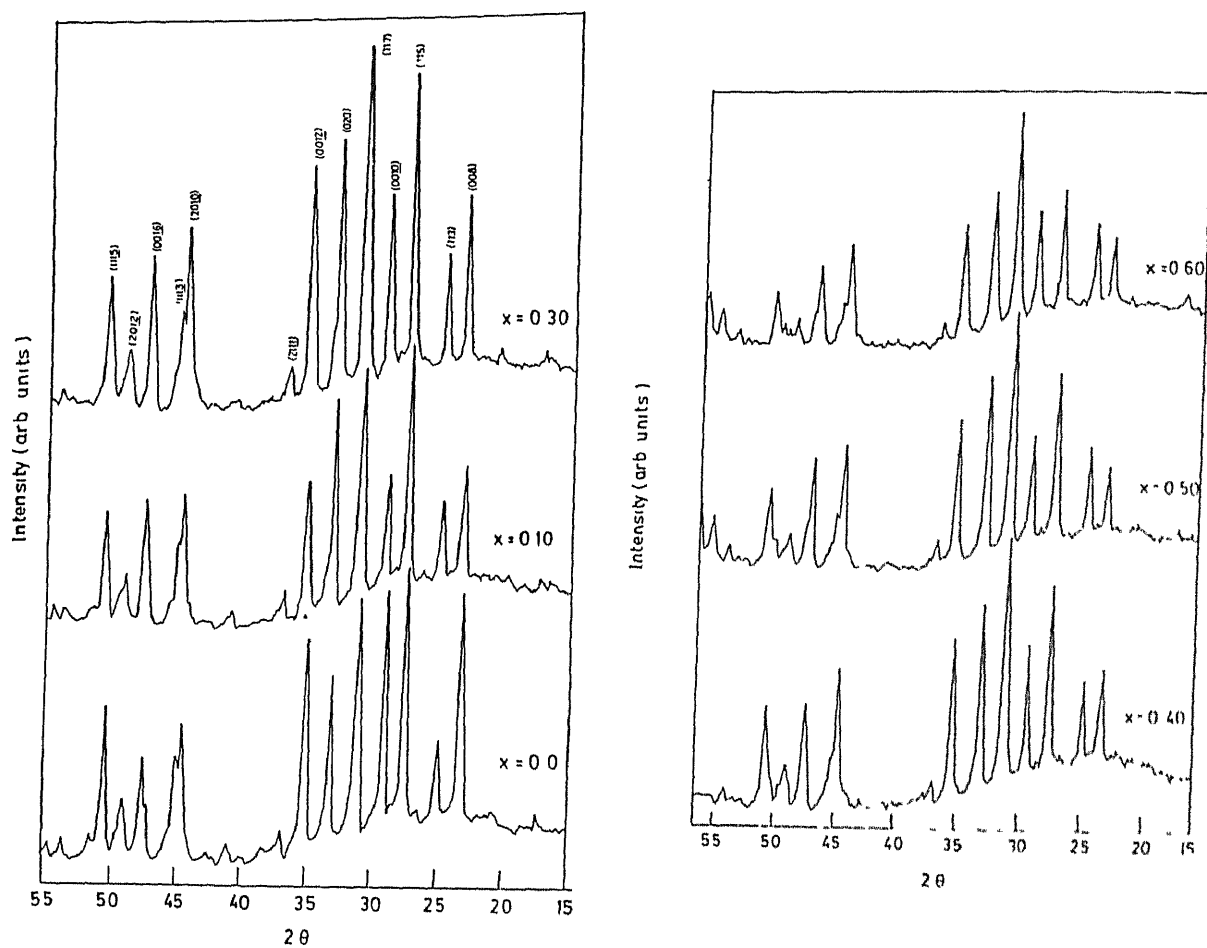


Fig. 5.2 XRD patterns of  $\text{Bi}_2\text{Sr}_2\text{Ca}_{1-x}\text{Sm}_x\text{Cu}_{1.95}\text{Co}_{0.05}\text{O}_{8+\delta}$  samples.

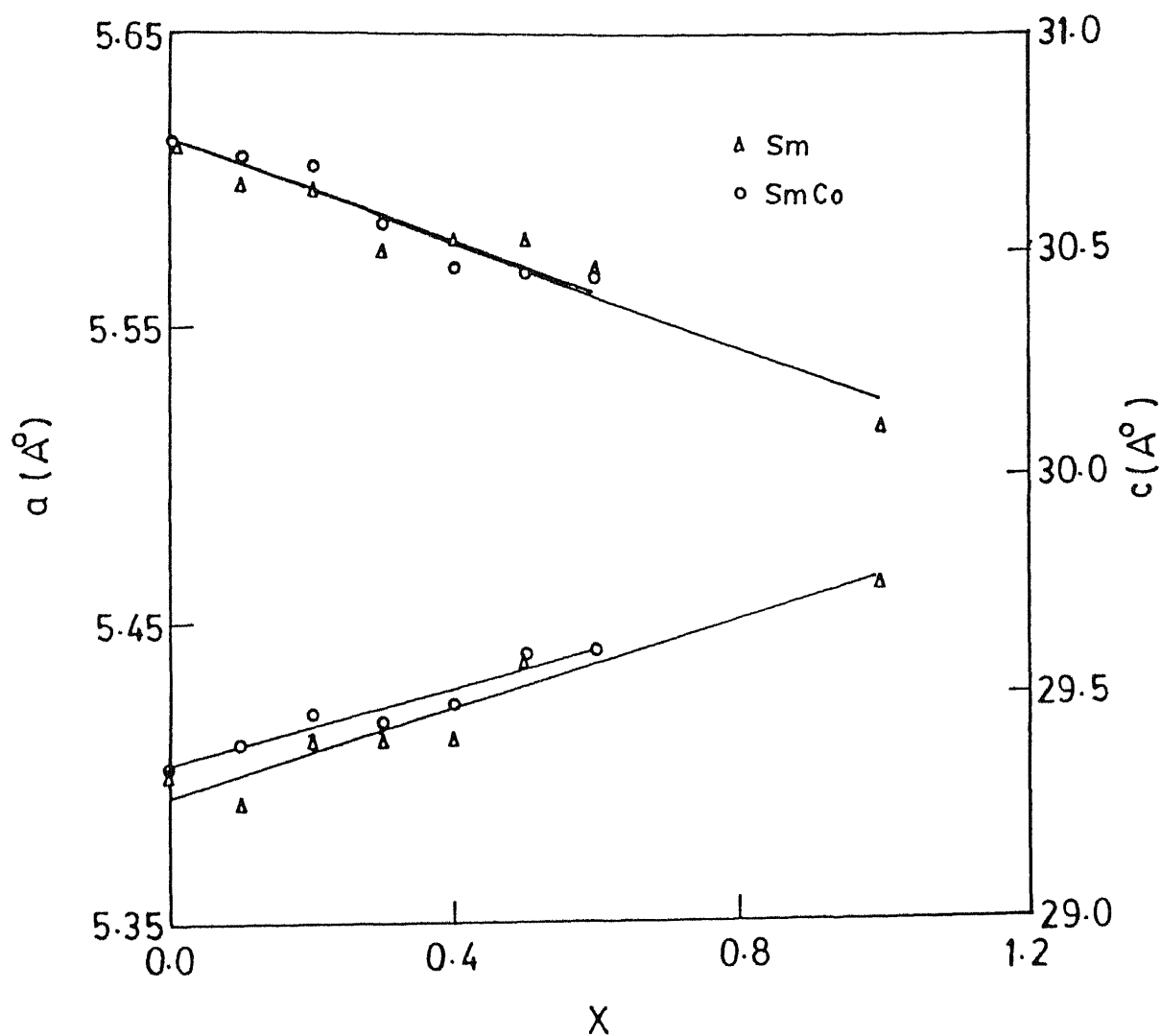


Fig. 5.3 Variation of lattice parameters  $a$  and  $c$  with Sm concentration  $x$  in  $\text{Bi}_2\text{Sr}_2\text{Ca}_{1-x}\text{Sm}_x\text{Cu}_2\text{O}_{8+\delta}$  (Sm system) and in  $\text{Bi}_2\text{Sr}_2\text{Ca}_{1-x}\text{Sm}_x\text{Cu}_{1.95}\text{Co}_{0.05}\text{O}_{8+\delta}$  (SmCo system).

The susceptibility signal measured per mg of the samples decreases with increasing values of  $x$ . Since the strength of the signal determines superconducting volume fraction, its decrease shows the decrease of superconducting volume fraction with  $x$ . In SmCo samples the susceptibility signal/mg is several times smaller than the same in Sm samples. The fact shows that small amount of Co ions in  $\text{CuO}_2$  plane has decreased superconducting volume fraction considerably.

The variation of transition temperature (defined as the onset temperature of Meissner signal) with  $x$  is shown in Fig. 5.5. In Sm samples  $T_c$  increases from 81K for  $x=0.0$  to 90K for  $x=0.2$  and then decreases with increasing  $x$ . On the other hand in SmCo samples  $T_c$  decreases from 70K for  $x=0.0$  to 64K at  $x=0.01$  and then remains constant upto  $x=0.2$ .  $T_c$  starts decreasing with further increase of  $x$  in this system. The increase of  $T_c$  in Sm samples is similar to that observed in Gd substituted samples (see Chapter 4). The increase is attributed to filling of excess holes by extra electrons provided by  $\text{Sm}^{3+}$  ions substituted for divalent  $\text{Ca}^{2+}$  ions. Surprisingly, SmCo samples do not show an increase of  $T_c$  though the samples were prepared in the same way as Sm samples. This can occur if the excess holes in this system get localized in the vicinity of impurity  $\text{Co}^{2+}$  ions in  $\text{CuO}_2$  plane.

We note from Fig. 5.5 that superconductivity vanishes for  $0.50 < x < 0.60$  in Sm samples whereas in SmCo samples it vanishes for  $0.30 < x < 0.40$ . The vanishing of superconductivity for values of  $x$  between 0.5 and 0.6 in Sm samples is identical to the Gd



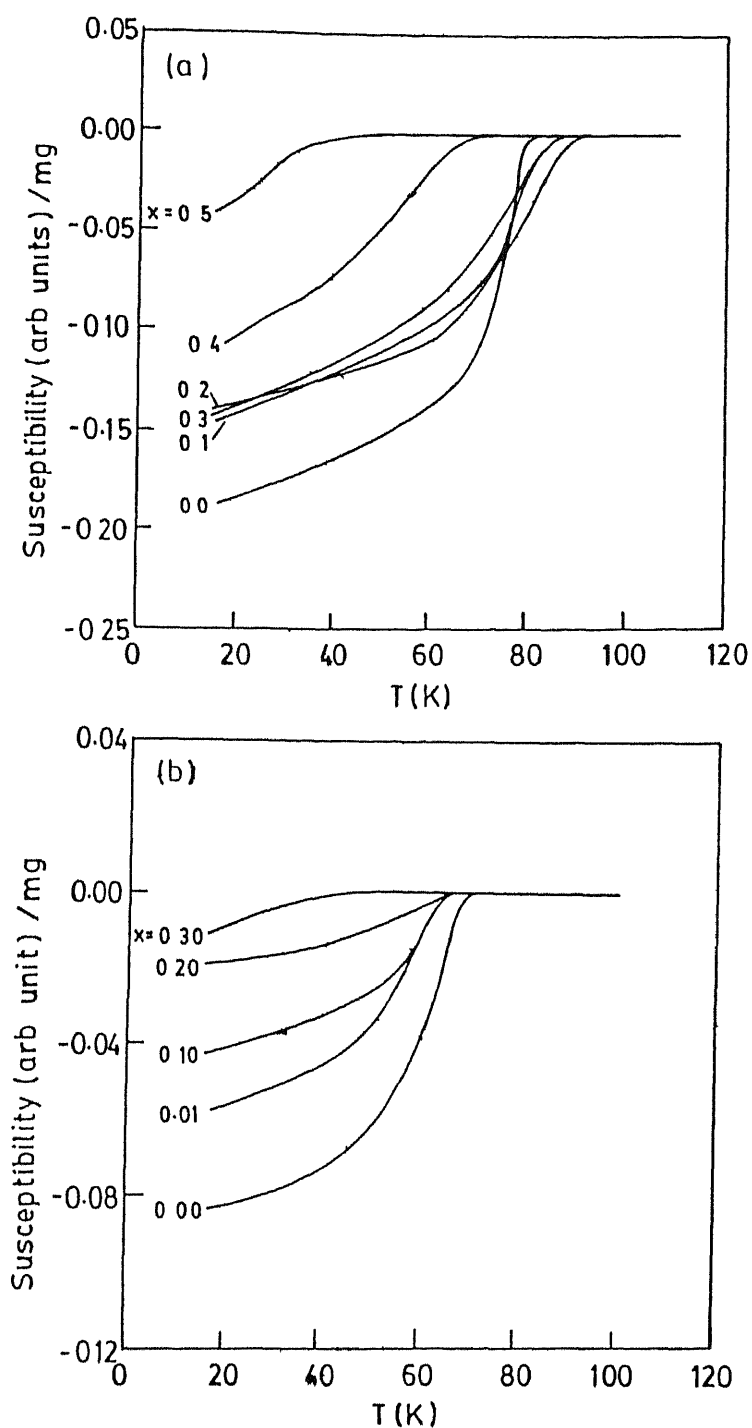


Fig. 5.4 AC susceptibility vs T of (a)  $\text{Bi}_2\text{Sr}_2\text{Ca}_{1-x}\text{Sm}_x\text{Cu}_2\text{O}_{8+\delta}$  samples and (b)  $\text{Bi}_2\text{Sr}_2\text{Ca}_{1-x}\text{Sm}_x\text{Cu}_{1.95}\text{Co}_{0.05}\text{O}_{8+\delta}$  samples.

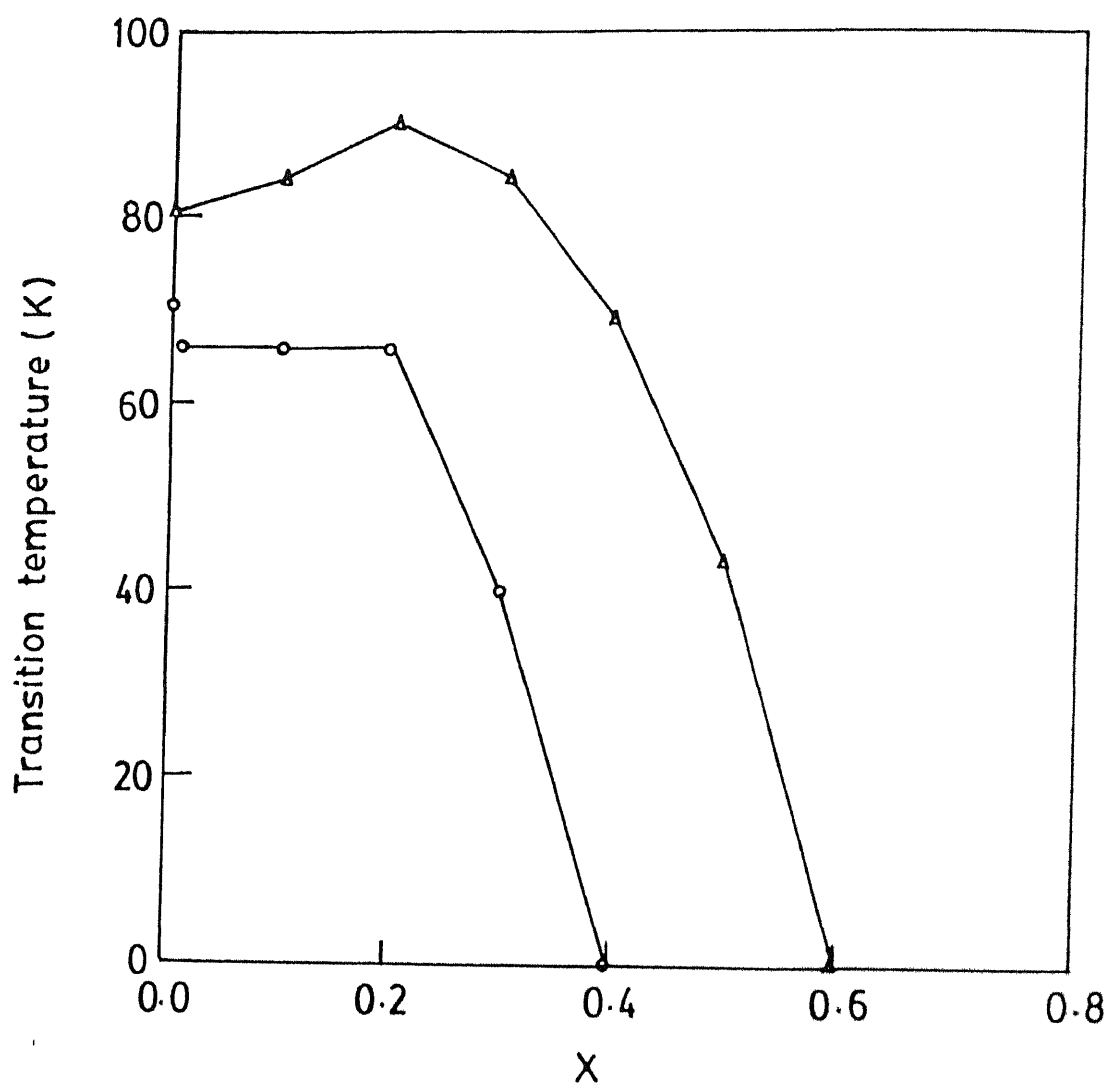


Fig. 5.5 Variation of transition temperature with Sm concentration  $x$  in  $\text{Bi}_2\text{Sr}_2\text{Ca}_{1-x}\text{Sm}_x\text{Cu}_2\text{O}_{8+\delta}$  (shown by triangles) and  $\text{Bi}_2\text{Sr}_2\text{Ca}_{1-x}\text{Sm}_x\text{Cu}_{1.95}\text{Co}_{0.05}\text{O}_{8+\delta}$  (shown by circles) systems.

doped 2:2:1:2 system. According to Abrikosov Gor'kov theory, the decrease of transition temperature due to a magnetic impurity is given by the relation [4]

$$\ln(T_c/T_{c0}) = \psi(1/2) + \psi(1/2 + \rho) \quad (5.1)$$

where  $T_{c0}$  is the transition temperature of the pure material and  $\psi$  is the digamma function. For a rare-earth impurity  $\rho$  is given as [5]

$$\rho = \frac{n_i N(E_F) j^2 (g_j - 1)^2 J(J+1)}{2kT_c} \quad (5.2)$$

where  $n_i$  is the number density of impurities,  $N(E_F)$  is the density of states at Fermi level,  $j$  is the exchange parameter,  $g_j$  is the Landé  $g$  factor and  $(g_j - 1)^2 J(J+1)$  ( $=\mu_j$ , say) is the de Gennes factor. It is obvious that for the same amount of rare earth impurity concentration, the decrease in transition temperature depends on  $\mu_j$ . The calculated values of  $\mu_j$  for  $\text{Sm}^{3+}$  and  $\text{Gd}^{3+}$  ions are 4.5 and 15.8  $\mu_B^2$  respectively. Despite the large difference of de Gennes factors of  $\text{Sm}^{3+}$  and  $\text{Gd}^{3+}$  ions, the superconductivity disappears in the same domain of  $x$  for both rare earth impurities. Since Abrikosov Gor'kov theory assumes s-state orbital angular momentum of the pairs, the above experimental fact may suggest non s-wave pairing in  $\text{Bi}_2\text{Sr}_2\text{Ca}_1\text{Cu}_2\text{O}_{8+\delta}$  system.

An important observation of  $T_c$  vs  $x$  curve of SmCo samples is that with increasing Sm concentration no rapid decrease in

$T_C$  is observed. Also the trend of decrease of  $T_C$  beyond  $x=0.20$  in SmCo sample is identical to that of Sm samples. This shows a negligible interplanar magnetic interaction in SmCo samples and suppression of  $T_C$  in both the systems is due to identical reasons. We must mention that in Fe substituted  $Gd_1Ba_2Cu_3O_{7-\delta}$  (1:2:3) system a decrease of  $T_C$  is observed upon quenching whereas similar Fe substituted  $Y_1Ba_2Cu_3O_{7-\delta}$  system shows an increase of  $T_C$  [6]. The quenching causes an increased Fe occupation on Cu(2)-plane sites in 1:2:3 system. The decrease of  $T_C$  in Gd 1:2:3 has been attributed to strong interplanar magnetic interaction [7]. The absence of such an interaction in SmCo system reflects higher anisotropic character of  $Bi_2Sr_2Ca_1Cu_2O_{8+\delta}$  system than  $Y_1Ba_2Cu_3O_{7-\delta}$  system.

#### 5.4 Resistivity Data:

The temperature dependence of resistivities of  $Bi_2Sr_2Ca_{1-x}Sm_xCu_2O_{8-\delta}$  (Sm samples) and  $Bi_2Sr_2Ca_{1-x}Sm_xCu_{1.95}Co_{0.05}O_{8+\delta}$  (SmCo samples) which show superconductivity is shown in Fig. 5.6(a and b). It is clear that Sm concentration affects transition width, increases normal state resistivity and residual resistivity.

The normal state resistivity ( $\rho_n$ ) as a function of Sm concentration ( $x$ ) is plotted in Fig. 5.7. Here  $\rho_n$  is defined as the resistivity value measured at 300K. Beyond  $x=0.40$  the  $\rho_n$  of SmCo samples increases much faster than Sm samples indicating that the system enters into insulating state rapidly with  $x$ . Following the arguments of chapter (4) this shows that SmCo

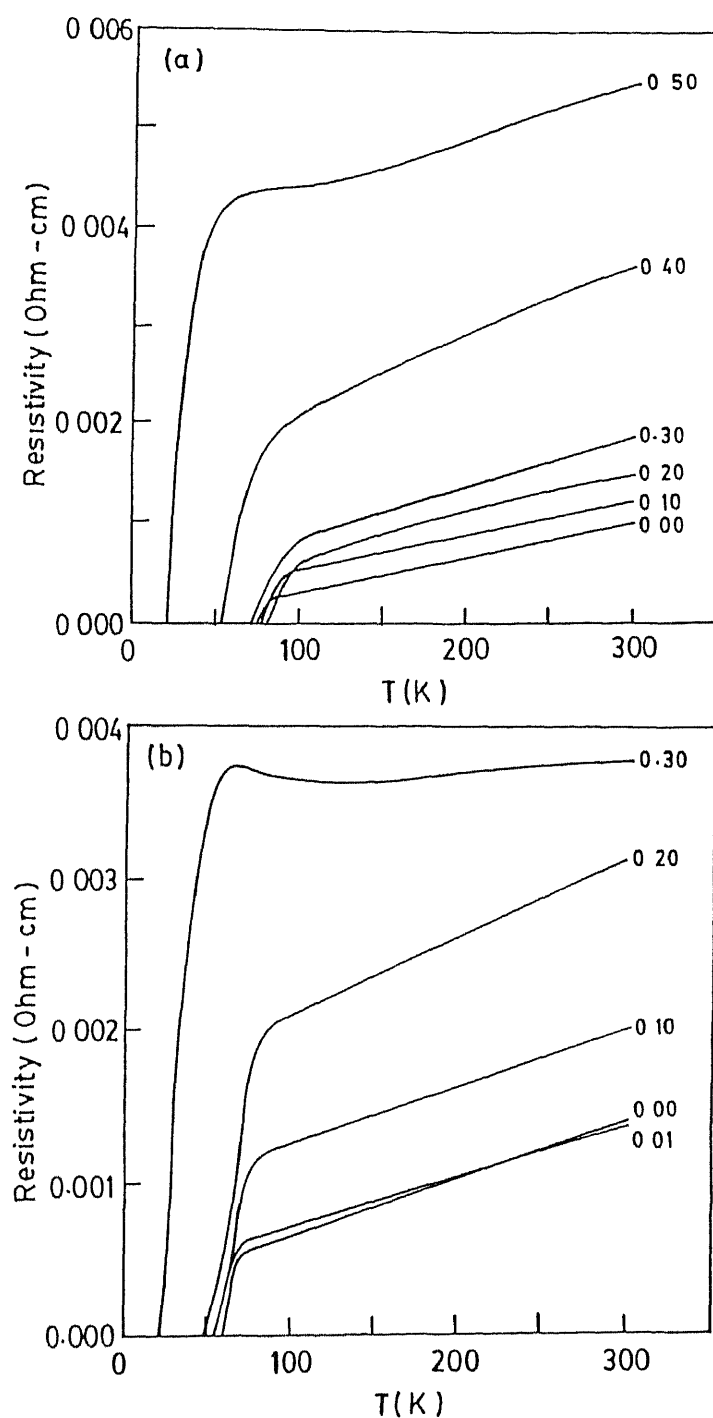


**Fig. 5.6** Temperature dependence of electrical resistivity of superconducting (a)  $\text{Bi}_2\text{Sr}_2\text{Ca}_{1-x}\text{Sm}_x\text{Cu}_2\text{O}_{8+\delta}$  samples and (b)  $\text{Bi}_2\text{Sr}_2\text{Ca}_{1-x}\text{Sm}_x\text{Cu}_{1.95}\text{Co}_{0.05}\text{O}_{8+\delta}$  samples.

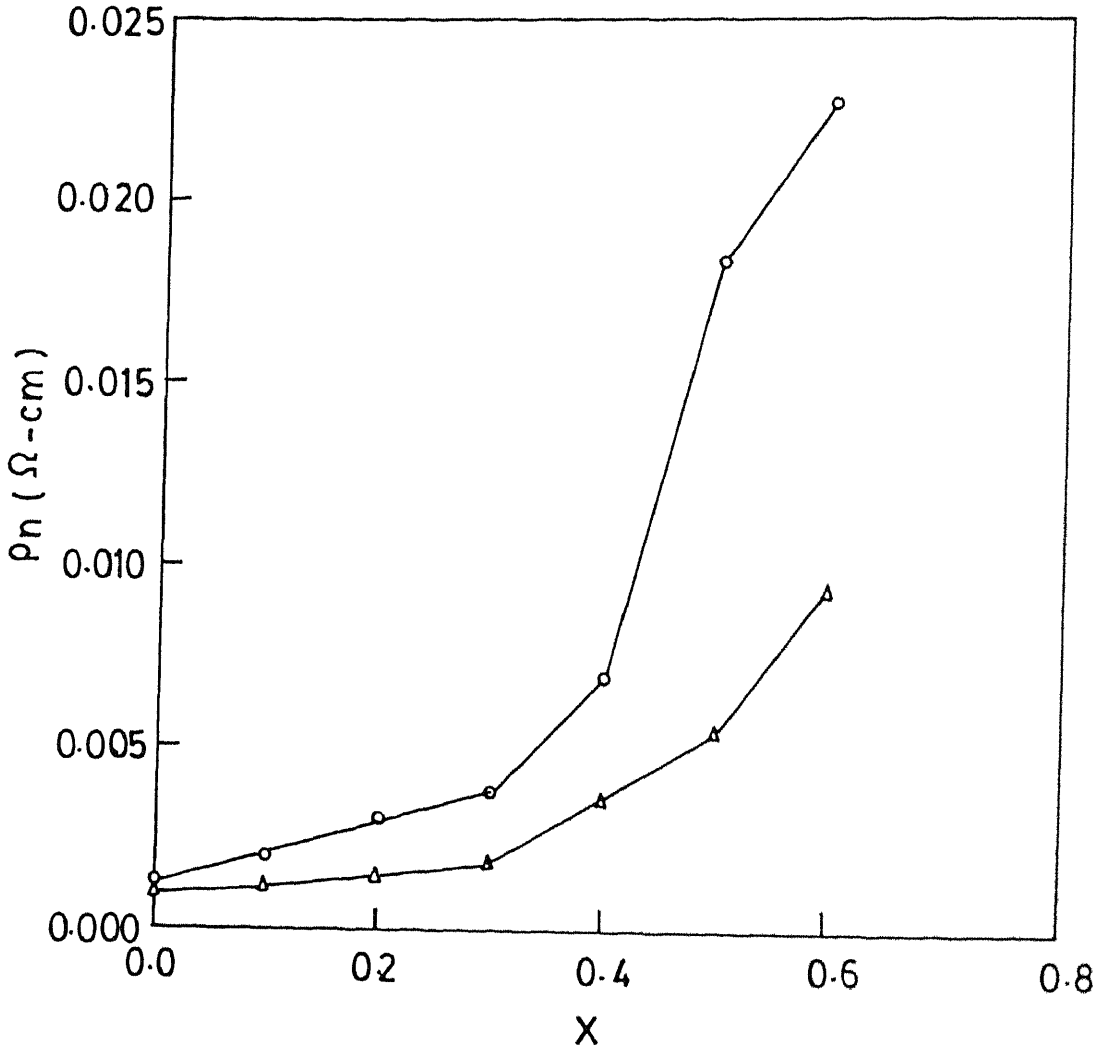


**Fig. 5.7** Room temperature resistivity ( $\rho_n$ ) vs Sm concentration  $x$  in  $\text{Bi}_2\text{Sr}_2\text{Ca}_{1-x}\text{Sm}_x\text{Cu}_2\text{O}_{8+\delta}$  (shown by triangles) and  $\text{Bi}_2\text{Sr}_2\text{Ca}_{1-x}\text{Sm}_x\text{Cu}_{1.95}\text{Co}_{0.05}\text{O}_{8+\delta}$  (shown by circles) systems.

samples have higher amount of disorder than Sm samples.

The variation of residual resistivity ( $\rho_0$ ) with  $x$  is shown in Fig. 5.8.  $\rho_0$  is obtained by fitting a straight line in the linear portion of normal state resistivity of superconducting samples. Residual resistivity arises due to impurity scattering in  $\text{CuO}_2$  plane. The higher values of  $\rho_0$  in SmCo samples therefore is in line with the presence of higher amount of impurity content in SmCo samples than in Sm samples.

In Fig. 5.9 we have shown the low temperature magnetoresistance measurement of SmCo  $x=0.4$  sample lying close to metal insulator transition regime. A positive magnetoresistance below 26K is observed in presence of a magnetic field of 3.5kG. At the lowest temperature of 14K measured by us applied field resistivity increases by 2% from the value when  $B=0$ . The low temperature resistivities of Sm  $x=0.60$  and SmCo  $x=0.50$  samples on the other hand remained invariant in presence of magnetic field.

According to the theory of localization and electron-electron interaction in a disordered system, a magnetic field produces various magnetoresistance behaviours [8]. The magnetoresistance of weak localization effect is negative because of suppression of coherent back scattering. On the contrary, both particle-hole diffusion channel and particle-particle channel of interaction term lead to a positive magnetoresistance. In particle-hole diffusion channel, interaction between electrons of nearly equal momenta are considered whereas in particle-particle channel, electrons of

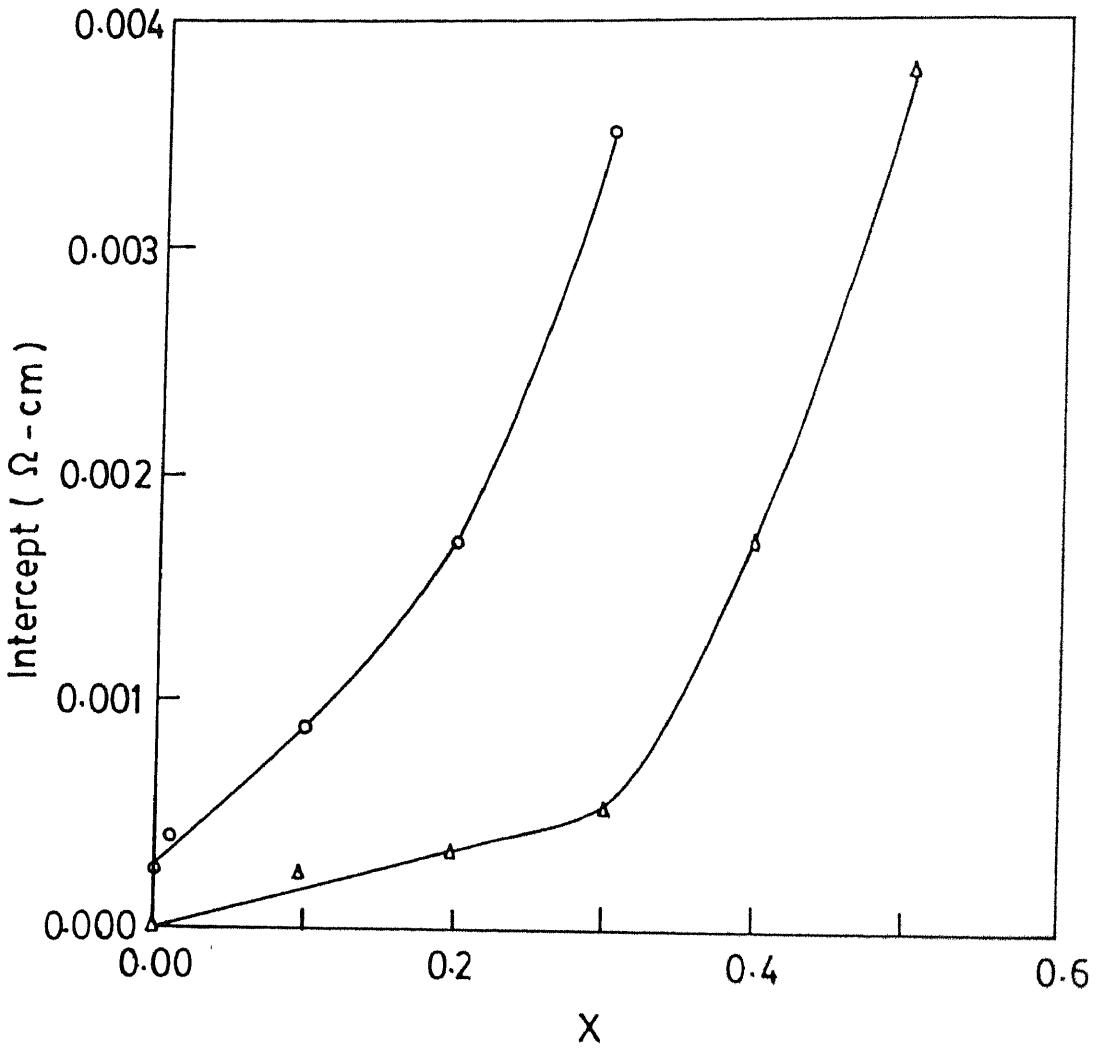


Fig. 5.8 Dependence of residual resistivity on Sm concentration  $x$  in  $\text{Bi}_2\text{Sr}_2\text{Ca}_{1-x}\text{Sm}_x\text{Cu}_2\text{O}_{8+\delta}$  (shown by triangles) and  $\text{Bi}_2\text{Sr}_2\text{Ca}_{1-x}\text{Sm}_x\text{Cu}_{1.95}\text{Co}_{0.05}\text{O}_{8+\delta}$  (shown by circles) systems.



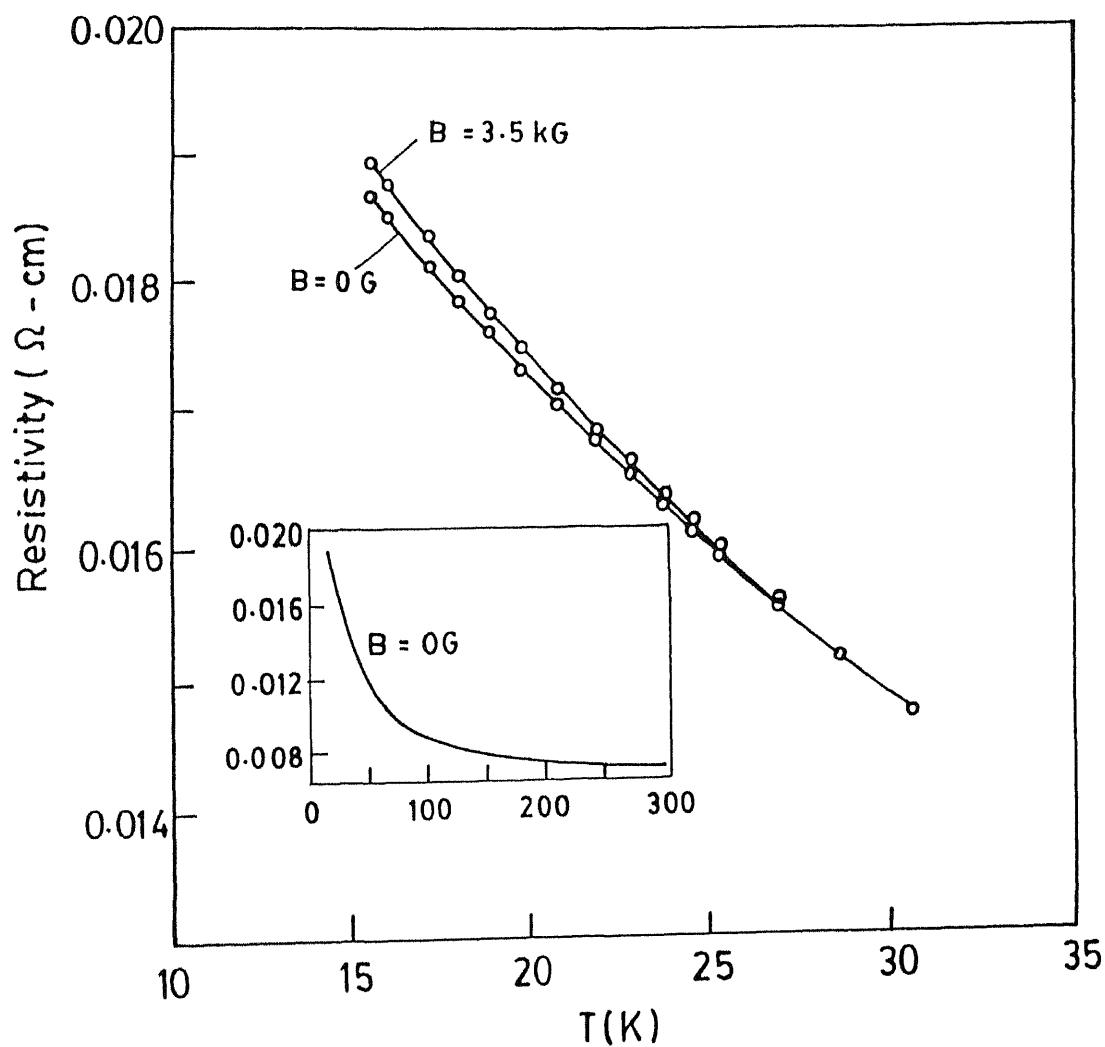


Fig. 5.9 Temperature dependence of magnetoresistivity of  $\text{Bi}_2\text{Sr}_2\text{Ca}_{0.6}\text{Sm}_{0.4}\text{Cu}_{1.95}\text{Co}_{0.05}\text{O}_{8+\delta}$  sample at low temperatures. The inset shows  $\rho$ - $T$  curve in zero field.

posite momenta are considered. The positive magnetoresistance particle-hole diffusion channel arises due to suppression of the direct channel from Zeeman splitting. The characteristic field where the Zeeman effect to play a role is described by  $g\mu_B B > kT$ . A similar condition applies to particle-particle channel of interaction term. Evidently, for interaction term to be effective in our case, the required magnetic field should exceed 15T. The single particle antilocalization in presence of strong spin-orbit scattering also leads to a positive magnetoresistance [9]. The plausibility of this mechanism lends support from strong spin-orbit scattering characteristic of  $\text{SmCo}_2$ . However, in this case the theory predicts a logarithmic increase of resistivity with decreasing temperature which is in agreement with our data.

Another possible mechanism which could give rise to magnetoresistance is the scattering of electrons by localized spins of Co ions. An applied magnetic field tends to align the localized spins parallel to the field and increases the energy cost of flipping them. In such a case a negative magnetoresistance is observed as the probability of an electron undergoing spin scattering with the localized spin is reduced [10]. It is clear that none of the mechanisms described above explain the positive magnetoresistance observed in  $\text{SmCo}_{0.6}\text{Fe}_{0.4}$  sample.

Fig. 5.10 and Fig. 5.11 show the results of magnetoresistance measurements for  $\text{SmCo}_{0.6}\text{Fe}_{0.4}$  sample annealed in presence of flowing oxygen at 600°C and 700°C respectively.

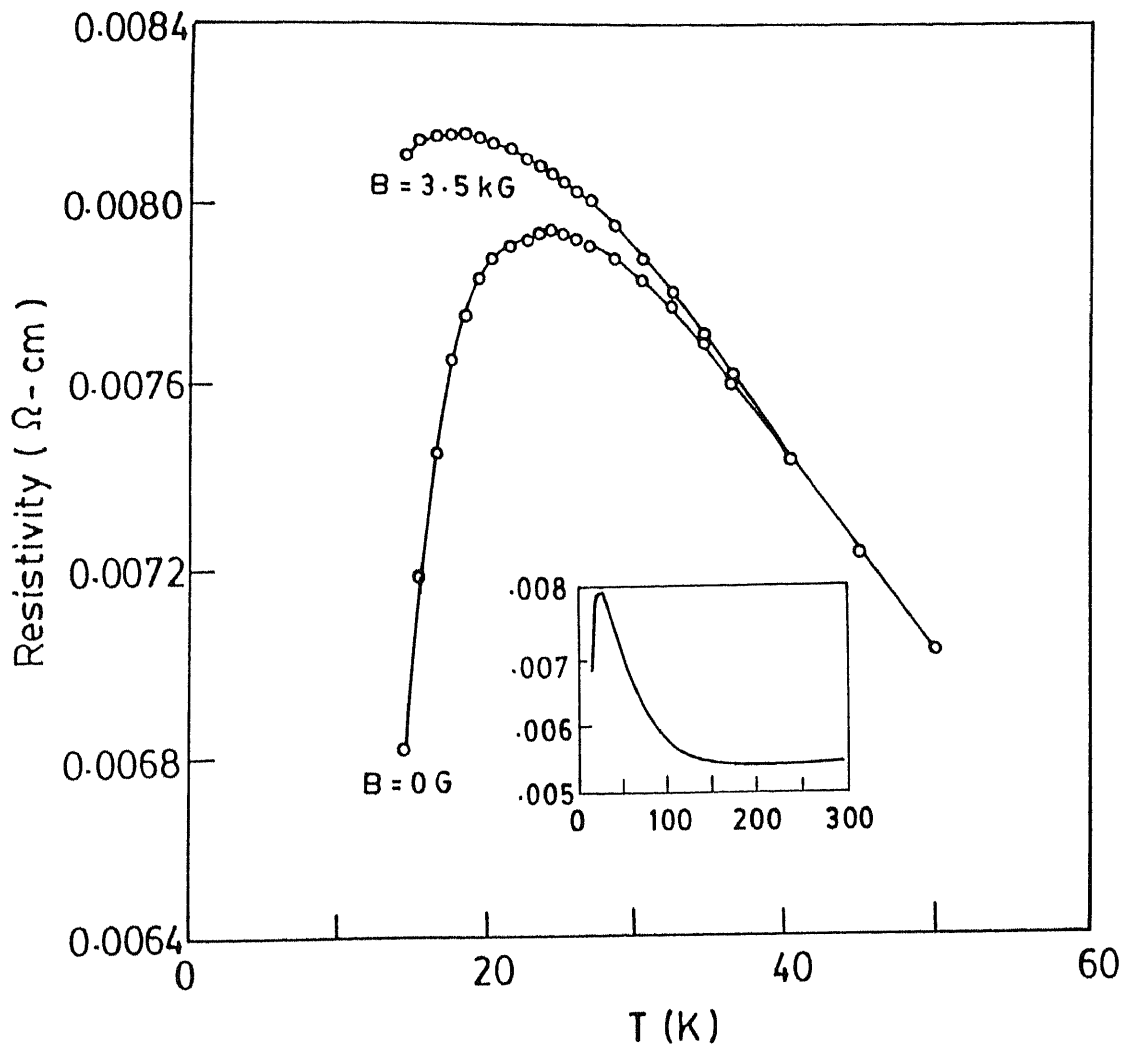
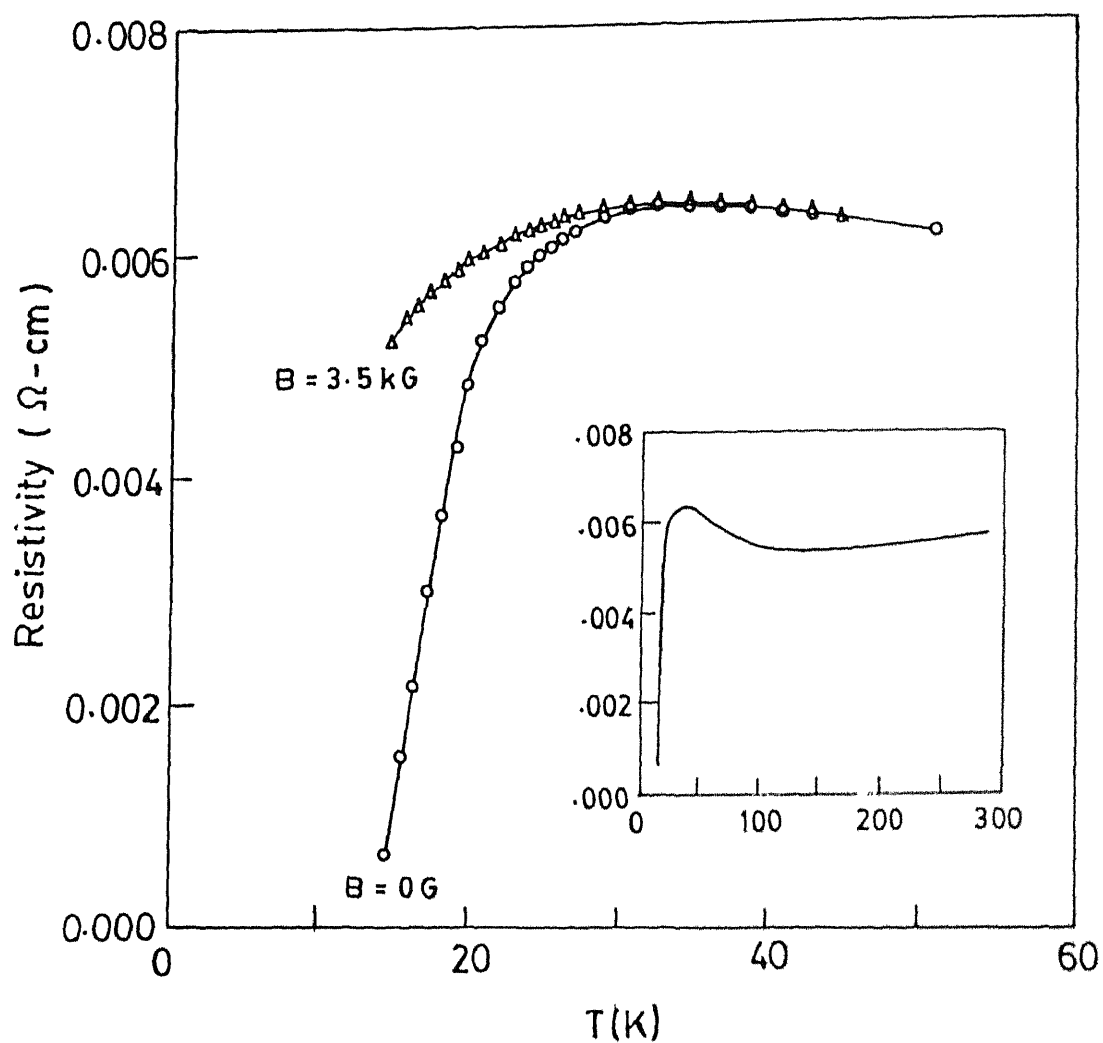


Fig. 5.10 Temperature dependence of magnetoresistivity of  $\text{Bi}_2\text{Sr}_2\text{Ca}_{0.6}\text{Sm}_{0.4}\text{Cu}_{1.95}\text{Co}_{0.05}\text{O}_{8+\delta}$  sample (annealed at  $600^\circ\text{C}$  in flowing oxygen) at low temperatures. The inset shows  $\rho$ -T curve in zero field.



**Fig. 5.11** Temperature dependence of magnetoresistivity of  $\text{Bi}_2\text{Sr}_2\text{Ca}_{0.6}\text{Sm}_{0.4}\text{Cu}_{1.95}\text{Co}_{0.05}\text{O}_{8+\delta}$  sample (annealed at  $700^\circ\text{C}$  in flowing oxygen) at low temperatures. The inset shows  $\rho$ - $T$  curve in zero field.

From the comparative values of resistivity it is evident that the annealing in presence of oxygen brings the systems towards metallic side. The annealing at 800°C in oxygen is found to show the reverse effect as the resistivity follows insulating behaviour.

We notice from Fig. 5.10, the oxygenation leads to the onset of superconducting transition at low temperature in absence of a magnetic field. The application of a magnetic field shows an unusual trend of  $\rho$ -T curve in Fig. 5.10. The resistivity increases to a maximum value and then tends to drop with temperature implying the onset of superconductivity. Similar maxima in magnetoresistivity has been observed in single crystal 2:2:1:2 system with magnetic field perpendicular to  $\text{CuO}_2$  plane [11,12]. These studies report the occurrence of giant resistive maxima either for out of plane magnetoresistance in as prepared 2:2:1:2 crystal or in-plane magnetoresistance at high fields ( $B \geq 3\text{T}$ ) in oxygen reduced crystals. A Lorentz force independent fluctuation induced dissipation in ref [11] and a non rigid vortex motion coupling the out of plane and in plane dissipations at pinning free temperatures in ref [12] were considered to be responsible for magnetoresistivity maxima. To examine the possibility of magnetoresistance maxima occurring due to above proposed mechanisms, we annealed  $\text{SmCo } x=0.30$  sample which is well on the metallic side under similar annealing conditions of  $\text{SmCo } x=0.40$  sample. The results of  $\text{SmCo } x=0.30$  sample are shown in Fig. 6.12. No resistivity maxima was observed in magnetic field and

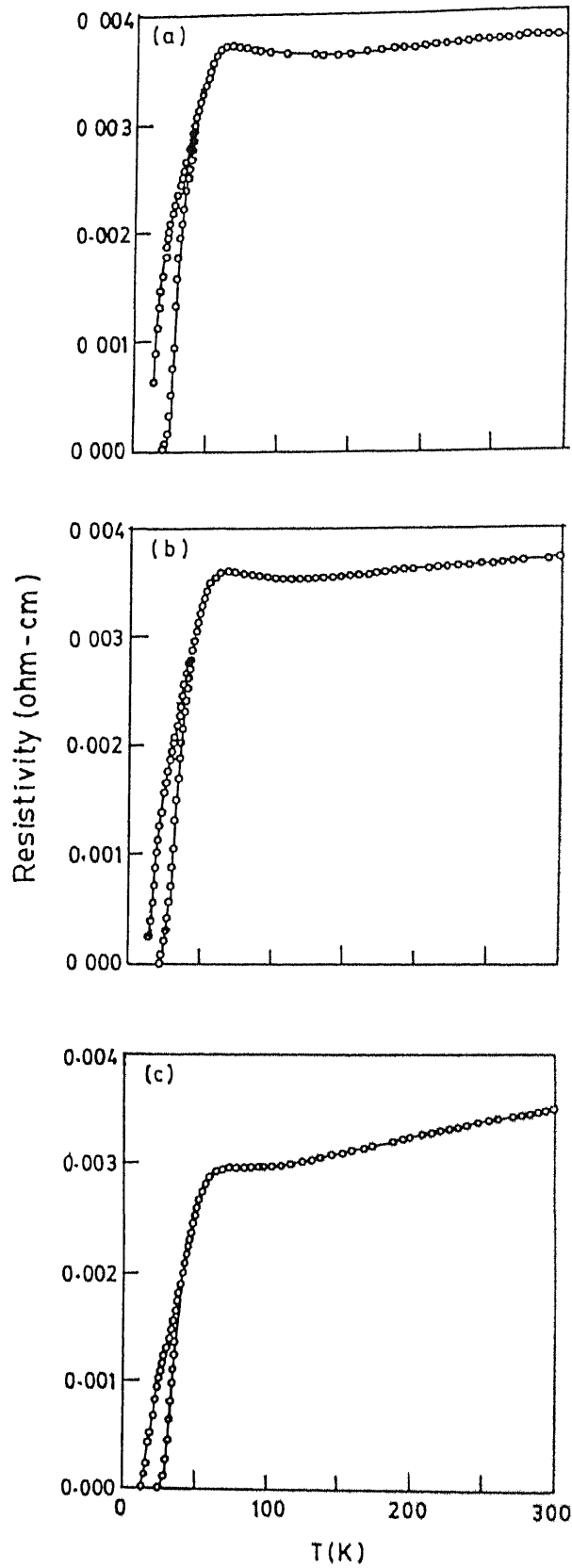


**Fig. 5.12** Temperature dependence of magnetoresistivity of  $\text{Bi}_2\text{Sr}_2\text{Ca}_{0.7}\text{Sm}_{0.3}\text{Cu}_{1.95}\text{Co}_{0.05}\text{O}_{8+\delta}$  sample (a) as prepared (b) and (c) annealed at 600°C and 700°C in flowing oxygen respectively.

the sample showed usual resistive transition broadening as observed in in-plane magnetoresistance of as prepared 2:2:1:2 crystal. Moreover, as we see from Fig. 5.11 the increase in resistivity in applied magnetic field disappears with the annealing of SmCo  $x=0.40$  sample at  $700^{\circ}\text{C}$  in oxygen. As discussed earlier annealing at this temperature drives the system more towards the metallic side.

The occurrence of positive magnetoresistance can be explained if we consider the formation of local magnetic moments on Cu spins close to the Co impurity in  $\text{CuO}_2$  plane. It has been shown that in a disordered metal the local moments lock themselves weakly into singlets in a zero field. The application of a magnetic field polarizes the spins giving rise to increased scattering and hence positive magnetoresistance [13]. The observed effect of magnetoresistivity maxima in the present system is due to competition between enhanced spin scattering in magnetic field and superconductivity. The effect seems to occur only for certain values of disorder as in the case of Si:P [13] close to metal insulator transition point.

The local moment formation does not necessarily lead to indicate the dominant mechanism for suppression superconductivity in SmCo systems as due to pair breaking inelastic scattering by moments. The hole filling by extra electron of  $\text{Sm}^{3+}$ , sudden increase in normal state resistivity, increase of residual resistivity and appearance of resistivity minima (which is a signature of incipient localization) in the resistivity curves of Sm  $x=0.50$  and SmCo  $x=0.30$  show that hole

filling and disorder effects as the dominant mechanism of suppression of superconductivity. However magnetoresistance results may suggest pair breaking scattering as the most probable mechanism for suppression of superconductivity in  $\text{Bi}_2\text{Sr}_2\text{Ca}_1\text{Cu}_{1-x}\text{Co}_x\text{O}_{8+\delta}$  system. This favours the mechanism proposed in ref [14] for the disappearance of superconductivity in Fe, Ni and Zn doped in  $\text{CuO}_2$  plane of 2:2:1:2 system.

The resistivity curves of the samples in the insulating state are shown in Fig. 5.13. The behaviour is similar to that has been observed in Gd doped 2:2:1:2 system. In the insulating state Fermi energy lies in the region of localized states which results in the phonon assisted variable range hopping (VRH) of conduction mechanism. For the sake of completeness we rewrite some of the required expressions of chapter (4). The VRH conductivity is given as

$$\sigma = \sigma_0 \exp\left(-\frac{T_0}{T}\right)^{\frac{1}{n+1}} \quad (5.3)$$

The characteristic temperature  $T_0$  is related to density of states  $N(E_F)$  at  $E_F$  as

$$T_0 = \frac{16\alpha^3}{kN(E_F)} \quad (5.4)$$

where  $\alpha^{-1}$  is the localization length. The least square fitting of  $\ln(\sigma)$  vs  $(T)^{-1/n}$  for  $n=2, 3$  and  $4$  in the present samples showed best fitting for  $n=4$ . In Fig. 5.14(a) we have shown  $\ln(\sigma)$  vs  $(T)^{-1/4}$  curves for two samples: Sm  $x=0.6$  and SmCo



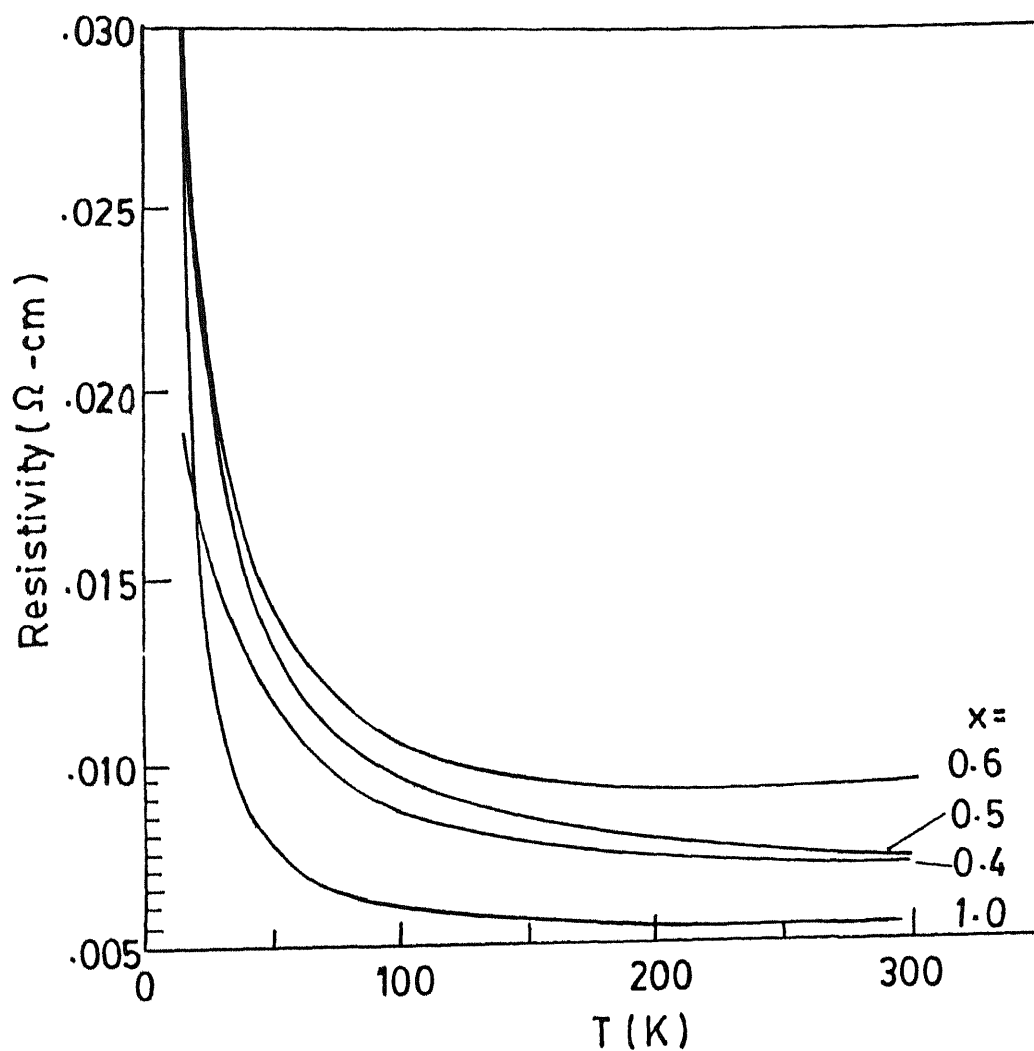
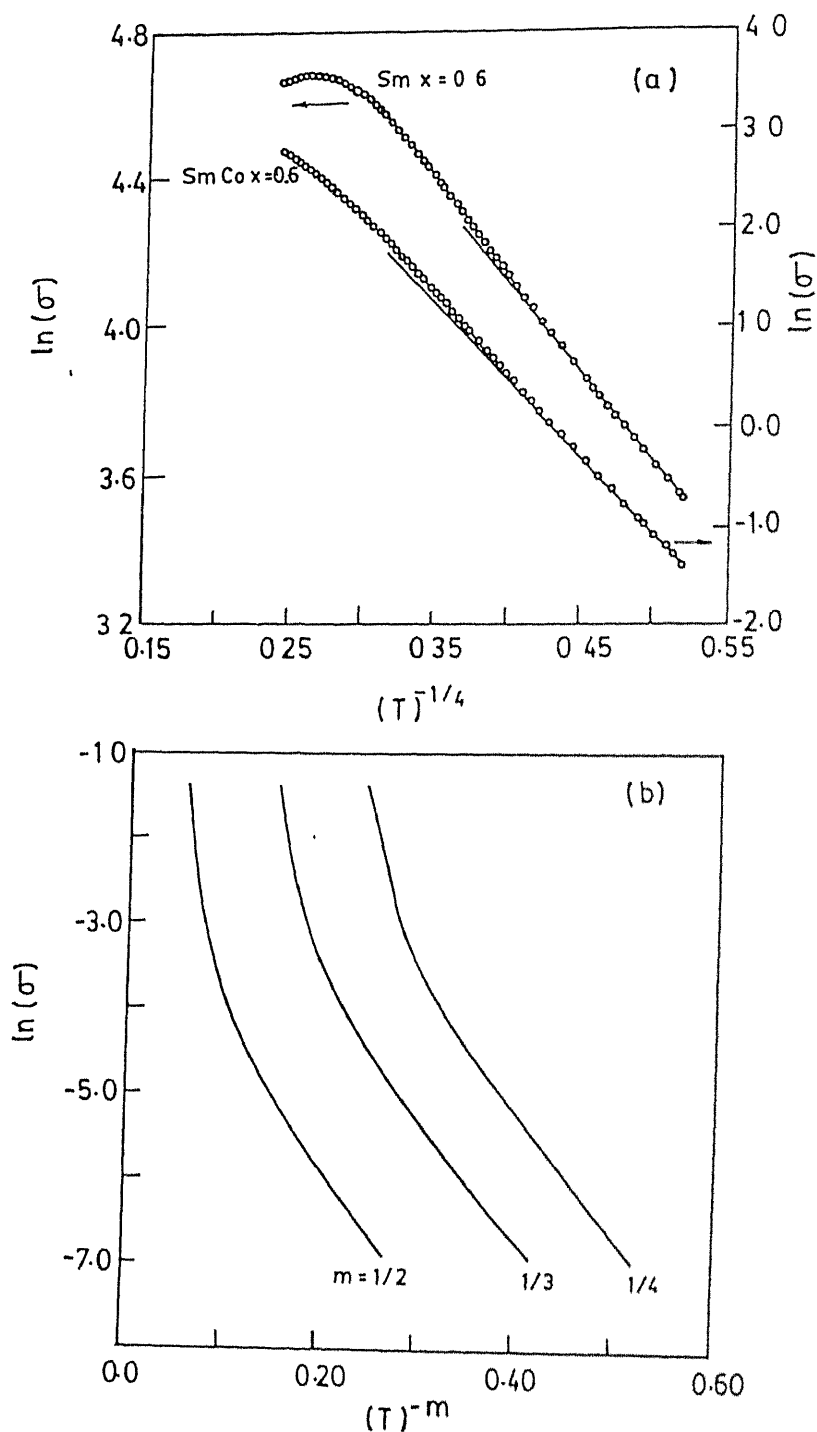


Fig. 5.13  $\rho$ - $T$  curves of Sm  $x=0.6$ , 1.0 and SmCo  $x=0.4$  (annealed at  $800^\circ\text{C}$  in oxygen), 0.5 samples. The current scale is for Sm  $x=0.6$  and SmCo  $x=0.4$  samples. For SmCo  $x=0.5$  and Sm  $x=1.0$  samples one small division is equal to 0.005 and 0.50 ohm-cm respectively.



**Fig. 5.14** (a)  $\ln(\sigma)$  vs  $(T)^{-1/4}$  plot for  $\text{Sm } x = 0.6$  and  $\text{SmCo } x = 0.6$  samples. (b)  $\ln(\sigma)$  vs  $(T)^{-m}$  plot of  $\text{Sm } x = 1.0$  sample for various values of exponent  $m$ .

$x=0.6$ . Fig. 5.14(b) shows  $\ln(\sigma)$  vs  $(T)^{-m}$  curves for Sm  $x=1.0$  sample for values of  $m=1/2$ ,  $1/3$  and  $1/4$ . It is evident that  $m=1/4$  yields a better fitting. Except in the case of Sm  $x=1.0$  a kink appears at around 30-35K in all the samples similar to that observed in Gd doped samples. In all these samples we found Ortuno and Pollak model (see section 3.6.3) best describing our data. The model has the special feature that density of states near  $E_F$  is concave in nature giving rise to discontinuity in  $\ln(\sigma)$  vs  $(T)^{-1/4}$  curve at low temperature. In Sm  $x=1.0$  sample probably the discontinuity appears at low temperature and hence was not observed.

We next calculate various VRH parameters for the samples. The hopping distance  $R$  of an electron from an initial occupied state to the final unoccupied state is given as

$$R = \left[ \frac{3}{2\pi\alpha N(E_F) kT} \right]^{\frac{1}{4}} \quad (5.5)$$

The activation energy which is the energy required for hopping of an electron from one site to another is expressed as

$$W = \frac{3}{4\pi R^3 N(E_F)} \quad (5.6)$$

It is evident that both  $R$  and  $W$  are temperature dependent quantities.

The VRH parameters for different samples are presented in Table 5.1. Density of states at Fermi energy was taken  $N(E_F)=10$  states/ev/cell [15] and was assumed constant as

varied. In the table we have included VRH parameters of Gd doped samples also. We notice that localization length tends to diverge as we approach metallic side from the insulating side. With increase of  $x$  localization length decreases in accordance with the fact that disorder increases and states near  $E_F$  become more localized. The divergence of localization length and the existence of  $(T)^{-1/4}$  behaviour of conductivity rather than  $(T)^{-1/2}$  behaviour which stands for strong Coulomb correlation indicate towards Anderson type metal-insulator transition in rare-earth doped 2:2:1:2 system.

In Anderson model [16,17] both localized and non-localized states coexist in the same band. Localized states are formed at the band tails due to disorder whereas the states in the center of the band remain extended for a moderately disordered system. The critical energy which separates localized and non-localized states is called mobility edge. Metallic conduction occurs when the Fermi energy lies in the region of non-localized states. Thus the transition from metallic state to insulating state occurs when Fermi level moves from region of non-localized states to that of localized states beyond the mobility edge. The Fermi level moves as a result of depletion of carriers caused by doping of rare-earth ions in 2:2:1:2 system [18].

### 5.5 Mossbauer Study:

Mössbauer study was carried out on  $\text{Bi}_2\text{Sr}_2\text{Ca}_{0.99}\text{Sm}_{0.01}\text{Cu}_{1.95}\text{Fe}_{0.05}\text{O}_{8+\delta}$  sample. AC susceptibility measurement showed transition temperature of this sample as

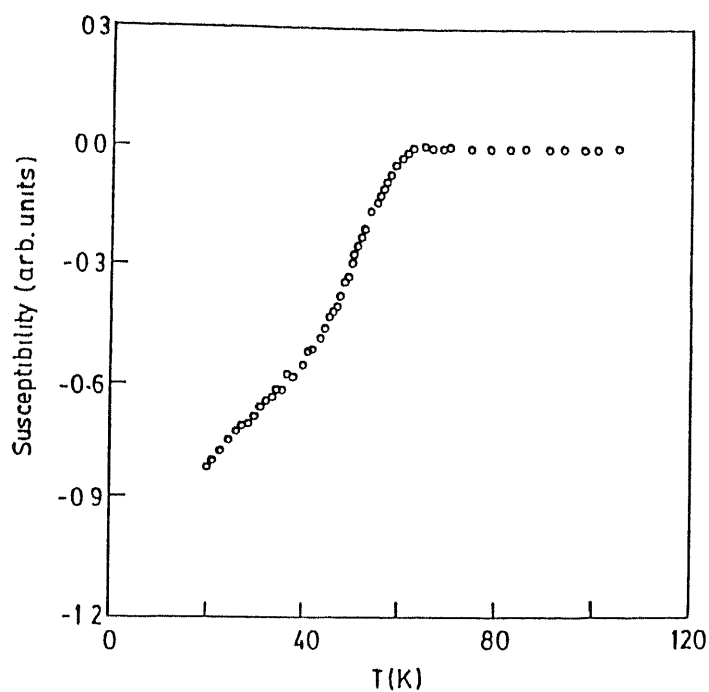


Fig. 5.15 Temperature dependence of susceptibility of  $x=0.01$   $\text{Bi}_2\text{Sr}_2\text{Ca}_{1-x}\text{Sm}_x\text{Cu}_{1.95}\text{Fe}_{0.05}\text{O}_{8+\delta}$ .

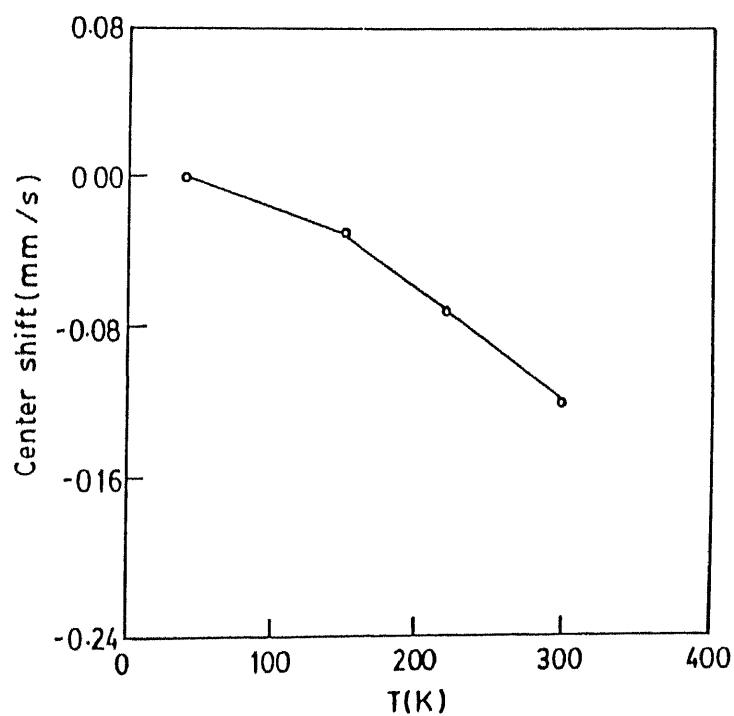


Fig. 5.16 Temperature variation of center shift of  $x=0.01$   $\text{Bi}_2\text{Sr}_2\text{Ca}_{1-x}\text{Sm}_x\text{Cu}_{1.95}\text{Fe}_{0.05}\text{O}_{8+\delta}$ .

63K. The susceptibility curve is shown in Fig. 5.15. The sharp transition shows that impurity ions are distributed homogeneously in this sample.

The room temperature Mossbauer spectrum of the sample consists of three pairs of doublets. The Mossbauer parameters isomer shift (I.S.), quadrupole splitting (Q.S.), line width (L.W.) and relative area (rel. area) are presented in Table 5.2. The parameters are found to be nearly same as that of only Fe doped 2:2:1:2 system. This shows that relatively small amount of Sm substitution has hardly affected the microstructure of this system.

The temperature dependence of Mossbauer parameters of the sample did not show an anomaly below the transition temperature. Quadrupole splitting was found to be same above and below the transition temperature. Like the Gd doped systems of the previous chapter, temperature dependence of isomer shift, as shown in Fig. 5.15, is well described by Debye model of the solids. The fitting yields the Debye temperature of this system as  $430 \pm 15$  K. The behaviour of the temperature dependence of Mossbauer parameters follow the same trend as in Gd substituted 2:2:1:2 system.

## 5.6 Conclusions:

Single phase  $\text{Bi}_2\text{Sr}_2\text{Ca}_{1-x}\text{Sm}_x\text{Cu}_2\text{O}_{8+\delta}$  (Sm system) and  $\text{Bi}_2\text{Sr}_2\text{Ca}_{1-x}\text{Sm}_x\text{Cu}_{1.95}\text{Co}_{0.05}\text{O}_{8+\delta}$  (SmCo system) have been synthesized. AC susceptibility measurements have shown systematic decrease of superconducting volume fraction with

increasing Sm concentration in both the systems. The former system reveals a parabolic dependence of  $T_c$  on Sm concentration. In the latter system a rapid decrease of  $T_c$  is observed only at higher Sm concentration. The trend of decrease of  $T_c$  in SmCo system suggested negligible interplanar correlation. A positive magnetoresistance is observed in SmCo  $x=0.40$  sample which is close to metal insulator transition. The suppression of  $T_c$  is discussed to be due to hole filling and disorder rather than Abrikosov Gor'kov mechanism. Variable range hopping of conduction mechanism is observed in the insulating state of both systems. The data suggest that metal insulator transition in rare earth doped  $\text{Bi}_2\text{Sr}_2\text{CaCu}_2\text{O}_{8+\delta}$  system is of Anderson type.

### 5.7 References:

1. A.S. Ermolenko, IEEE Trans. Magn. MAG-12, 992 (1976).
2. H. Nagel, A.J. Perry, and A. Menth, J. Appl. Phys. 37, 2662 (1976).
3. J.H. Wernick and S. Geller, Acta Crystallogr. 12, 662 (1959).
4. A.A. Abrikosov and L.P. Gor'kov, Sov. Phys. JETP 12, 1243 (1961).
5. R.M. White and T.H. Geballe, Solid State Phys. Vol 15, 264 (1979).
6. T.R.S. Prasanna, R Chatterjee, R.C. O'Handley and G. Kalonji, Phys.Rev. B 46, 448 (1992).

- 
7. T.R.S. Prasanna, R.C. O'Handley, G. Kalongji and G.C. Papaefthymiou, *Phys. Rev. B* **47**, 3374 (1993).
  8. P.A. Lee and T.V. Ramakrishnan, *Rev. Mod. Phys.* **57**, 287 (1985).
  9. S. Hikami, A.I. Larkin and Y. Nagaoka, *Prog. Theor. Phys.* **63**, 707 (1980).
  10. M.T. Béal-Monod and R.A. Weiner, *Phys. Rev. B* **170**, 552 (1968).
  11. G. Briceño, M.F. Crommie and A. Zettl, *Phys. Rev. Lett.* **66**, 2164 (1991).
  12. J.W.P. Hsu, D.B. Mitzi, A. Kapitulnik and M. Lee, *Phys Rev Lett* **67**, 2095 (1991).
  13. S. Sachdev, *Phys. Rev. B* **39**, 5297 (1989).
  14. B. vom Hedt, W. Lisseck, K. Westerholt and H. Bach, *Phys. Rev. B* **49**, 9898 (1994).
  15. R.A. Fisher, S. Kim, S.E. Lacy, N.E. Phillips, D.E. Morris, A.G. Markelz, J.Y.T. Wei and D.S. Ginley, *Phys. Rev. B* **38**, 11942 (1988).
  16. P.W. Anderson, *Phys. Rev.* **109**, 1492 (1958).
  17. N.F. Mott and E.A. Davis, *Electronic Processes in Non-Crystalline Materials* (Clarendon, Oxford, 1979)
  18. M.A. van Veenendaal, R. Schlattmann, G.A. Sawatzky and W.A. Groen, *Phys. Rev. B* **47**, 446 (1993).



Table 5.1

	$T_o$ (K) ( $\times 10^3$ )	$\alpha^{-1}$ (Å°)	$R$ (Å°) (at 20K)	$W$ (meV) (at 20K)
Sm $x=0.60$	0.5	22.5	21.3	0.8
Sm $x=1.0$	49.7	5.0	14.6	2.5
SmCo $x=0.40$ as prepared	0.08	43.0	25.2	0.5
SmCo $x=0.40$ annealed at 800°C in $O_2$	2.6	13.3	18.7	1.2
SmCo $x=0.50$	3.2	12.5	18.4	1.3
SmCo $x=0.60$	58.1	4.7	14.5	2.6
Gd $x=0.58$	0.04	53.5	26.5	0.4
Gd $x=0.60$	4.0	11.5	18.0	1.4
Gd $x=0.65$	12.4	7.9	16.4	1.8

Table 5.2

Doublet	I.S. (mm/s)	Q.S. (mm/s)	L.W. (mm/s)	rel. area
A	0.18	1.91	0.29	12
B	0.25	1.46	0.45	57
C	0.26	0.66	0.58	31

## CHAPTER 6

### Electrical and Magnetic Properties of $\text{Zn}_x\text{Ca}_{1-x}\text{Fe}_2\text{O}_4$ system

#### 6.1 Introduction:

Since the discovery of high temperature superconductors by Bednorz and Muller [1] various attempts have been made to obtain newer oxide superconductors with high transition temperature. Kulkarni et.al. [2] reported, on the basis of decrease of electrical resistance and magnetic susceptibility, superconducting phase in  $\text{Zn}_{0.5}\text{Ca}_{0.5}\text{Fe}_2\text{O}_4$  system with the onset of superconductivity around a dramatically high temperature of 200K. The existence of such a high temperature superconducting phase in ferrites would have considerable technological implications. Ladds et.al. [3] using a wide range of experimental techniques showed that though there were significant changes of physical properties around 200K consistent with phase transformation there was no evidence for onset of superconductivity in this system. These studies discussed the possibility of superconducting phase in  $\text{Zn}_{0.5}\text{Ca}_{0.5}\text{Fe}_2\text{O}_4$  system only, while other concentrations of Zn in  $\text{Zn}_x\text{Ca}_{1-x}\text{Fe}_2\text{O}_4$  system remained unexplored. Moreover, the mentioned system is a two phase system consisting of calcium

ferrite ( $\text{CaFe}_2\text{O}_4$ ) phase and zinc ferrite ( $\text{ZnFe}_2\text{O}_4$ ) phase. One of these phases  $\text{CaFe}_2\text{O}_4$  phase shows long range antiferromagnetic order below 200K. The existence of superconductivity would indicate the coexistence of superconductivity and antiferromagnetism below 200K in these systems. The coexistence would lend support to the theories of high  $T_c$  superconductor which consider magnetic interaction as an important factor in stabilizing the superconducting ground state [4,5]. Therefore, we prepared a series of samples  $\text{Zn}_x\text{Ca}_{1-x}\text{Fe}_2\text{O}_4$  with  $x=0.0, 0.2, 0.4, 0.5, 0.6, 0.8$  and  $1.0$  in order to detect possible superconducting phase by examining physical properties and also to resolve the controversy generated by Ladds et.al.

## Results and Discussions:

The sample preparation has been described in chapter 2. In this section we present the results of the various experiments as well as the discussions.

### 6.2. X-ray Study:

X-ray powder diffraction pattern of the samples were recorded using  $\text{CrK}\alpha$  radiation. The analysis of the diffractograms shows that except for  $x=0.8$  and  $x=1.0$  all samples possess two distinct phases: Calcium ferrite (Ca-ferrite) phase and zinc ferrite (Zn-ferrite) phase. Ca-ferrite phase has orthorhombic structure [6] whereas Zn-ferrite has normal spinel structure [7]. The spinel

structure of Zn-ferrite is essentially a cubic structure with Zn ions filling the tetrahedral interstices and the Fe ions octahedral interstices. The vertices of these tetrahedra and octahedra are occupied by oxygen ions. The two phase behaviour of the samples is in confirmation with that found by Pandya and Kulkarni et.al. and Gorter et.al. [8]. It is well known that in an X-ray diffraction pattern of a two phase system, the intensity of diffraction peaks of a particular phase depends on the concentration of that phase in the mixture [9]. We measured integrated area using a planimeter and found from the ratio of the sum of intensities of diffraction peaks that approximately 20% of  $\text{Ca}^{2+}$  ions in the formula unit of  $x=0.2$ ,  $0.4$  and  $0.6$  diffuse to the cubic phase while in the case of  $x=0.5$  it is only 10%. In the case of  $x=0.5$  ratio value of  $\text{ZnFe}_2\text{O}_4$  phase is found to be less than that in other members of the series. This shows that some of  $\text{Zn}^{2+}$  ions diffuse to the orthorhombic cell too.  $x=0.8$  and  $x=1.0$  were found to be single phase consisting of  $\text{ZnFe}_2\text{O}_4$  structure. Hence except for  $x=0.8$  and  $x=1.0$  neither of the phases are pure and they should preferably be called  $\text{Ca}(\text{Zn})$ -ferrite phase and  $\text{Zn}(\text{Ca})$ -ferrite phase. In the next section we discuss the Mossbauer measurements of the samples.

### 6.3 Mossbauer Hyperfine Parameters:

Figures 6.1 and 6.2 show the Mossbauer spectra of  $\text{Zn}_x\text{Ca}_{1-x}\text{Fe}_2\text{O}_4$  at 300K and 77K respectively. At 77K,  $x=0.2$ ,  $0.4$  and  $0.6$  samples show a quadrupole doublet and a magnetic sextet whereas  $x=0.5$  and  $0.8$  show only a quadrupole doublet. At room

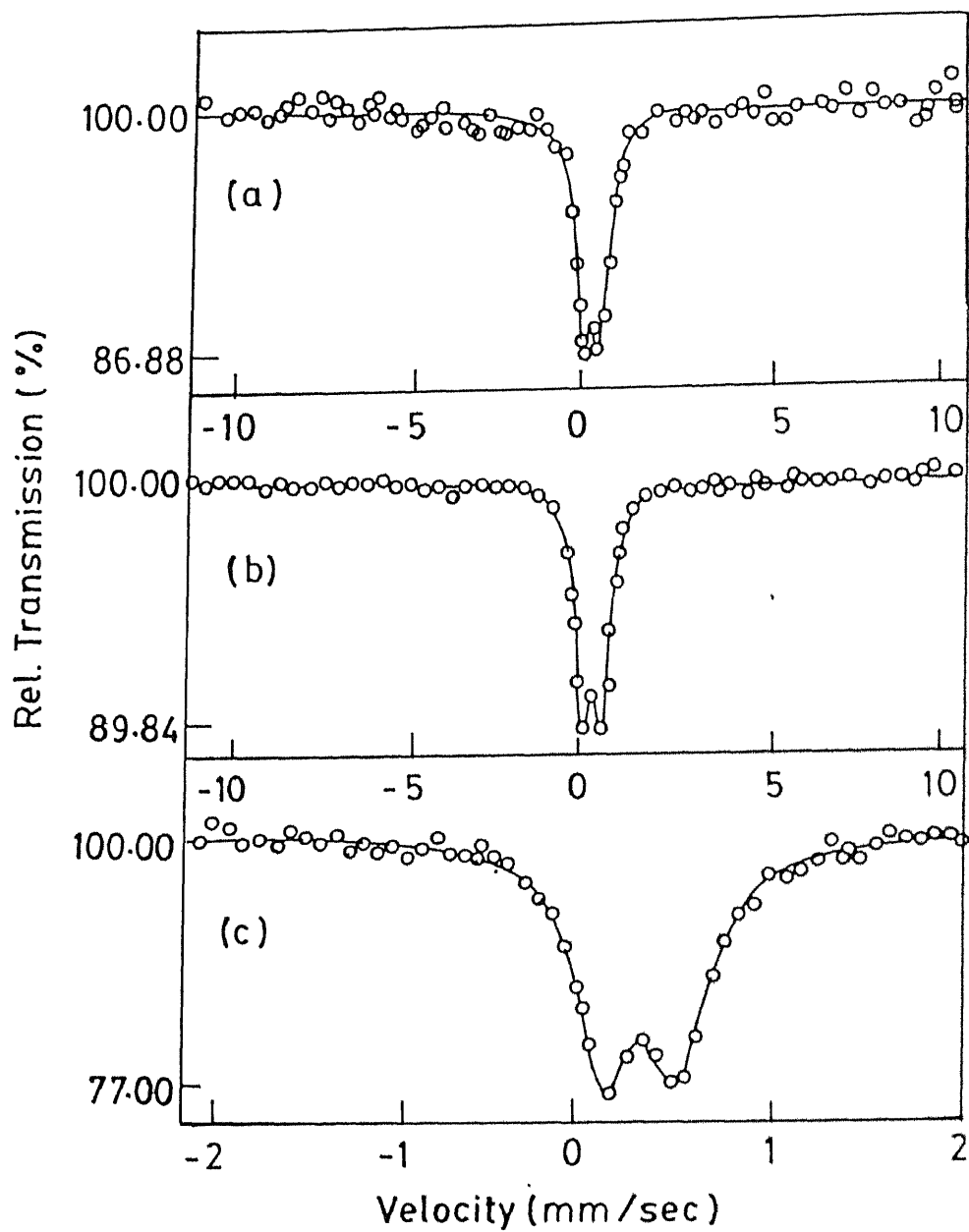


**Fig. 6.1** Mossbauer spectra of  $\text{Zn}_x\text{Ca}_{1-x}\text{Fe}_2\text{O}_4$  at 300K for (a)  $x=0.2$ , (b)  $x=0.5$  and (c)  $x=0.8$ .

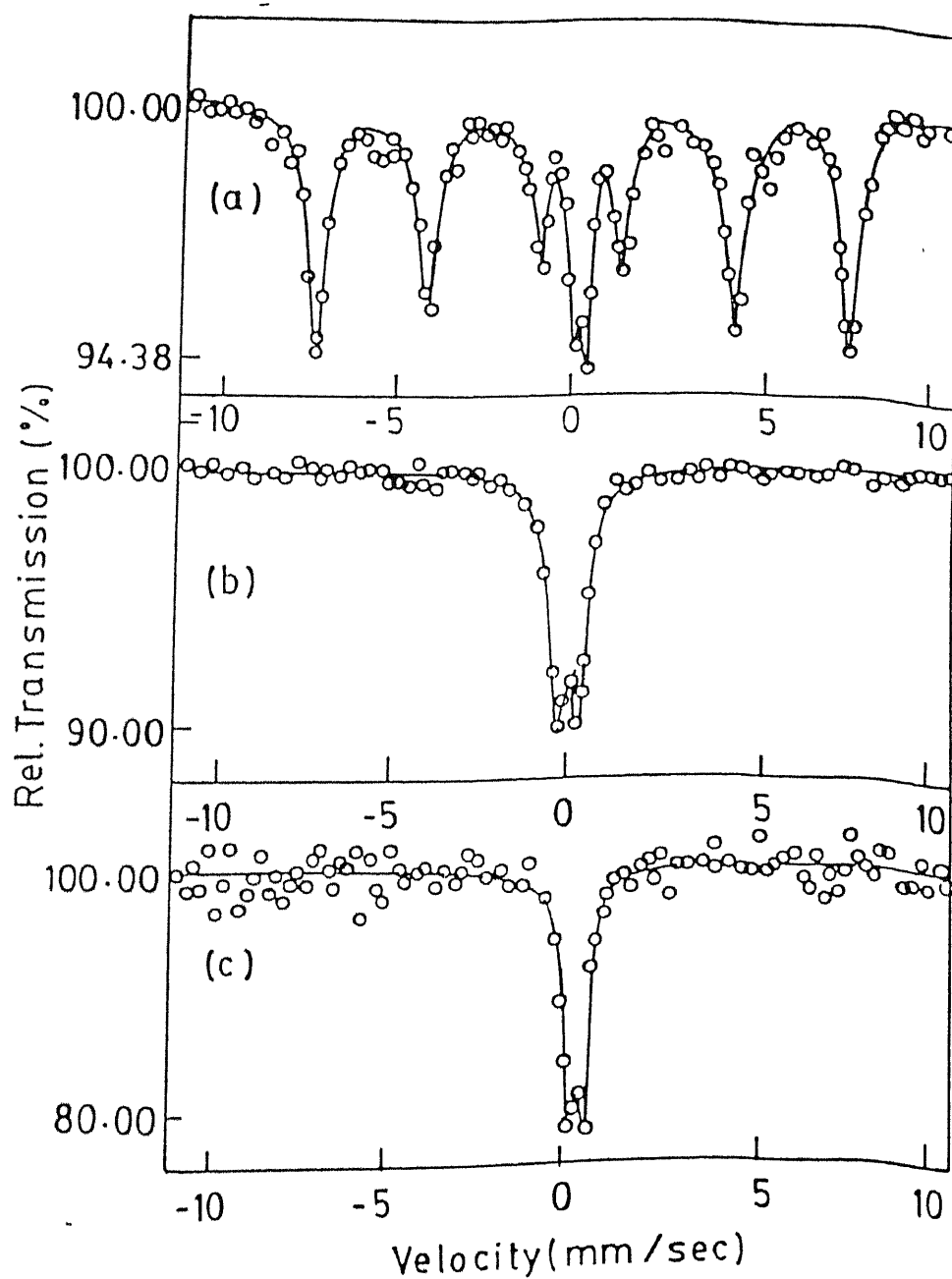


Fig. 6.2 Mössbauer spectra of  $\text{Zn}_x\text{Ca}_{1-x}\text{Fe}_2\text{O}_4$  at 77K for (a)  $x=0.2$ , (b)  $x=0.5$  and (c)  $x=0.8$ .

temperature, all the samples show a quadrupole doublet.

The liquid nitrogen data for  $x=0.2$ ,  $0.4$  and  $0.6$  samples show clearly that there are in these systems, Fe sites with two different environments, one with a non-cubic electronic charge density around it and the other belonging to a magnetic lattice. At  $77\text{K}$ , the magnetic sextet shows no evidence of quadrupole splitting. Hence, at this temperature, the environment of the 'magnetic' Fe ion has cubic symmetry.

Ca(Zn)-phase is orthorhombic and has two distinct Fe-sites  $4\text{C(I)}$  and  $4\text{C(m)}$  at the centers of two differently distorted octahedra of oxygen. One expects that the room temperature Mossbauer spectra should reveal two quadrupole doublets for this phase corresponding to two different Fe-sites. But Hudson and Whitefield [10] concluded from their room temperature Mossbauer study of  $\text{CaFe}_2\text{O}_4$  that the separate doublets for these two sites could not be resolved. Hence for all practical purposes, the two iron sites in  $\text{CaFe}_2\text{O}_4$  have to be taken as equivalent sites. Based on their arguments we conclude that there are two iron sites in our samples, one belonging to the Ca(Zn)-ferrite phase and the other belonging to the Zn(Ca)-ferrite phase. It is well known that  $\text{CaFe}_2\text{O}_4$  has Neel temperature  $T_N$  close to  $200\text{K}$  [11] and  $\text{ZnFe}_2\text{O}_4$  has  $T_N$  around  $15\text{K}$  [12]. Hence for each of the samples with  $x=0.2$ ,  $0.4$  and  $0.6$ , the sextet spectrum is due to the Fe in an antiferromagnetic sublattice in Ca(Zn)-ferrite phase and the doublet spectrum is for Fe ion in Zn(Ca)-ferrite phase. It appears that the entry of small amount of Zn in Ca-ferrite has corrected the



distortion of the oxygen octahedron about Fe ion so that no quadrupole splitting is observed in the magnetic sextet.  $H_{\text{eff}}$  for  $x=0.2$ ,  $0.4$  and  $0.7$  obtained from the six line finger pattern are  $443 \pm 1$ ,  $428 \pm 1$  and  $440 \pm 1$  kOe respectively, showing that Ca and Zn diffusion did not affect the exchange process in a significant manner.

The variation of quadrupole splitting  $\Delta E_Q$  with Zn concentration ( $x$ ) at room temperature (R.T.) as well as liquid nitrogen temperature (L.N.T.) is shown in Fig. 6.3. The variation of line widths  $\Delta H$  (full width at half maximum) with  $x$  at the two temperatures is shown in Fig. 6.4. The values of  $\Delta E_Q$  and  $\Delta H$  for  $x < 0.8$  at 300K except for the case of  $x=0.5$ , are higher than their values at 77K.  $x=0.8$  and  $x=1.0$  which show single phase behaviour have nearly similar values of  $\Delta E_Q$  and  $\Delta H$  at 77K and 300K. The large values of  $\Delta H$  for  $x=0.2$ ,  $0.4$ ,  $0.5$  and  $0.6$  at room temperature suggest that there are two or more doublet patterns with the same isomer shift in each spectrum but those could not be resolved. Neglecting at the moment  $x=0.5$  case,  $\Delta E_Q$  remains almost constant as  $x$  increases at 77K. The line widths,  $\Delta H$ , also show the similar trend at 77K starting from the instrumental value of  $0.28 \text{ mm/sec}$  for  $x=0.2$ . However, at room temperature and at low concentrations,  $\Delta E_Q$  shows a jump from their 77K values of  $0.33 \text{ mm/s}$  to  $0.47 \text{ mm/s}$  and the half widths to approximately double their low temperature values. These two facts imply that the environment of Fe goes to a more disordered arrangement at room temperature. Also, at this temperature  $\Delta E_Q$  decreases with the increase of concentration,

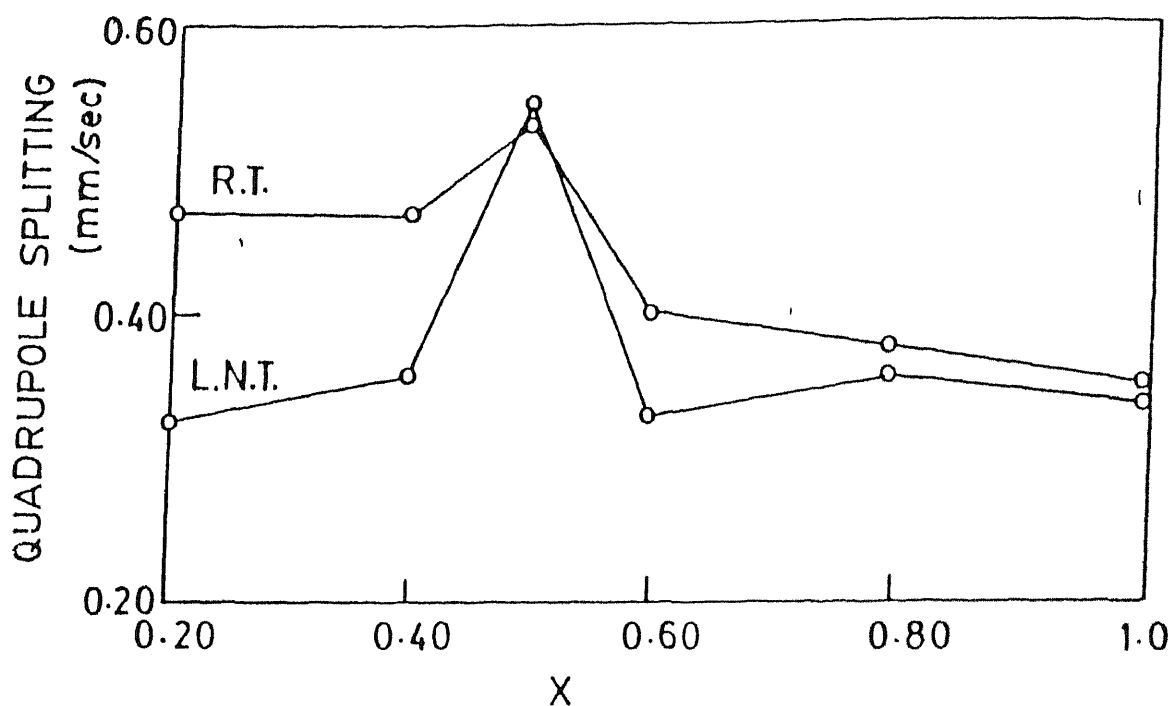


Fig. 6.3 Variation of quadrupole splitting with Zn concentration  $x$  in  $\text{Zn}_x\text{Ca}_{1-x}\text{Fe}_2\text{O}_4$  system.

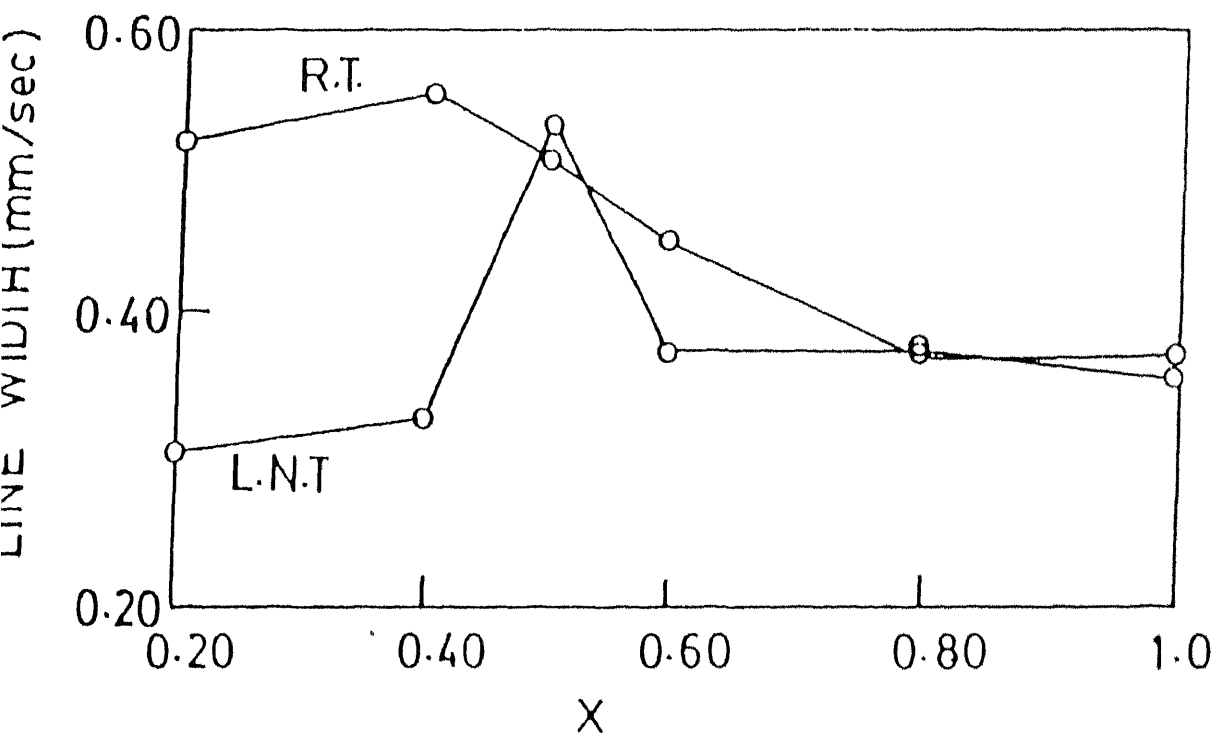


Fig. 6.4 Variation of line width with zinc concentration  $x$  in  $\text{Zn}_x\text{Ca}_{1-x}\text{Fe}_2\text{O}_4$  system.

unlike its behaviour at the low temperature. Thus Ca and Zn transfers and the corresponding disorder is a complex process which can not be tracked by the present measurements.

The sample  $x=0.5$  shows different behaviour from other samples. From x-ray diffraction nothing unusual is found and like other systems in its neighbourhood, this one is also a mixed phase system. The only special feature is that Ca transfer to the Zn-ferrite phase is smaller than that in the other sample. This simple fact gives it a special characteristic in that all its physical properties are anomalous as compared to other systems. At liquid nitrogen as well as at room temperature it has maximum  $\Delta E_Q$  values and also about maximum  $\Delta H$  values. But what is more significant is that its  $\Delta E_Q$  is the same at room temperature as in the liquid nitrogen temperature and its  $\Delta H$  values are approximately the same at these two temperatures. It appears that all the oxygen, calcium and zinc configurations are frozen for this temperature. Also, a noteworthy feature of this system is that even though the samples on its either side in the x-scale namely  $x=0.2$ ,  $0.4$  and  $0.6$  showed a sextet at 77K, this showed only a doublet at that temperature. That is, its specific Ca and Zn configurations have destroyed the superexchange mechanism.

The variation of Isomer shift (I.S.) which was measured with respect to metallic iron foil is shown in Fig. 6.5. Again at  $x=0.5$  it shows a behaviour different from other samples. At  $x=0.5$  I.S. is maximum and its values at 77K and 300K being

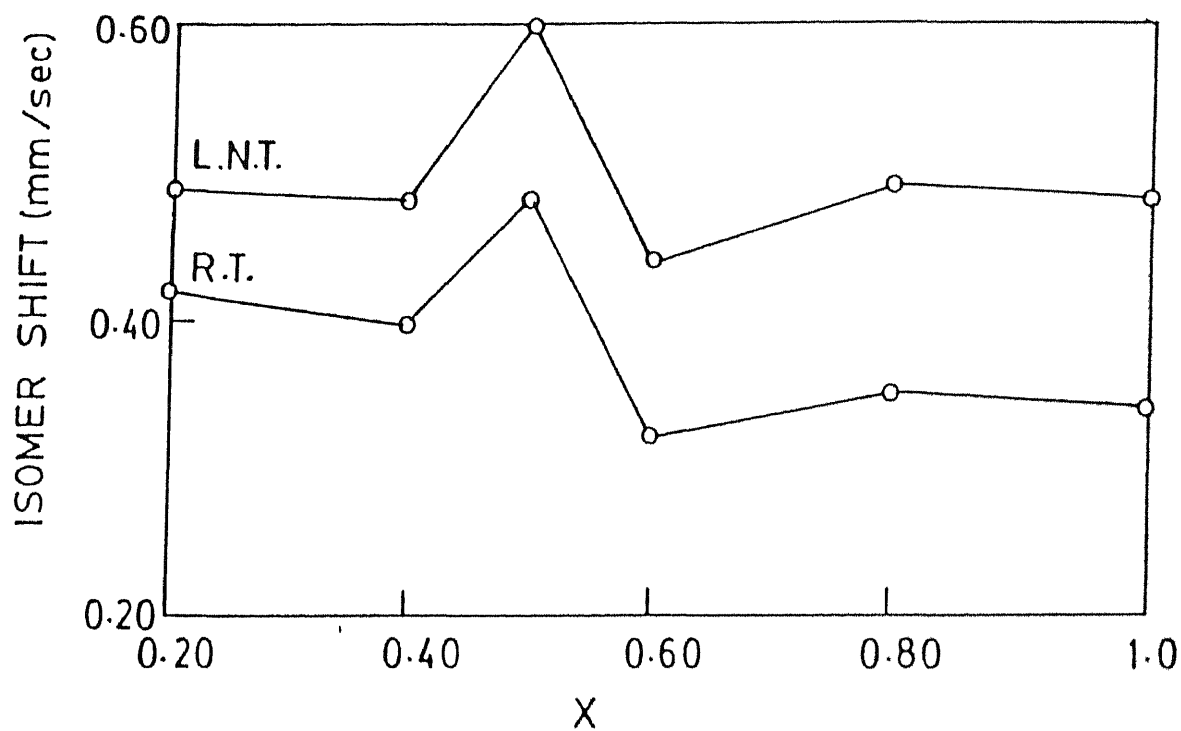


Fig. 6.5 Variation of isomer shift with zinc concentration  $x$  in  $\text{Zn}_x\text{Ca}_{1-x}\text{Fe}_2\text{O}_4$  system.

$0.59 \pm 0.01$  and  $0.48 \pm 0.01$  mm/s respectively. The room temperature I.S.  $0.34 \pm 0.01$  mm/s and quadrupole splitting  $0.35 \pm 0.01$  mm/s obtained for  $x=1.0$  sample is in agreement with the previously reported values by J Evans et.al. [13]. Since the spectra of Ca(Zn)-ferrite and Zn(Ca)-ferrite are not resolved, the calculated isomer shift is a common isomer shift of the mixed phase samples.

It is evident that I.S. remains almost constant with concentration change excluding  $x=0.5$  at liquid nitrogen temperature whereas, at room temperature it has a small linear decrease with increase of Zn. This implies that the Zn-substitution and the consequent diffusion at room temperature affects the s-electron density at iron nuclei. The presence of one set of isomer shift and quadrupole splitting shows that exchange of ions through diffusion have taken place only between distorted octahedral sites of Ca(Zn)-ferrite phase and tetrahedral site Zn(Ca)-ferrite phase. Had it not been the case,  $\text{Fe}^{3+}$  ions would have gone to the tetrahedral or similar sites and we would have two sets of values of isomer shift and quadrupole splitting. The increase in isomer shift at 77K for all values of  $x$  is attributed to thermal red shift between the source at 300K and absorber at 77K.

#### 6.4 Magnetization Measurement:

The room temperature magnetization measurements were performed on a vibrating sample magnetometer upto a maximum field of 11kG. The samples showed characteristic behaviour of

paramagnetic phase. The results of the magnetization measurements corroborate the absence of the sextet and hence ordered magnetism at room temperature.

### 6.5 EPR Study:

EPR spectra of all samples in powder form were recorded at room temperature and liquid nitrogen temperature at X-band frequency ( $\sim 9.2$  GHz). The same technique is used to detect superconductivity through the characteristic non resonant type microwave absorption signal at low magnetic field near zero. The low field absorption signal observed below transition temperature in all high temperature oxide superconductors provides a nondestructive and highly sensitive way to study the evolution of superconductivity in the samples [14-17]. We did not observe any low field microwave absorption signal in any of the samples down to liquid nitrogen temperature.

At room temperature two resonant signals are observed in all the samples. These resonant signals lie at fields corresponding to  $g \sim 2$  and  $g \sim 4$ .  $g$  values are calculated using  $h\nu = g\mu_B H$  where  $\nu$  is the microwave frequency  $\mu_B$  is the Bohr magneton and  $H$  is the resonance field. The  $g \sim 2$  signal shows a rather broad symmetrical line shape and peak to peak line width  $\Delta H$  could be measured for this signal. The temperature dependence of this signal is quite interesting. Although its position does not change down to 77K its width  $\Delta H$  changes substantially. The values of  $\Delta H$  measured at 300K and 77K for different samples and the ratio  $\Delta H(300K)/\Delta H(77K)$  corresponding

to  $g \sim 2$  are given in Table 6.1. It is interesting to note that the line width ratio shows a minima at  $x=0.5$ .

In the present systems, EPR spectra may result from paramagnetic  $\text{Fe}^{2+}$  or  $\text{Fe}^{3+}$  ions. Since  $\text{Fe}^{2+}$  has short spin lattice relaxation time its EPR can be observed only at temperatures close to liquid Helium [18]. Therefore, the observed EPR signal is due to  $\text{Fe}^{3+}$  ion. The EPR signals are the overlap spectra of  $\text{Fe}^{3+}$  in the two phases namely  $\text{Ca}(\text{Zn})$ -ferrite and  $\text{Zn}(\text{Ca})$ -ferrite because in both the phases  $\text{Fe}^{3+}$  lies in approximately identical environment and the individual spectra overlap beyond resolution.

The EPR signals in the samples may originate due to presence of two types of environment around  $\text{Fe}^{3+}$  in the crystal, one due to regular octahedra and another due to axially distorted octahedra. The peak at  $g \sim 2$  results from the regular octahedra and  $g_{\parallel}$  component of axially distorted one. The peak at  $g \sim 4$  arises due to  $g_{\perp}$  component of the axially distorted octahedral environment around  $\text{Fe}^{3+}$ . In all the samples broad  $\Delta H$  is observed. This may result from either short spin relaxation time of  $\text{Fe}^{3+}$  ion which from uncertainty principle gives large linewidth or from an exchange interaction of  $\text{Fe}^{3+}$  ion with other paramagnetic species. In the case of spin lattice relaxation the line width decreases due to lesser number of excitation of phonons. This rules out the possibility of presence of spin lattice relaxation in the system. On the other hand, the exchange interaction causes narrowing of resonance lines as the temperature is lowered if the spins are

like whereas it causes broadening of resonance lines when unlike spins are involved. Moreover, anisotropic exchange interaction also, contributes to the broadening [18]. The observed line width and its temperature dependence suggests an exchange between  $\text{Fe}^{2+}$  and  $\text{Fe}^{3+}$  spin states and it becomes more anisotropic at 77K due to diffusion of ions. The value of  $g \sim 2$  indicates absence of appreciable spin-orbit coupling.

## 6.6 Resistivity Study:

### 6.6.1 Small Polaron Theories of Resistivity:

The resistivity behaviour of the samples could be explained on the basis of small polaron theories. Hence we summarize the important features of these theories as the basis of the analysis of the experimental data.

The polaron is an electron which moves through the lattice carrying with it a distortion of the lattice near the site it occupies. The size of the polaron is measured by the size of the induced lattice distortion. If the linear dimension of the distortion becomes comparable to or smaller than lattice parameter it is said that a small polaron is formed.

It can also be decided energetically whether small polaron picture can be applied. The question is whether the energy  $E_b$  gained by localizing the electron at a certain lattice site and allowing the lattice particle to relax to their new displaced equilibrium position is larger than the band energy. The latter corresponds to the energy gained by a single conduction



electron in the rigid lattice because of its tendency to delocalize itself. This energy is of the order of the bandwidth  $2J$  where  $J$  is two center resonance integral. Thus the criterion for the small polaron formation is given by

$$E_b > 2J \quad (6.1)$$

The theory of conduction by small polaron has been mainly developed by Holstein [20] and Friedman [21]. A characteristic feature of small polaron conduction is a transition between conduction in a polaron band and conduction by hopping. Above a critical temperature, order of which is  $\theta_D/2$  where  $\theta_D$  is Debye temperature, the dominant conduction mechanism is thermally activated hopping in which the electron-site change is accompanied by emission and absorption of many phonons. Below the critical temperature, the conduction is in polaron band characterized by site transfer in which phonon occupation numbers are unchanged. The model followed by Holstein assumes a linear chain of diatomic molecules placed at equal distance from each other. Mott and Austin has incorporated in the theory the case when a disorder is also present in the system. Three temperature zones have been discussed in their paper [22]:

(a). At high temperature small polaron theory predicts dominant conduction mechanism by thermally activated hopping through emission and absorption of many phonons. Electrical conduction occurs only when in the course of thermal fluctuation a site

with a self trapped electron attains a configuration equivalent to neighboring unoccupied site. It is to be expected that the electrons would transfer preferentially to those cations which are closest to the host ion site. An electric field when applied can be viewed as leading to a preferential diffusion of electrons through the lattice and a net current results. Once an electron transfers between sites, the local deformation pattern relaxes dissipating the distortion energy to the material as a whole. Mott derived the following expression for hopping conductivity when some random field in the solid separates the energies of an electron on the two centres say by an amount  $W_D$  [23]

$$\sigma = \nu c (1-c) \left( \frac{e^2}{RkT} \right) \exp(-2\alpha R) \exp(-W/kT) \quad (6.2)$$

where  $c$  is the ratio of concentration of two different cations valences  $\nu$  is the phonon frequency,  $R$  is the mean distance between ions,  $\alpha$  is the rate of decay of wave function and  $W$  is the activation energy given by

$$W = W_H + (1/2) W_D \quad (6.3)$$

where  $W_H$  is the polaron hopping energy and  $W_D$  is the average change in energy in going from site to site.

(b). As the temperature is lowered a temperature is reached when multi phonon process ceases and main contribution to

conductivity is from jumps in which a single optical phonon is absorbed and emitted. For intermediate temperature the expression for mobility for non-adiabatic (in which during each fluctuation the chance of an electron transfer is small) process is

$$\mu_D = 2 \left( \frac{ea^2}{kT} \right) \left( \frac{J}{\hbar} \right)^2 \pi^{1/2} \tau \exp(-W/kT)$$

where 
$$\tau = \frac{1}{4} \hbar (W_H kT)^{-1/2} \left[ \sinh(\frac{1}{2} \hbar \omega_0 \beta) / \frac{1}{2} \hbar \omega_0 \beta \right]^{1/2}$$

$$W = \left( W_H / \frac{1}{4} \hbar \omega_0 \beta \right) \tanh \left( \frac{1}{4} \hbar \omega_0 \beta \right)$$

$$\beta = \frac{1}{kT} \quad (6.4)$$

The above expression for mobility is true for perfectly periodic one dimensional lattice and is only valid for  $T \geq \theta_D/4$ . Since application of an electric field gives a preferential direction of motion to electrons through lattice the above expression can be applied to bulk systems where the energies of the two sites differ by an amount  $W_D$ . This should lead to a term  $\exp(-W_D/kT)$  in the conductivity. The polaron electric conductivity can be defined in terms of drift mobility as [24]

$$\sigma = n e \mu \quad (6.5)$$

where  $n$  is the concentration of polaron and  $e$  is the electric charge that is equal to that of a free electron. Therefore,

expression for conductivity in the intermediate region becomes

$$\sigma = (A/T) (W/kT) (\hbar\omega_0/2k)^{-1/2} \left[ \sinh(\hbar\omega_0/2kT) \right]^{1/2} \times \\ \exp \left[ (-4W_H/\hbar\omega_0) \tanh(\hbar\omega_0/2kT) - W_D/kT \right]$$

$$\text{where } A = \pi^{1/2} n e^2 a^2 J^2 / k^2 \hbar \quad (6.6)$$

(c). At low temperature according to small polaron theory conduction takes place in a small polaron band which is extremely narrow. According to Holstein [20], for perfectly periodic lattice, mobility decreases as temperature increases from  $T=0K$ . Polaron effective mass for non adiabatic process can be defined as

$$m_p = (\hbar^2/2Ja^2) \exp(\gamma) \\ = m^* \exp(\gamma) \quad (6.7)$$

where  $m^*$  is the rigid lattice effective mass. The quantity  $\gamma$  depends upon the vibrational energy of the ions and is constant only for the temperature  $T \leq \theta_D/4$  when the zero point motion of ions is dominant. At higher temperature  $\gamma$  leads to

$$\gamma(1 + 4kT/\hbar\omega_0) \quad (6.8)$$

giving an exponential increase in  $m_p$  with temperature and a rapid decrease in mobility.

### 6.6.2 Resistivity Results and Discussions:

In order to see the variation of room temperature resistivity as a function of  $x$  we have plotted the same in Fig. 6.6. It is evident that the resistivity values for these bulk samples fall in the semiconductor range. In contrast for high  $T_c$  superconductors the observed room temperature resistivity is usually in the milliohm-cm range. It is therefore highly unlikely to observe superconductivity in these systems. However, an interesting point of this curve is that at  $x=0.5$  the resistivity shows a minimum value.

The variation of resistivity with temperature for three typical samples  $x=0.2$ ,  $0.5$  and  $0.8$  is shown in Fig. 6.7. As we see resistivity increases as the temperature is lowered and below a certain temperature it remains constant. The plots show the experimental points and fitted curves using small polaron theories (Eqns. 6.2 and 6.6) in the intermediate and high temperature zones. As the orbitals of Zn and Ca ions are completely filled, conducting electrons are provided by iron ions. Electron transport is usually ascribed to  $Fe^{2+}-Fe^{3+}$  exchange between these sites and it is d electron which interact strongly with the lattice to form small polaron. A reasonably good fitting is observed and parameters obtained from fitting are given in Table 6.2. This analysis shows clearly that the samples are semiconductors with values approaching insulators at low temperatures.

The curve fitting yields the values of various parameters which appear in Eqns. 6.2 and 6.6. These parameters are Debye

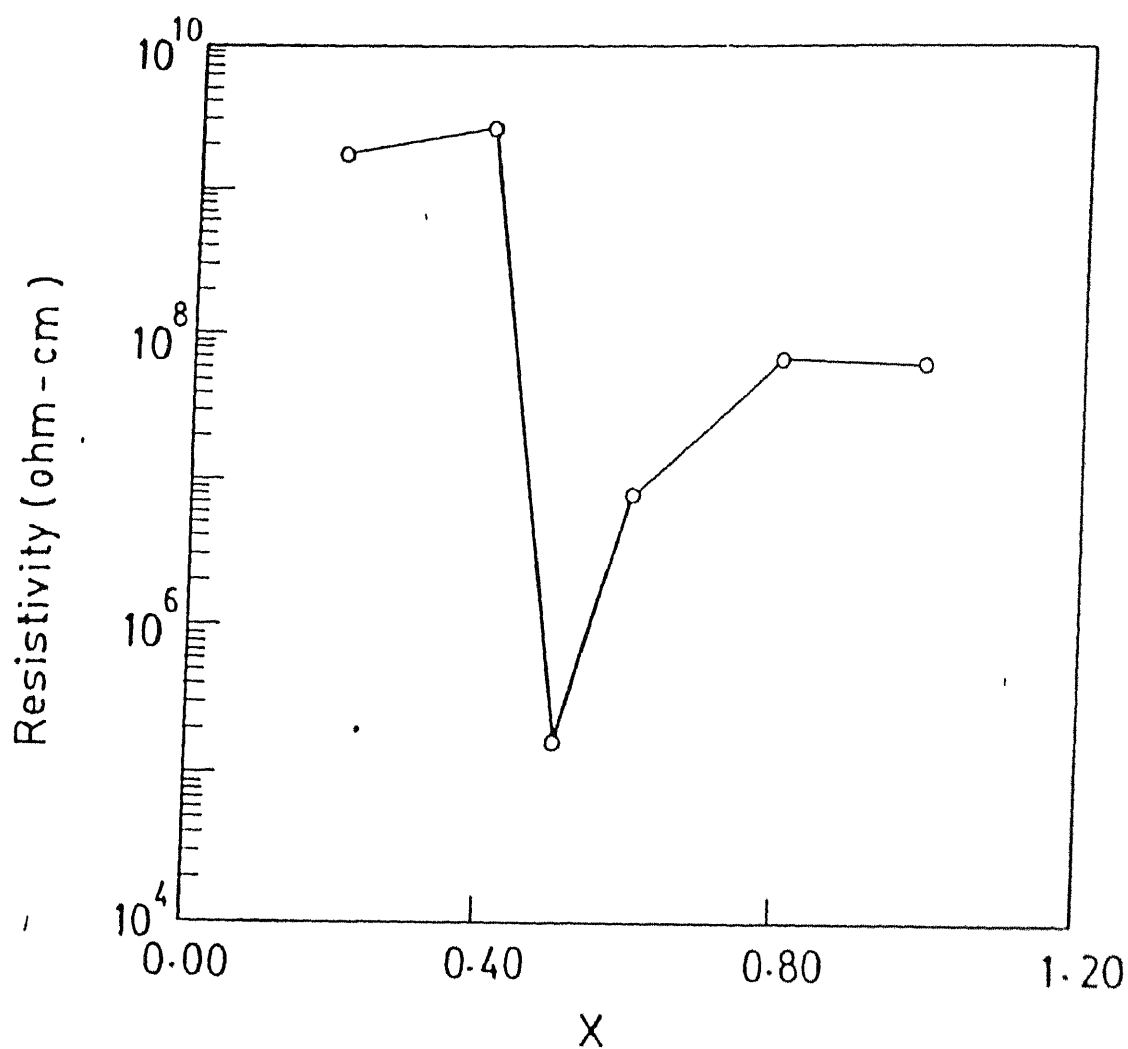


Fig. 6.6 Electrical resistivity of  $\text{Zn}_x\text{Ca}_{1-x}\text{Fe}_2\text{O}_4$  as a function of zinc concentration  $x$  at 300K.

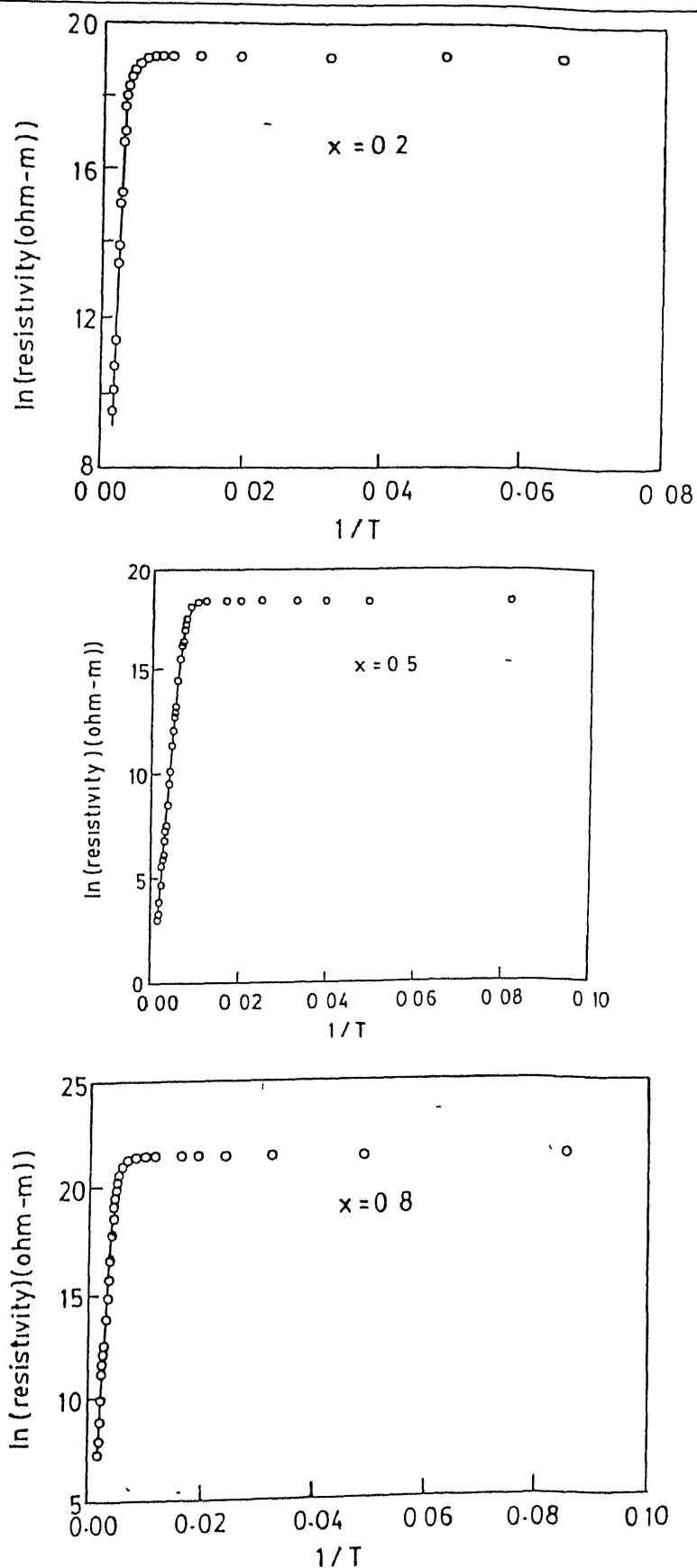


Fig. 6.7 Temperature dependence of resistivity for  $x=0.2$ ,  $x=0.5$  and  $x=0.8$  in  $\text{Zn}_x\text{Ca}_{1-x}\text{Fe}_2\text{O}_4$  system.

temperature  $\theta_D$ ; activation energy  $W$ , the energy difference between two sites due to disorder  $W_D$ , and the polaron hopping energy  $W_H$  which is a measure of barrier height between two sites. As for the approximate theoretical value of  $W_D$  we have Miller and Abrahams formula [25]

$$W_D = \frac{0.4 e^2}{K R} \quad (6.9)$$

where  $R$  is the mean distance between the ions and  $K$  is the dielectric constant. For Zn-ferrite  $K=10$  as determined by Miles et.al. [26] and  $R=4.5\text{\AA}$ . These values of  $K$  and  $R$  give  $W_D=0.128\text{eV}$ . The agreement with the experimental value  $0.085\text{eV}$  is reasonably good considering the fact the contribution of grain boundaries on the activation energy has not been taken account of in the theory. Again as we have seen from X-ray diffraction studies that  $x=0.8$  sample contains only the Zn-ferrite phase. However, we see that  $W_D$  has values two times or more for other samples as compared to the  $x=1.0$  phase. Evidently, the diffusion of  $\text{Ca}^{2+}$  ions have increased the random field effect. Moreover, among the mixed phase systems  $x=0.5$  has the minimum ( $0.153\text{eV}$ ) and  $x=0.2$  has the maximum ( $0.339\text{eV}$ ) values of  $W_D$ . This again shows that  $x=0.5$  sample has a rather definite ionic configuration whereas the  $x=0.2$  sample has extensive diffusion generated disorder.

The two components of the activation energy  $W_D$  and  $W_H$  are plotted against  $x$  in Fig. 6.8. It may be noted that  $W_H$  follows the same trend as  $W_D$  upto  $x=0.6$  showing that diffused  $\text{Ca}^{2+}$  in



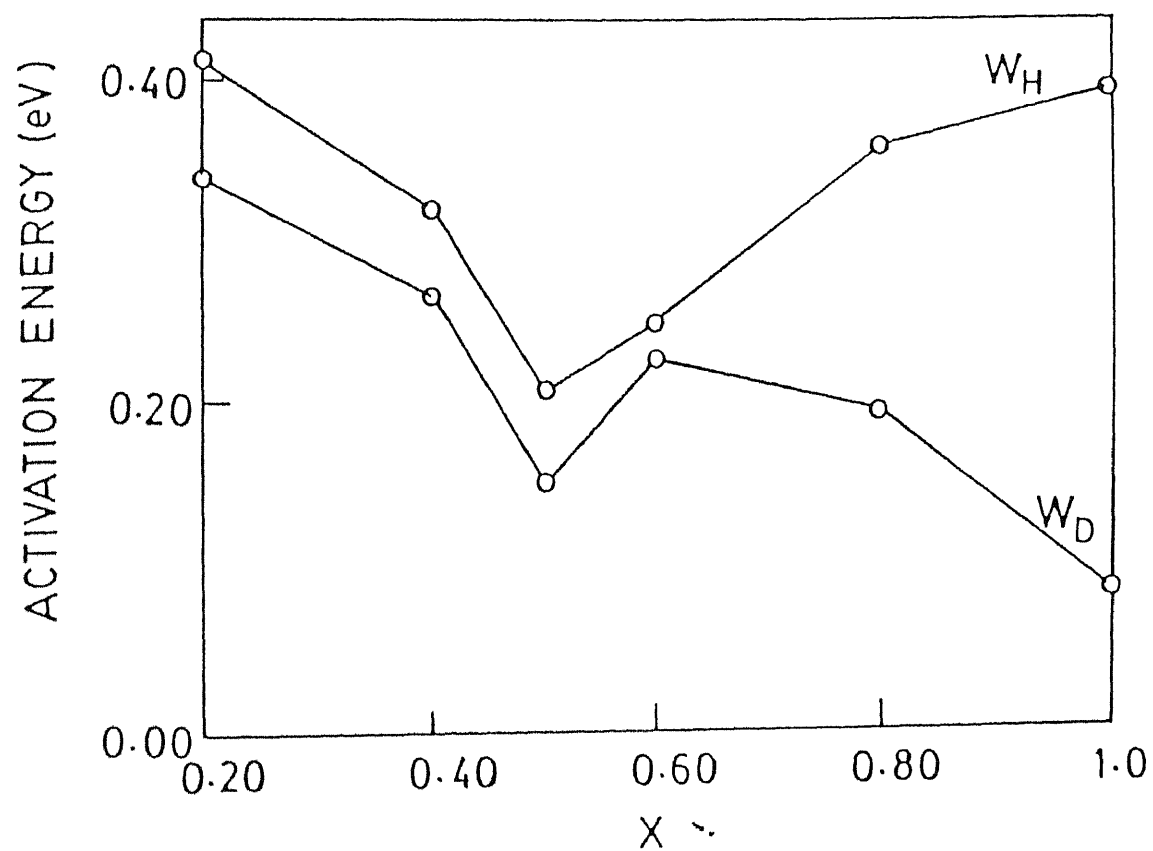


Fig. 6.10 Variation of activation energy with zinc concentration  $x$  in  $\text{Zn}_x\text{Ca}_{1-x}\text{Fe}_2\text{O}_4$  system.

mixed phase systems plays a dominating role in building up the potential barrier between two neighbouring  $\text{Fe}^{2+}$  ions. However, in Zn-ferrite phase, pure or less pure,  $\text{Zn}^{2+}$  plays a dominating role for creating potential barrier since  $W_H$  and  $W_D$  differ significantly for  $x=0.8$  and  $1.0$ .

At low temperatures when  $T \leq \theta_D/4$  the resistivity of all the samples, except  $x=1.0$  does not change with the decrease of temperature. This feature is not new for semiconductors [27]. What is new is the fact that this starts at a relatively high temperature. However in our case,  $\theta_D/4$  is high 125K-167K, neglecting the case of  $x=0.5$  where it is 83.34K. In this range, the zero point motion of the ions remain the dominant mechanism of conductivity. As a consequence of this [22] the effective mass of polaron will also be independent of temperature and therefore, the resistivity will remain constant. The polaron in this temperature region moves like a heavy particle in polaron band with its effective mass much greater than in the absence of electron - phonon interaction.

### 6.7 Conclusions:

In the present study we have shown that  $\text{Zn}_x\text{Ca}_{1-x}\text{Fe}_2\text{O}_4$  ( $0.2 \leq x \leq 0.8$ ) is a mixed phase system consisting of two phases, Ca-ferrite and Zn-ferrite phase in which a substantial amount of  $\text{Ca}^{2+}$  ions diffuse into Zn-ferrite phase and some amount of  $\text{Zn}^{2+}$  ions diffuse into Ca-ferrite phase. The consequence of diffusion is that the difference between the octahedral environment of  $\text{Fe}^{3+}$  ions is substantially decreased. As a

result Mossbauer and EPR parameters are nearly same except for the fact at low temperature the Ca(Zn)-ferrite phase shows antiferromagnetism. The temperature dependent conductivity shows a semiconductor behaviour and the data can be very well interpreted within the framework of small polaron theory, by the polaron hopping mechanism in a system with a small amount of disorder. The data for all measurements show anomaly for the  $x=0.5$  case. The most important result of the study is that  $\text{Zn}_x\text{Ca}_{1-x}\text{Fe}_2\text{O}_4$  system is not a high temperature superconductor for entire concentration range of Ca. This also settles the controversy generated by Ladds et.al.

#### 6.8 References:

1. J.G. Bednorz and K.A. Muller, Z. Phys B **64**, 189 (1986).
2. R.G. Kulkarni, H.N. Pandya, R.V. Upadhyay, H.N. Joshi, G.L. Budha and S.N. Rao, Solid State Commun **68**, 101 (1988).
3. D.A. Ladds, G.A. Saunders, P.J. Ford, D.P. Almond, Chang Fanggao, Z. Othaman, S.J. Bending, S. Smith, B.F. Chapman, R.A.L. Sullivan, Li Mahosa and Q.A. Pankhurst, Solid State Commun. **78**, 413 (1991).
4. V.J. Emery, Phys. Rev. Lett. **58**, 2794 (1988).
5. A. Aharmony et.al. Phys. Rev. Lett. **60**, 1330 (1988).
6. B.F. Decker and J.S. Kasper, Acta. Cryst. **10**, 332 (1957).
7. E.J.W. Verwey and E.L. Heilmann, J. Chem. Phys. **15**, 174 (1947).
8. E.W. Gorter, Philips Res. Repts. **9**, 357 (1954).

- 
9. B.D. Cullity, Elements of X-ray Diffraction (Addison-Wesley, USA, 1967)
  10. A.Hudson and H.J. Whitfield, J. Chem. Soc. A 376 (1967).
  11. L.M. Corliss, J.M. Hastings and W. Kunmann, Phys. Rev. 160, 408 (1967).
  12. F.K. Lotzering, J. Phys. Chem. Solids 27, 130 (1966).
  13. J. Evans, S.S. Hafner and H.P. Weber, J. Chem. Phys. 55, 5282 (1971).
  14. K.W. Blazey, K.A. Muller, J.G. Bednorz, W. Berlinger, G. Amoretti, E. Buuggiu, A. Vera and F.C. Motachotta, Phys. Rev. 36, 7241 (1987).
  15. R. Durny, I. Hautala, S. Durcharme, B. Lee, O.G. Symko, P.C. Taylor, D.J. Zheng and J.A. Xu, Phys. Rev. 36, 2361 (1987).
  16. K.A. Muller, M. Takashige and J.G. Bednorz, Phys. Rev. Lett. 58, 1143 (1987).
  17. E.J. Pakulis and T. Osada, Phys. Rev. B 37, 5940 (1988).
  18. W. Low and M. Weger, Phys. Rev. 118, 1130 (1960).
  19. G.C. Upreti and R.S. Saraswat, Magn. Reson. Rev. 73, 215 (1982).
  20. T. Holstein, Ann. Phys. 8, 325 (1959).
  21. L. Friedman, Phys. Rev. 135, 233 (1964).
  22. I.G. Austin and N.F. Mott, Adv. Phys. 18, 41 (1969).
  23. N.F. Mott, Adv. Phys. 16, 49 (1967).
  24. J. Appel, Solid State Phys. 21, 235 (1968).
  25. Allen Miller and Elihu Abrahams, Phys. Rev. 120, 745 (1960).

26. P.A. Miles, W.B. Westphal and A. Von Hippel, Rev. Mod. Phys. 29, 279 (1957).
27. C.S. Hung and J.R. Gliessman, Phys. Rev. 96, 1226 (1957).

TABLE 6.1

x	$\Delta H$ (kG)		$\frac{\Delta H (LNT)}{\Delta H (RT)}$
	RT	LNT	
0.2	0.50	0.85	1.70
0.4	0.45	0.75	1.67
0.5	0.52	0.85	1.63
0.6	0.45	0.80	1.78
0.8	0.75	1.35	1.80
1.0	0.48	Broad	

TABLE 6.2

x	$\theta_D/2$	W(eV)	$W_D$ (eV)	$W_H$ (eV)
0.2	333.33	0.581	0.339	0.412
0.4	322.56	0.456	0.268	0.322
0.5	166.67	0.285	0.153	0.209
0.6	250.00	0.364	0.228	0.250
0.8	263.00	0.457	0.196	0.359
1.0	285.00	0.435	0.085	0.393

## Summary of Conclusions

In the present work we have studied two different problems related to superconductivity. The first problem deals with effect of rare-earth substitution (Gd and Sm) in  $\text{Bi}_2\text{Sr}_2\text{Ca}_1\text{Cu}_2\text{O}_{8+\delta}$  system. The second problem is the search for superconductivity in  $\text{Zn}_x\text{Ca}_{1-x}\text{Fe}_2\text{O}_4$  system. The conclusions of the thesis can be summarized as follows:

(i) The substitution of Gd and Sm in  $\text{Bi}_2\text{Sr}_2\text{Ca}_1\text{Cu}_2\text{O}_{8+\delta}$  system have been found to decrease the  $c$  lattice parameter and an increase in  $a$  lattice parameter. The substitution leads to an increase in transition temperature for low impurity concentration. For higher impurity concentration a decrease in transition temperature observed and superconductivity eventually vanishes. The trend of decrease of transition temperature for both rare earth impurities is found to be identical and is independent of their magnetic moments. The Hall effect measurement of Gd doped samples show decrease of hole concentration. The results of resistivity measurements reveal that although the doping is in charge reservoir, it generates disorder in  $\text{CuO}_2$  plane.

We have shown that suppression of superconductivity in these systems is not the result of magnetic pair breaking effect (Abrikosov Gor'kov mechanism) but is due to hole filling and disorder. The disorder causes localization of charger carriers and drives the system in the insulating state. Room

temperature Mossbauer measurements of Gd doped samples also reveal localization of charge carriers. The insulating state is described by 3D variable range hopping (VRH) mechanism. The data fit well with a model having density of states near  $E_F$  concave in nature. The experimental evidences indicate that metal insulator transition in rare earth doped  $\text{Bi}_2\text{Sr}_2\text{Ca}_1\text{Cu}_2\text{O}_{8+\delta}$  is of Anderson type. Whether the transition from metallic state to insulating state is continuous or discontinuous can be proposed as a future problem.

(ii) The temperature dependence of center shifts of superconducting and insulating samples is well described by Debye model of solids. No phonon softening is observed below  $T_C$  in superconducting samples and motion of Fe atoms remain harmonic.

(iii) Magnetoresistance measurement of a low Gd doped sample indicates the presence of temperature dependent activation energy for flow of flux lines. A positive magnetoresistance is observed in barely insulating  $\text{Bi}_2\text{Sr}_2\text{Ca}_{0.6}\text{Sm}_{0.4}\text{Cu}_{1.95}\text{Co}_{0.05}\text{O}_{8+\delta}$  sample. Annealing the sample in flowing oxygen shows an unusual magnetoresistance maxima.

(iv) We have shown that  $\text{Zn}_x\text{Ca}_{1-x}\text{Fe}_2\text{O}_4$  is not a high  $T_C$  superconductor for entire concentration range of  $x$ . The study follows from a report of existence of superconducting phase with dramatically high transition temperature of 200K in  $\text{Zn}_{0.5}\text{Ca}_{0.5}\text{Fe}_2\text{O}_4$ . The results of Mossbauer, EPR and resistivity though show an anomaly at  $x=0.5$ . The resistivity data have been described within the framework of small polaron model.

### List of Publications

1. Electrical and Magnetic Properties of  $\text{Zn}_x\text{Ca}_{1-x}\text{Fe}_2\text{O}_4$  ( $x=0.0-1.0$ ) System  
Sandeep Singh, R.C. Srivastava, Prem Chand, D.C. Khan and P.E. Wigen, Solid State Commun. 85, 45 (1993).
2. Study of Hall Effect, Electrical Resistivity and Magnetoresistance in  $\text{Bi}_2\text{Sr}_{2-x}\text{Gd}_x\text{Ca}_1\text{Cu}_2\text{O}_{8+\delta}$  ( $x=0.0-0.65$ ) Systems, Sandeep Singh and D.C. Khan  
Physica C 222, 233 (1994).
3. Mössbauer Study of  $\text{Bi}_2\text{Sr}_{2-x}\text{Gd}_x\text{Ca}_1\text{Cu}_2\text{O}_{8+\delta}$  System  
Sandeep Singh and D.C. Khan (to be communicated)



123033

**A**<sub>D</sub>**123633**

This book is to be returned on the date last stamped.

The image shows a document page with a prominent vertical line running down the center. On either side of this line, there are faint, illegible markings that appear to be text or data. The overall quality is poor, with significant noise and low contrast, making the content unreadable. The markings on the left side seem to be organized in a structured manner, possibly as a list or table, but the details are lost. The right side also contains faint, scattered markings.

PHY-1995-D--SIN-STU